

ELECTROCHEMICAL STUDY OF CORROSION PHENOMENA IN ZIRCONIUM ALLOYS

by

Nicole M. Treeman
Lieutenant, United States Navy

B.S. Civil Engineering 1997
Worcester Polytechnic Institute

Submitted to the Department of Nuclear Engineering
in Partial Fulfillment of the Requirements for the Degrees of

Nuclear Engineer's Degree

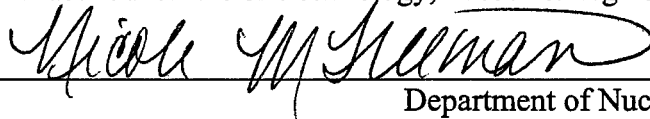
and

Master of Science in Nuclear Engineering
at the
Massachusetts Institute of Technology

June 2005

© Massachusetts Institute of Technology, 2005. All rights reserved.

Signature of Author: _____



Department of Nuclear Engineering
May 20, 2005

Certified by: _____



Ronald G. Ballinger, Sc.D.

Professor of Nuclear Science and Engineering and Material Science and Engineering
Thesis Supervisor

Certified by: _____



Ronald M. Latanision, Ph.D.

Professor Emeritus of Material Science and Engineering
Thesis Reader

Accepted by: _____



Jeffrey A. Coderre, Ph.D.

Associate Professor of Nuclear Science and Engineering
Chairman, Committee for Graduate Students

DISTRIBUTION STATEMENT A

Approved for Public Release
Distribution Unlimited

20060516056

ELECTROCHEMICAL STUDY OF CORROSION PHENOMENA IN ZIRCONIUM ALLOYS

by
Nicole M. Treeman

Submitted to the Department of Nuclear Engineering
on May 20, 2005 in Partial Fulfillment of the
Requirements for the Degrees of
Nuclear Engineer
and
Master of Science in Nuclear Engineering

Abstract

Shadow corrosion of zirconium alloy fuel cladding in BWR environments, the phenomenon in which accelerated corrosion is experienced when the cladding surface is in close proximity to other metals, has become a potentially life-limiting issue for BWR fuel. Recent results from experimentation at MIT, Halden, and Studvik suggest that a galvanic coupling drives the phenomenon between the cladding and the adjacent material. However, the actual processes involved are not understood. One key parameter that would help in the understanding of the phenomenon would be a measurement of the actual corrosion current between fuel cladding and adjacent materials in the actual in-reactor environment.

The limitations placed on the burn-up of uranium oxide fuel correlates to the amount of corrosion seen through a directly measurable oxide thickness on the waterside of the zirconium alloy cladding. This oxide corrosion product directly correlates to distance from structural components, leading to the effect commonly referred to as shadow corrosion. In recent experiments, Studvik determined that there are large ECP differences associated with Inconel and zirconium alloys that correlate to increased galvanic current density when the materials are coupled.

In this thesis research, four electrode pairs were used to measure galvanic current densities in the irradiation environment: Pt-Pt, Zircaloy 2 (Zr-2)-Pt, Inconel (X-750)-Pt, and Zr-2-X-750. To determine the changes in the coolant water conductivity due to the presence of radiolysis products, electrochemical potential measurements of Pt-Pt coupled electrodes were analyzed. Finally, attempts to characterize the observed oxide behavior using measurements from Electrochemical Impedance Spectroscopy (EIS), also known as Alternating Current Impedance, were conducted.

Through the measurements taken, analysis of the mechanisms potentially causing the shadow corrosion phenomenon was conducted. The results of the observations included:

- Measurement of increased conductivity of coolant water correlating to increases in reactor power.
- Measurement of increased galvanic current measurements correlating to increases in reactor power.

Thesis Supervisor: Ronald G. Ballinger

Title: Professor of Nuclear Engineering and Material Science and Engineering

Dedication and Acknowledgements

This experiment would not have been possible without the initial hypothesis and experimental design of Il Soon Hwang of Seoul National University. His guidance and patience in mentoring my early understanding of electrochemical affects of corrosion and alternating current impedance were instrumental in the execution and analysis of this experiment.

The funding for this experiment was provided by Electric Power Research Institute, Inc. (EPRI) and Kurt Edsinger.

I also extend my gratitude to Kevin Miu for his assistance with the initial Visual Basic® programming and Pete Stahle for his revisions to the program during in-core experimentation. I would also like to thank Pete for his assistance in design, assembly, and installation of the experimental assembly. Additionally, the in-core experimental support, along with advice regarding handling radiological material, of Dr. Gordon Kohse and Yakov Ostrovsky greatly broadened my scope of knowledge.

I would also like to thank the Nuclear Reactor Operations staff, particularly Ed Lau, for their support during experimentation. I would also like to thank the Reactor Radiation Protection Program staff, Fred McWilliams, Beth Rice, Doug LaMay, and Rich Dresios, for their assistance in training me for reactor access to conduct experimentation, radiation safety, and activity calculations for the experiment approval.

Finally, I would like to express my deepest gratitude to Professor Ron Ballinger. His direct and candid guidance greatly shaped this experiment and my MIT experience. His ability to instill confidence enabled me to obtain my educational goals at MIT. I look forward to his interaction with my future career in Navy Nuclear Power.

I dedicate this manuscript to my husband, Loren Reinke, and our daughter, Ariadne Treeman-Reinke. Your unending support, understanding, and love gave me the strength and courage to obtain my goals. I am truly blessed and thankful to have you in my life.

Table of Contents

ABSTRACT.....	3
DEDICATION AND ACKNOWLEDGEMENTS.....	4
TABLE OF CONTENTS	5
1. INTRODUCTION AND BACKGROUND	8
1.1. ZIRCONIUM IN THE NUCLEAR INDUSTRY	8
1.2. DEFINITION OF THE SHADOW CORROSION PHENOMENA	9
1.3. METALLURGICAL BACKGROUND.....	10
1.3.1. STRUCTURAL AND COMPOSITIONAL PROPERTIES OF ZIRCONIUM ALLOYS	10
1.3.2. HISTORY OF USE OF ZIRCONIUM ALLOYS AS NUCLEAR FUEL CLADDING.....	12
1.3.3. IDENTIFIED LIMITATIONS OF ZIRCONIUM ALLOYS IN NUCLEAR ENVIRONMENTS.....	13
1.3.4. CURRENT TRENDS OF IMPROVEMENT IN ZIRCONIUM ALLOYS	15
1.4. IMPACT ON DESIGN AND LICENSING.....	16
1.5. NRC CONCERNS.....	17
1.6. PAST DEVELOPMENTS IN UNDERSTANDING THE SHADOW CORROSION PHENOMENA	18
1.7. NRC DOCUMENTATION	19
1.8. THESIS PROBLEM DESCRIPTION	21
1.9. OUTLINE OF THIS THESIS	21
1.10. REFERENCES.....	22
2. ELECTROCHEMICAL ANALYSIS	25
2.1. ELECTROCHEMICAL POTENTIAL	25
2.2. GALVANIC CURRENT	26
2.3. ALTERNATING CURRENT IMPEDANCE.....	27
2.4. REFERENCES.....	31
3. EXPERIMENTAL DESIGN	32
3.1. DESIGN OF THE ELECTROCHEMICAL MEASUREMENT ASSEMBLY AND EXPERIMENT	33
3.1.1. ELECTROCHEMICAL MEASUREMENT EQUIPMENT.....	36
3.2. COMPUTER PROGRAMS	38
3.3. EXPERIMENTATION IN LABORATORY ENVIRONMENT	39
3.4. MITR-2 CHARACTERISTICS.....	40
3.5. REFERENCES.....	45
4. EXPERIMENTAL RESULTS AND DISCUSSION	46

4.1.	GALVANIC CURRENT DATA GATHERED.....	46
4.2.	CONDUCTIVITY DATA GATHERED	48
4.3.	GALVANIC CURRENT AND CONDUCTIVITY ANALYSIS	52
4.4.	OBSTACLES ENCOUNTER DURING EXPERIMENTATION	53
4.5.	REFERENCES.....	56
5.	<u>CONCLUSIONS.....</u>	<u>57</u>
5.1.	REITERATION OF HYPOTHESIS	57
5.2.	COMPARISON OF EXPERIMENTAL RESULTS WITH EXPECTED RESULTS	57
	<u>APPENDIX A – PT-PT COUPLE GRAPHS</u>	<u>59</u>
	<u>APPENDIX B – ZR-PT COUPLE GRAPHS</u>	<u>77</u>
	<u>APPENDIX C – X750-ZR COUPLE GRAPHS</u>	<u>95</u>
	<u>APPENDIX D – X750-PT COUPLE GRAPHS.....</u>	<u>113</u>
	<u>APPENDIX E – ECP DATA.....</u>	<u>131</u>
	<u>APPENDIX F – GALVANIC DATA</u>	<u>134</u>

List of Figures

Figure 1.1 Zr-O Phase Diagram [1.6]	11
Figure 2.1 Ideal Nyquist Plot	29
Figure 2.2 Ideal Bode Plots	30
Figure 3.1: Top down view of specimen arrangement in module [3.1]	33
Figure 3.2: Side view of specimen arrangement in module [3.1]	35
Figure 3.3: Electrochemical monitoring equipment arrangement	37
Figure 3.4 Reactor Top [3.2]	40
Figure 3.5 Coolant Flow through Rig (Note: Not to scale)	42
Figure 3.6 Letdown system from experimental assembly to recirculation pump [3.1]	43
Figure 3.7 Charging tank, letdown monitoring equipment, and chemistry control area	44
Figure 4.1 Galvanic Current V. Reactor Power	46
Figure 4.2 Zircaloy-2 Resistance V. Time in Reactor	47
Figure 4.3 Resistivity Comparison between Zircaloy- 2 and X-750 at 4 MW	48
Figure 4.4 Pt-Pt correlation chart	49
Figure 4.5 Coolant Conductivity, as measured by Pt-Pt electrode, V. Reactor Power	50
Figure 4.6 Letdown Conductivity Measurement V. Reactor Power	51
Figure 4.7 Coolant Conductivity, as measured by Pt-Pt electrode, V. Time at 4 MW Power	52
Figure 4.8 Zr-2-Pt Measured Galvanic Current V. Pt-Pt Measured Conductivity	53
Figure 4.9 Zr-2-X-750 Measured Galvanic Current V. Pt-Pt Measured Conductivity	53

List of Tables

Table 1.1 Alloying elements in Zircaloy 2 and 4	11
Table 1.2: Thermal properties of Zircaloy 2 (α phase) [1.13]	17
Table 4.1: Experimental Conditions	55

1. Introduction and Background

1.1. *Zirconium in the Nuclear Industry*

As the nuclear industry grew into a feasible and economical means of providing power for the propulsion of Navy ships and submarines, electrical generation for municipal and industrial use, and innovative means for medical and scientific research, requirements for improving the fuel used arose. Due to natural availability, uranium was the chosen fuel; however, it suffered from significant limitations. Uranium in pure form, like many metals, is highly reactive, particularly in the aqueous environment expected in a nuclear reactor [1.1]. The high rate of corrosion experienced by uranium, possibly leading to flaking of oxidized particles that potentially can become entrained in the water cycle of a nuclear reactor leading to widespread contamination issues, lead to the exploration of uranium dioxide (UO_2) as fuel. While UO_2 is far less reactive, since oxidation has already taken place, a new concern arose. This concern relates directly to the fission process and containment of radioactive fission products.

During the fission process, the binding energy of an atom changes due to the energy of the interacting neutron. Neutron interaction can lead to the original (parent) atom either splitting into two new atoms, with the release of a subsequent neutron to decrease the Z – number (the sum of the neutrons and protons in the atomic nucleus) back to more stable value, or in the form of decay. There are three primary forms of decay: α , β , and γ . γ - decay is the emission of high-energy photons. β - decay is the emission of an electron or positron for which the Z - number of the atom remains constant, but the atomic (A) number increases or decreases by one. The predominant decay is β – decay, or electron emission. The final decay type is α – particle emission, in which a ^4He ion is released. In each of the decay processes, the created (daughter)

atom may be unstable, leading to subsequent decay of various elemental isotopes with independent properties.

Due to the various properties of the parent and daughter atomic isotopes, it became important to be able to isolate the fission products from the remainder of the plant systems and external environment. The proposed means was to sheath the fuel in a second, non-reactive alloy with high corrosion resistance and low neutron affinity. The two alloys recommended were stainless steel and zirconium. Both alloys provided high corrosion resistance and the ability to withstand the high temperatures and stresses present within a nuclear reactor. However, stainless steel has a significantly higher affinity for thermal neutrons, meaning that more uranium would need to be fissioned to create enough neutrons to sustain required reaction rates [1.1]. Based predominantly on this fact, zirconium alloys were chosen to sheath, or clad, the fuel.

With the increasing demand for cleaner, efficient, and more reliable forms of energy, the nuclear industry continues to explore ways to maximize the utilization of fuel while minimizing the amount of hazardous waste produced. With innovative fuel management schemes developing to match current burn-up allowances, the nuclear industry continues to seek safe means to increase burn-up. One of the limiting factors for fuel burn-up is the amount of corrosion of the zirconium alloy cladding. This corrosion occurs in several forms, but one unique form of particular interest is the so-called shadow corrosion.

1.2. Definition of the Shadow Corrosion Phenomena

One of the potentially most system limiting forms of zirconium alloy corrosion is shadow corrosion. Shadow corrosion is a localized form of “normal” oxidation in which the rate of oxidation is accelerated due to the presence of a “shadowing” material in proximity in an irradiation environment. However, the causes of shadow corrosion continue to elude scientists

and industry managers alike, first identified over three decades ago. Observations of metallic materials near the Zircaloy indicate that the Zircaloy is often less noble than the corresponding metallic structure and the corresponding corrosion mirrors the form of the more noble component [1.2].

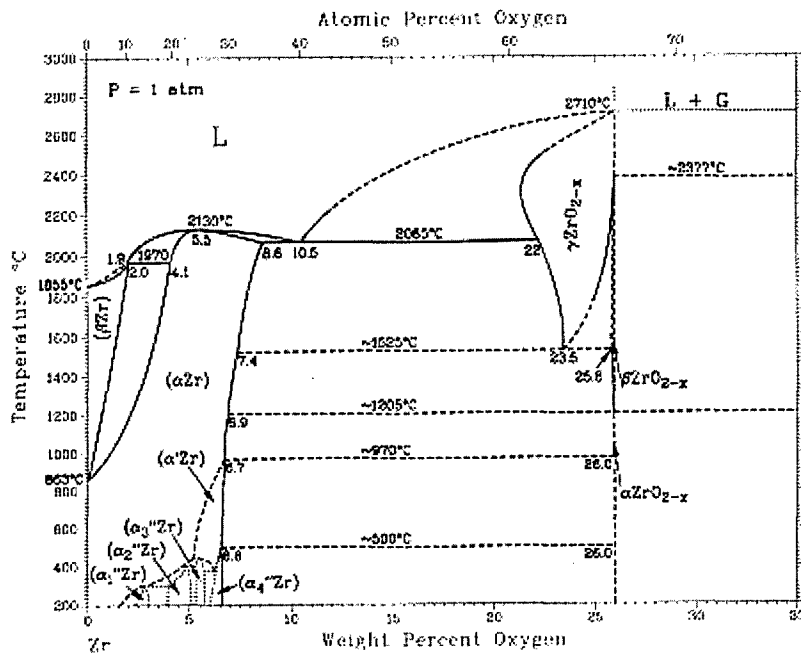
In early investigations of shadow corrosion, the phenomena appeared to be closely related to common nodular corrosion. Nodular corrosion, in BWRs, is attributed to the radiolysis and boiling process enabling oxygen accumulation in the environment. However, nodular corrosion is greatly reduced with rigorous control of second-phase particle size and adjustment of annealing times after a late β -quench during cladding fabrication [1.3].

1.3. Metallurgical Background

1.3.1. Structural and Compositional Properties of Zirconium Alloys

Zirconium use as cladding material in nuclear reactors emerged in the mid-1950s and expanded rapidly as commercial water reactors entered the power industry [1.4]. Pure zirconium exhibits characteristics that make it a desirable choice for use as a material in nuclear reactors. However, zirconium has high reactivity with oxygen and, in the form used for fuel cladding, exhibits a strongly anisotropic hexagonal close packed (HCP) crystal structure. Pure zirconium at room temperature and pressure crystallizes an α phase of the hexagonal close packed structure [1.5]. Figure 1.1 shows a Zr-O phase diagram. The phase diagram indicates that at the expected operational temperatures of 288°C, zirconium remains in the α phase. The lattice parameters for the α phase are $a = 3.2312 \text{ \AA}$ and $c = 5.1477 \text{ \AA}$. The β phase of zirconium is body centered cubic, and begins to form at the grain boundaries of the α phase crystals when the metal is heated above 866°C [1.7]. The lattice parameter for the β phase of zirconium is $a = 3.6090 \text{ \AA}$ [1.8].

Figure 1.1 Zr-O Phase Diagram [1.6]



However, pure zirconium is soft and demonstrates lower corrosion resistance than stainless steel alloys in high temperature, aqueous environments due to the oxide becoming non-adherent. In order to improve the expected performance of zirconium, alloys were created to improve yield and tensile strength, as well as corrosion resistance [1.9]. The most commonly used zirconium alloys are Zircaloy 2 or 4, for which the chemical compositions are provided in Table 1.1 [1.8].

Table 1.1 Alloying elements in Zircaloy 2 and 4

Alloying Element	Zircaloy 2 (weight %)	Zircaloy 4 (weight %)
Tin	1.20 – 1.70	1.20 – 1.70
Iron	0.07 – 0.20	0.18 – 0.24
Chromium	0.05 – 0.15	0.07 – 0.13
Nickel	0.03 – 0.08	----
Zirconium	Balance	Balance

Both Zircaloy 2 and 4 exhibit recrystallized microstructures at room temperature that consist of equiaxed grains (equal size in all three orthogonal directions) of α phase Zr with Sn in solid solution and the other alloying elements forming intermetallic compounds with Zr [1.8]. The deficient properties experienced in using pure zirconium as cladding are remedied through using the alloying elements. Some elements earlier thought to be impurities also impact some of the deficiencies of using pure zirconium. The addition of tin to the Zircaloy aids in the α phase stabilization, increases corrosion resistance, and strengthens the alloy. The remaining alloying elements, iron, chromium, and nickel, also promote corrosion resistance. Several elements originally thought to act solely as impurities in Zircaloy are oxygen, carbon, and silicon. Oxygen has since been found to serve as a solid solution strengthener and α phase stabilizer. During β heat treatments, carbon helps in attaining the right texture, while silicon results in improved corrosion resistance [1.8]. Given the expected nuclear reactor environment of 250-350°C, with pressures nominally around 7 MPa for boiling water reactors (BWRs) and 15 MPa in pressurized water reactors (PWRs), it can be expected that zirconium alloys will remain in the α phase, or hexagonal close packed structure.

1.3.2. History of Use of Zirconium Alloys as Nuclear Fuel Cladding

As nuclear power gained momentum, designs emerged utilizing water as a coolant and moderator. Despite the lower reactivity of UO_2 as a fuel, concerns remained about containment of the fission and corrosion products in the coolant. Initial decisions regarding the use of a second material to serve as a protective sheath evolved. The characteristics of the sheathing material stemmed from required performance criteria: good operational performance in a high temperature, aqueous environment; low susceptibility to corrosion in a high temperature,

aqueous environment; and low absorption cross section for thermal-spectrum neutrons.

Zirconium was one of the of elemental metals meeting these requirements [1.9].

Initial tests indicated that zirconium corrosion behavior depended on the orientation of the individual grains or texture of the material. The fabrication texture resulted in regions of nodular corrosion predominantly on grain boundaries between two grains demonstrating lower oxidation rates. Using transition metals to alloy the zirconium reduced the occurrence of nodular corrosion, leading to the development of a more uniform oxide layer less susceptible to spalling [1.3].

With the trends to reactor designs requiring higher temperatures and pressures, and the economics of operating reactors driving operators to push for higher burnups and hence enrichments, the NRC continues to investigate the limitations of current claddings. While Zr-based alloys do have significant neutronic advantages compared to stainless steels, the more extreme operating conditions, coupled with the limitations from shadow corrosion and other means of corrosion, cause concern from a regulatory standpoint. Changes in the properties of the cladding include embrittlement, higher internal pin pressure from built up fission product gases, and fuel expulsion during reactivity initiated accidents. The nature of these limitations derives, in significant part, from the limitations of the zirconium alloys.

1.3.3. Identified Limitations of Zirconium Alloys in Nuclear Environments

One of the elements originally considered an impurity was oxygen. This element greatly affects the slip behavior of the alloy in proportion to its concentration within the matrix. However, the interaction of the aqueous environment is important to create the oxide layer that serves as protection from further corrosion. This oxide layer creates a passive region resistant to corrosion, but reduces the amount of base material in the cladding. This reduction in the original

alloy thickness is further aggravated by cracking of the protective oxide layer, leading to increased localized corrosion. The creation of this oxide layer also creates vacancies within the base alloy, potentially leading to changes in the mechanical properties of the alloy. The concentration of vacancies leads to increased diffusion paths for strained atoms leading to higher creep rates. This creep can lead to excessive plastic deformation.

The injected vacancies from the removal of a metal ion into the oxide layer have multiple potential paths. One is in-situ vacancy annihilation at the oxide/alloy interface. If this annihilation does not occur, then the vacancy may precipitate out and can contribute to void formation [1.10]. The voids created, or grown, affect the corrosion resistance, mechanical, and thermodynamic properties of the alloy. This includes elevated levels of oxygen in the alloy just beneath the oxide layer leading to reduced ductility and fracture toughness [1.11].

In addition to the elevated levels of oxygen, irradiation of zirconium alloys creates "black-dot," or clusters of irradiation created, defects, small dislocation loops, short line dislocations, and dislocation entanglements [1.11]. The three dislocation related defects occur on the prismatic plane with an $\langle a \rangle$ - type Burgers vector at lower fluences, and associated fuel burnup. Burnup is the measurement of the amount of fissile uranium consumed during the fission process. At higher burnups (fluence), there is an increase in mechanical disturbance leading to breakaway oxidation, breakaway creep and growth, decreases in ductility, and increases in brittle-type fracture behavior [1.11].

The exposure of metallic materials in the nuclear environment can lead to unique phenomena. A crystal lattice can be easily described as atomic nuclei occupying lattice sites with a sea of electrons filling the remaining volume. This configuration allows for entrance of alpha particles and high-energy neutrons into the lattice. The alpha particles tend to congregate

in regions around voids and other defects leading to pockets of helium and alteration of creep behavior within the crystal.

The high-energy neutrons, in the simplest sense, act like a billiard ball striking one nucleus and potentially jarring it loose from its lattice site. This now-free atom may interact with other lattice sites or become a self-interstitial. In either case, this potentially raises the energy of the crystal and leads to easier corrosion of the lattice.

As an alloy is exposed to a flux of high-energy particles, displacement of the original elements creates dislocations and other crystalline defects affecting the mechanical and crystalline properties of the alloy. With oxidation creating the potential for supersaturation of vacancies in the base alloy, along with collection of vacancies into voids, and increasing the oxygen content in the region below the oxide layer, the properties of the alloy greatly change with increased fuel burnup. The natural corrosion, exacerbated by the impinging high-energy neutrons, also enables diffusion of hydrogen into the alloy creating embrittlement or diffusion of fission products into the overall system or environment. While the processing of the alloy cladding is accomplished to align the texture for best strength and desired properties, including annealing to reduce initial existing defects, there are other means of improving the alloy itself. Through exploration of different alloying compositions with elements added to assist in corrosion resistance and diffusion mitigation, the goal of developing a clad material allowing for higher burnup and higher fuel efficiency may be achieved.

1.3.4. Current Trends of Improvement in Zirconium Alloys

While general corrosion is alleviated through the tailoring of precipitates and other characteristics of the alloy, there have been observances of increased localized corrosion. This corrosion has been partially reduced through additions of various alloying elements that change

the precipitates formed. One of the emerging elements is Nb, which reduces localized corrosion through preferential corrosion of precipitates, dependent on the amount of Nb added with respect to the saturation levels within the alloy [1.12].

Many of the traditional means of altering the crystalline structure through annealing, cold working, and/or quenching fail to maintain long-term viability in the nuclear environment. The fluctuations of thermal stresses from different operational states create dynamic situations with regard to failure mechanisms, such as creep, and creation of means for greater dislocation interaction potentially changing the material through hardening mechanisms, creation of Frank-Reed sources, or diffusional paths for impurity atoms. The interaction with impinging neutrons and alpha particles leads to the creation of vacancies and interstitials, along with their affects on structure and mechanical properties. These neutrons may also interact with water creating radiolysis products, potentially changing the water chemistry in LWR coolant channels.

1.4. Impact on Design and Licensing

The fuel costs per fuel cycle derive from the cost of yellowcake and processing. Once the facility is built and operating within design capacity, the cost of processing remains constant, the changes in fuel costs remain primarily dependent on the price for yellowcake the manufacturer paid. Typical fuel cycles center on a refueling period ranging from 12 to 24 months, with the majority operating with an 18-month period. Dependent on the minimization of the number of required shutdowns for refueling, and maximization of fuel burn-up, the percentage of the fuel rods replaced also varies.

Typical water-cooled reactor designs include fuel enrichment around 3% U-235, with the balance principally comprised of U-238 [1.13]. American enrichment plants typically use a gaseous diffusion process. After the fuel is entered into the reactor core for two to three

refueling cycles, depending on the planned rotation, the burn-up limit prior to discharge is driven by the average burn-up of the peak rod, set at 60 gigawatt-days per ton of heavy metal [1.14].

In addition, the NRC imposes limitations over the operation of the reactor. These limitations, imposed to assure safety of the overall system including cladding, include average cladding temperature less than 1200°C (roughly 2200°F) during a LOCA for BWRs and PWRs and no incipient melting of the fuel at centerline temperature during normal operation. The typical operating temperatures of BWRs and PWRs are in the vicinity of 300°C. This is significantly lower than the melting point of Zircaloy 2, seen in Table 1.2.

Table 1.2: Thermal properties of Zircaloy 2 (α phase) [1.13].

Property	Zircaloy 2
Density (kg/m ³)	65,000
Melting Point (°C)	1850
Linear thermal expansion coefficient (/°C)	5.9 x 10 ⁻⁶
Thermal conductivity (W/m°C)	13 (400°C)

1.5. NRC Concerns

NRC limitations on fuel burnup extend beyond the concerns of oxide thickness of fuel cladding. Among the additional concerns, two dominated this research: core component bowing and cladding degradation. Both of these concerns have direct relation to shadow corrosion.

Core component bowing, and its associated hazards, were identified as a concern to the NRC through an Information Notice in September of 1989 [1.15]. Initial causes were determined to be from ineffective modeling and the increased oxidation of fuel rods near once-burned assemblies with highly exposed fuel channels [1.15]. Although alteration of licensing

limits and core design has occurred, successful modeling and mitigation of shadow corrosion was developed in response to the bowing reported in 1989. However, in March of 2003, GE reported that new data suggested shadow corrosion caused bowing in a channel near a control rod blade [1.16].

Cladding degradation is the second readily noted affect of shadow corrosion. The NRC limits the predicted fuel rod oxidation in order to increase the reliability of fuel cladding integrity during accident scenarios. The limitation on acceptance criteria, in accordance with 10 CFR 50.46(b) is that the maximum total oxidation of the cladding is not to exceed 0.17 times the total thickness of the cladding before oxidation. The intent of this limitation is to reduce the expectation of brittle fracture, and subsequent rupture, of fuel cladding due to the alterations in the cladding properties. Since it has been noted that both irradiation time and temperature influence oxidation, the study of shadow corrosion easily lends itself to investigation of proposals to alter existing NRC criteria.

1.6. Past Developments in Understanding the Shadow Corrosion Phenomena

An initial characteristic observed regarding shadow corrosion is the dependence of the phenomenon on irradiation. The predictability of Zircaloy thickness changes when the sample is exposed to a radiation environment. Early explanations identified the possibility that the activation of materials, inducing increased β radiation, enhanced the oxide growth in the form of shadow corrosion. However, experimentation conducted at MIT concluded that this was not the instrumental factor, but indicated a strong electrochemical component to the phenomenon [1.17].

Despite the indications of an electrochemical aspect of shadow corrosion, difficulties in replication of the phenomenon ex-core through experimentation indicated additional variables were at play [1.18]. Since the elimination of the β radiation hypothesis, tests at Halden and

Studvik have further examined the criteria for shadow corrosion. The Halden test reactor performed two testing cycles, one in 1998 and the other in 1999, designed to test the effects of spacers and geometry on shadow corrosion. The results of the Halden and MIT tests demonstrated the inverse proportionality of distance between the "shadowing" component and the Zircaloy to oxide thickness [1.18].

Also demonstrated in these tests was the electrochemical effect, which appears to be a galvanic couple augmented by irradiation damage to the oxide layer enhancing the growth rate and possibly electron transport assistance from γ radiation [1.19]. The latest experimentation from Studvik offers continued support for galvanic corrosion, with two notable discrepancies [1.19]. The first discrepancy is that there is no apparent coupling device for Zircaloy and other materials in-core. The second discrepancy is that there is no increased corrosion when Zircaloy is coupled to a dissimilar metal in ex-core experimentation. Through experimentation with electrically isolated samples using sapphire, the galvanic corrosion aspect of shadow corrosion was suppressed. The same experiment also provided support for the theory that photoconductivity, a form of electromagnetic radiation effect, participates in the phenomenon [1.19].

1.7. NRC Documentation

As previously stated, the NRC has identified the issue of shadow corrosion as a factor in the limitation of the allowable burn-up of fuel due to the uncertainty in oxide thickness. In non-irradiated environments, zirconium and its alloys form a protective oxide layer that serves as an effective barrier to corrosion. This oxide layer serves as an electrical insulator that prohibits the transfer of electrons from the metallic matrix into the aqueous medium, while prohibiting the adsorption of oxygen to the surface limiting continued oxide formation. In non-irradiated

environments, the limitation on observed, effective ion transport from the primary metal matrix through the oxide to the aqueous solution occurs at approximately two nm [1.20].

The primary characteristic of the oxide that creates this limitation is the susceptibility to spalling. However, the first action by the NRC found in the precursor research for this report came in the form of an Information Notice issued in September 1989 [1.21]. In the Notice 89-69 (Loss of Thermal Margin Caused by Channel Box Bow), initial causes cited included inaccurate modeling and estimates of the minimum critical power ratio. However, in August of 2003, the NRC issued a supplement to the original finding stating that although alterations in modeling and analysis, initial manufacturing of fuel and cladding, and differential irradiation growth mitigated channel box bowing, shadow corrosion also induced the condition [1.15].

In compliance with 10 CFR 21.21(a)(1) GE Nuclear Energy (GENE) issued a notification regarding the proof that shadow corrosion also contributes to fuel channel bow [1.22]. Tied to the channel bow is the position of the control blade with respect to the channel during the initial fuel cycle. The comments made in the report state that the fuel channel experience absorbed hydrogen –induced growth of the channel wall closest to the control blade resulting in bowing later in component life. The principal causes of the increased shadow corrosion correlate to the criteria for galvanic corrosion: larger cathodic region when compared to the anode and smaller gap between the control blade and the fuel assembly. In the case reported, the BWR/6 lattice, noted to be afflicted by shadow corrosion-induced bowing, the control blade is larger than blades characterized in modeling and the gap between the blade and fuel assembly is uniquely smaller.

The findings observed in Studvik, Halden, and MIT experimentation, as well as the observations from the GENE report, assisted in formation of a hypothesis for experimentation

and a related thesis. The primary goal of the experimentation was to explore the possible existence of galvanic current between Zircaloy and dissimilar metals in the irradiation environment. This current is expected to result from alterations in the conductivity measured in the coolant water and/or the materials themselves. Lastly, the final goal was an attempt to measure the oxide characteristics through electrochemical impedance spectroscopy (EIS).

1.8. Thesis Problem Description

In order to support the galvanic current aspect of the hypothesis on the causes of shadow corrosion, an electrochemical experiment measuring the potentials and currents between samples of Pt, Zircaloy-2 (Zr-2), and Inconel (X-750) was conducted. The primary goals of this experiment and subsequent thesis were to reinforce the findings of the evidence of the galvanic couple dependency for shadow corrosion and the changes in the coolant due to radiolysis. In order to accurately provide evidence of the galvanic couple, measurements of the reduction in the conductivity of the high purity, low conductivity water used as coolant were conducted through the use of a Pt-Pt electrode couple.

1.9. Outline of this thesis

In this chapter we introduced the concept of shadow corrosion, provided background on the motivation for the research conducted, and presented the initial hypothesis.

Chapter 2 discusses the methodology and background of electrochemical analysis including electrochemical potential and galvanic current measurement. Also included in this chapter are the relation of these characteristics with respect to corrosion, means of measurement available, and expected values from experimentation.

Chapter 3 discusses the experimental design. Included in this chapter are the characteristics of MITR-2, MIT's research reactor, design of the assembly used in-core and ex-core, and supporting equipment. Incorporated with the supporting measurement equipment are the computer codes used in the analysis and data collection.

The fourth chapter covers the results obtained from in-core and ex-core experimentation, including obstacles encountered in experimentation. Chapter 5 conducts an analysis of the results given in Chapter 4.

Finally, Chapter 6 gives the conclusions from the experimentation, including deviations from expectations and recommendations for future work to further investigate the phenomenon of shadow corrosion.

1.10. References

- [1.1] Adams Atomic Engines, Inc., Protection for Fuel Elements: Ensuring Safety, http://www.ans.neep.wisc.edu/~ans/point_source/AEI/dec95/cladding.html, Atomic Energy Insights, Volume 1, Issue 9, December 1995.
- [1.2] Ramasubramanian, N., Shadow Corrosion, Journal of Nuclear Materials 328 (2004), pages 249-252.
- [1.3] Zirconium in the Nuclear Industry, Proceedings of the 4th International Conference, held at Stratford-upon-Avon, England, June 26-29, 1978, ASTM STP-681.
- [1.4] Hixson, Robert S., George T. Gray, and Dennis B. Hayes, Shock Compression Techniques for Developing Multiphase Equations of State, <http://www.fas.org/sgp/othergov/doe/lanl/pubs/las28/hixson.pdf>, Los Alamos Science, Number 28, 2003.

- [1.5] Sandvik Special Metals Corporation, Zirconium Alloy Fuel Clad Tubing: Engineering Guide, First Edition, December 1989.
- [1.6] ASM International, Binary Alloy Phase Diagrams, Volume 3, 1990.
- [1.7] International Nuclear Safety Center, "Zircaloy Heat Capacity," http://www.insc.anl.gov/matprop/zircaloy/zircp/fmt_html.pdf, Nov. 13, 1997.
- [1.8] O'Donnell, J. R., Design, Construction, and Commissioning of an In-core Materials Testing Facility for Slow Strain Rate Testing, Ph. D. Thesis, Massachusetts Institute of Technology, September 1994
- [1.9] Cox, B., Some thoughts on the mechanisms of in-reactor corrosion of zirconium alloys, Journal of Nuclear Materials, 336 (2005), pages 331-368.
- [1.10] Gibbs, G. B. and R. Hales, The Influence of Metal Lattice Vacancies on the Oxidation of High Temperature Materials, Corrosion Science, Volume 17, 1977.
- [1.11] Chung, H. M. and T. F. Kassner, Cladding metallurgy and fracture behavior during reactivity-initiated accidents at high burnup, Nuclear Engineering and Design, Volume 186, Issue 3, December 1998.
- [1.12] Nikulina, A. V., Shebaldov, P. V., Shishov, V. N., Peregud, M. M., Ageenkova, L. E., Rozhdestvenskii, V. V., Solonin, M. I., Bibilashvili, Yu. K., Lavrenyuk, P. I., Lositskii, A. F., Ganza, N. A., Kuz'menko, N. V., Kotrekho, V. A., Shevnin, Yu. P., Markelov, V. A., "Zirconium-based alloy containing Nb, Fe, O, Si, Ni, and C for nuclear reactor core components," US Patent Application, US6776957, 1999.
- [1.13] Todreas, Neil E. and Mujid S. Kazimi, Nuclear Systems I: Thermal Hydraulic Fundamentals, Hemisphere Publishing Corporation, 1990.

- [1.14] NRC Meeting transcript, Briefing on High-Burnup Fuel Issues, <http://www.nrc.gov/reading-rm/doc-collections/commission/tr/1997/19970325a.html>, March 25, 1997.
- [1.15] NRC Information Notice 89-69, Loss of Thermal Margin Caused by Channel Box Bow, <http://www.nrc.gov/reading-rm/doc-collections/gen-comm/info-notices/1989/in89069.html>, September 29, 1989.
- [1.16] NRC Event Notification Report, <http://www.nrc.gov/reading-rm/doc-collections/event-status/event/2003/20030609en.html>, June 9, 2003.
- [1.17] Châtelain, Anthony R., Enhanced Corrosion of Zirconium-Base Alloys in Proximity to Other Metals: the "Shadow Effect", S.M. Thesis, Massachusetts Institute of Technology, MA, February 2000.
- [1.18] Andersson, B., M. Limbäck, G. Wikmark, E. Hauso, T. Johnsen, R.G. Ballinger, and A.-C. Nystrand, Test Reactor Studies of the Shadow Corrosion Phenomenon, Zirconium in the Nuclear Industry: Thirteenth Symposium, pages 583-613.
- [1.19] Lysell, Gunnar, Ann-Charlotte Nystrand, and Mats Ullberg, Shadow Corrosion Mechanism of Zircaloy, ASTM, 2002.
- [1.20] Cox, B., Mechanisms of Zirconium Alloy Corrosion in Nuclear Reactors, The Journal of Corrosion Science and Engineering, Vol.6, paper 14, 2003.
- [1.21] NRC Information Notice 89-69: Loss of Thermal Margin Caused by Channel Box Bow, September 29, 1989.
- [1.22] GENE report, Part 21 Notification: Fuel Channel Bow Reportable Condition and 60-Day Interim Notification, MFN 03-012, March 3, 2003.

2. Electrochemical Analysis

Electrochemical measurements of dissimilar metal couples in aqueous solutions are a means of understanding the rate and characteristics of observed corrosion phenomena.

Measurements to characterize the corrosion observed are either direct current or alternating current, depending on the information desired about the electrode/electrolyte system. Direct current measurements include electrochemical potential- and galvanic current-based. Alternating current measurements are commonly referred to as electrochemical impedance spectroscopy (EIS). EIS enables creation of equivalent circuits that mimic observed characteristics of the electrode internal resistivity, electrolyte conductivity, and associated Helmholtz double layers created by adsorption of electrolyte onto the surface of the electrodes. Using models developed from EIS, the nature of the oxide layer (thickness, conductivity, etc.) can be obtained.

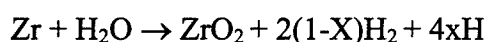
2.1. Electrochemical Potential

As dissimilar metallic electrodes are placed in contact, either directly or through an aqueous solution, there is a transfer of electrons as the electrodes take on the role of cathode or anode. As the oxidation and reduction reactions occur, a galvanic cell is developed. The electrons on the anode are released from the metallic matrix as the ions are released into the aqueous solution in the initial half-cell reaction. The second half-cell reaction, taking place on the cathode, removes the more noble ions from the solution and returns them, along with free electrons to the cathodic electrode.

The rate of the respective half-cell reactions creates a current differential between the electrodes due to the flow of electrons. The current correlates to a voltage based on the resistance inherent to the components in the electrode system. This voltage between the cathode

and anode, when no current is present, is commonly referred to as the corrosion potential. The magnitude of the cell voltage varies dependent on the metals paired as the anode and cathode. Experimental values have been measured for many of the commonly used values for standard reduction potentials of many elements, often with respect to the standard hydrogen electrode (SHE) at 25°C, 1 M or 1 atm.

The necessity for specifying the reference temperature indicates that there is a strong dependence on temperature for the potential. Also factoring into the potential are the concentrations of the oxidized and reduced species in their respective half-cell reactions. The expected reaction contributing to oxide formation on Zircaloy is seen below.



From this reaction, the potential develops and is modeled by the Nernst equation. From experimentation conducted by Cox, the potential is approximately -1.1V at 300°C and limited by the electrochemical isolation created by the oxide layer [2.1]. Without radiation, the oxide layer limits the migration of electrons from the metallic lattice effectively limiting corrosion. However, the oxide layer in irradiation fields appears to demonstrate characteristics inconsistent with the oxide formed without radiation and radiolysis products. The oxide that forms in the irradiation environment demonstrates electrochemical characteristics similar to porous oxides. This enables easier transport of electrons to the aqueous solution, leading to linear growth of oxide thickness [2.1].

2.2. Galvanic Current

The current measures the flow of electrons from one material to the other through the electrodes as the pair acts as an anode/cathode system. In this system, the corrosion rate of each electrode shifts in response to the relative electrochemical nobility of the electrode. The noble

electrode performs the role of the cathode, where reduction takes place. The anode, conversely, experiences an increase in corrosion rate.

Also affecting the corrosion rate of the anode/cathode couple is the ratio of surface areas. Ideally, it is desirable for a significantly larger anodic surface area when compared to the cathodic surface area. For the experiment conducted in this thesis research, the surface area ratio used was 1:1.

However, in addition to the surface area ratio and relative potential of each of the samples, temperature and pressure, along with the composition of the aqueous solution, affect the couple. In reactor studies, particularly those in BWRs, the coolant chemistry appears to dominate the response of the system. The characteristics of the coolant in the BWR lead to expectations that the aqueous solution used, high purity, low conductivity water, should serve as electrical insulation of the materials, thus preventing the galvanic couple from forming. However, through radiolysis, the inclusion of species, such as e_{aq}^- , H^+ , H , OH , O , HO_2 , H_2 , and H_2O_2 , alters the expected conductivity of the electrolyte. This alteration should be evident through the changes in conductivity.

2.3. Alternating Current Impedance

In many materials, using alternating current measurements of the changes in potential of corroding material reduces the effect of induced polarization or passivity experienced with direct current measurements [2.2]. The ability to measure near-actual potential values led to experiments measuring and hypothesizing about corrosion of materials based on electrolyte concentration and electrochemical characteristics of the surface of the corroding material. As a foundation of alternating current use in corrosion analysis, Warburg, in the late nineteenth century, determined that changes occur in the concentration of the oxidizing and reduced

materials with periodic regularity, corresponding to the alternation of the applied current [2.2]. Using this determination, Warburg hypothesized that the changes in concentration acted as an electrical circuit composed of a resistance and capacitance. This modeling of the electrochemical behavior of the corroding material is commonly used in development and understanding of corrosion behavior today.

Despite the desire to use EIS to observe in situ corrosion, observations illustrate that the alternating current used can alter the corrosion phenomena resulting in a shift in the polarization curves in active/passive metals, effectively removing the passive region [2.2]. Experiments investigating the shift in the polarization curves determined uncompensated ohmic drop (UOP) removed the passivity region in active/passive metals [2.3]. Other observations of the affects of EIS include increased corrosion in materials, dependent on exposure environment, e.g. electronegative metals in soil [2.2]. However, despite the observations of changes in behavior for specific materials and environments, EIS methodology evolved with procedures compensating for unwanted interactions and affects allowing determinations of the in situ behavior of many materials, enabling increased understanding of the kinetics of corrosion reactions through development of equivalent circuits. These circuits can then be used to perform elapsed time evaluations of corrosion or other virtual experiments matching the original compositions of electrode/electrolyte system measured using EIS. As many corrosion experiments are difficult to reproduce exactly, the ability to create equivalent electrical circuits allows modeling and calculations of expected corrosion behavior in different environments.

EIS is commonly used to measure general corrosion rates in terms of equivalent circuits, attributing capacitance to the Helmholtz double layer and resistance to the layer of oxide or corrosion products on the surface of the corroding material. Using corrosion monitoring devises,

such as frequency or impedance response analyzers, potentiostatic or galvanostatic controllers, and various computer programs, the measured impedance allows determination of a simple circuit to resemble the material. However, several possible circuits can model the same measured impedance. Further testing is required, along with regression-type analysis, to determine the circuit best representing the measured corrosion process for a given material. One plot commonly used in EIS is the Nyquist plot, seen in Figure 2.1, which measures imaginary vs. real impedance. This division enables identification of three primary values: polarization resistance (R_p), uncompensated resistance (R_u), and maximum phase angle (ω_{max}). R_p is the overvoltage of the system at zero current density and R_u is the resistance of the oxide layer.

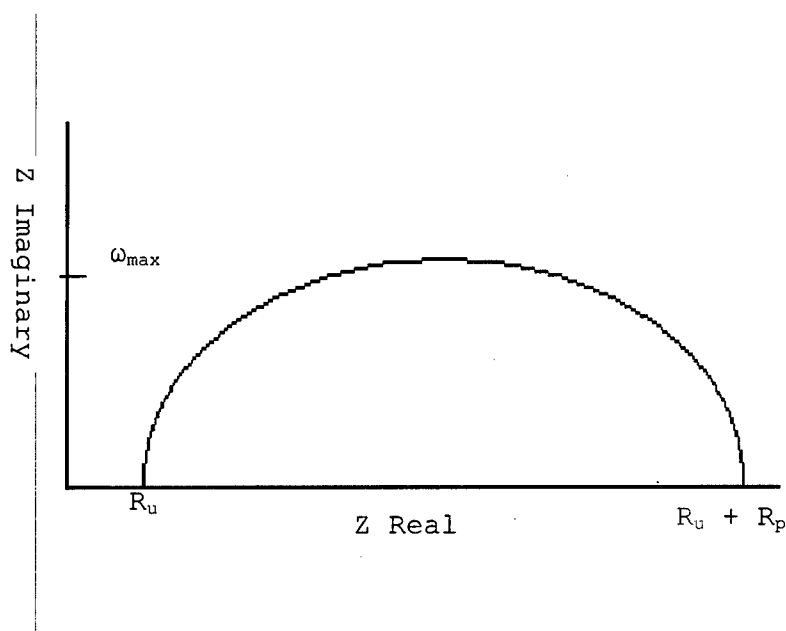


Figure 2.1 Ideal Nyquist Plot

Using the Nyquist Plot, R_p and R_u are calculated from the intersections of the plot with the real axis and the capacitance of the double layer (C_{dl}) calculated from the maximum point of the plot with respect to the imaginary axis (ω_{max}) give the basic, expected equivalent circuit. One of the advantages of EIS is that knowledge of the exact relationship between activation

polarization and the rate of reaction represented by current density, commonly referred to as the Tafel slope, for the anode and cathodes is not required. This is because the changes in the corrosion rate affecting R_p are beyond the normal range of values in most electrochemical systems [2.4]. Another advantage is the ability to compute C_{dl} directly from the Nyquist Plot. This is possible from taking the inverse of the product of R_p and ω_{max} . A second plotting method used frequently in EIS is the Bode Plot method, seen below.

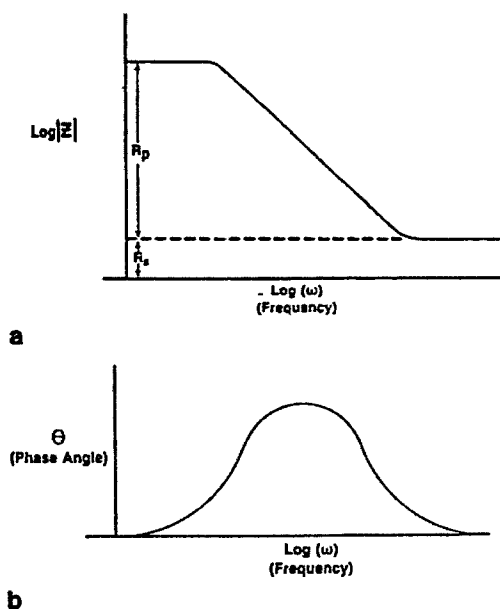


FIGURE 7 – (a) and (b): Bode type of plots of circuit in Figure 6.

Figure 2.2 Ideal Bode Plots

The two Bode Plot types consistently used from the Bode Plot method are the Bode Magnitude Plot and the Bode Phase Plot. As seen in Figure 2.2, the upper plot is the Bode Magnitude Plot, a log-log plot of the absolute value of impedance vs. frequency. The lower plot in Figure 2.2 is the Bode Phase Plot, a semi-log plot of phase angle vs. frequency. Using the Bode Plot method to find the equivalent C_{dl} is also possible. Using the Bode Phase Plot, ω_{max} found corresponds to the frequency where the magnitude of the phase angle is of greatest value.

(It is important to mention that the value of ω_{\max} in the Bode Phase Plot usually does not match the value from the Nyquist Plot.) The equation, from Kelly, et al, to calculate C_{dl} from Bode Plots is [2.4]:

$$C_{dl} = (\omega_{\max} * R_p)^{-1} (1 + R_p/R_s)^{1/2}.$$

Both the Bode Plots and Nyquist Plot created from EIS software, potentiostat, and frequency response analyzers allow for the creation of the equivalent circuit representing the electrical analog of the corroding material.

2.4. References

[2.1] Cox, B., Mechanisms of Zirconium Alloy Corrosion in Nuclear Reactors, The Journal of Corrosion Science and Engineering, Vol.6, paper 14, 2003.

[2.2] Venkatesh, S. and Der-Tau Chin, "The Alternating Current Electrode Processes", Israel Journal of Chemistry, Vol. 18, pages 56-64, 1979.

[2.3] Mansfeld, Florian, "The Effect of Uncompensated Resistance on the True Scan Rate in Potentiodynamic Experiments", NACE – Corrosion, Vol. 38, No. 10, pages 556-559, October 1982.

[2.4] Kelly, Robert G., John R. Scully, David W. Shoesmith, and Rudolph Buchheit, Electrochemical Techniques in Corrosion Science and Engineering, Marcel Dekker, Inc., New York, 2003.

3. Experimental Design

The main means of measurement of electrochemical properties involves placing samples of the metal or metal alloy to be characterized in a conductive solution, either aqueous or polymer, and measuring the potential and current between one of the samples to a second sample. Each of the samples is called an electrode, with the electrode to be measured dubbed the working electrode. Common experimental practices utilize a three-electrode system. In the standard three-electrode system, the electrode paired with an electrode called the counter electrode. The third electrode is the standard electrode, or reference electrode, and is used to provide a basis for the measurement.

The standard means of measuring the electrochemical potential is determining the difference in the voltage produced with respect to a reference. Commonly used reference electrodes, in a three-electrode system include the standard hydrogen electrode, standard silver/silver chloride electrode and standard calomel electrode. Since current was the primary variable desired, not potential, a two-electrode system was used in this work.

A two-electrode system only measures the voltage produced between the working and counter electrodes, without a reference. In order to determine the contribution of each electrode to the overall cell voltage, a series of two electrode measurements conducted between Zircaloy/X750, X750/Pt, and Zircaloy/Pt give the opportunity to determine the true electrochemical nature of the oxidation reaction in the irradiation environment. A final Pt/Pt electrode system was used to measure the conductivity of the electrolyte. In this experiment, this electrode should provide support (or non-support) of the hypothesis that the radiolysis process sufficiently alters the conductivity of the water to induce a galvanic couple between Zircaloy cladding and dissimilar metals.

In order to determine the changes in the galvanic current and the conductivity of the water, measurements were conducted using a specially designed assembly in the MIT reactor in two primary conditions: zero power and approximately 4 MW power. The zero power readings offered baseline galvanic current and potential values used to determine trends based on time and power. Additional “spot” measurements were made at 1 through 3 MW.

3.1. Design of the Electrochemical Measurement Assembly and Experiment

Figure 3.1 illustrates the arrangement of the samples selected for analysis that included Zircaloy 2 (Zr-2), a Ni-based alloy (X-750), commonly used as a structural material within the reactor core area, and Pt, known to be more noble when compared to the two alloyed materials. The sample sizes allowed for uniform exposure area of 7 cm² for each material respective to the other samples inside the experimental assembly. The constant exposure area normalizes the electrochemical values due equal area of the cathode and anode for adsorption of the electrolyte constituents for reaction.

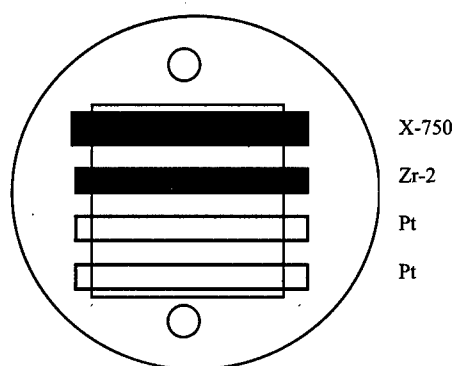


Figure 3.1: Top down view of specimen arrangement in module [3.1]

Uniform spacing of each sample at 0.7 mm and electrical isolation of the Zr-2, X-750, and Pt samples was controlled by spacers made of plastic for laboratory bench testing and alumina for autoclave and reactor testing. The size of the samples and the uniform spacing enabled a cell constant of 0.01/cm, matching a conductivity cell used in conjunction with the conductivity meter. This isolation leaves the possibility of the galvanic couple determined completely by the aqueous medium and its properties. The high purity water expected in the reactor and ex-core testing has sufficiently high resistivity contributing to the theoretical electrical isolation of the samples. However, the radiolysis products produced during irradiation are hypothesized to lower the conductivity of the water enabling the galvanic couple to occur.

The experiment required two stages of data collection: ex-core and in-core. The ex-core experimentation included bench and autoclave testing with an assembly resembling the one inserted into MITR-2. The primary difference between the assembly inserted into MITR-2 and the configuration used in the laboratory testing was the omission of the flow shielding placed around the assembly placed in the reactor to direct the flow along the length of the samples, seen in Figure 3.2. The flow shield was omitted in the autoclave experimentation in order to allow the water around the samples to freely communicate with the bulk solution.

The experimental set-up required the ability to control the flow through the experiment, ensuring near equivalency in the flow rates at each face of the specimens. The shroud used to control the flow patterns, along with the flow channel, is seen in the side view of the experimental assembly, Figure 3.2. Also seen in this diagram are the coaxial leads used to connect the specimens with the monitoring equipment in order to measure the electrochemical data during the insertion into the autoclave or reactor core.

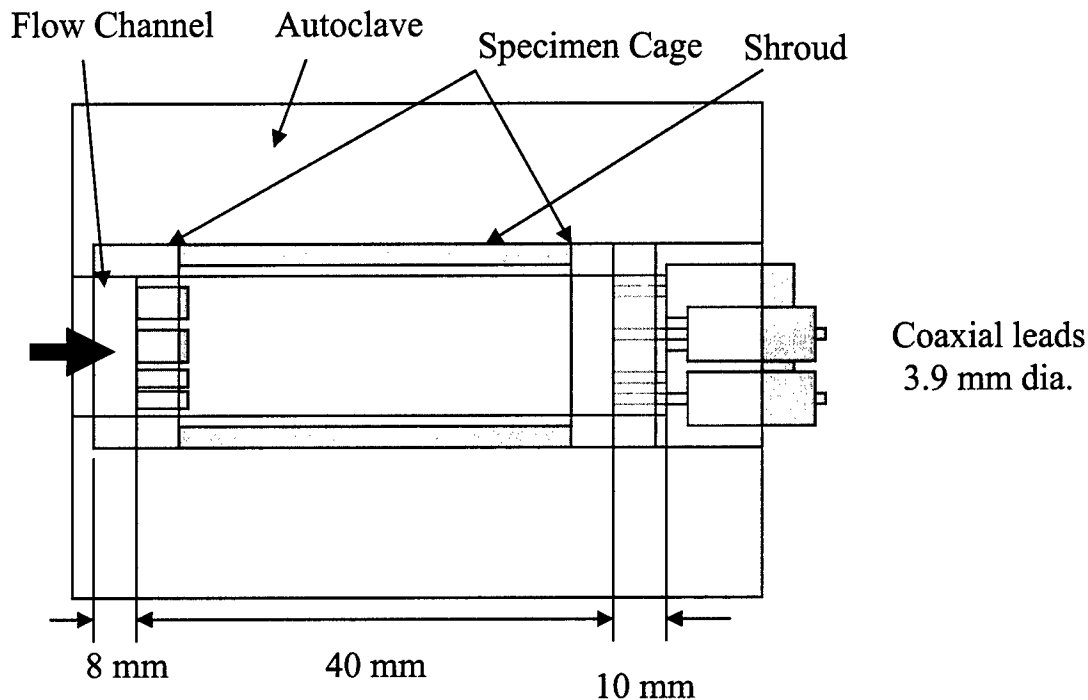


Figure 3.2: Side view of specimen arrangement in module [3.1]

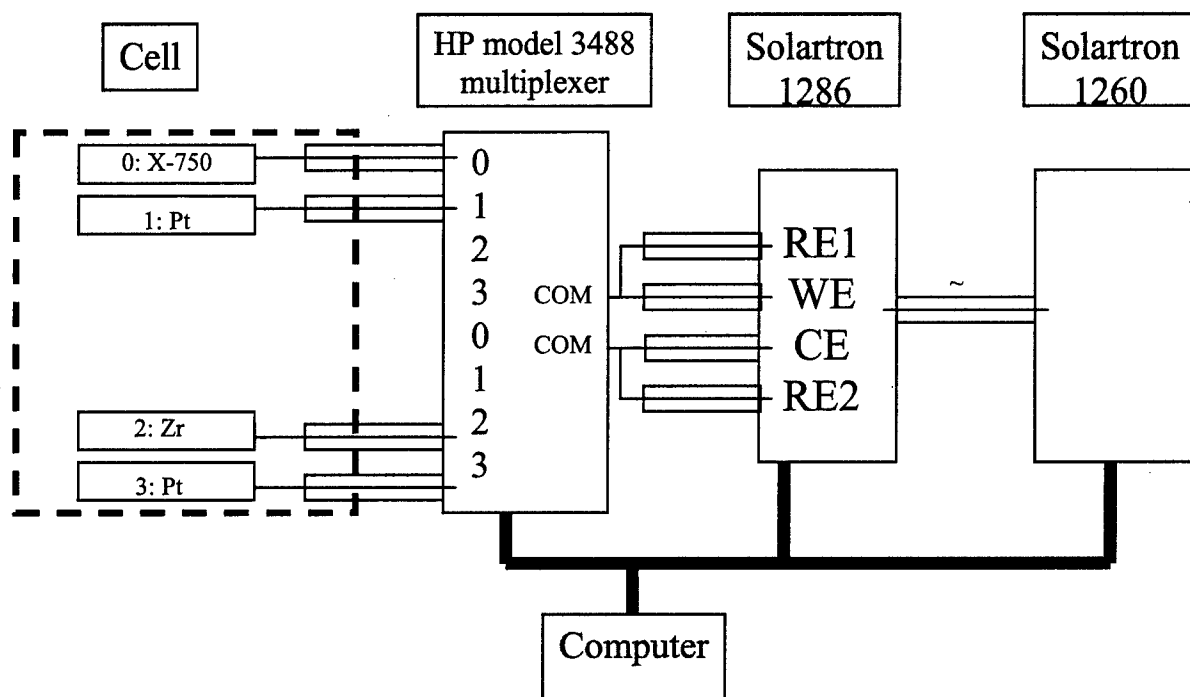
In order to minimize the contribution of the connections to the overall cell potential, the connectors were plated with Ni. The Ni-plated end of the connectors was spot welded to the electrode. After spot welding was completed, the welded ends were covered with 0.001 thickness stainless steel shim material to reinforce the weld. The area covered was 0.5 mm^2 on each side of the sample.

The coaxial connections were then welded into a 0.16-inch diameter Ti tube. The connection wire was sheathed in insulation to prevent shorting of the connection to the sample with the individual tubing. The four individual sample wire protection tubes were then inserted into a larger Ti sheath that was welded to the end of the experimental assembly. The large tube was then inserted into the reactor core with the individual sample connections attached to shielded coaxial leads and cords. The coaxial cords were the primary connections to the electrochemical measuring equipment.

3.1.1. Electrochemical Measurement Equipment

There were four primary pieces of electrochemical equipment used in the course of this experiment: Solartron 1250 Frequency Response Analyser, Solartron 1286 Electrochemical Interface, Keithley Model 617 Programmable Electrometer, and Thornton 200CRS Conductivity/Resistivity Instrument. In addition to the electrochemical equipment, a HP 3488A Switch/Control Unit and IBM ThinkPad® 760CD were used to control and record the experimental data gathering. The required connections between the electrochemical equipment are seen in Figure 3.3. The numbers on the multiplexer correspond to the available ports on the circuit card, four of the eight ports were used, two per output channel. The Solartron 1286 has four input ports used for electrochemical measurements. Reference 1 and 2 (RE1 and RE2) are provided for three- and four-electrode systems, where a reference electrode is used in measurements. In two-electrode configurations, RE1 is shorted to the working electrode and RE2 is shorted to the counter electrode, also seen in Figure 3.3.

Figure 3.3: Electrochemical monitoring equipment arrangement



The Solartron 1286 is designed to measure DC electrochemical properties of electrodes, in two-, three-, or four-electrode configurations. For each electrode configuration, two values are measured: the voltage differential and the current between the working and counter electrodes. The current is defined as positive when current measured flows out of the working electrode and into the counter electrode.

The Solartron 1250 measures the gain and phase characteristics of the electrode couple tested. The primary controlling mechanism is the ZPlot® software loaded onto the ThinkPad®, which issued the commands to the equipment and gathered the returned data. The primary function of the Solartron 1250 is to use alternating current to gather electrochemical data with minimal disruption to the electrodes and their properties. There are three main sections of the Solartron 1250: an electrical stimulus generator, which produces a sinusoidal, square, or

triangular waveform, and two analyzers, one conducting single point measurements and the other conducting point-to-point measurements.

The Keithley 617 was used to verify the readings obtained from the Pt-Pt couple in the reactor core. The measurements obtained from the Keithley 617 were of conductivity, and in the constant current mode. Also used to measure the resistance in the Pt-Pt couple was the Thornton 200CRS. However, the Thornton meter experienced failure during the in-core experimentation warranting replacement of the unit with the Keithley 617. Initial ex-core bench testing was conducted using the Thornton meter with later ex-core testing conducted with the Keithley 617.

3.2. *Computer Programs*

In order to ensure proper entry of commands into the electrochemical equipment, a routine in Visual Basic® controlled the switching unit, Solartron 1286 and 1260. This routine created an Excel® workbook containing individual worksheets for each of the tested couples: X-750/Pt, X-750/Zr, Zr/Pt, and Pt/Pt. For each worksheet used, the routine gathered the potential and galvanic current data by controlling the Solartron 1286. The routine also possessed an embedded algorithm to control an alternating current impedance measurement program, ZPlot®.

ZPlot® issues commands to the Solartron equipment and records the returned data to determine alternating current impedance. The results returned are displayed in the associated program, ZView®. The data can be represented as either a Bode or Nyquist plots. From these plots, equivalent circuits for the oxide film, base metal, and electrolyte may be produced.

The data gathered from the electrochemical equipment was sent directly into workbooks created for each session of data collection. In this format, the ZPlot® data was extracted. The Zplot® data then was entered into the comma-separated variable format and edited using

Wordpad®. After editing, the format was readable using ZView® and could be used to create associated Nyquist and Bode plots.

3.3. Experimentation in Laboratory Environment

There were two phases to the ex-core experimentation, one completed using a bench assembly and the second in an autoclave in reactor. The bench assembly was used primarily to test the Pt-Pt conductivity measurement correlation to the measurements observed using the Thornton conductivity meter. A second motivation to the bench testing was to ensure that the Visual Basic® programs to control the experimental equipment performed the necessary measurements. The initial phase of laboratory experimentation was conducted with a replica assembly with plastic spacers instead of the alumina ceramic spacers. The substitution was made because the environment in which the testing was conducted did not require the resiliency of ceramic. The testing on the bench was conducted first in an open beaker, due to the desire to test the operability of the program. Later testing was conducted in enclosed electrochemical experimentation glass flasks that enabled entry of the experimental assembly, the probe for the Thornton conductivity meter, direct feed of high-purity, low conductivity water into the flask. In order to vary the conductivity of the aqueous solution, potassium chloride was used.

For the second phase of ex-core experimentation, the aqueous solution used was high purity, low conductivity water. In order to preserve the desired qualities of the water, the water was sent directly to the experimental set-up from the purifier via plastic tubing. The conductivity of the water was measured in situ, in addition to the conductivity measurements obtained from the Pt-Pt couple. Due to prior potential contamination of the system, an in-line single filter system was placed downstream of the autoclave and was used to purify the system water to resistivity levels near 15MΩ/cm. Two electric heaters were wrapped around the exterior of the

autoclave enabling the water temperatures to be raised to 300°C, at 1500 psi for non-irradiated readings of environments comparable to BWR operating conditions.

3.4. *MITR-2 Characteristics*

The in-core experimentation was designed as a closed-loop system. This design, herein after referred to as a “loop,” enables control of the water chemistry and temperature without significantly altering the operation of MITR-2, MIT’s research reactor. The primary experimental loop was inserted through the top of the reactor via one of the three ports used for experimentation, seen in Figure 3.4. The MITR-2 is a light water cooled PWR reflected by heavy water. The following descriptions illustrate the individual components of the experimental loop set-up, which strongly resembled the ABB experimentation conducted by Châtelain, containing the experimental assembly containing the four specimens of Zr-2, X-750, and Pt [3.2].



Figure 3.4 Reactor Top [3.2]

The water chemistry and temperature of the water flowing past the specimens was intended to resemble the environment experienced inside a BWR. The focus of this water

chemistry is the oxygen and hydrogen water chemistry used in BWRs to attempt to control the affects of the radiolysis products, hypothesized to be a leading contributor to shadow corrosion. Additionally, the water conductivity in the letdown system was monitored to determine the alterations seen ex-core due to longer-lived radiolysis products, such as H_2O_2 . The main loop contained a heating unit, comprised of a molten lead bath and recirculation pump to ensure adequate flow rate through the experimental assembly.

Reactor coolant water flows down the external surface of the experimental assembly at a flow rate of approximately 20L/min. After it reaches the bottom of the thimble, it enters the experimental assembly, crosses the samples, and returns to the heater and recirculation pump. There is a small portion of the overall experimental loop that is redirected after exposure to the samples to monitoring equipment in the letdown system. It is this portion of the flow, assumed to be representative of the bulk solution, that is measured for dissolved H_2 , dissolved O_2 , and overall conductivity. The water flow path through the main loop is seen in Figure 3.5 [3.2].

Two principal components of the in-core assembly are the autoclave and thimble. The autoclave is a 4.572 m long (grade 9) titanium tube running from the bottom to the top of the reactor. The autoclave diameter is 3.175 cm. The main function is to serve as a pressure barrier for the high-pressure high-temperature water and external environment. It also removes the nuclear heating from the in-core section [3.3]. The thimble is outside the autoclave and is made of Al6061-T6, an aluminum alloy. It is the only component of the experimental assembly in direct contact with the reactor coolant. It is designed to serve as an insulating boundary due to the CO_2 gas purge inside the thimble. The operational temperature of MITR-2 reactor coolant is 50°C , and exposure of the coolant to the temperatures in the experimental assembly adversely affects the reactivity in-core.

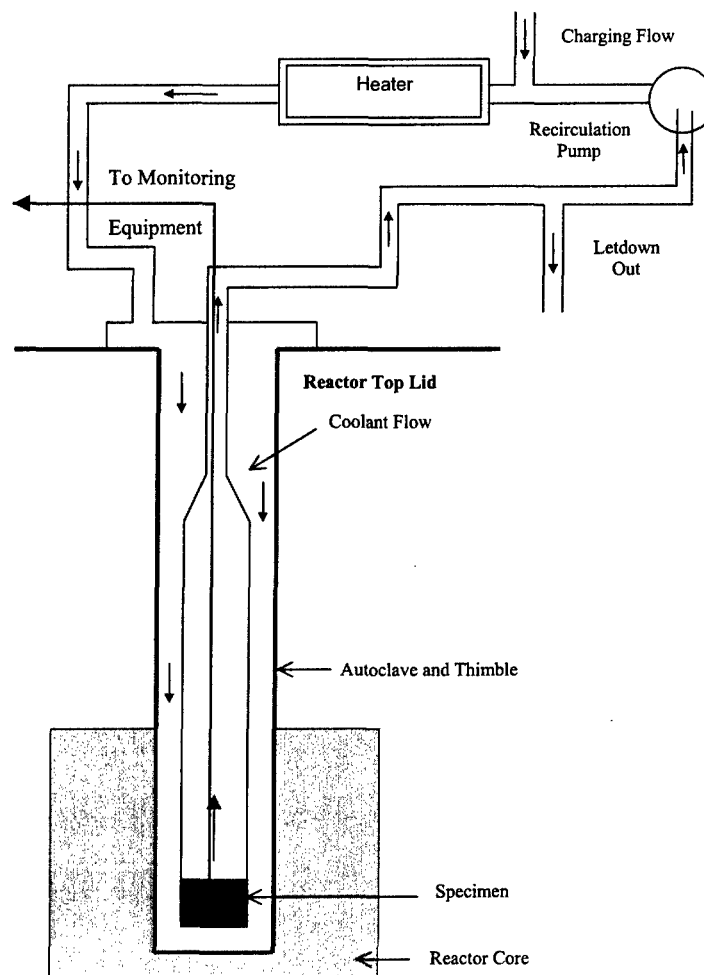


Figure 3.5 Coolant Flow through Rig (Note: Not to scale)

To minimize the radiation dose emitted by the letdown system, including the heater and recirculation pump, a covering of 5 cm layer of lead sheet, supported on a steel frame, along with lead bricks were installed on the reactor top. There is also additional tubing leading to the pump from the exit flow of loop water from the reactor top to allow for decay of short-lived isotopes, such as N-16 to further reduced the emitted radiation. The shielding and pump are seen in Figure 3.6.



Figure 3.6 Letdown system from experimental assembly to recirculation pump [3.1]

The letdown system monitoring equipment was located on a raised platform adjacent to the top of the reactor with the computer used to log the data from Labview®. This data included automated gathering of temperature, flow rate, and dissolved H_2 and O_2 from the letdown system. Figure 3.7 gives depiction of the assembly and the charging system associated with the letdown system. The letdown tank served to regulate the atmosphere experienced by the experimental assembly.

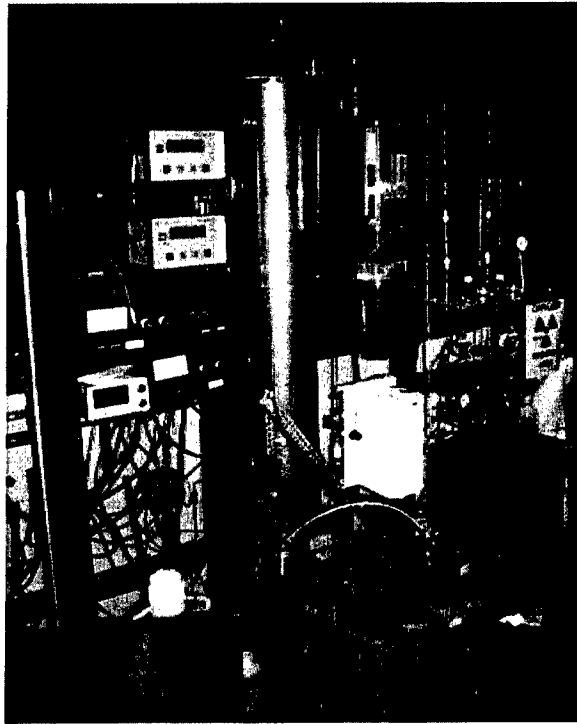


Figure 3.7 Charging tank, letdown monitoring equipment, and chemistry control area

The water temperature across the specimens is controlled to simulate the expected operational temperatures in BWRs. The temperature relay is set to regulate the temperature at 288°C. Temperature of the loop is monitored near the samples through a thermocouple inserted into the assembly and at the heater outlet. The pressure for the assembly is set at 1500 psi to prevent boiling of the water and control the density of the water exposed to the samples. Lower density water would minimize the ability of the aqueous solution to serve as an electrolyte to complete the galvanic couple.

The heater in the loop assembly automatically shuts off and must be manually reset if one of the following eight conditions exists:

1. Loop water temperature near samples exceeds 290°C.
2. Loop water temperature falls near samples below 260°C.

3. Loop water temperature at heater outlet exceeds 295°C.
4. Heater lead bath temperature exceeding 370°C.
5. Main loop pressure exceeding 1500psi.
6. Main loop pressure falls below 1200psi.
7. Low charging tank water level.
8. Low auxiliary cooling water flow.

The justification for the actuation of the safety shutdown is to minimize the impact of ruptures in the tubing associated with the loop or loss of electrolyte into the thimble.

The heater used to heat the leadbath is comprised of twelve strip heaters that surround two stainless steel tubes. These tubes contain the letdown electrolyte and serve as a heat conduit enabling the transfer of heat from the leadbath to the water prior to reentry into the reactor.

3.5. *References*

[3.1] Peter Stahle, 2004.

[3.2] Châtelain, Anthony R., Enhanced Corrosion of Zirconium-Base Alloys in Proximity to Other Metals: the "Shadow Effect", S.M. Thesis, Massachusetts Institute of Technology, MA, February 2000.

[3.3] MIT Design Report, Enhanced Corrosion of Zirconium-Base Alloys in Proximity to Other Material: "The Shadow Effect", December 3, 1998.

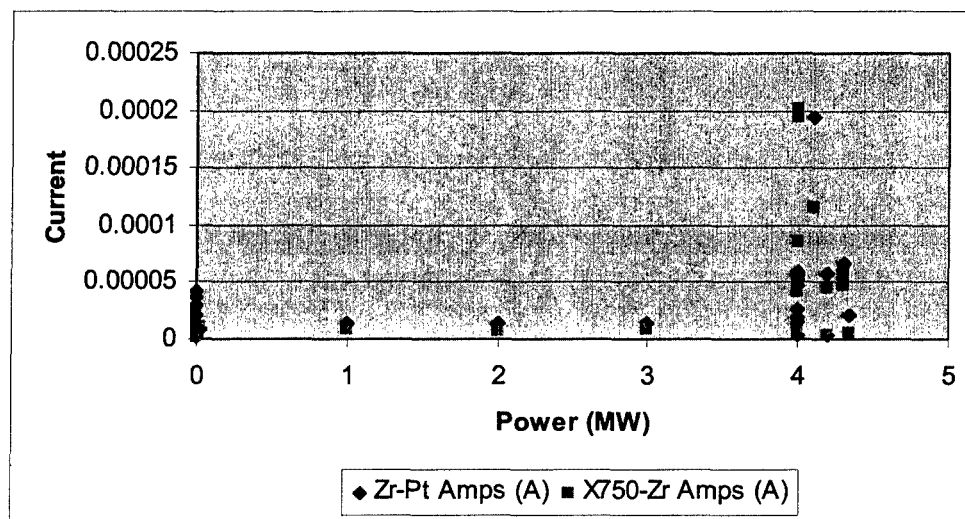
4. Experimental Results and Discussion

In evaluation of the collected data, the couples between Pt and Zircaloy-2, Zircaloy-2 and X750, and Pt with Pt were expected to provide the significant insight into the corrosion process. Appendices A through D present the time value graphs of electrochemical measurements.

4.1. Galvanic Current Data Gathered

Figure 4.1 shows a plot of galvanic current v. power. Figure 4.1 illustrates that the current increases with reactor power. This supports the hypothesis of increased coupling due to the alterations in oxide properties and radiolysis products. However, there appears to be a threshold power above which the current increases.

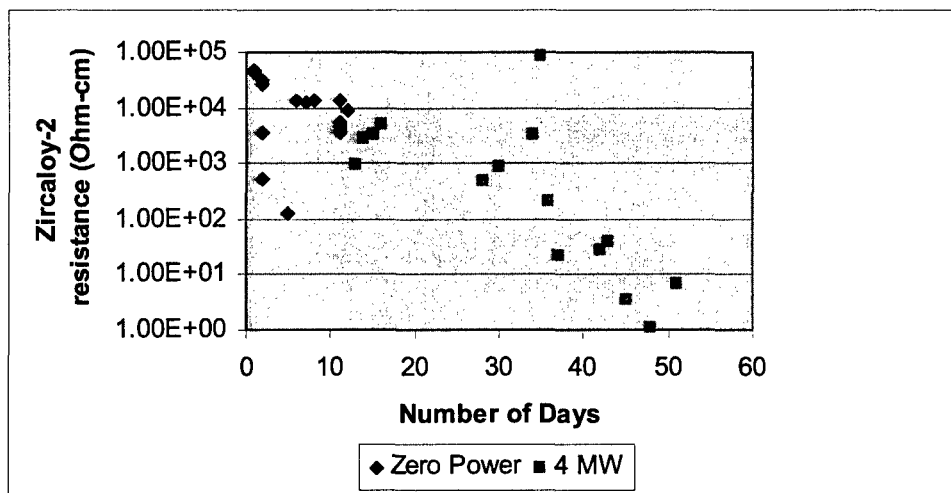
Figure 4.1 Galvanic Current V. Reactor Power



Seen in Figure 4.2, the change in resistance of the Zircaloy is greatly affected by reactor power. After reactor power increased to 4 MW, the resistance is observed to decrease at a higher rate, seen by the solid line. The two highest resistivity readings occurred at the initial insertion of the experimental assembly into the reactor with zero reactor power, as seen in Figure 4.2. The

slope of the change in resistance with respect to time appears to increase slightly after the reactor reaches 4 MW power.

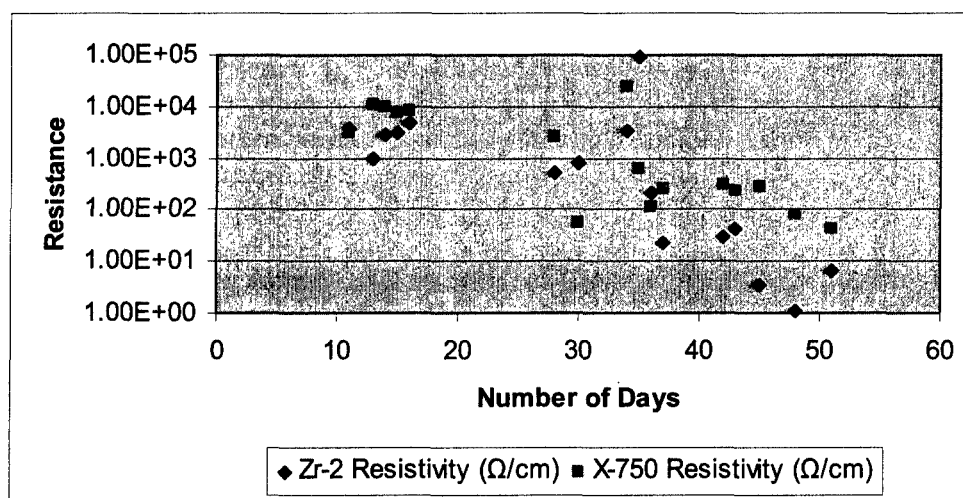
Figure 4.2 Zircaloy-2 Resistance V. Time in Reactor



The measurements of the changes in the potential of the Zircaloy with respect to reactor power relative to Pt indicate changes in the system resistivity. Previous experimentation determined that without radiation effects, Zircaloy becomes increasingly noble due to the growth of the protective oxide film [4.1]. As seen in Figure 4.3, the resistance to current flow of the Zircaloy and associated oxide layer, when the calculated resistance of the water is removed, is seen to decrease, and the rate of decrease is dependent on reactor power. This supports the hypothesis by Cox that the oxide characteristics change due to the radiation effects, assuming constant resistivity in the bulk Zircaloy matrix.

Comparing the resistivity of the Zirconium alloy to the X-750, the predominant relationship is that the X-750 experiences a lower rate of decrease in resistance to current flow as seen in Figure 4.3. This predominance supports the observation that shadow corrosion is related primarily to changes in the Zircaloy, while still affected by changes in the dissimilar metal couple system.

Figure 4.3 Resistivity Comparison between Zircaloy- 2 and X-750 at 4 MW



4.2. Conductivity Data Gathered

The Pt-Pt couple gives the resistivity of the water based on the resistance, calculated by Ohm's Law, from the voltage and current during the ECP measurement. This value was also obtained directly by connecting the couple to either the Keithley 617 or Thornton conductivity meter. The expected characterization is that the resistivity would decrease, correspondingly, conductivity would increase, with reactor power.

The measured results from the individual two-electrode system of coupled Pt-Pt electrodes at 22°C and atmospheric pressure are seen below in Figure 4.4. In order to correlate the data obtained in-core with an expected value ex-core, a best-fit line was created using the following equation:

$$\text{Pt-Pt value} = 0.065964 (\text{Thornton value})$$

Where all units are S/cm.

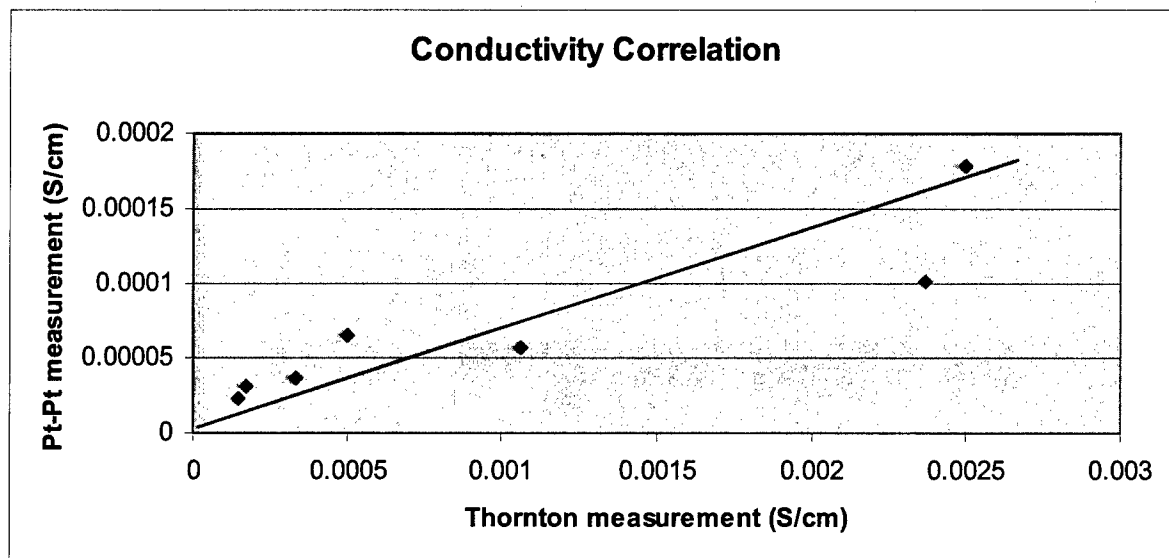


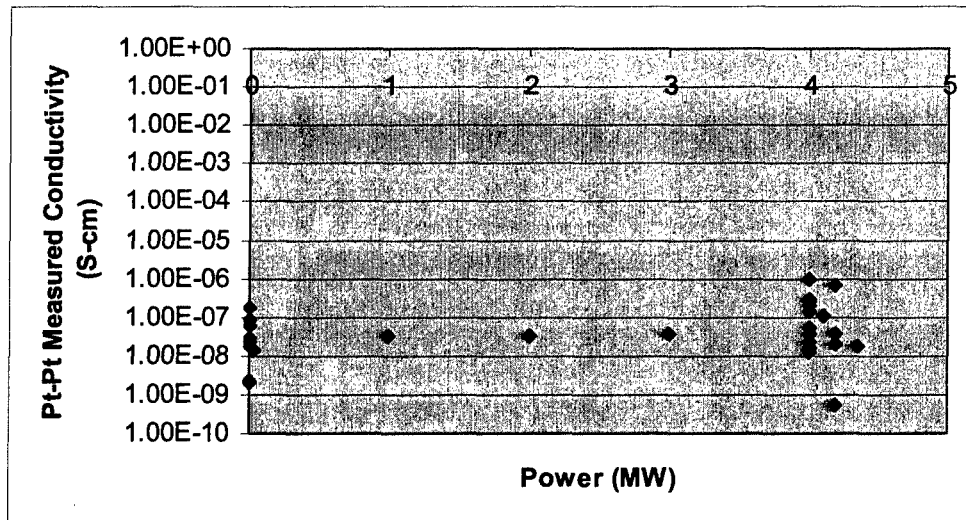
Figure 4.4 Pt-Pt correlation chart

This correlation indicates that there is a linear relationship between the measurements conducted by the conductivity meter and the Pt-Pt couple. This validates the assumption that the measurements conducted within the core will reflect the differences in conductivity measured by the couple of Pt-Pt electrodes.

Analysis of the in-core data gathered starts with the basis of the experimental hypothesis; radiolysis alters the chemical concentrations of the coolant, affecting the conductivity. This hypothesis was tested using the potential values obtained from the Pt-Pt coupling of electrodes. Appendix E illustrates the values of the Pt-Pt electrodes for potential and current measured, Ohm's Law was used to calculate resistivity and conductivity at operating power. All calculations of resistivity and conductivity acknowledge that flow of electrons determines the sign of the values for voltage and current. Correspondingly, the absolute value for the resistivity and conductivity is analyzed due to higher importance of the magnitude of the electron flow impediment. Seen in Figure 4.5, the values obtained for conductivity at no reactor power are

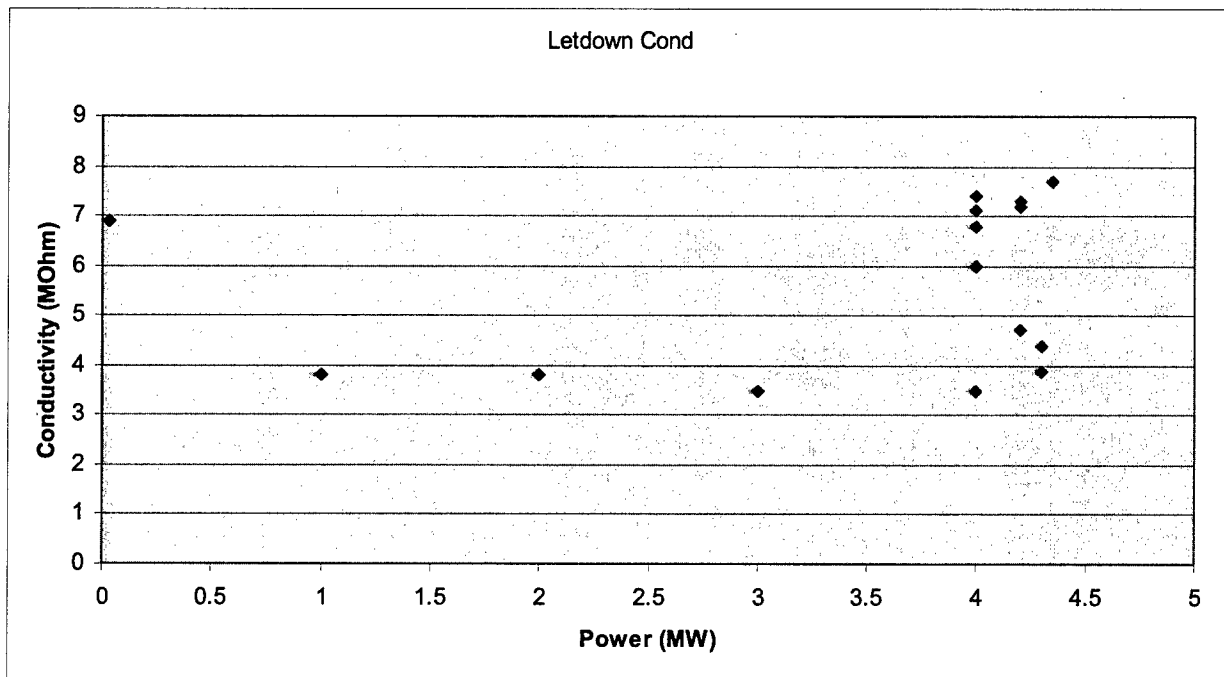
scattered over a notably smaller, and lower, range than the values measured at 4 MW power. This data also shows the apparent threshold effect observed in the current.

Figure 4.5 Coolant Conductivity, as measured by Pt-Pt electrode, V. Reactor Power



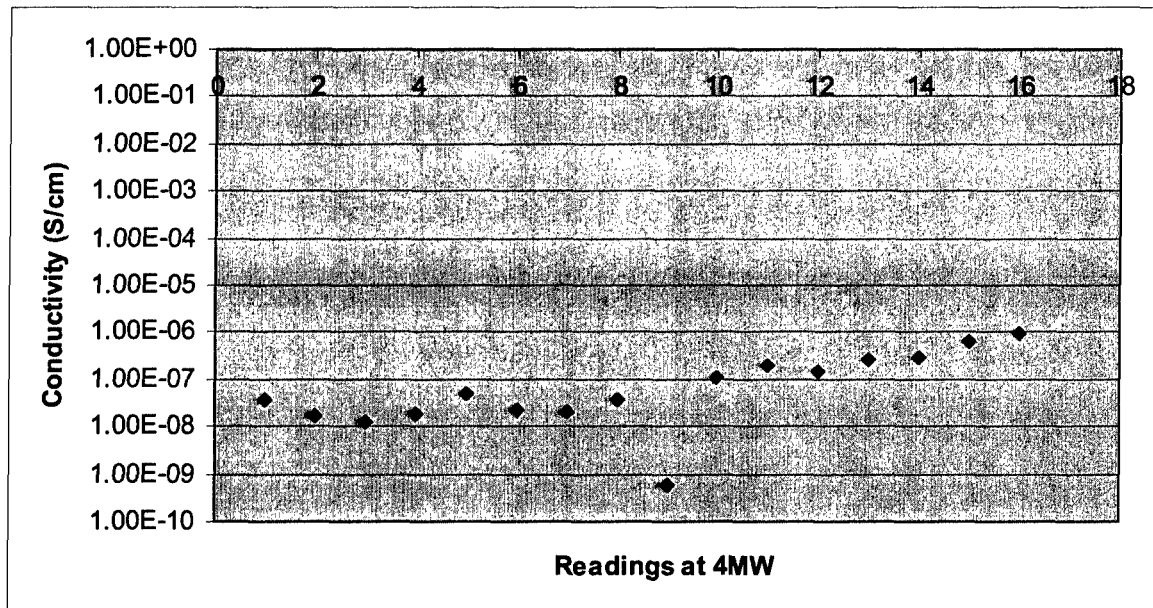
The measured values are plotted in Figure 4.5. While the data are scattered, the general trend is an increase in the measured conductivity with increases in reactor power. This is supported by the conductivity measurements obtained in the letdown system, seen in Figure 4.6.

Figure 4.6 Letdown Conductivity Measurement V. Reactor Power



The results support the initial hypothesis that reactor power alters the conductivity of the high purity, low conductivity reactor coolant water via radiolysis. Also of note, is the relatively constant value in the conductivity at 1, 2, and 3 MW power. This measurement suggests a 4 MW threshold of power, and associated neutron flux, required for notable changes in the conductivity of the coolant. Observing the time dependence of change at 4 MW power illustrates that the conductivity also increases with time at power, seen in Figure 4.7.

Figure 4.7 Coolant Conductivity, as measured by Pt-Pt electrode, V. Time at 4 MW Power



This observation indicates time-dependency, in addition to the observed power dependency.

4.3. Galvanic Current and Conductivity Analysis

The conductivity of the coolant and the galvanic current of the measured systems increase with reactor power, Figures 4.8 and 4.9 indicate correlation at 4 MW between conductivity measured by the Pt-Pt electrode and corresponding measurements of galvanic current between pairings of Pt and Zr-2 and X-750 and Zr-2 electrodes, respectively.

Figure 4.8 Zr-2-Pt Measured Galvanic Current V. Pt-Pt Measured Conductivity

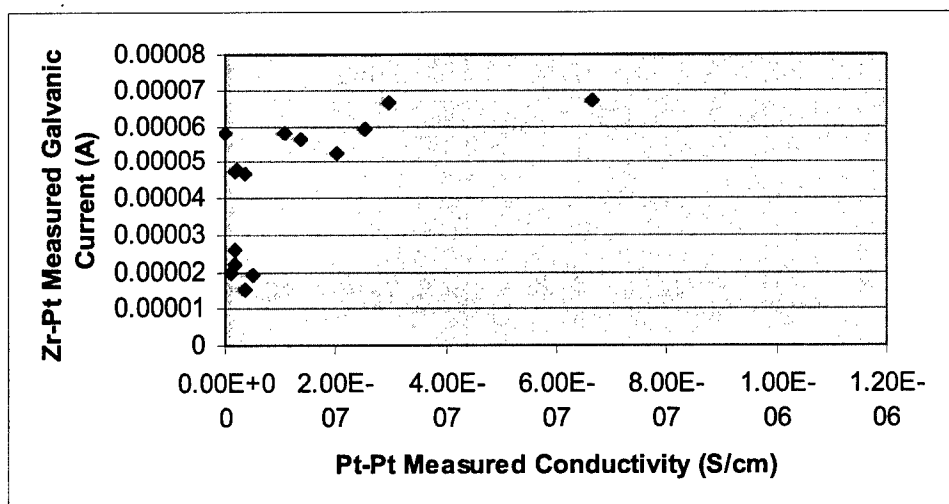
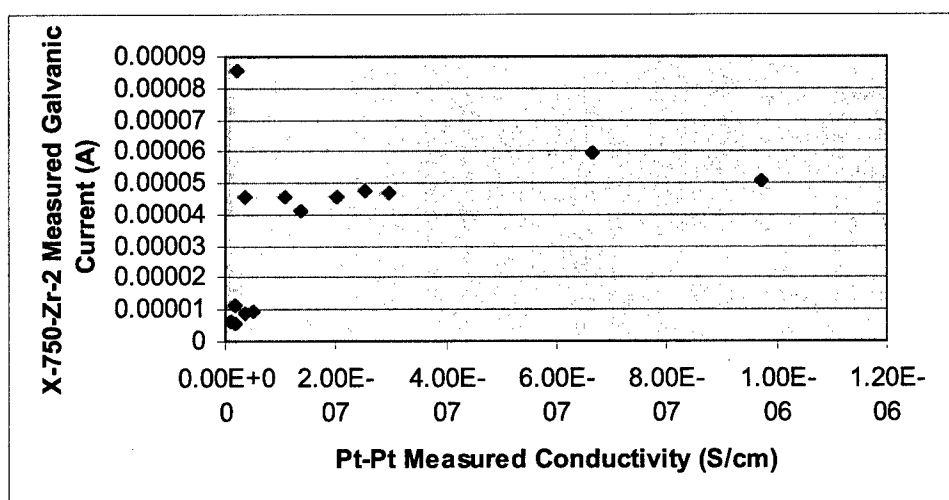


Figure 4.9 Zr-2-X-750 Measured Galvanic Current V. Pt-Pt Measured Conductivity



These findings support the hypothesized correlation between conductivity and galvanic current.

4.4. Obstacles Encounter During Experimentation

After installation of the experimental assembly into the reactor, there were several deviations from the initial design of the experiment. Among the deviations, technical issues

arising from the Visual Basic® code written to gather the data caused the ThinkPad® to suspend normal functioning during data collection or dump physical memory causing the data taken in that session to be erased. Initial laboratory testing indicated minor flaws in the first Visual Basic® program, a revision was completed prior to implementation in the reactor. This second version was initially used in the in-core testing. After the installation, the program was further tested and revised to assist with ease of data acquisition. However, the third version created duplicates of the Pt-Pt couple data, overwriting the X750-Pt couple data, and left the data set incomplete. The program was altered for a fourth time, and this program was used for the duration of the experimentation.

Initial laboratory attempts to create the associated EIS plots indicated high levels of electrical noise being gathered with the data. In order to minimize the noise in the data, the connections from the end of the titanium tubes containing the wires connected the samples were shielded using a specially designed brass connector. The connector screwed into the end of the coaxial connector and covered the end of the titanium tube to reduce exposure to superfluous fields that may induce the noted noise. Also noted to contribute to the noise was the coaxial cables used to connect the samples to the electrochemical equipment. Using an oscilloscope, it was noted that some of the wires created noise due to insufficient connections or shielding. Along with the brass shields, replacing the faulty wires reduced the noise noticed in the laboratory environment.

Despite the ability to reduce the noise in the laboratory environment, there remained significant noise in the alternating current impedance data gathered in-core. When compared to the ideal plots in chapter 2, the desired locations of the indicative points that are used in creation of the equivalent circuits are unintelligible. With the excessive electrical noise seen, there is no

ability to determine the corrosion rate and conductivity of the oxide forming on the zirconium alloys.

There were also significant issues with controlling the expected water chemistry. Despite the introduction of hydrogen through the charging tank, the levels of dissolved oxygen at 4 MW remained significantly higher than the desired level. During experimentation, the levels of dissolved oxygen exceeded the desired levels of 200 ppb, with nominal values ranging from 100 to over 500 ppb. Dissolved hydrogen measured in the letdown system also never reached the desired level of 30 ppb. Average values of dissolved hydrogen in the let down system were around 11 ppb during 4 MW operations. During the period of heater inoperability, the levels of dissolved hydrogen and oxygen spikes, giving values of approximately 400 to 600 ppb for hydrogen and 1.5 ppm for oxygen. The desired test conditions and measured conditions during experimentation are seen in Table 4.1.

Table 4.1: Experimental Conditions

	Desired Experimental Conditions	Actual Experimental Conditions
Temperature	280°C (520°F)	80°C (174°F) to 280°C (520°F)
Dissolved Hydrogen	30 ppb	11 ppb to 600 ppb
Dissolved Oxygen	200 ppb	100 ppb to 1.5 ppm

The deviations from the desired values resulted from deficiencies in the primary experimental loop, included malfunction of the leadbath heating unit. The malfunction was due to a steam leak within the heater assembly leading to water being released onto the reactor top. In addition to the issue of water leaking onto the top, there was the potential for steam etching on surfaces contacted by the high-pressure steam leading to a larger rupture and further contamination and/or damage. Evaluated data omitted the period of heater inoperability. While the heater underwent repairs, the experiment remained in place, but the temperature dropped

from the expected regime of approximately 280°C (520°F) to 80°C (174°F). Even after repairs were conducted, the temperature never exceeded 250°C (480°F).

4.5. *References*

[4.1] Cox, B., Mechanisms of Zirconium Alloy Corrosion in Nuclear Reactors, The Journal of Corrosion Science and Engineering, Vol.6, paper 14, 2003.

5. Conclusions

The results of this research represent the first attempt to evaluate dynamic behavior, including coupled current, potential and oxide character, of cladding and structural materials in an actual reactor core at LWR operating temperature. The task was daunting and, although there was an expectation of quantitative results, in the end due to the difficulties experienced, the results were only semi-quantitative. Future experiments will benefit from the lessons learned in this initial attempt.

5.1. *Reiteration of Hypothesis*

In order to evaluate the galvanic current aspect of the hypothesis on the causes of shadow corrosion, an electrochemical experiment measuring the potentials and currents between samples of Pt, Zircaloy-2, and Inconel (X-750) was conducted. The goal of this experiment was to seek evidence of the galvanic couple dependency for shadow corrosion. In order to accurately provide evidence of the galvanic couple, measurements of the reduction in the conductivity of the high purity, low conductivity water used as coolant were conducted through the use of a Pt-Pt electrode couple. Additionally, galvanic current measurements were made.

5.2. *Comparison of Experimental Results with Expected Results*

The results of this research have shown that:

1. Radiolysis increases the conductivity of the coolant to the point where corrosion current may be possible between materials in close proximity.
2. Current flows between Zircaloy-2 and structural materials in the in-core environment.

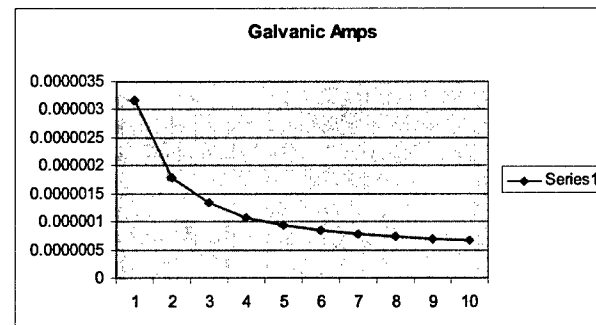
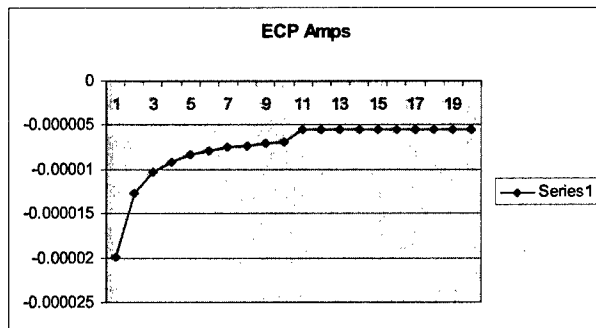
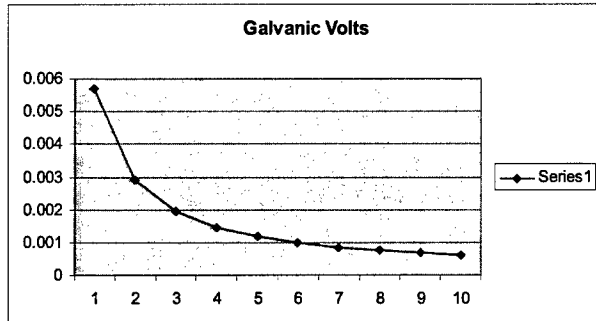
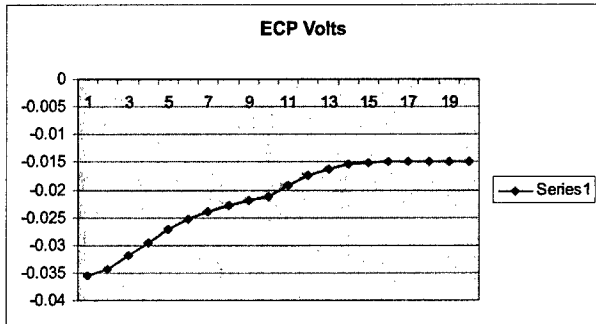
Note: While current between Zircaloy-2 and structural materials has been identified, further work and analysis is required to determine the exact nature of this current.

Sources of current could include redox current from water as well as corrosion current.

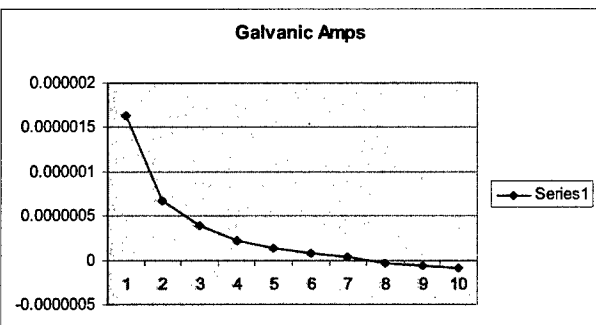
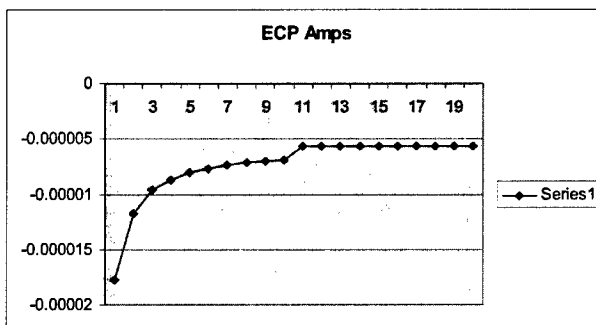
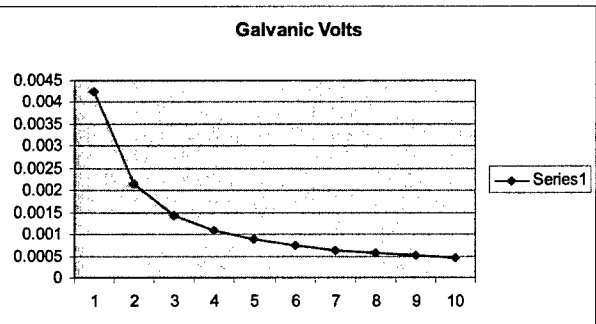
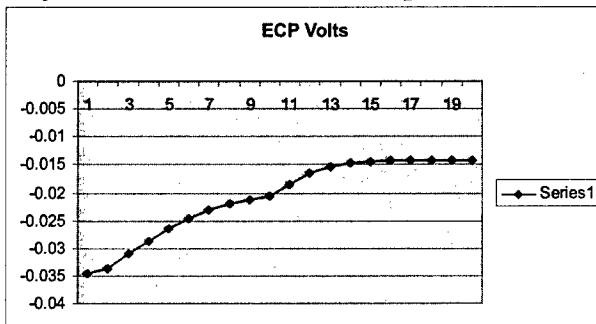
3. There is an apparent threshold in reactor power – flux- above which current is observed. One would expect that were the observed current due only to redox effects, that there would be a linear relationship between flux and current.
4. While the exact oxide composition changes related to the electrochemical observations remains unknown, the indications that resistivity change in Zircaloy, and its associated oxide, exist, as previously hypothesized by Cox, giving a new avenue of exploration for the understanding of the shadow corrosion hypothesis. Further metallurgical and compositional analysis of the oxide film post-irradiation may result in better understanding of the root causes of shadow corrosion.

Appendix A – Pt-Pt Couple Graphs

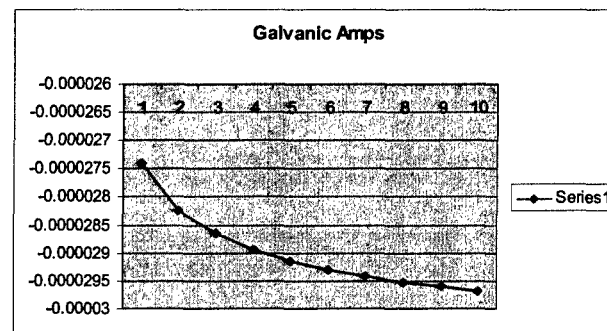
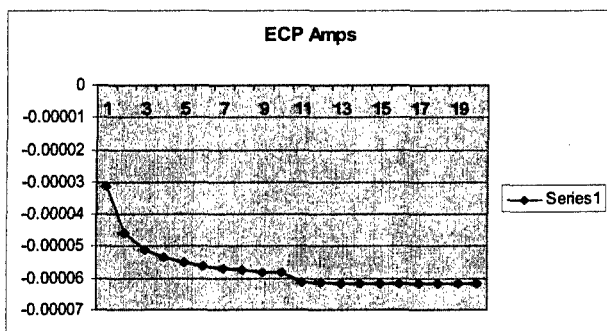
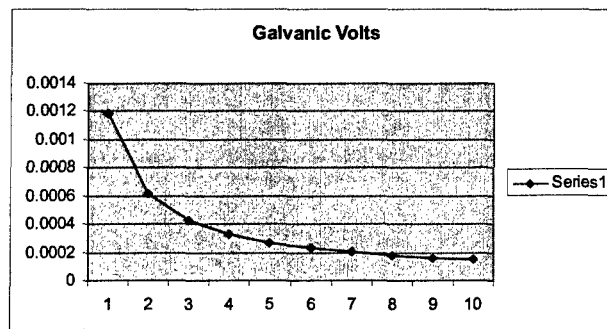
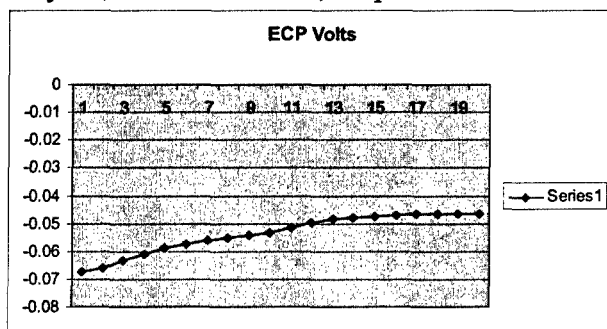
May 27, 2004 – first run, no power



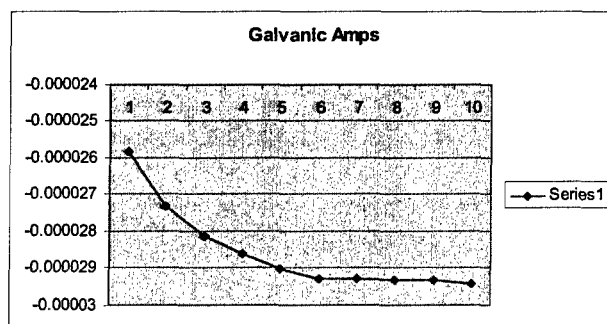
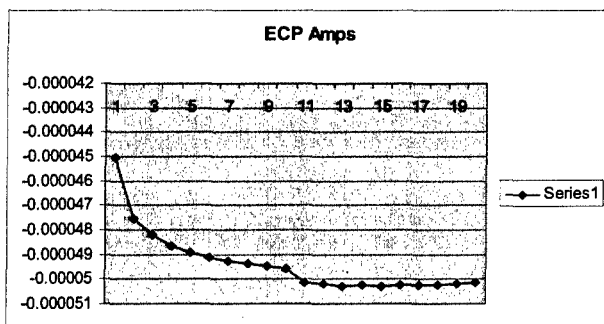
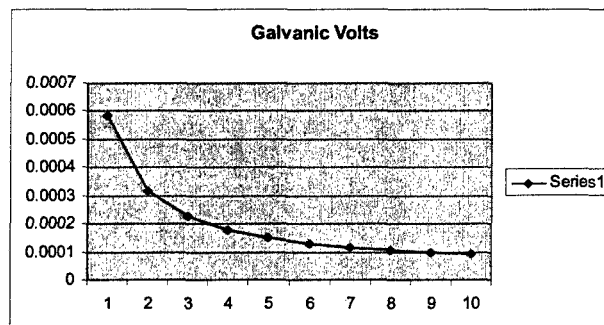
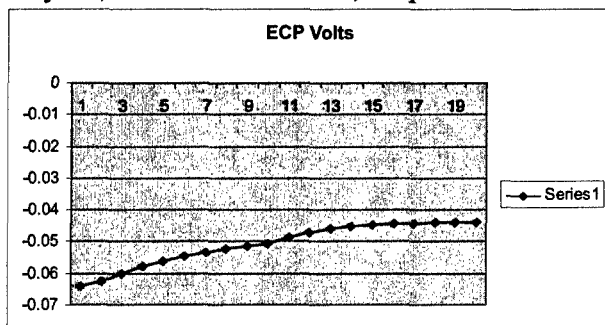
May 27, 2004 – second run, no power



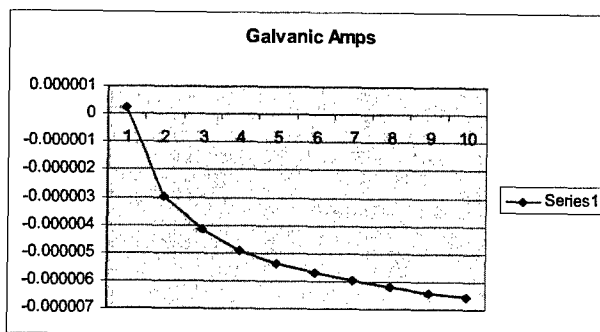
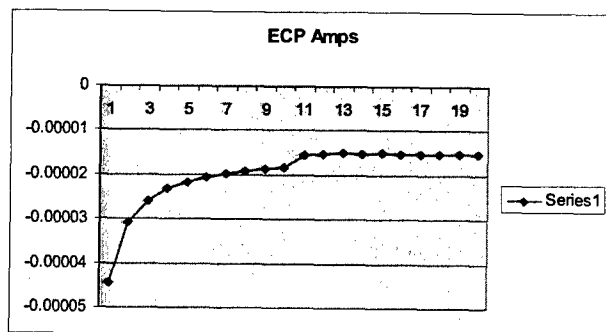
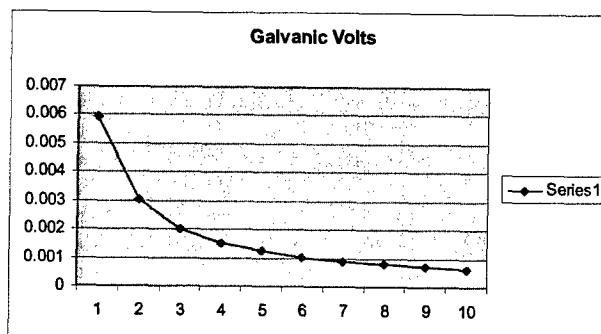
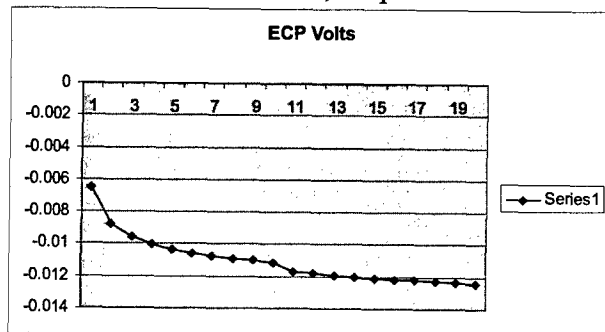
May 28, 2004 – first run, no power



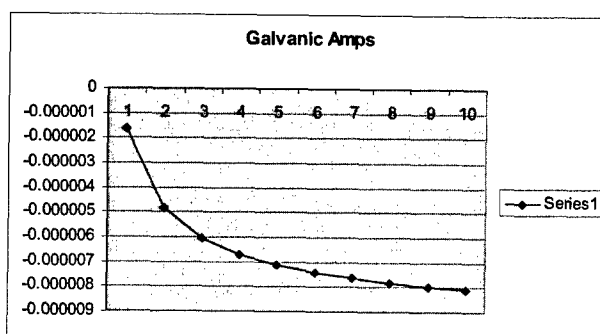
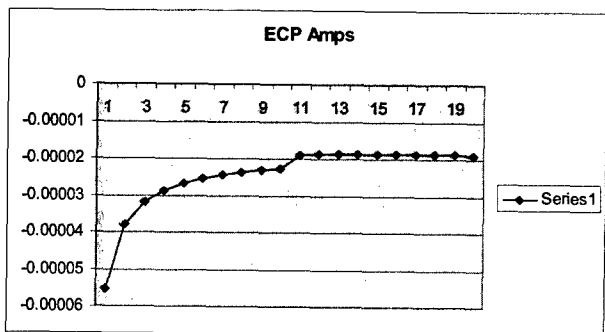
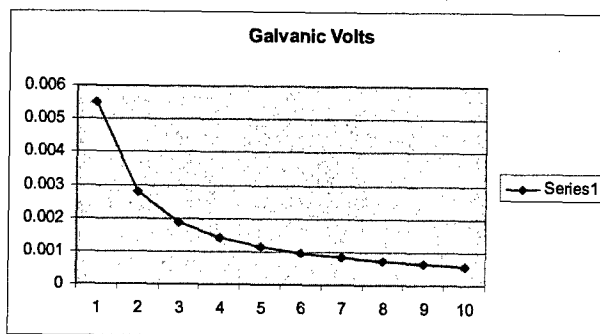
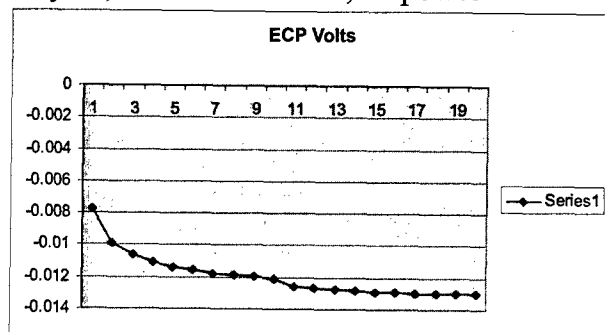
May 28, 2004 – second run, no power



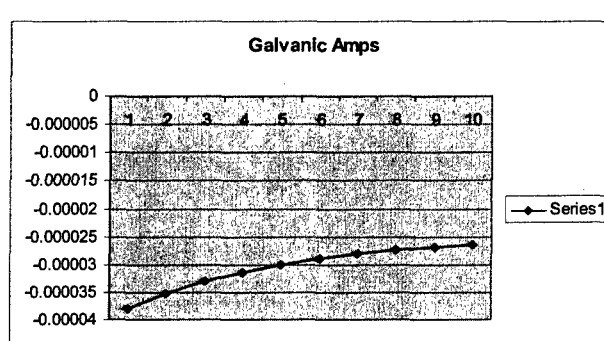
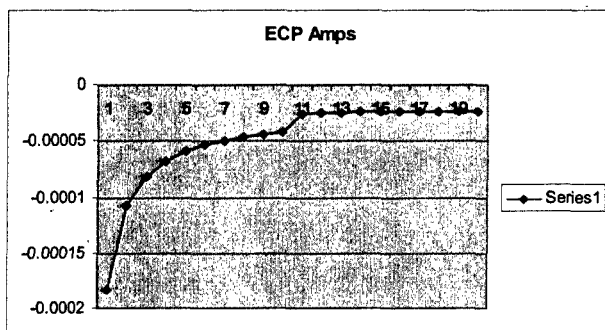
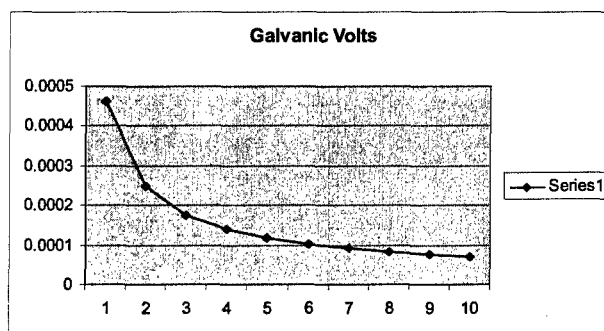
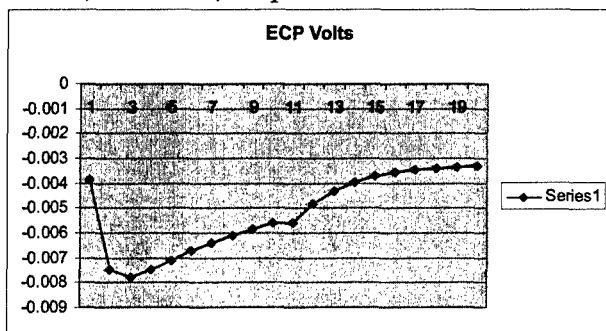
May 28, 2004 – third run, no power



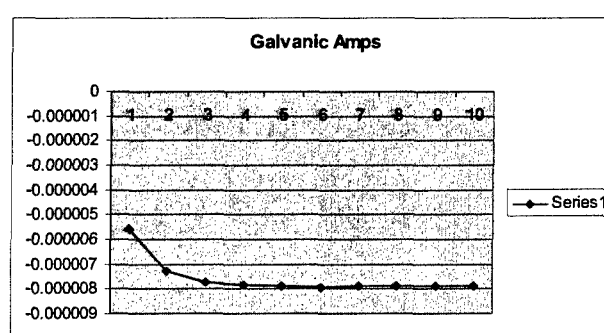
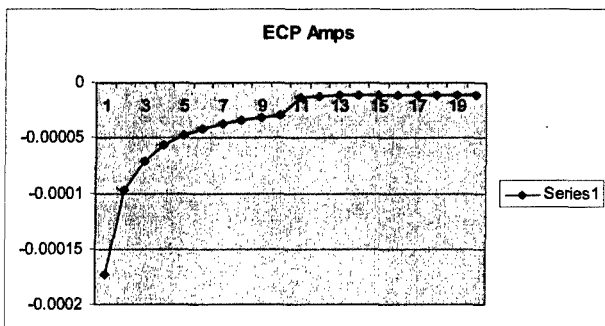
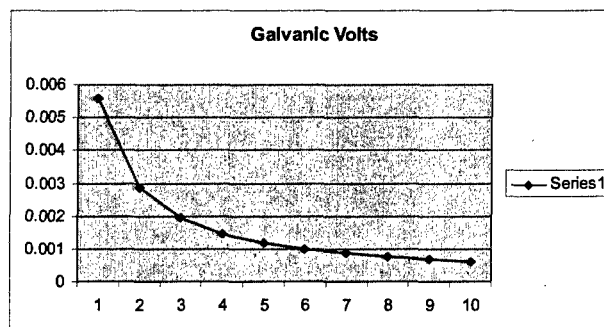
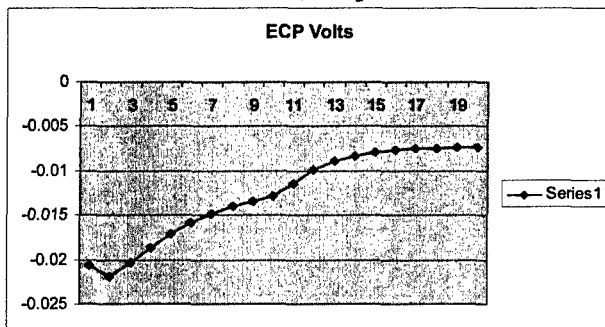
May 28, 2004 – fourth run, no power



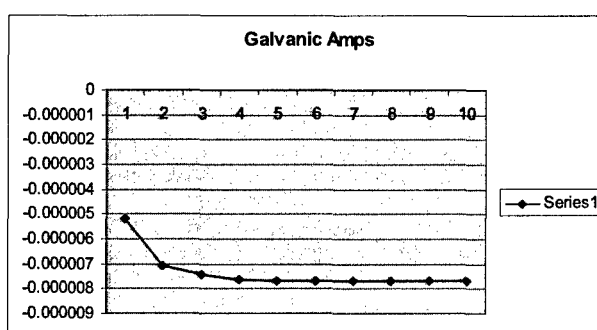
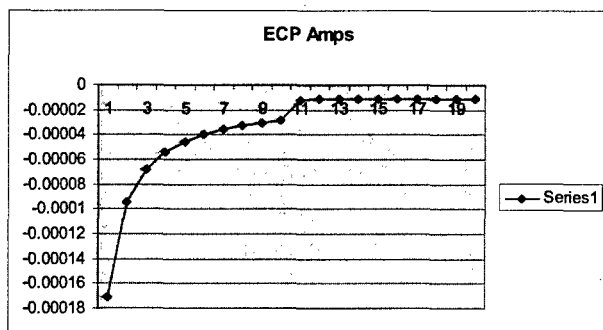
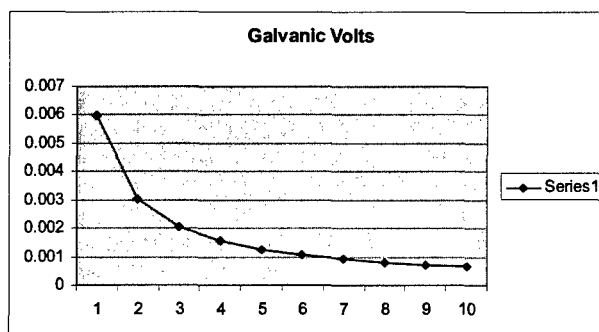
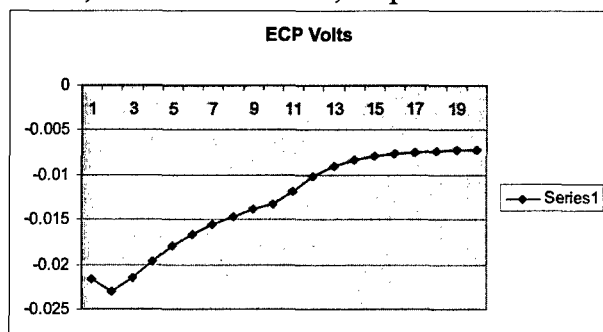
June 3, 2004 run, no power



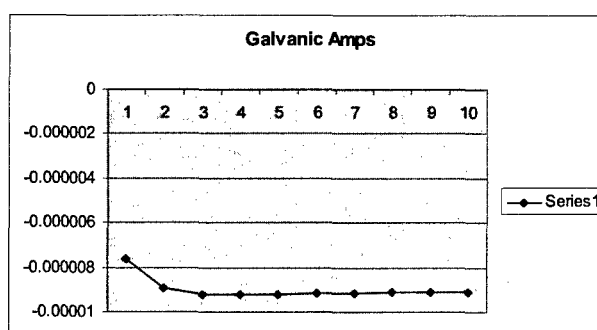
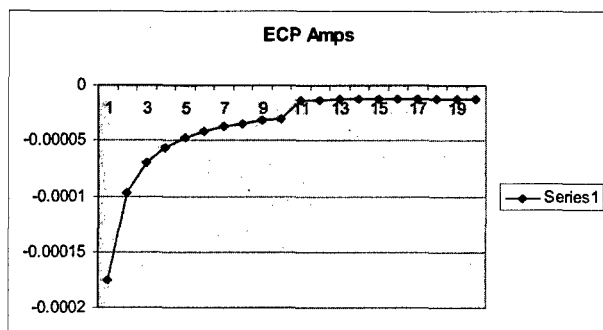
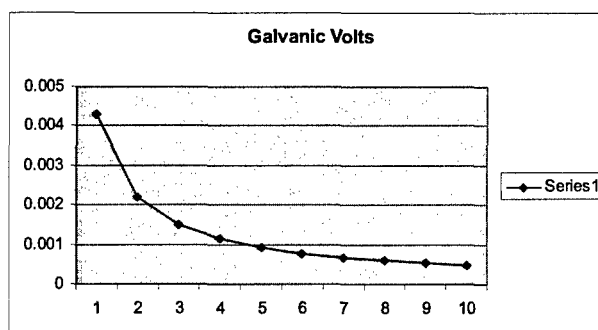
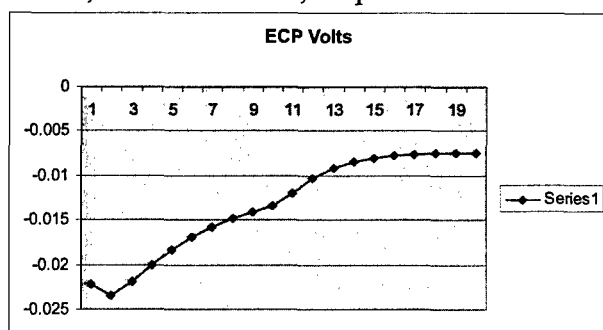
June 4, 2004 – first run, no power



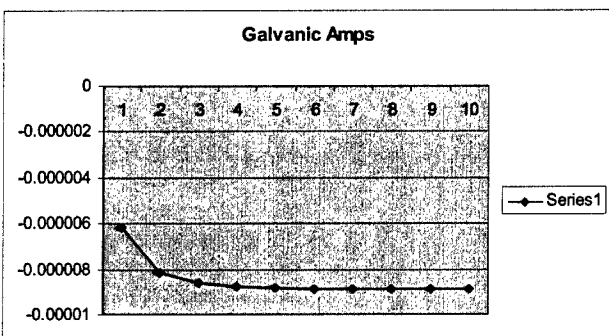
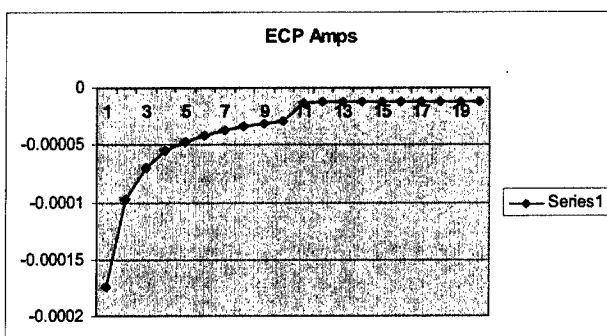
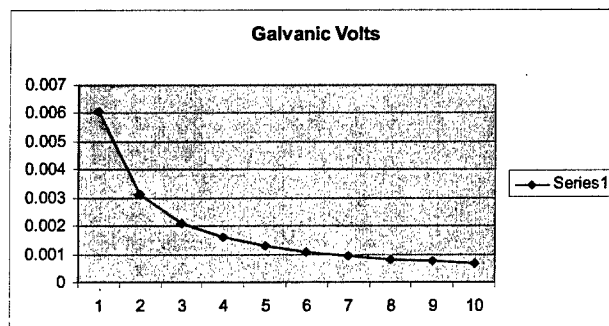
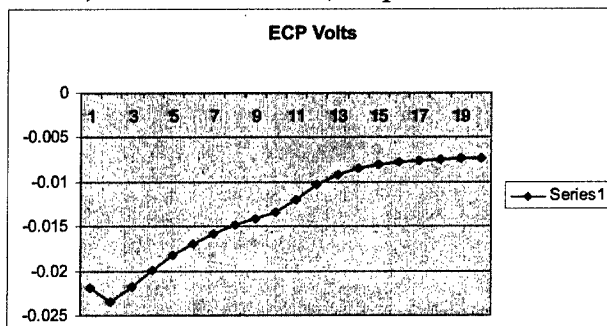
June 4, 2004 – second run, no power



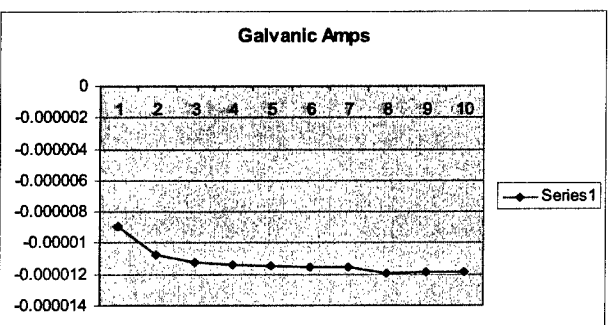
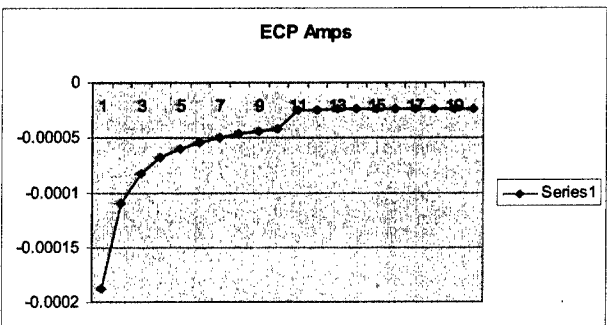
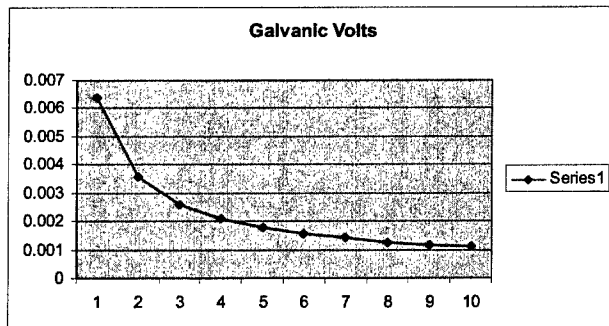
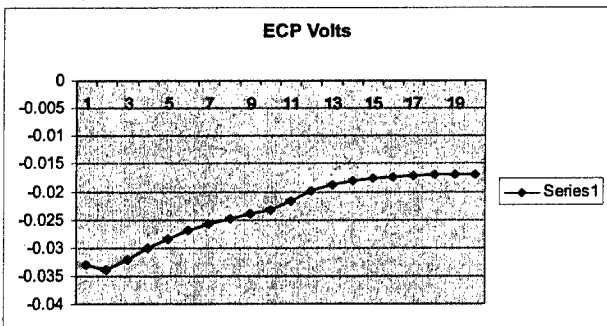
June 4, 2004 –third run, no power



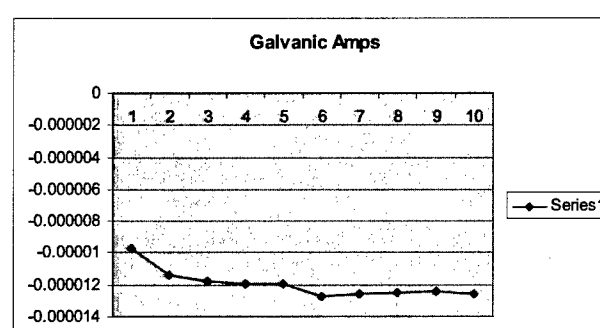
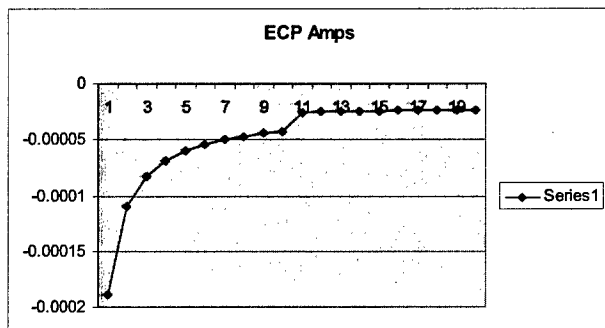
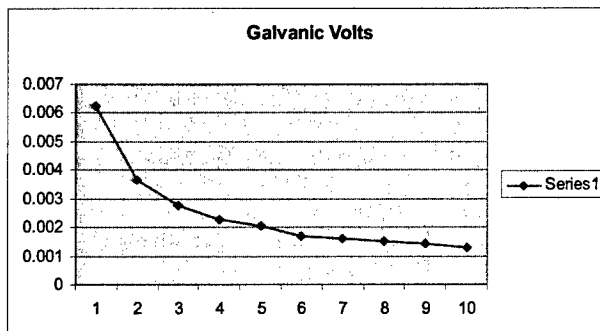
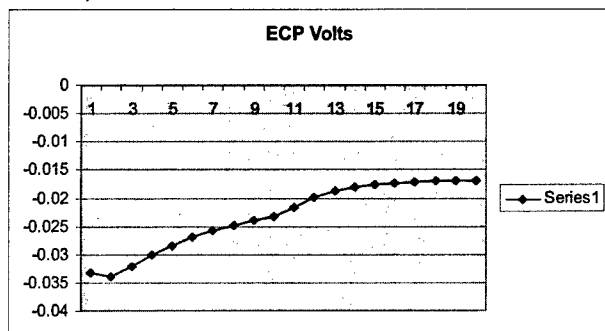
June 4, 2004 – fourth run, no power



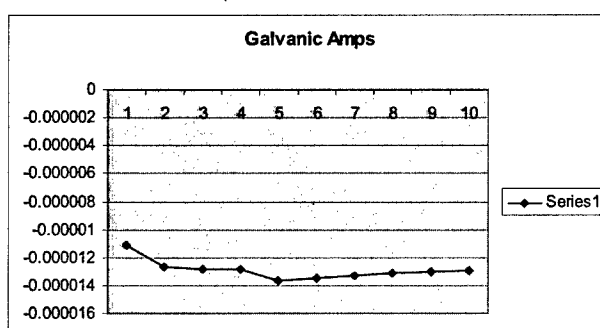
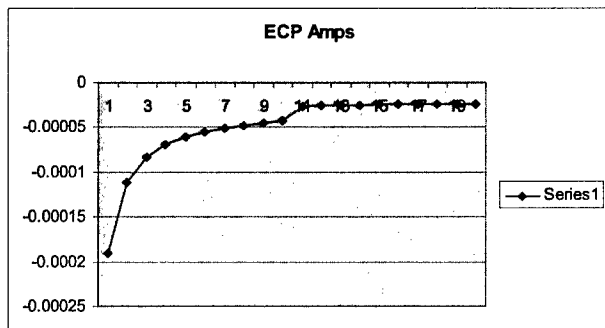
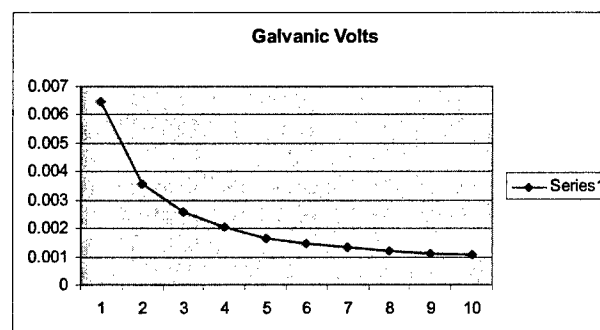
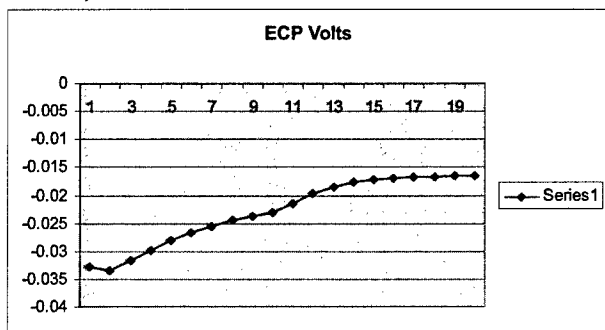
June 4, 2004 – 1 MW run



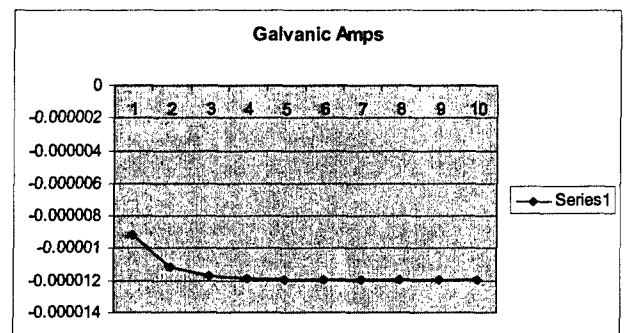
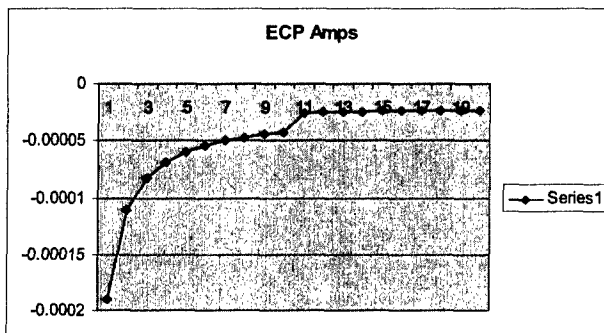
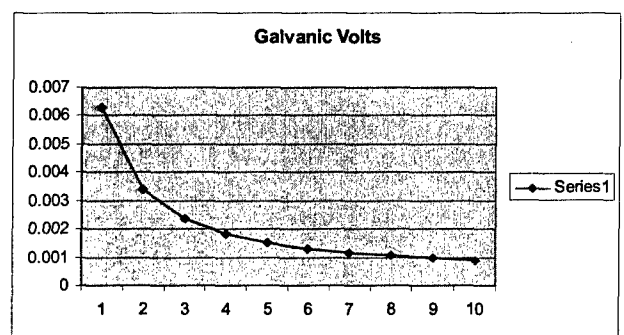
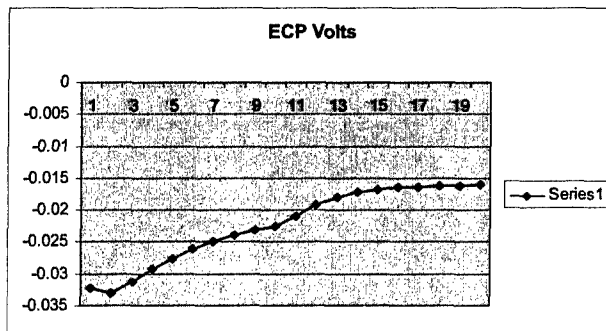
June 4, 2004 – 2 MW run



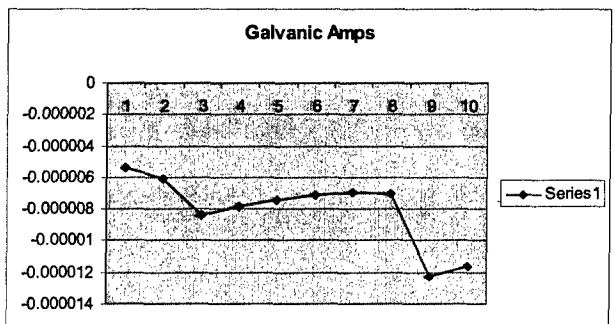
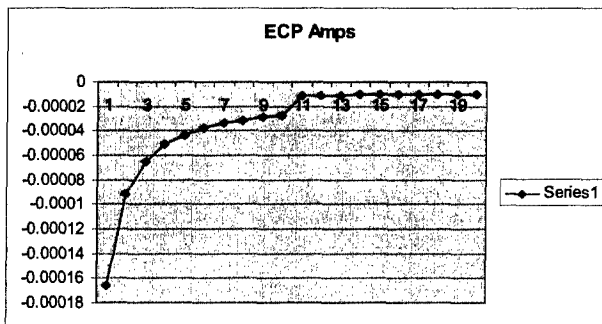
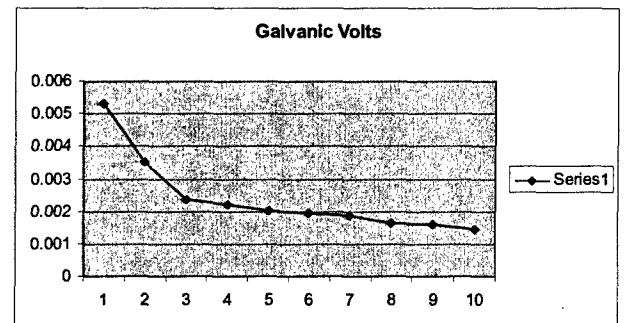
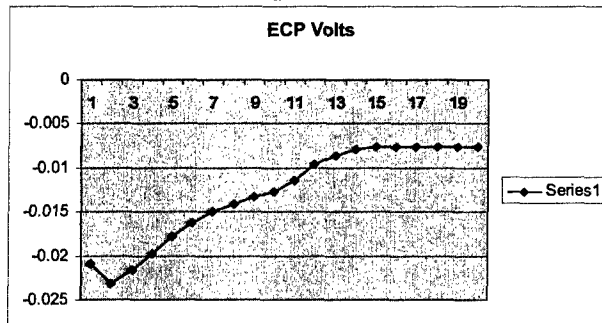
June 4, 2004 – 3 MW run



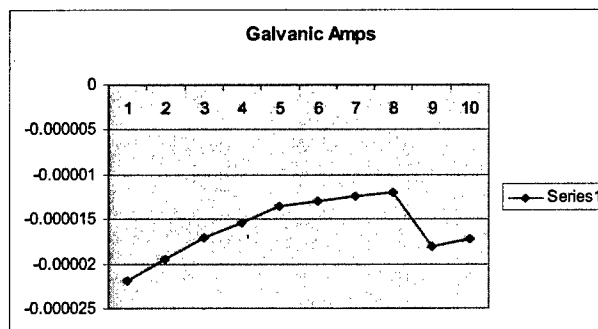
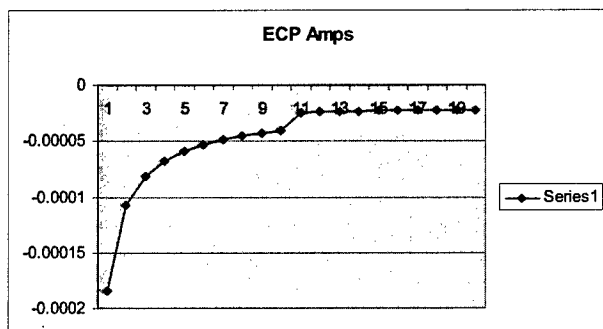
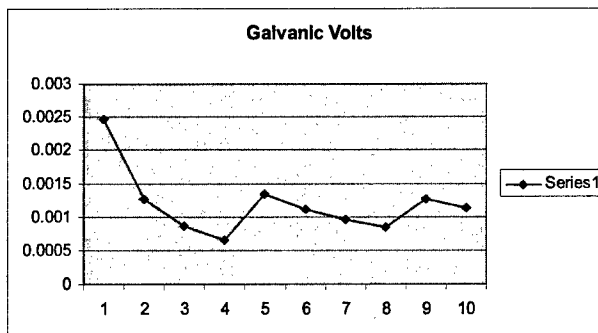
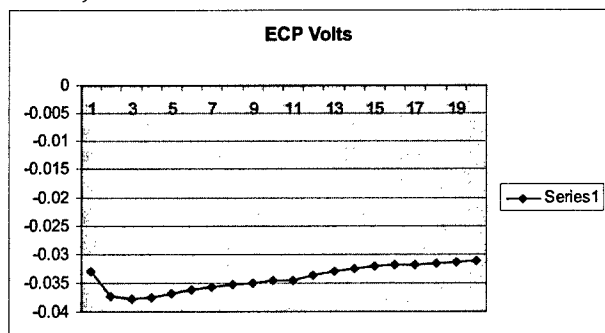
June 4, 2004 – 4 MW run



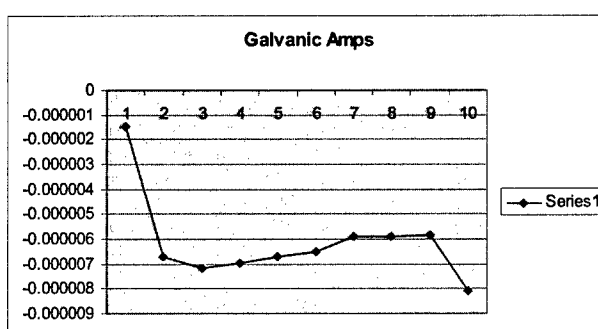
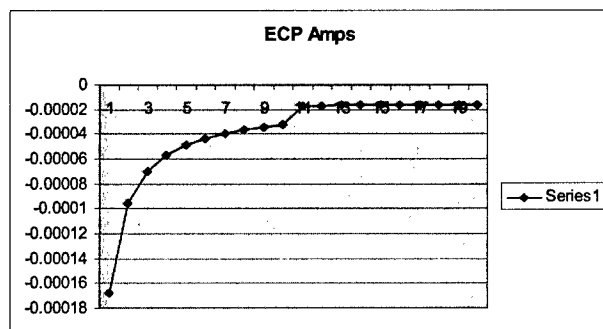
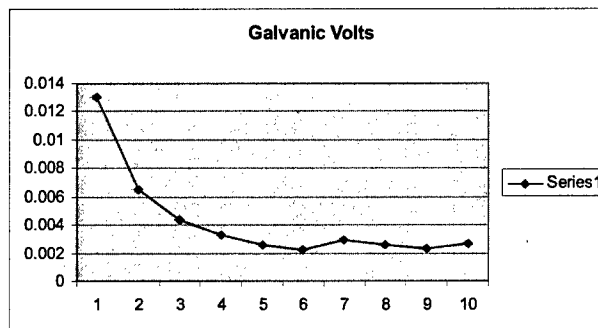
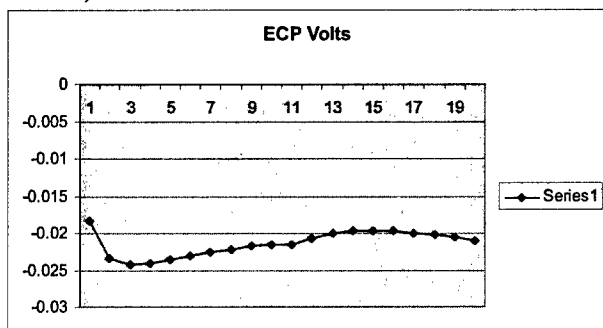
June 7, 2004 run, no power



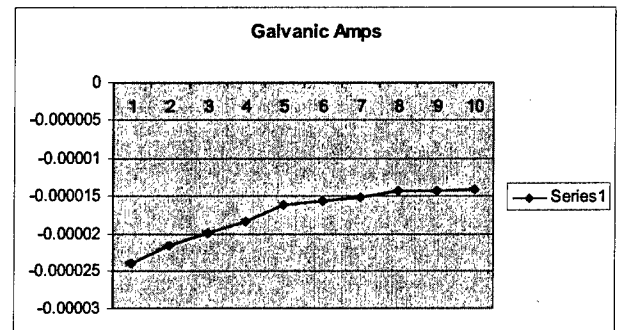
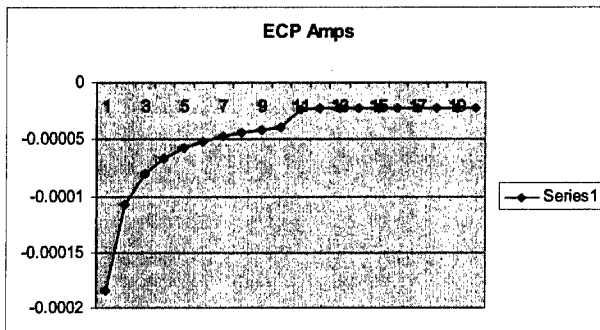
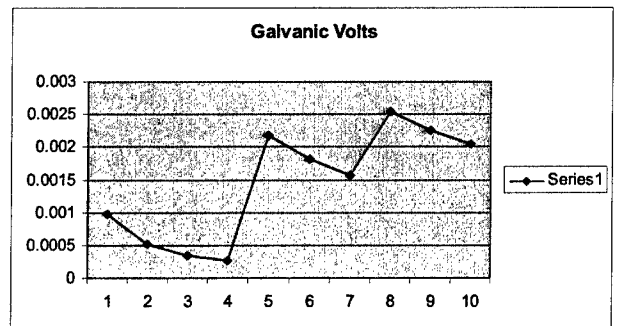
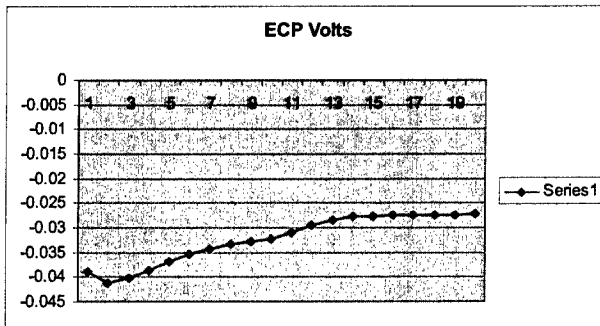
June 8, 2004 – 4 MW run



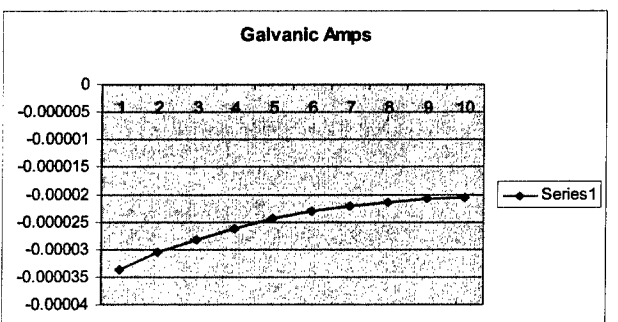
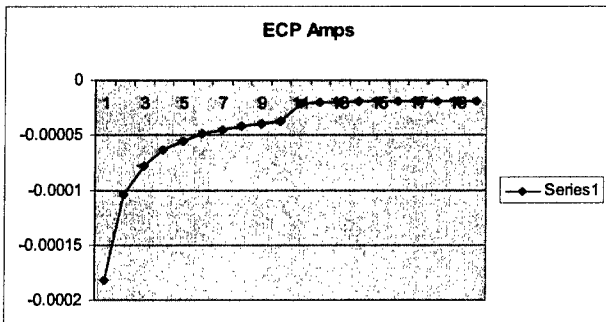
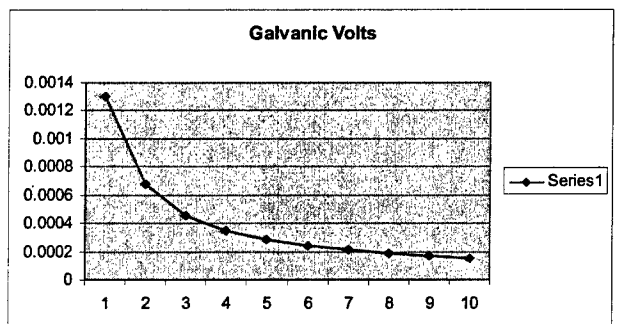
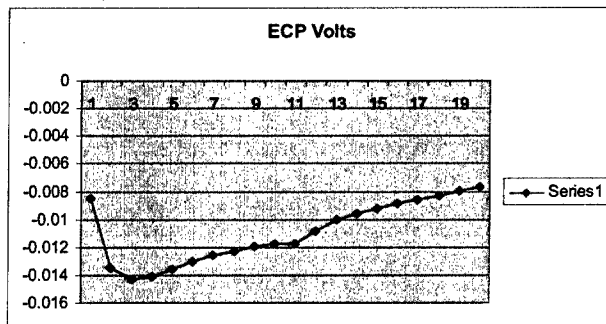
June 9, 2004 – 4 MW run



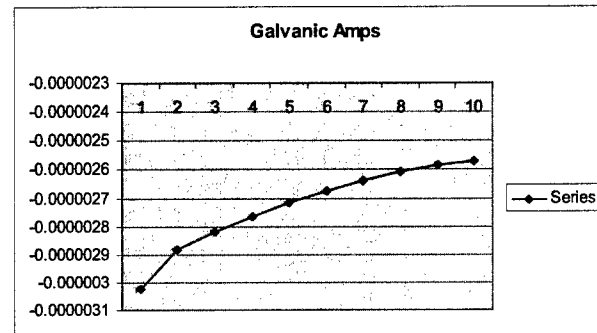
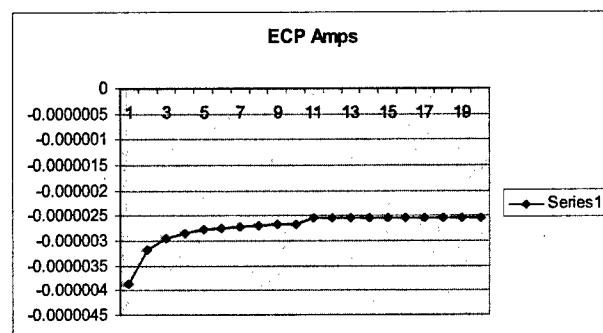
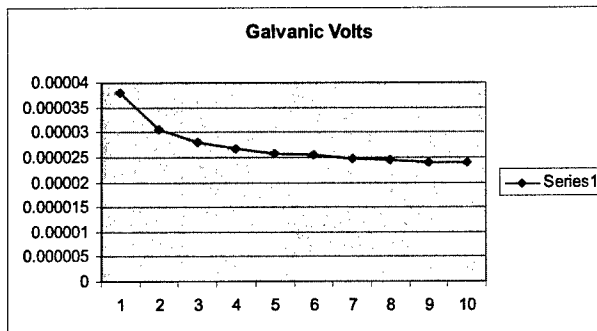
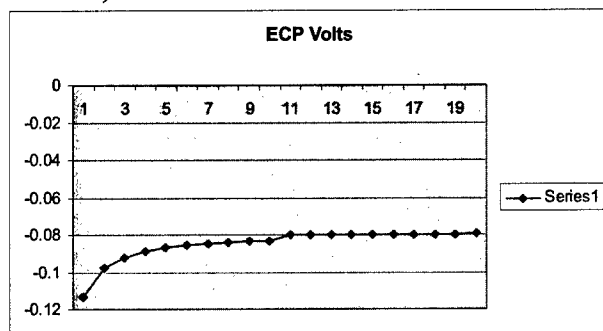
June 10, 2004 – 4.35 MW run



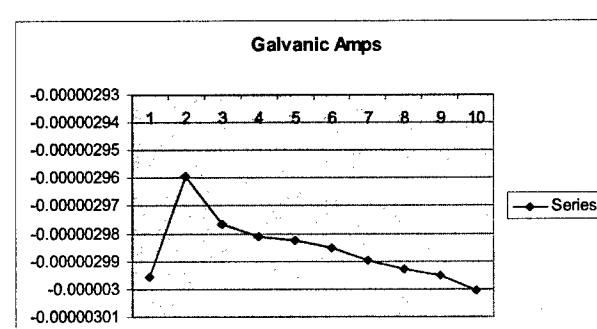
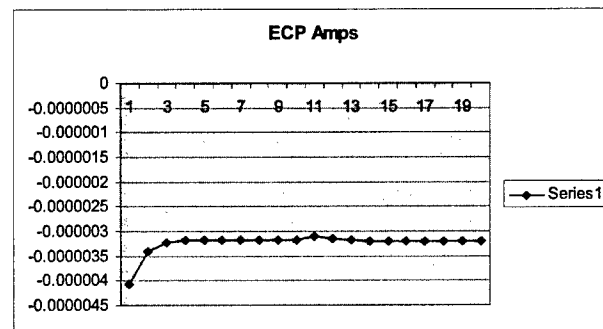
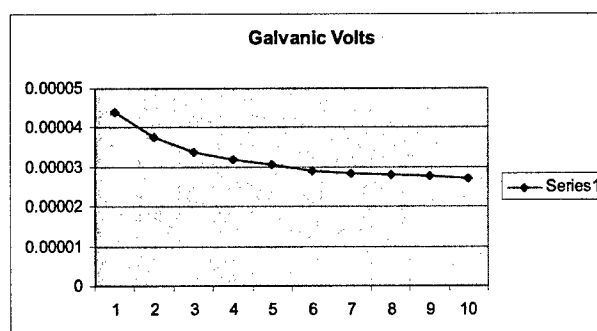
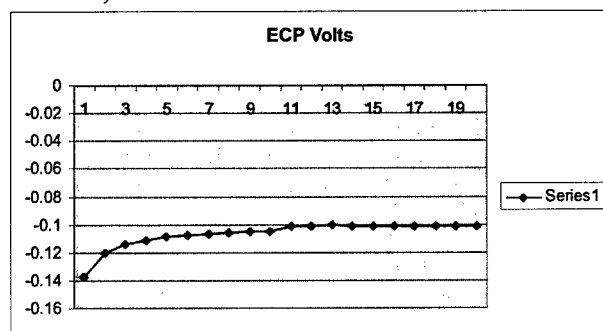
June 11, 2004 – 4 MW run



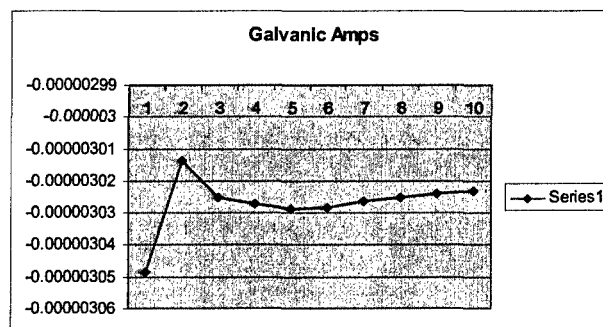
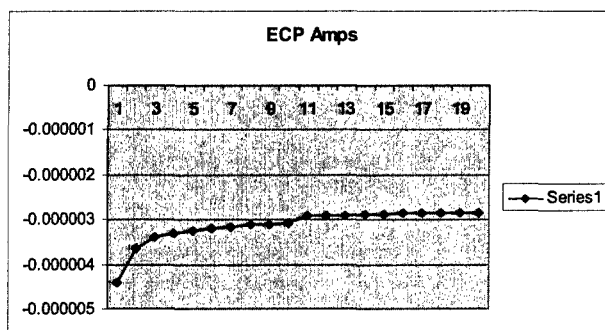
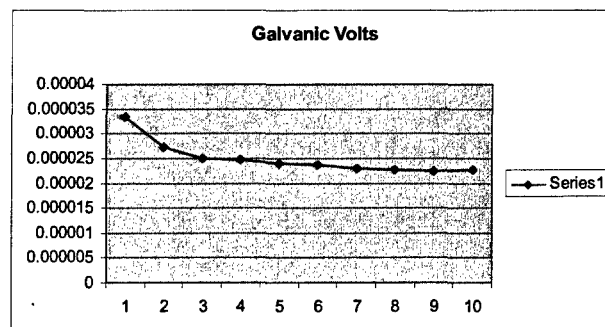
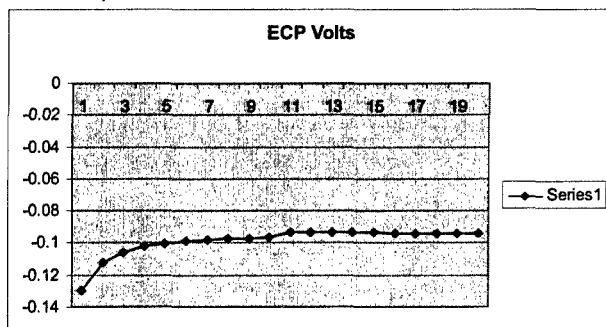
June 14, 2004 – 4 MW run



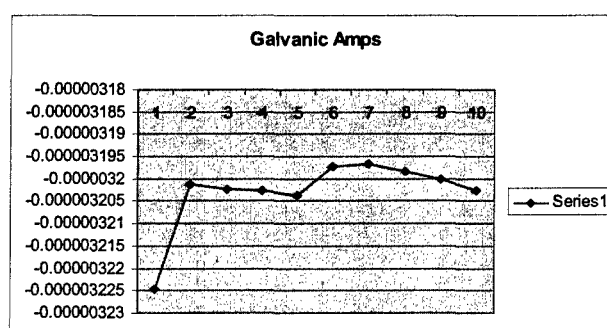
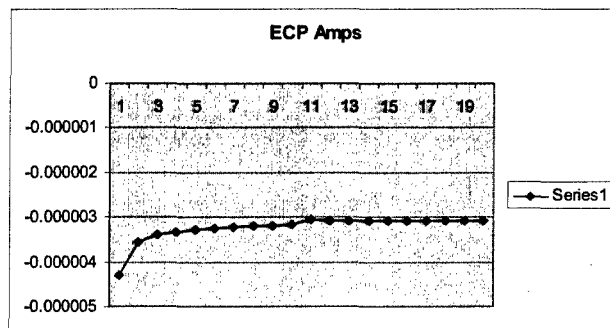
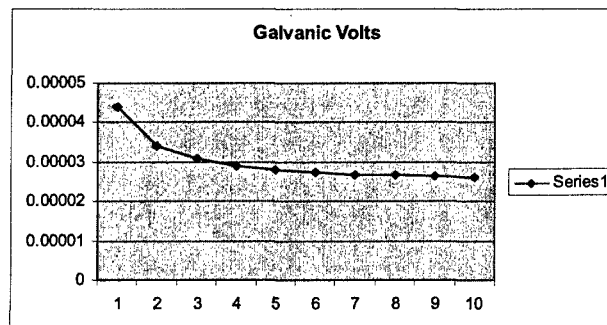
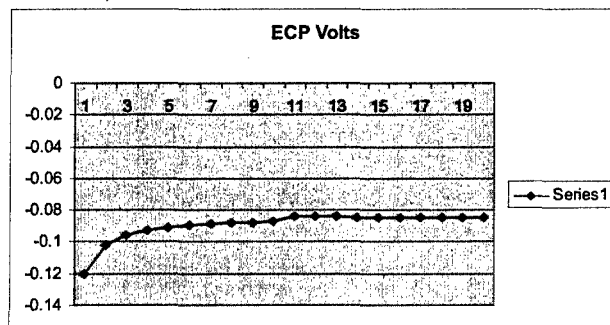
June 15, 2004 – 4 MW run



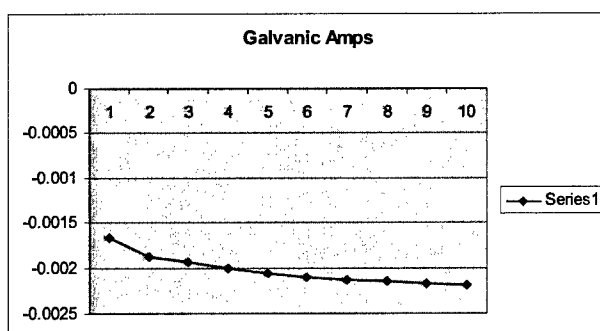
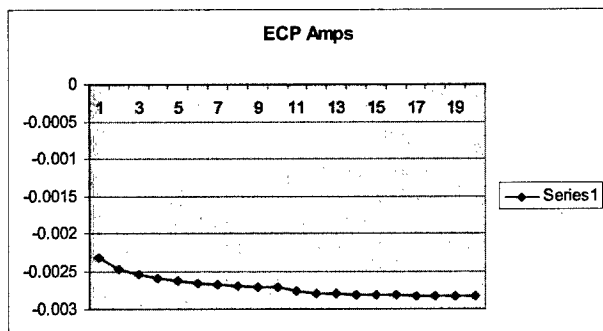
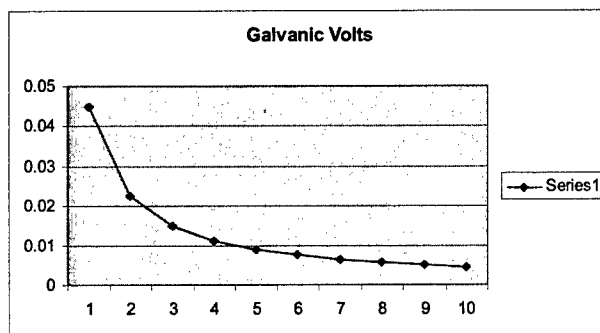
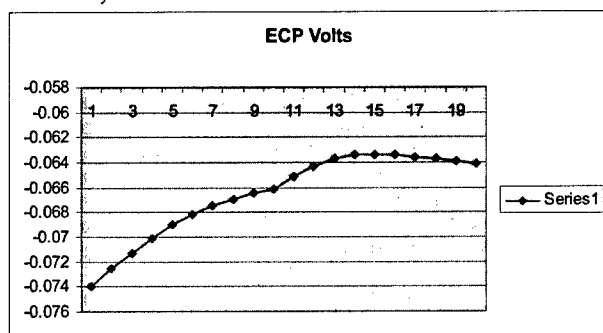
June 16, 2004 – 4 MW run



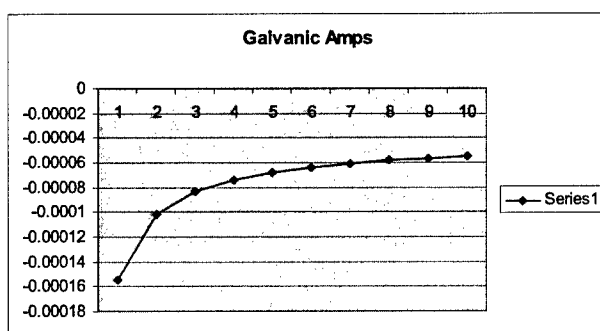
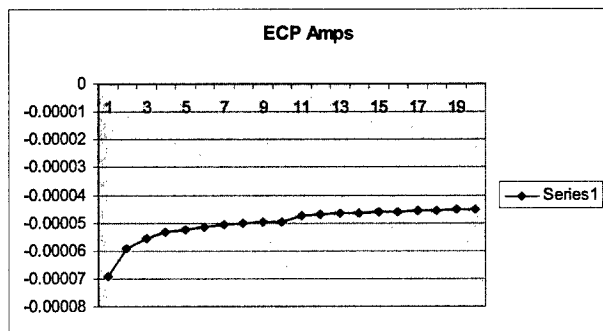
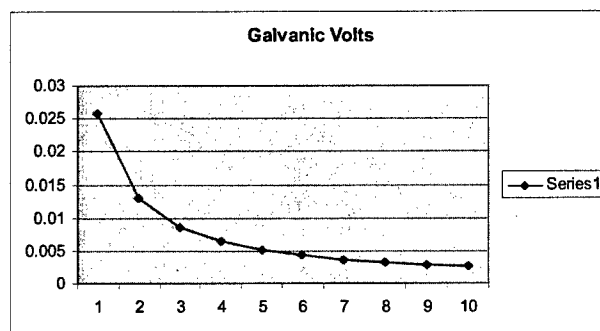
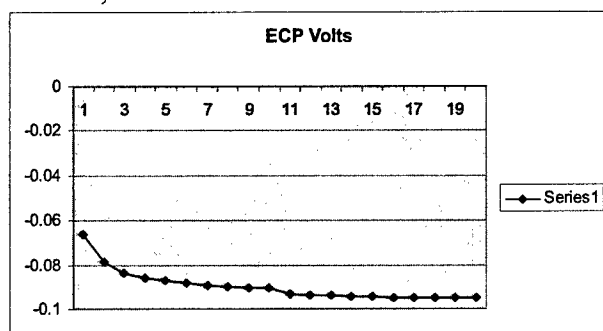
June 18, 2004 – 4 MW run



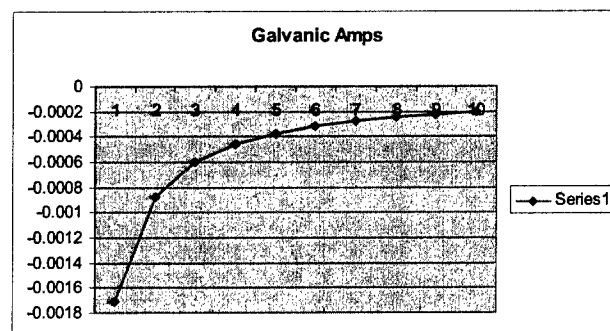
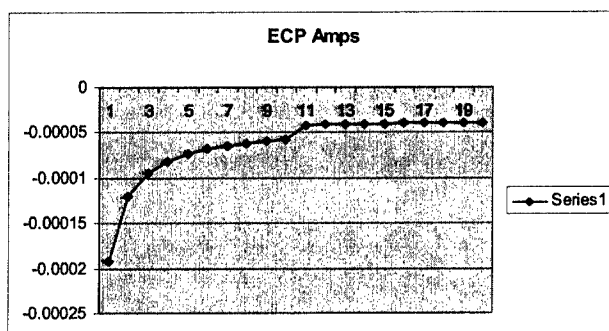
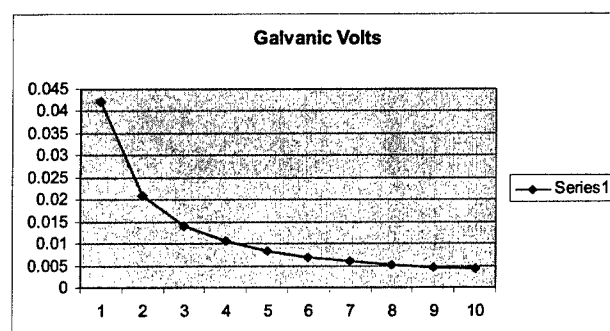
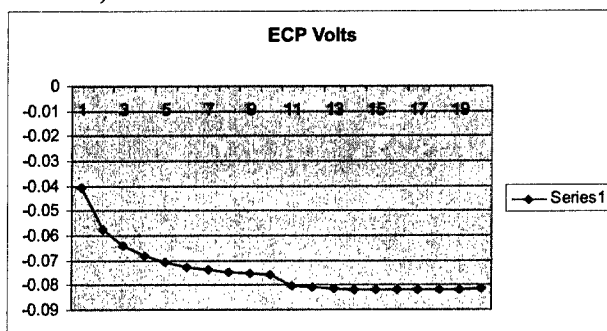
June 22, 2004 – 4 MW run



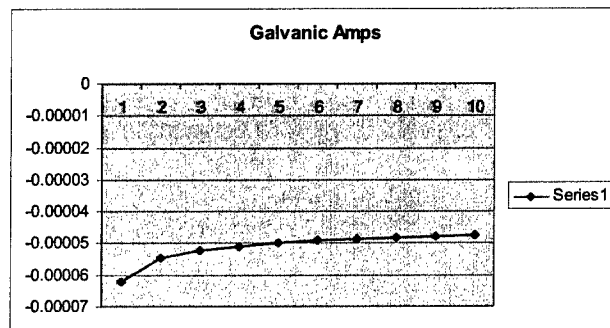
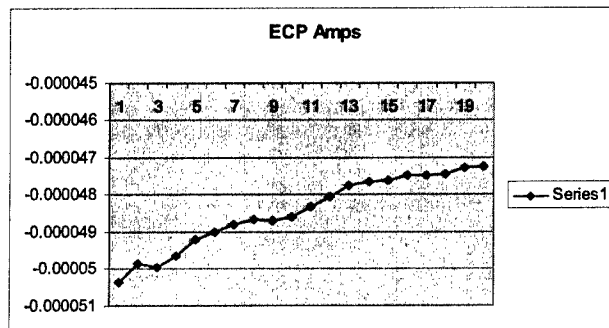
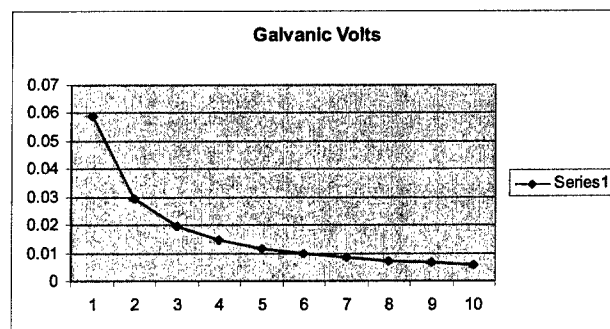
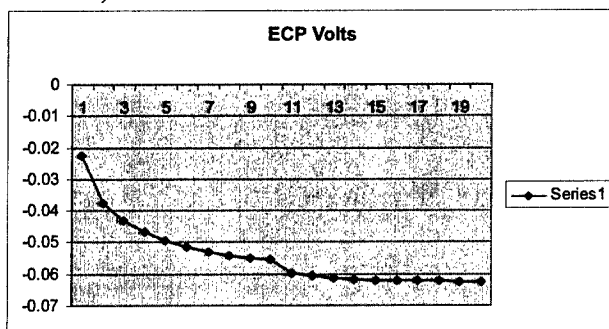
June 23, 2004 – 4 MW run



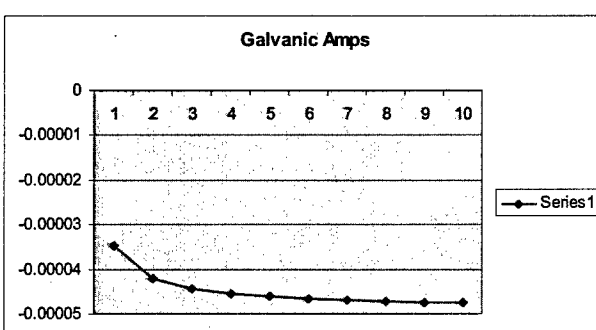
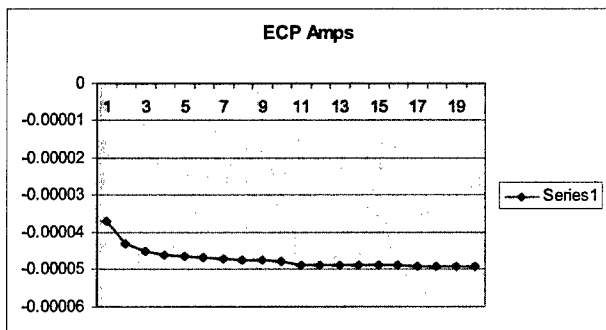
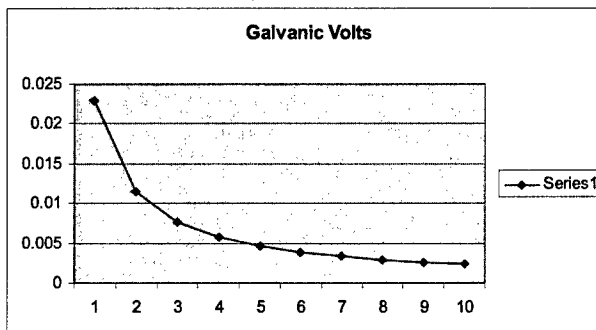
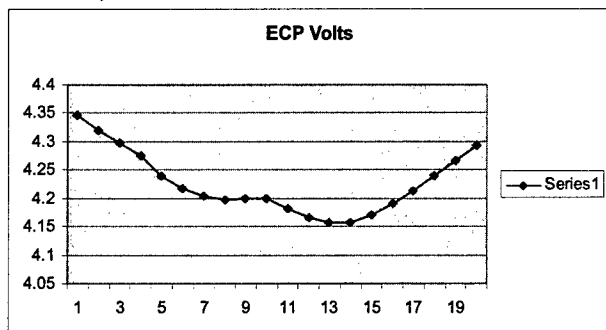
June 24, 2004 – 4 MW run



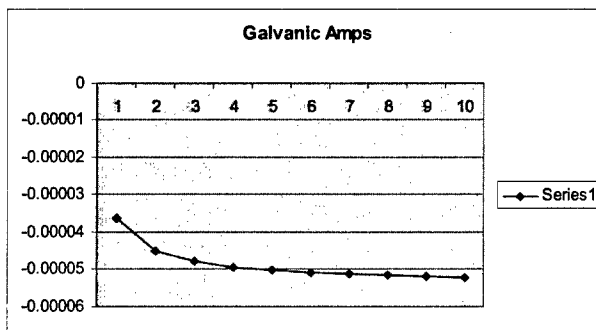
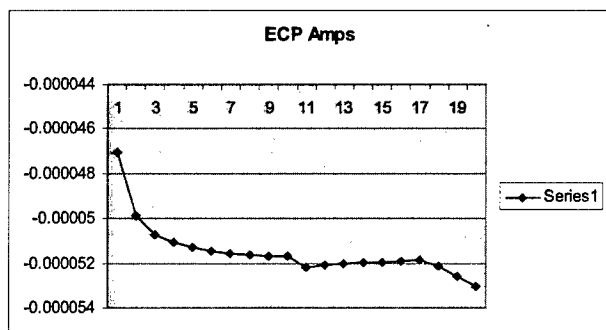
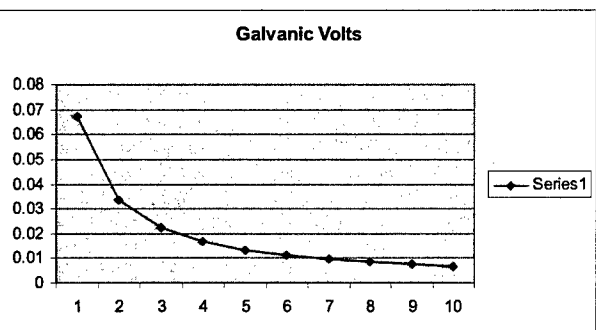
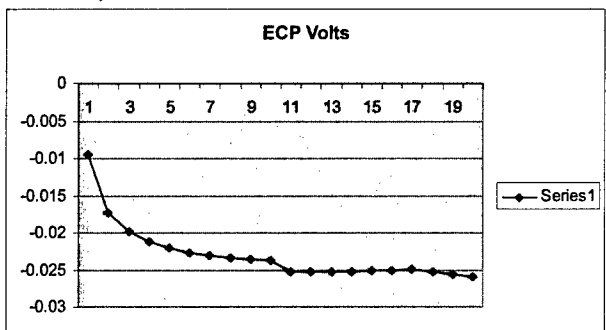
June 28, 2004 – 4 MW run



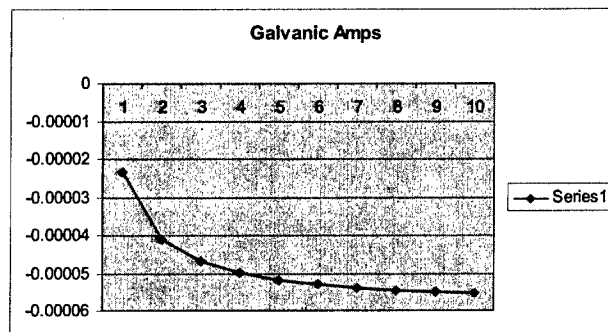
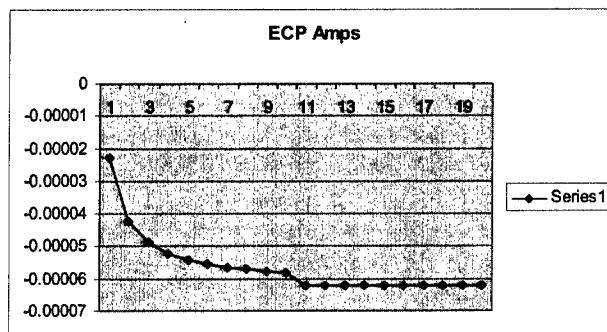
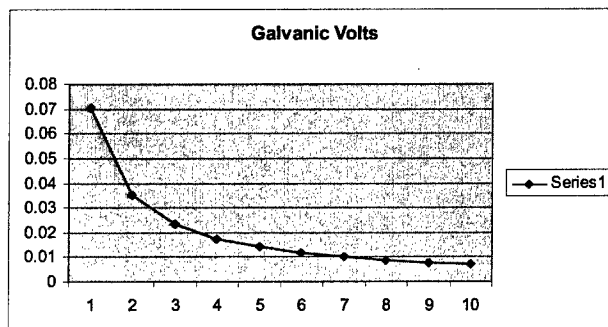
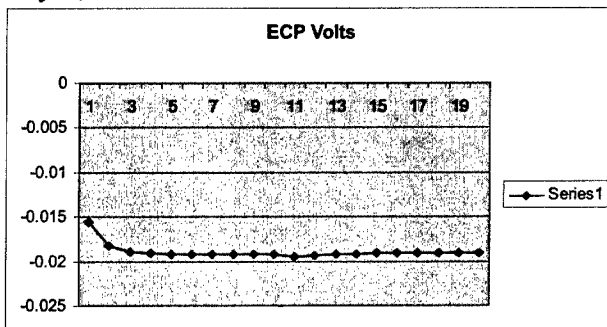
June 29, 2004 – 4 MW run



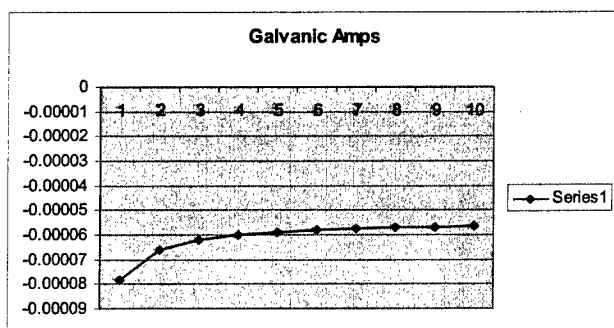
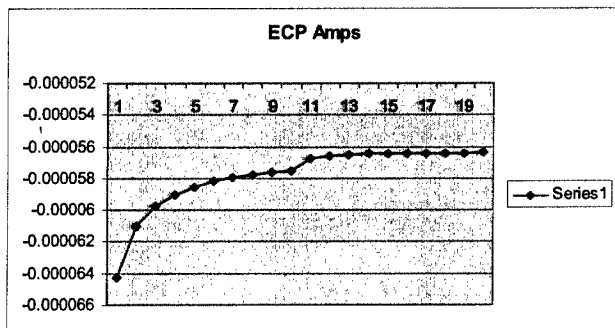
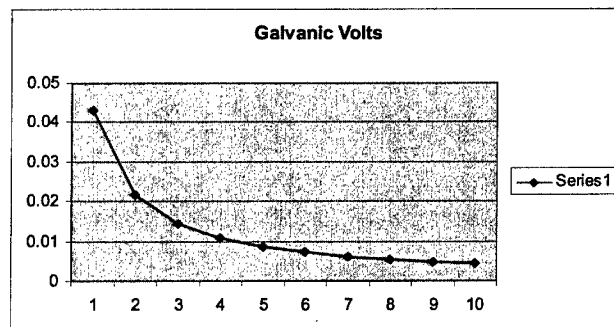
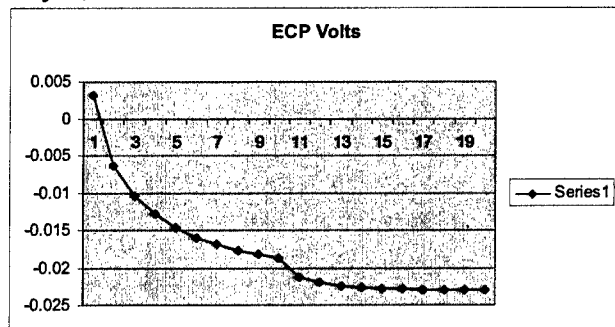
June 30, 2004 – 4 MW run



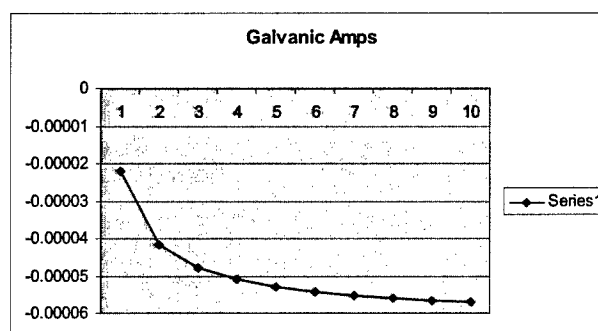
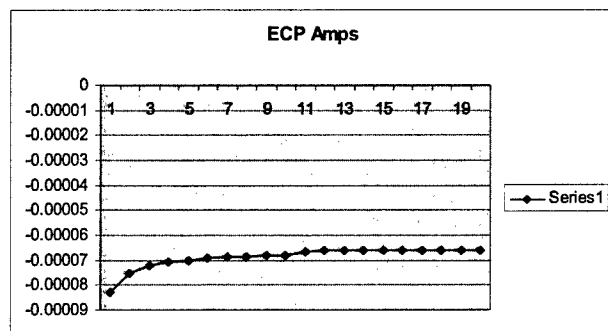
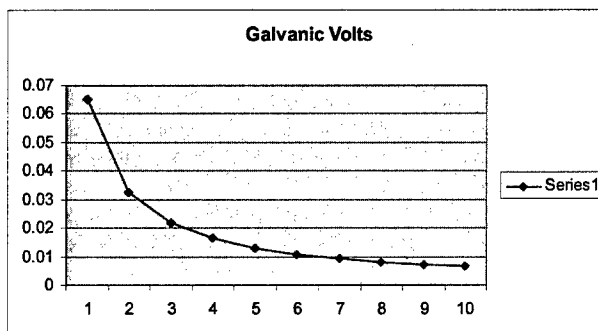
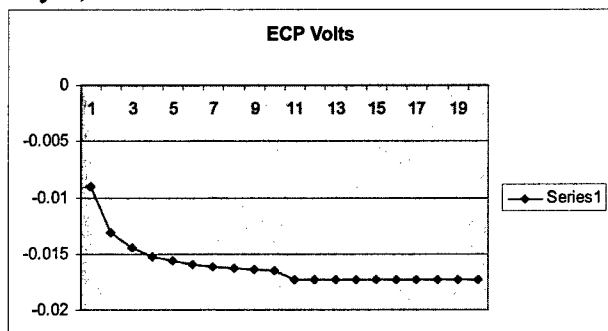
July 2, 2004 – 4 MW run



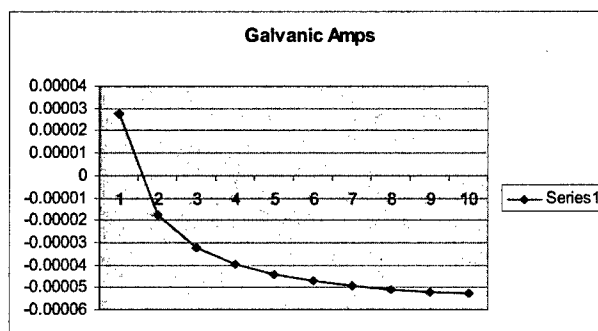
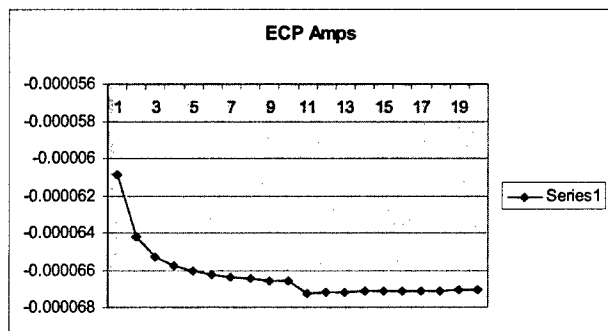
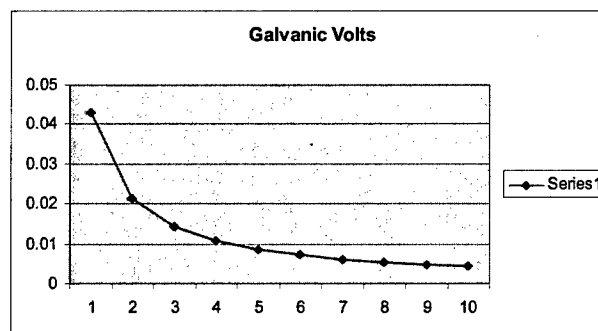
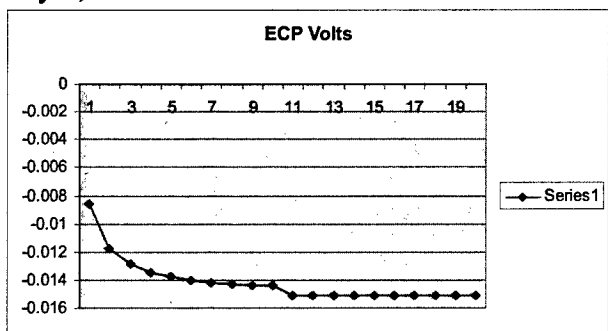
July 6, 2004 – 4 MW run



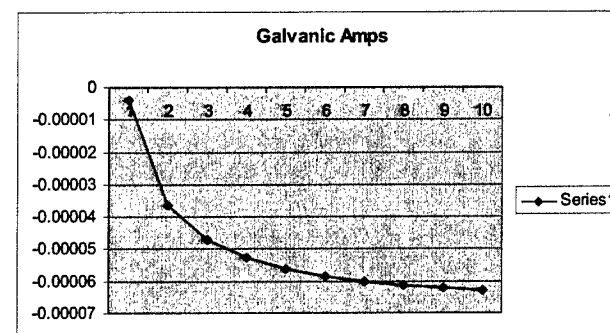
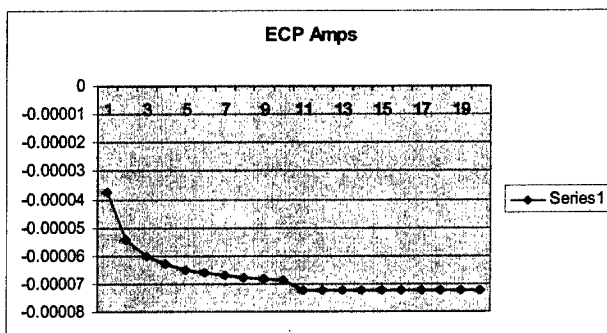
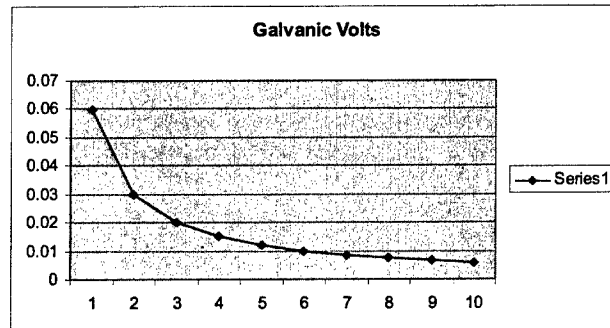
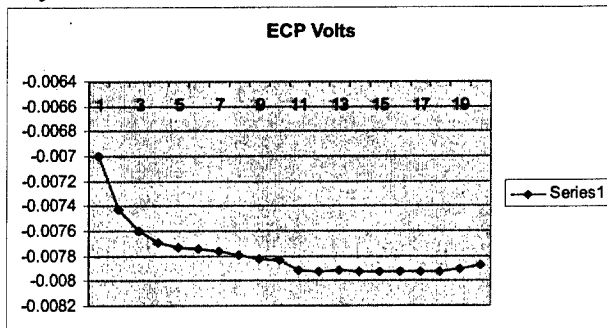
July 7, 2004 – 4 MW run



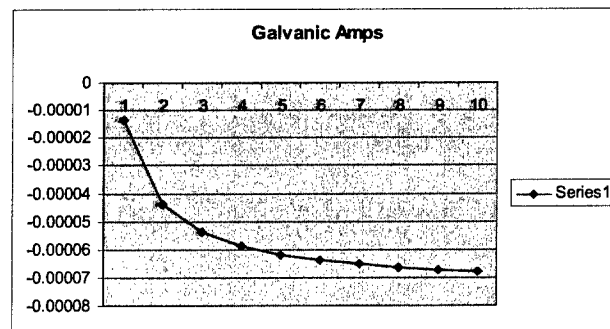
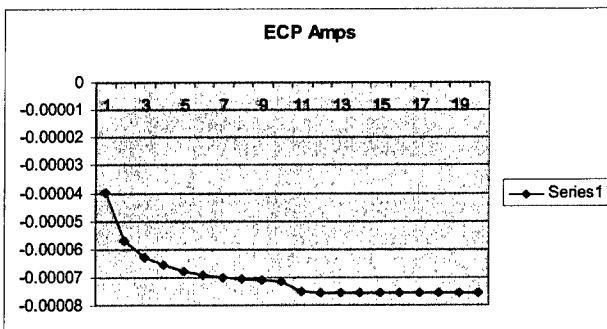
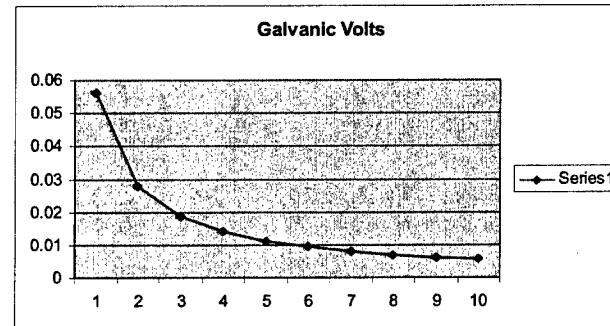
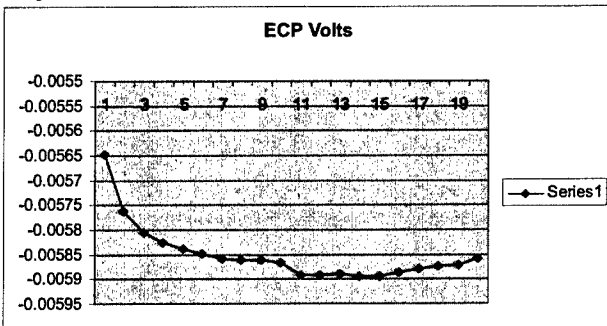
July 9, 2004 – 4 MW run



July 12, 2004 – 4 MW run

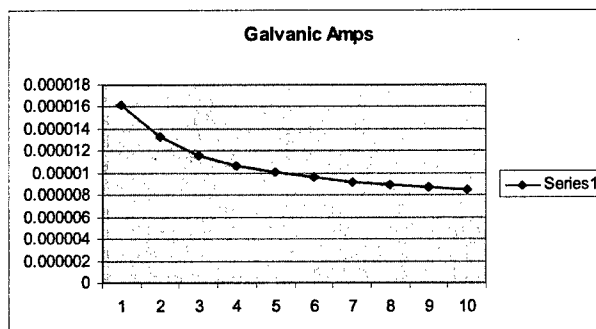
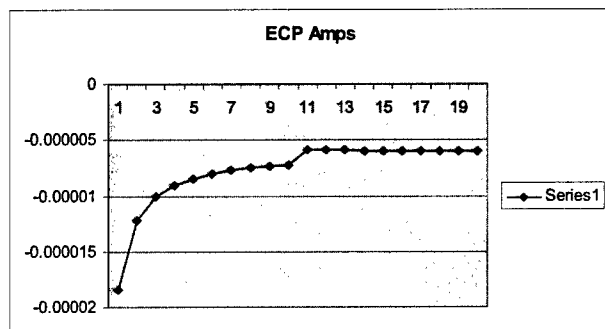
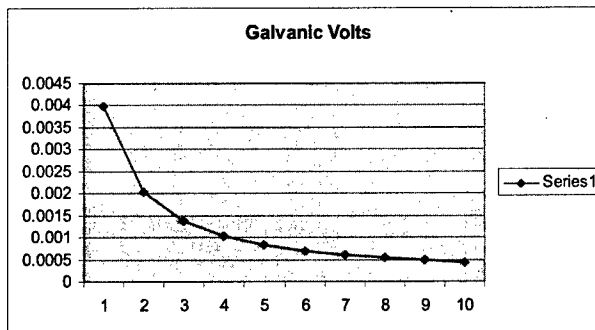
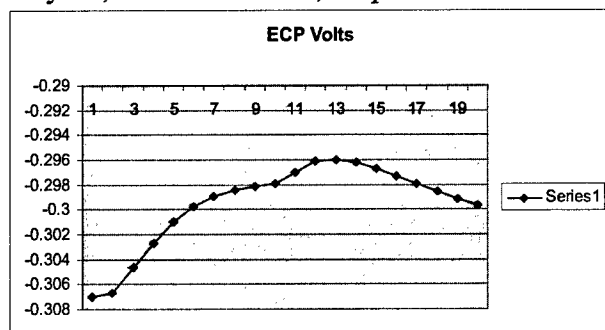


July 15, 2004 – 4 MW run

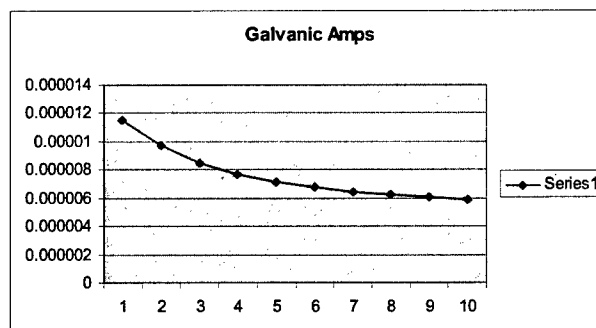
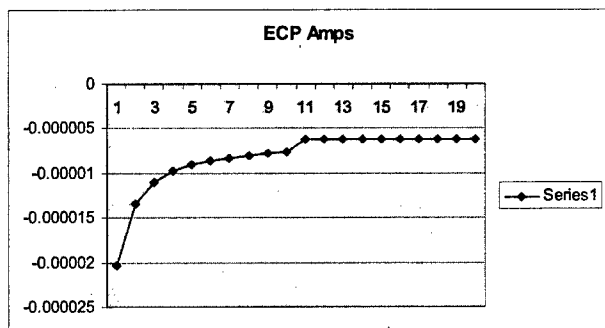
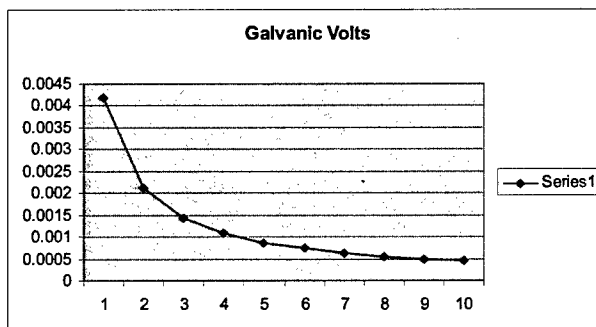
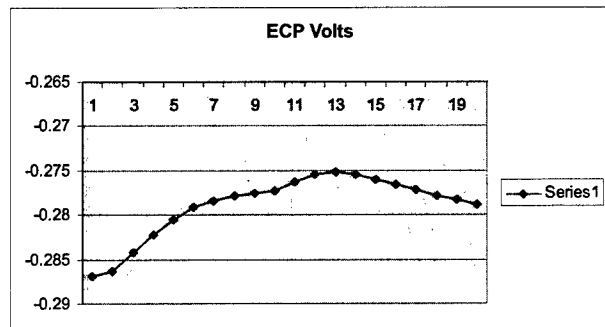


Appendix B – Zr-Pt Couple Graphs

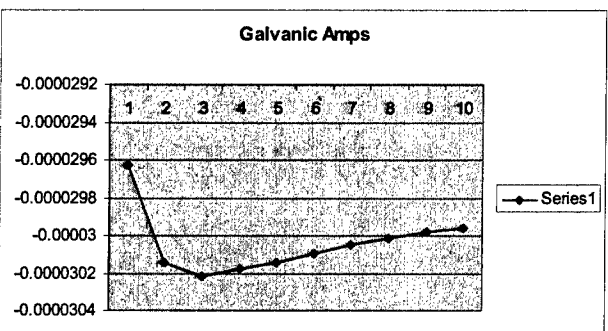
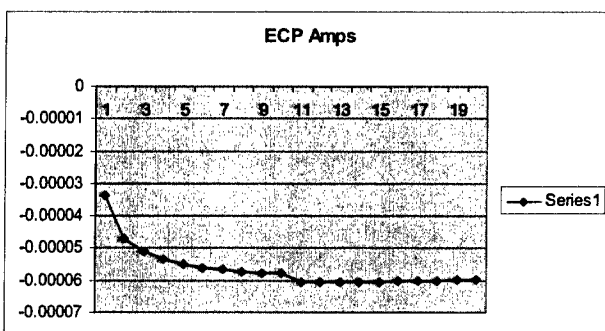
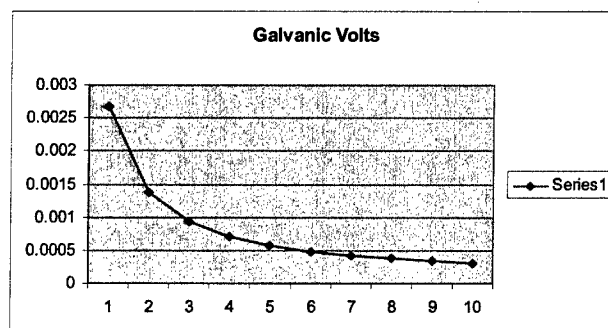
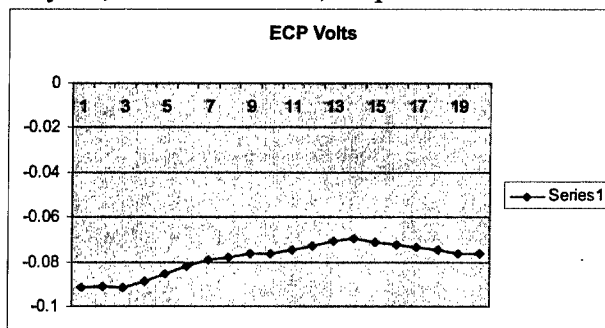
May 27, 2004 – first run, no power



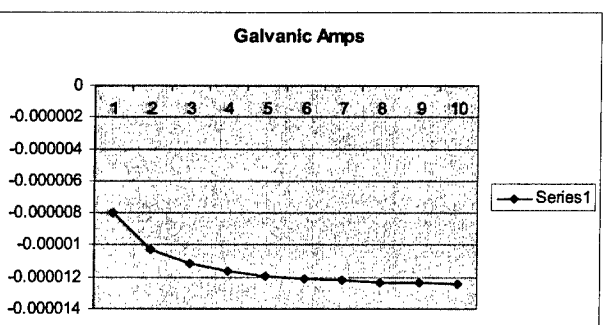
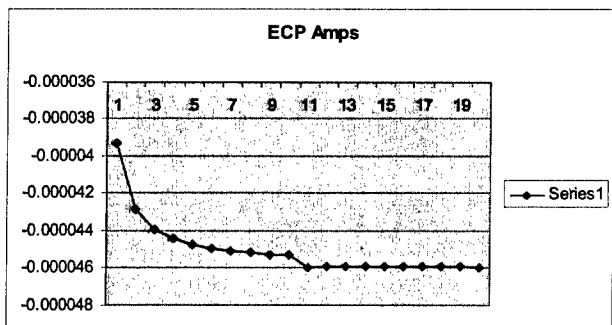
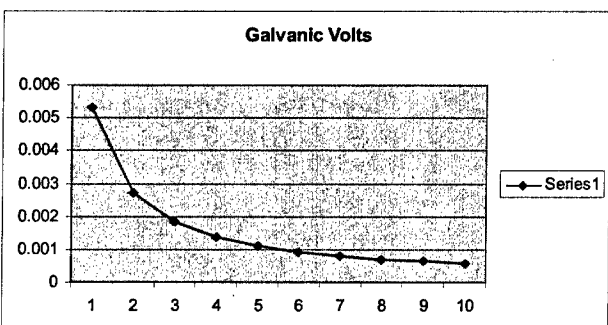
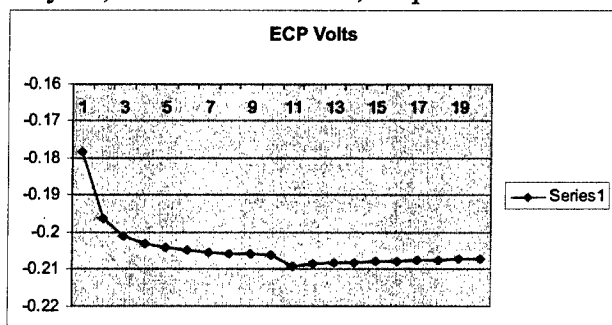
May 27, 2004 – second run, no power



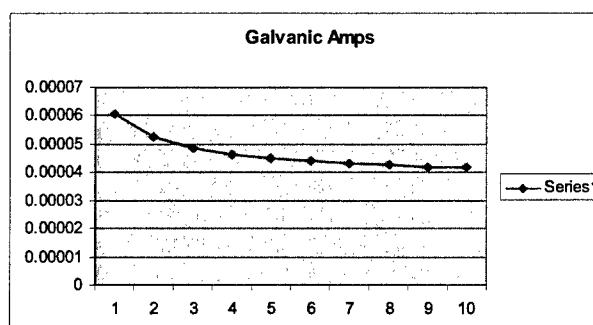
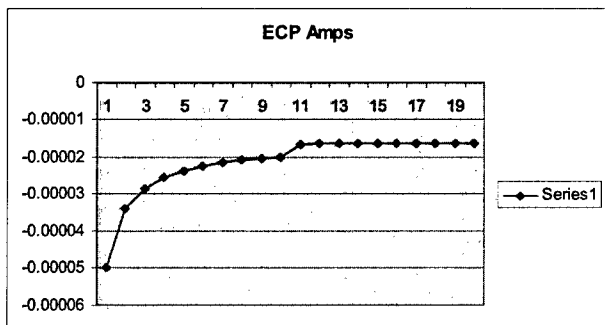
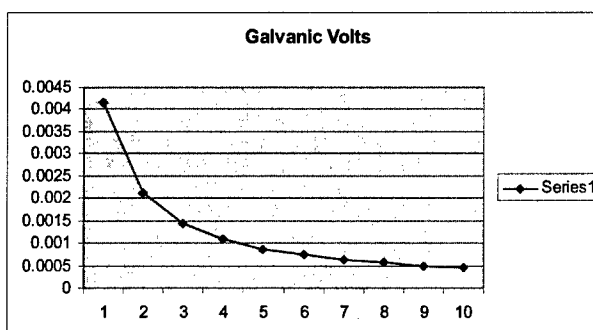
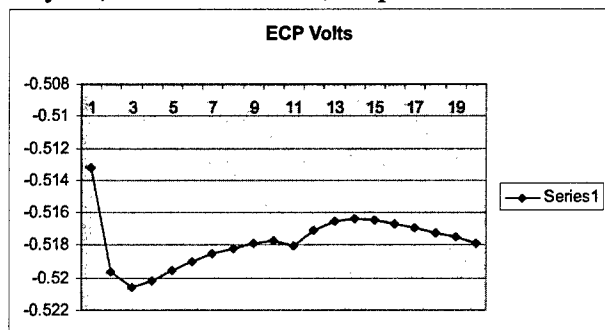
May 28, 2004 – first run, no power



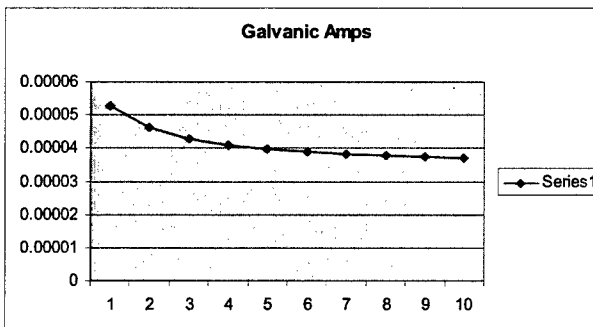
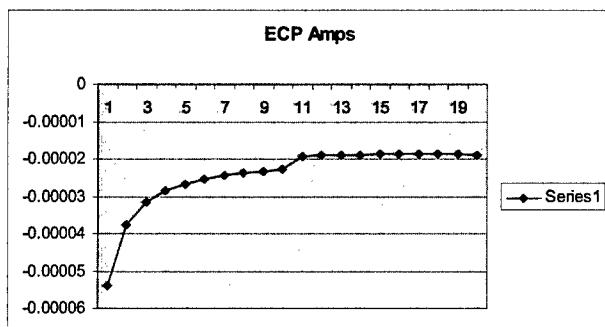
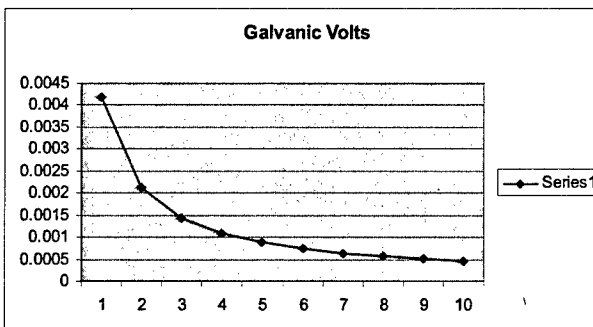
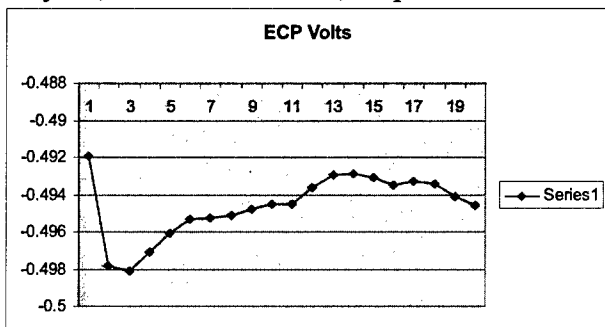
May 28, 2004 – second run, no power



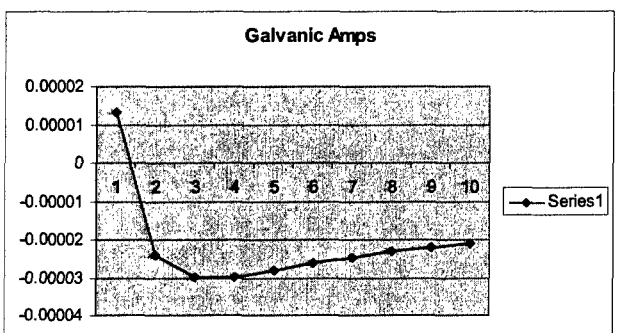
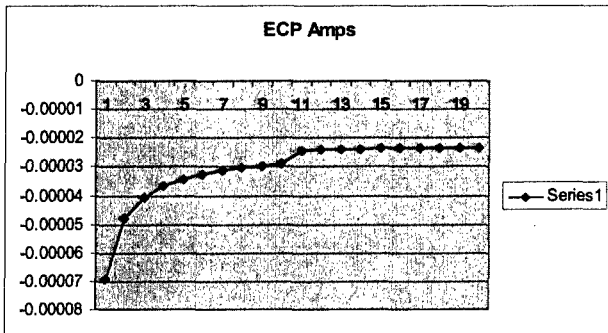
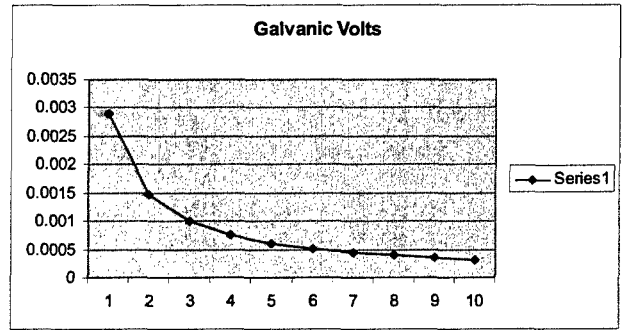
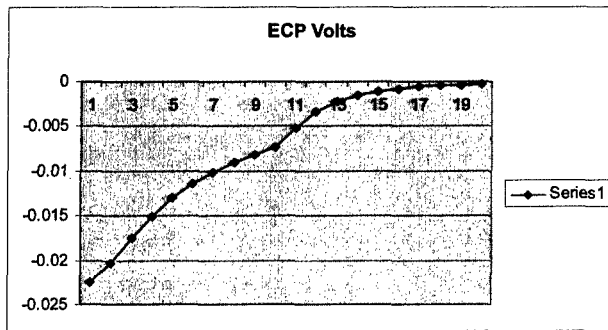
May 28, 2004 – third run, no power



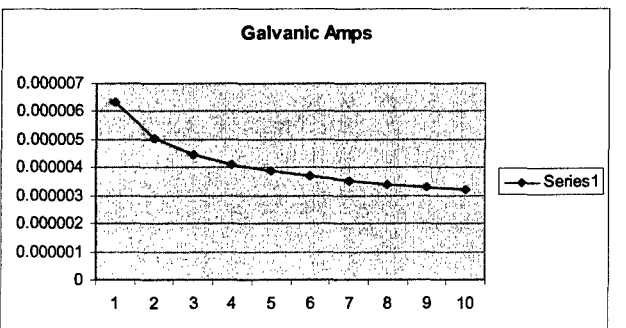
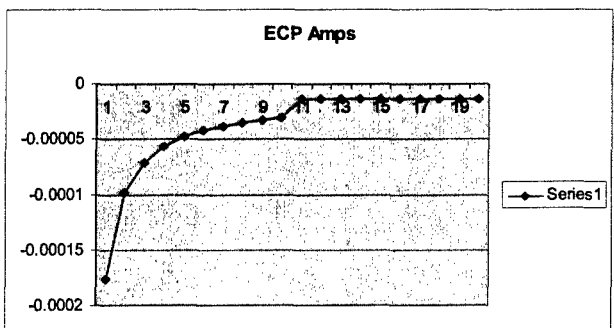
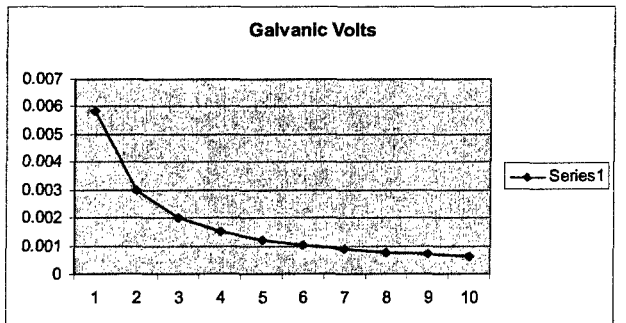
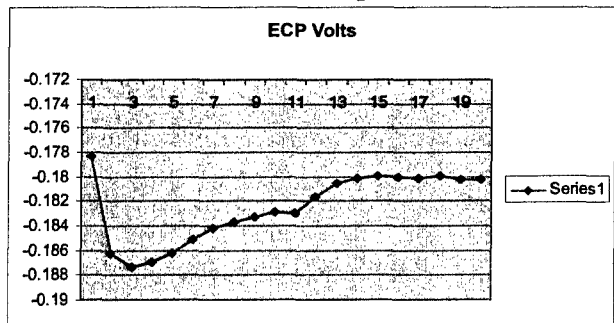
May 28, 2004 – fourth run, no power



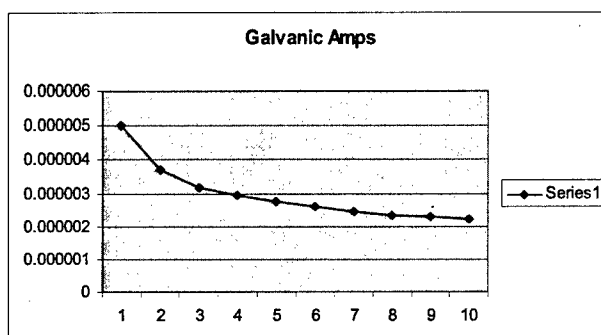
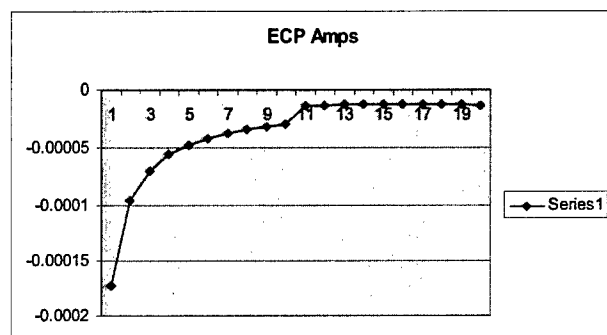
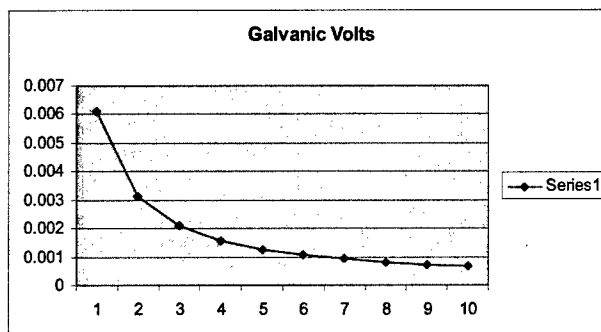
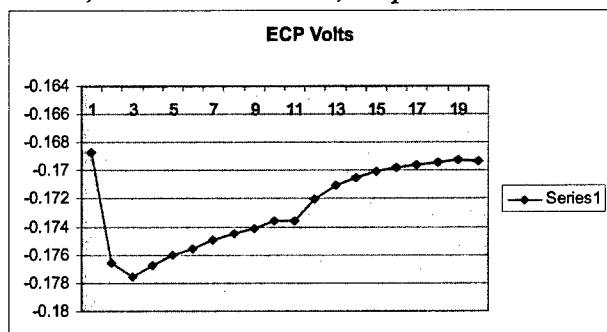
June 3, 2004 run, no power



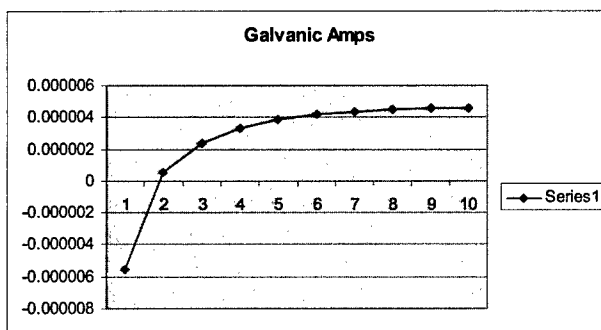
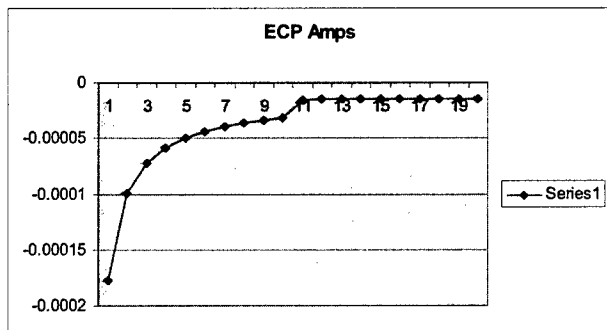
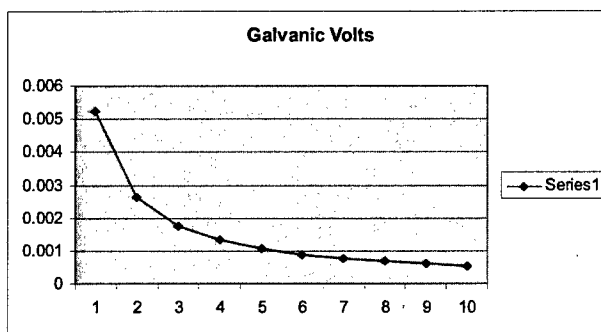
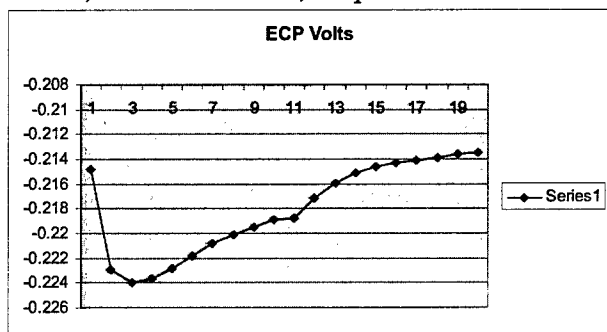
June 4, 2004 – first run, no power



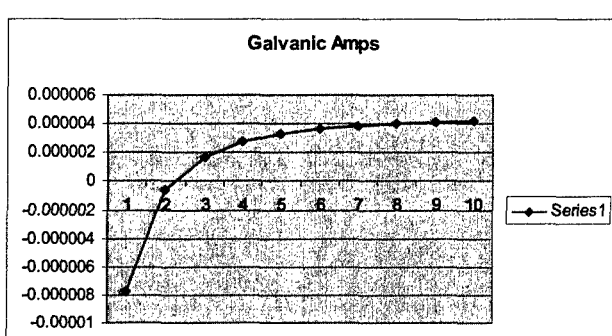
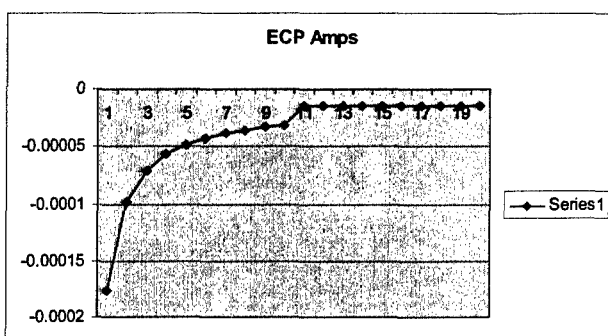
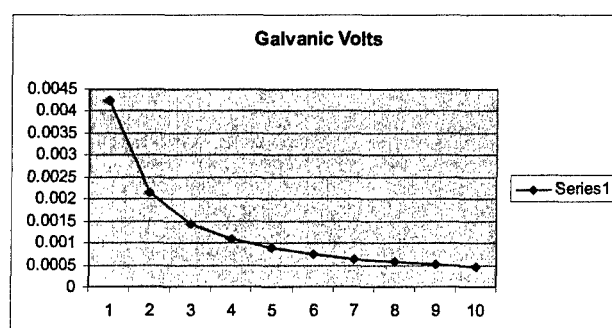
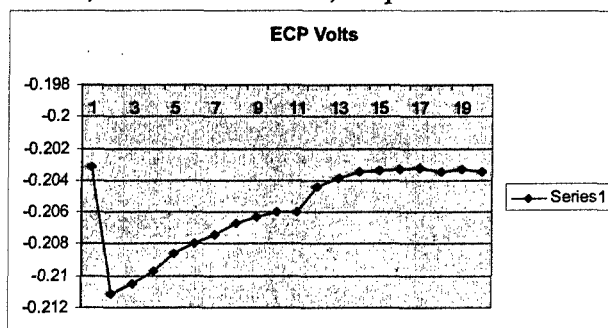
June 4, 2004 – second run, no power



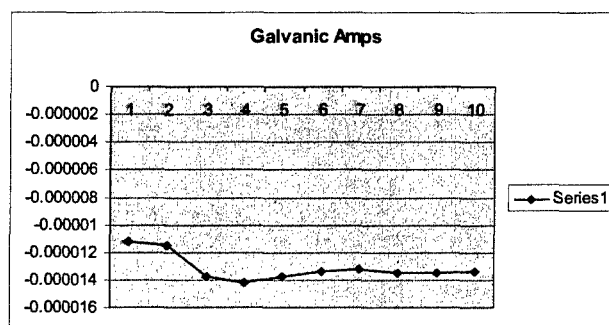
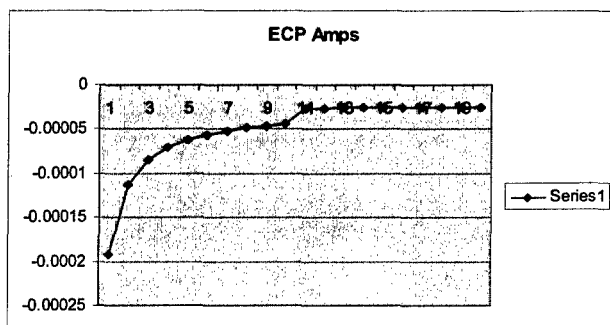
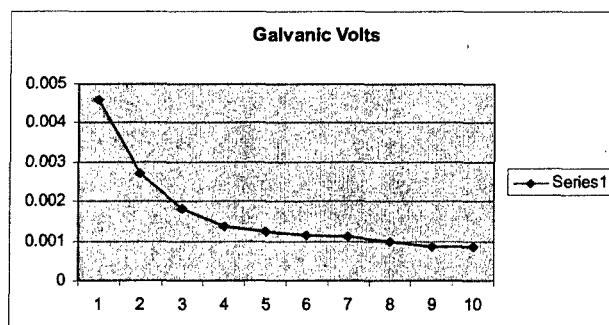
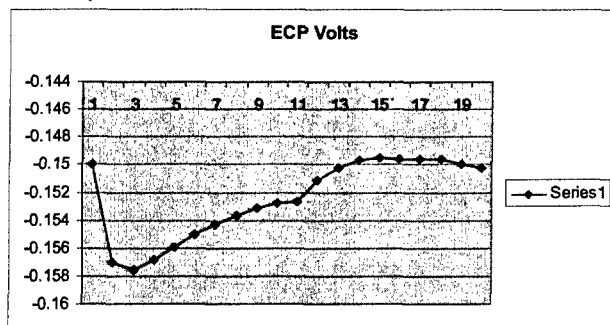
June 4, 2004 – third run, no power



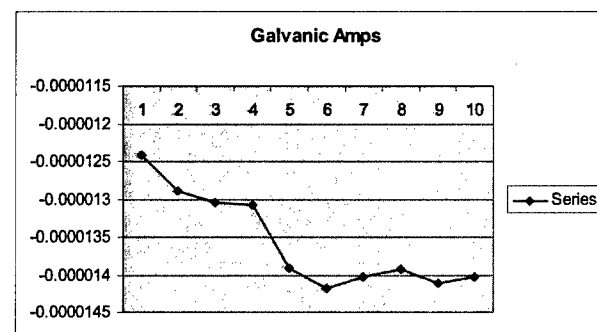
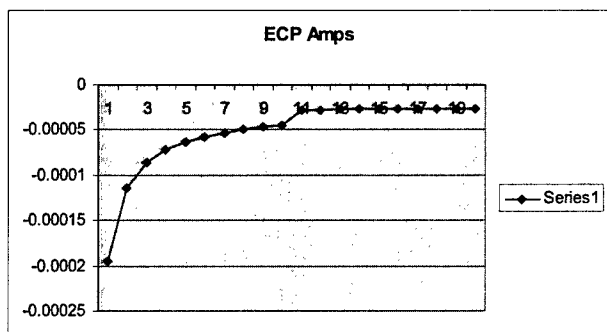
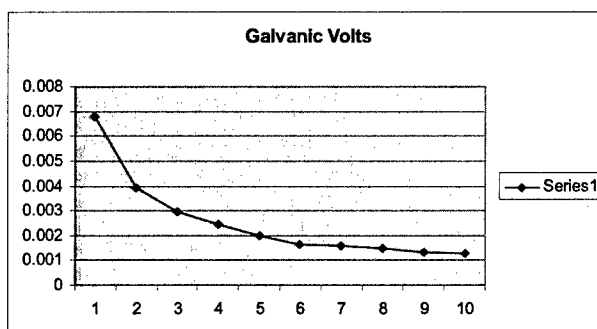
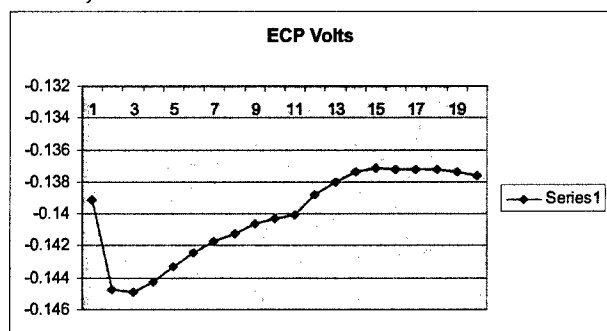
June 4, 2004 – fourth run, no power



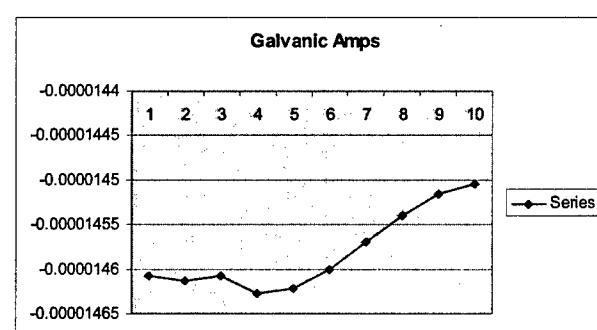
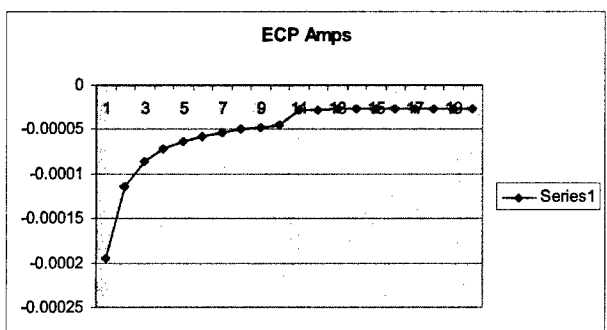
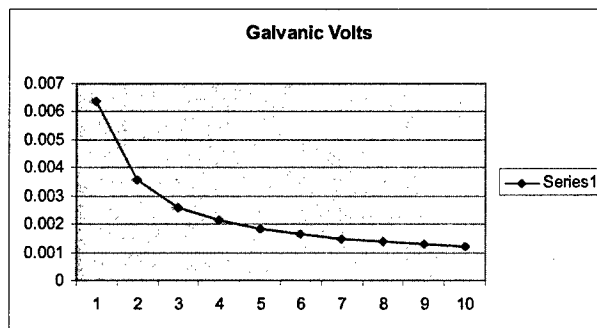
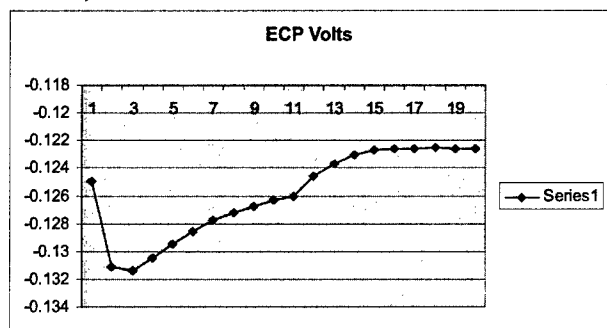
June 4, 2004 – 1 MW run



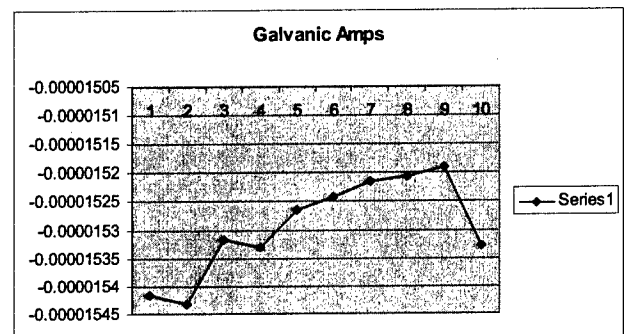
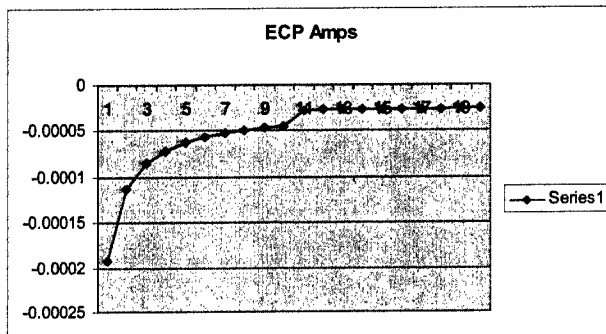
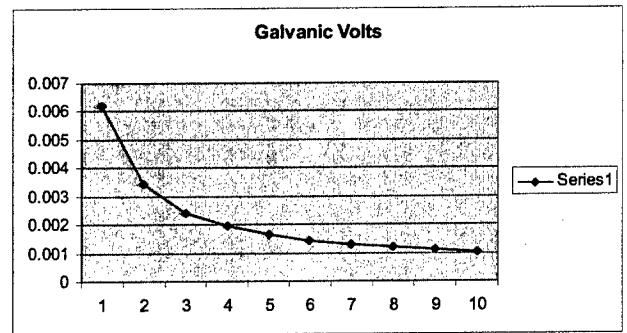
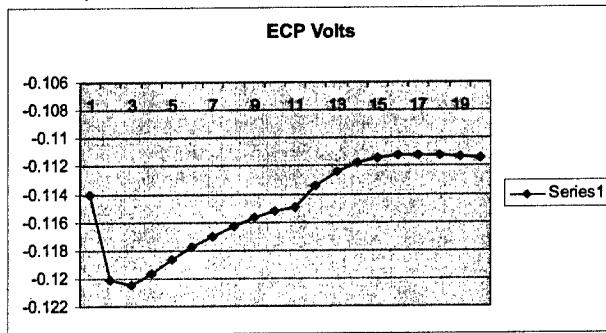
June 4, 2004 – 2 MW run



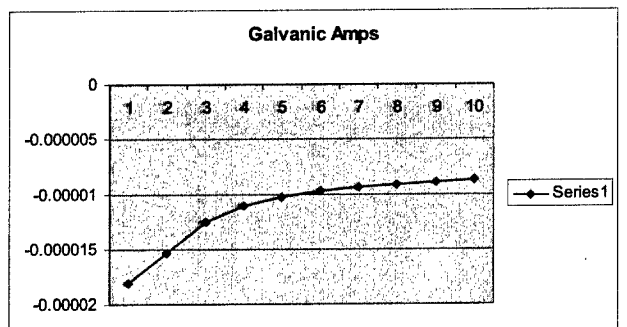
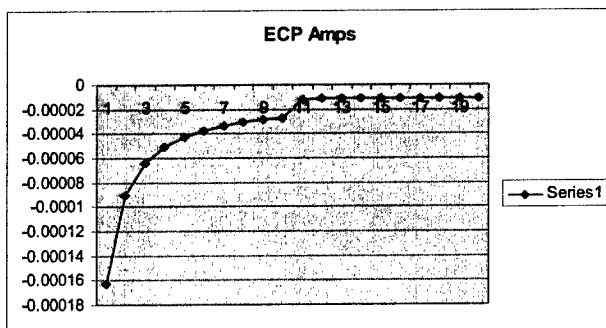
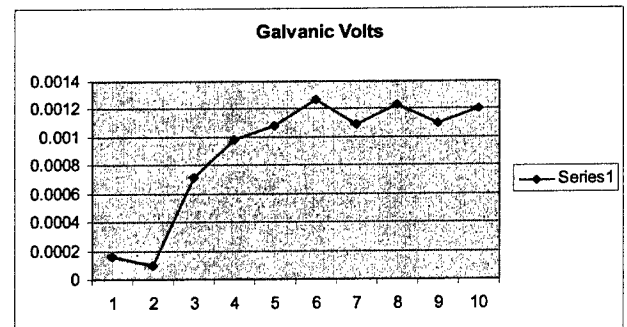
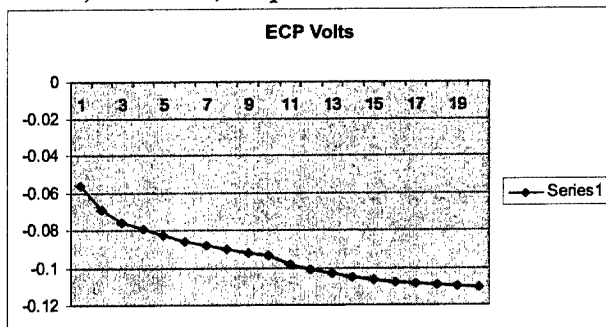
June 4, 2004 – 3 MW run



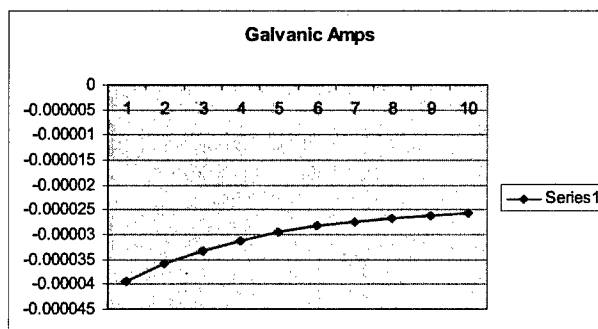
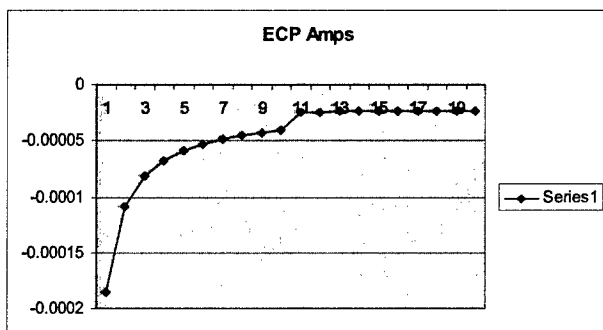
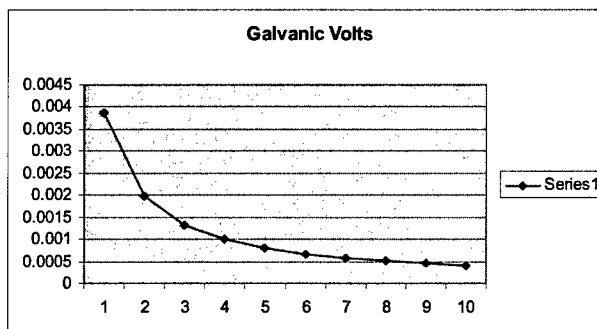
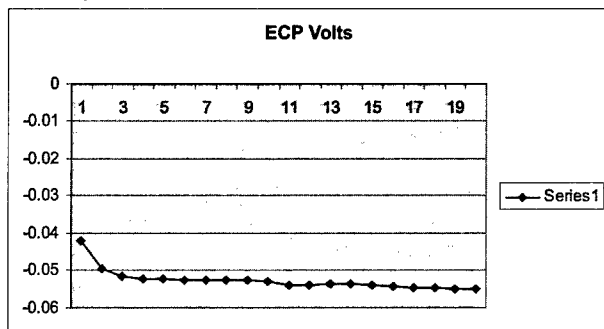
June 4, 2004 – 4 MW run



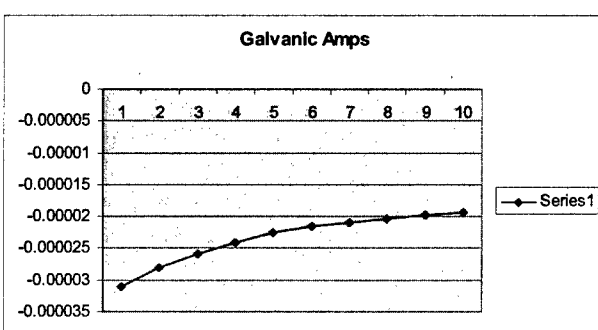
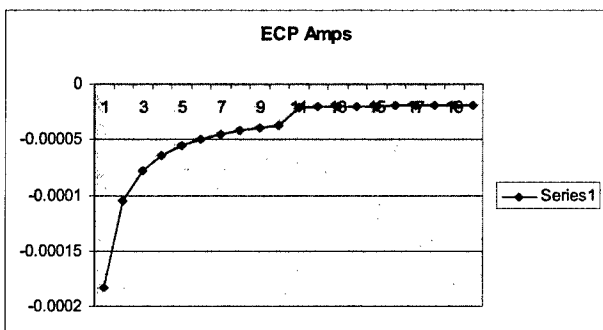
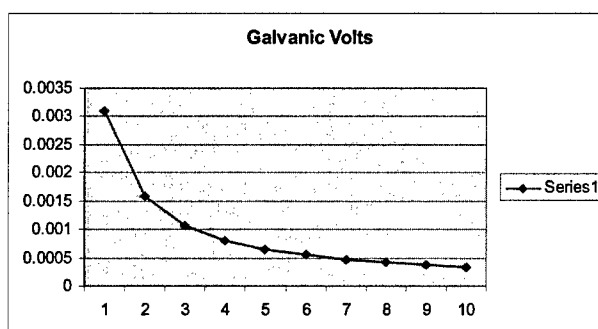
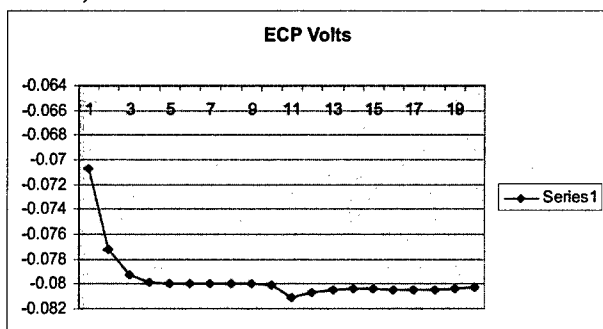
June 7, 2004 run, no power



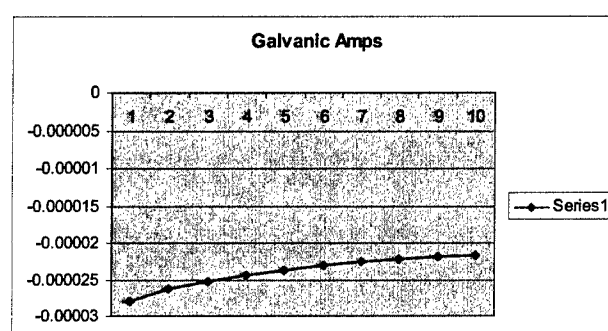
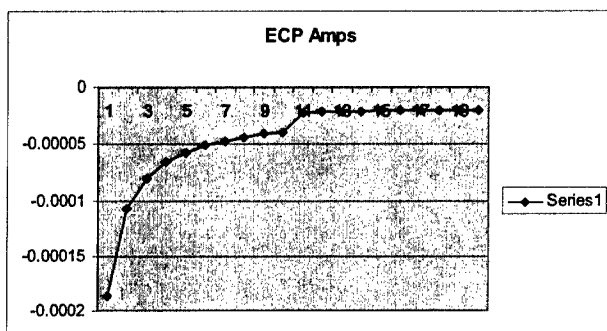
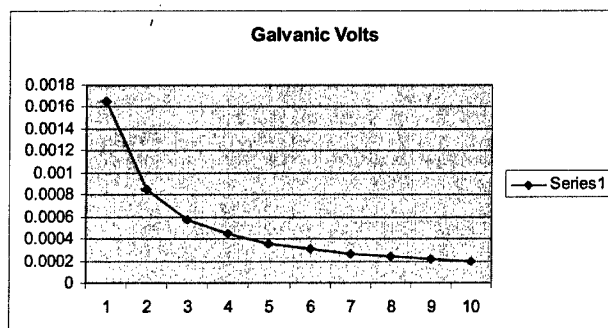
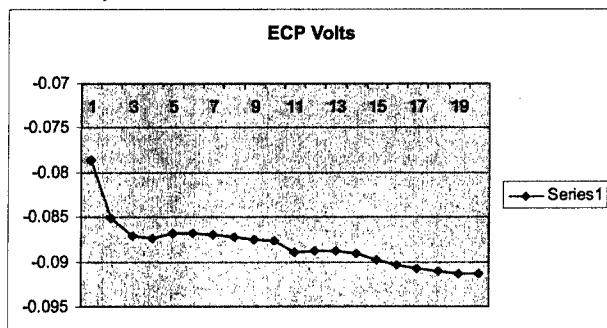
June 8, 2004 – 4 MW run



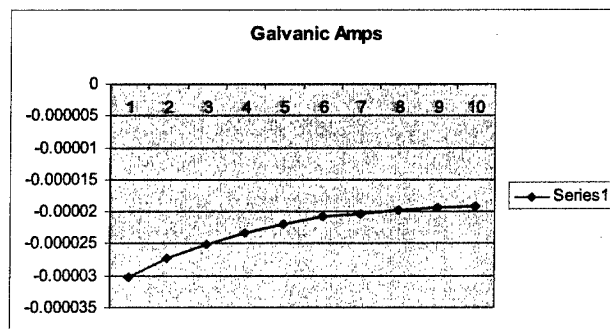
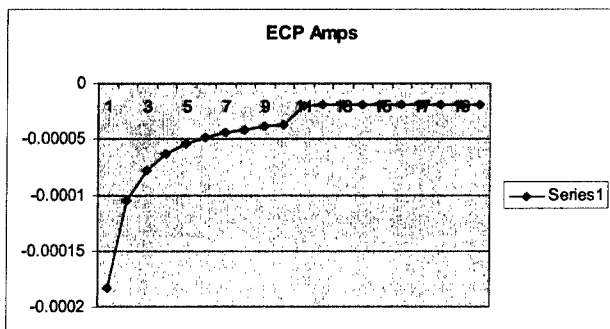
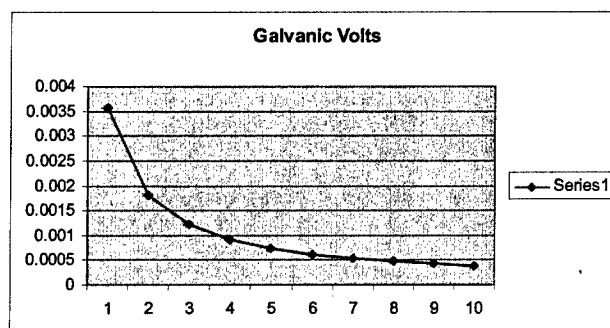
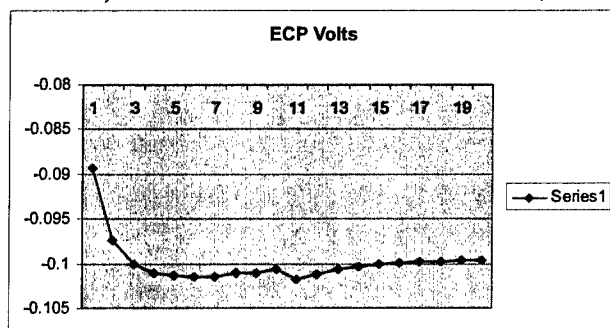
June 9, 2004 – 4 MW run



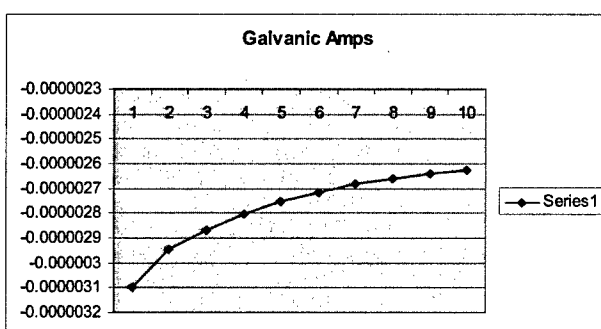
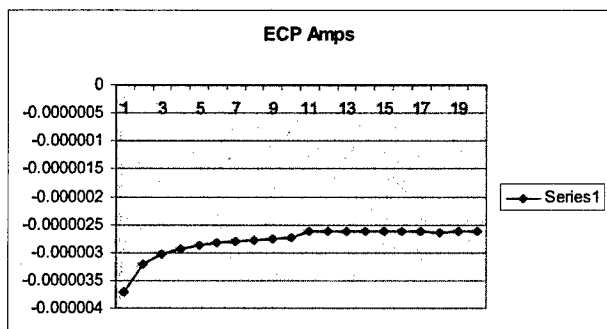
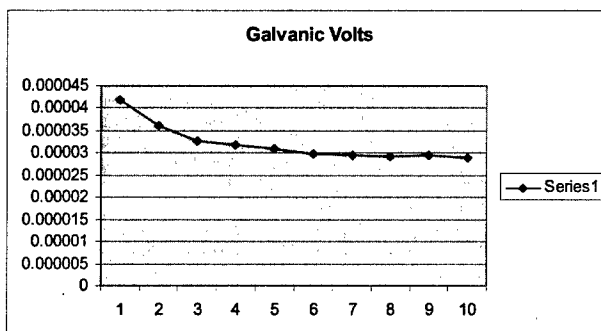
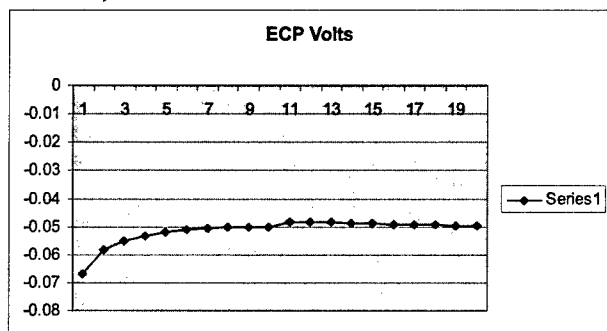
June 10, 2004 – 4.35 MW run



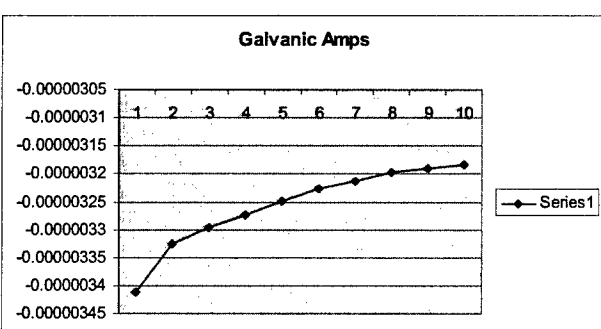
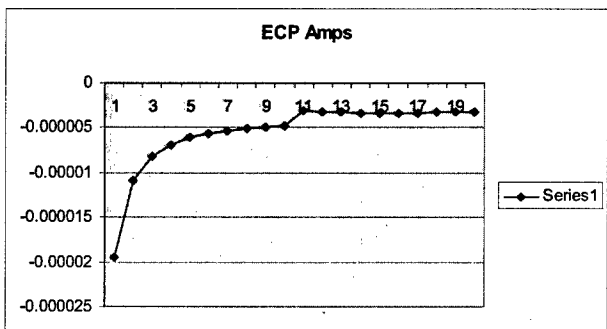
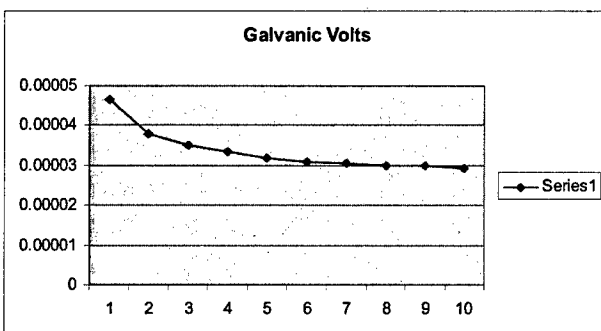
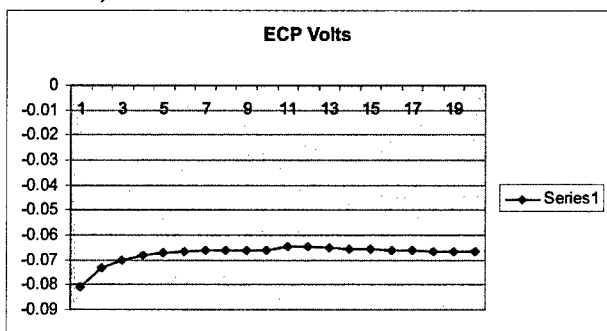
June 11, 2004 – 4 MW run



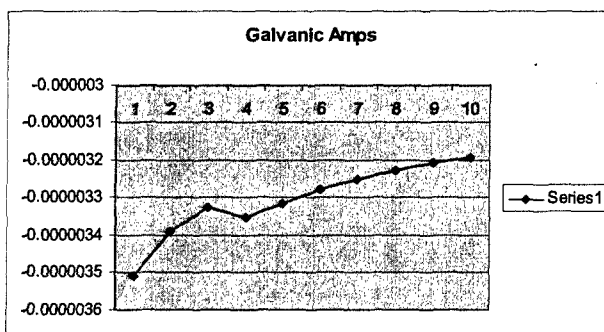
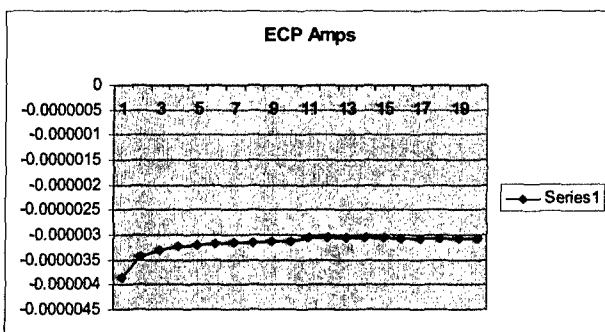
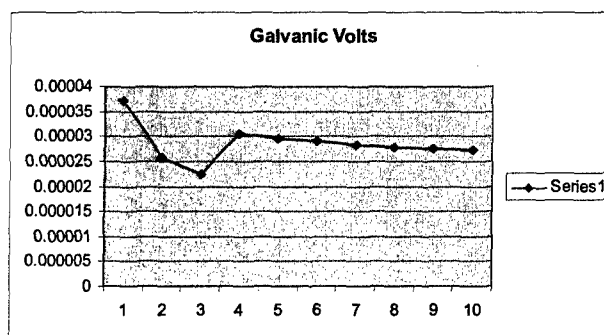
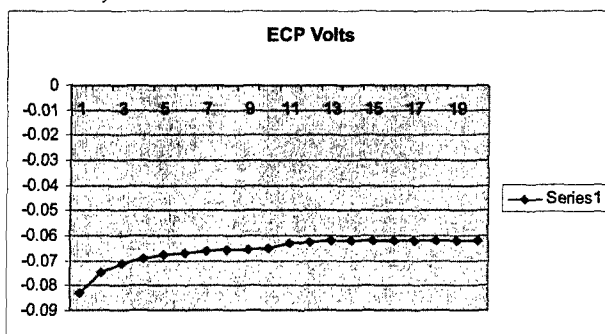
June 14, 2004 – 4 MW run



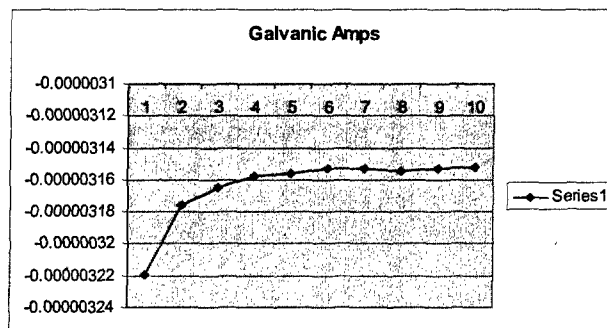
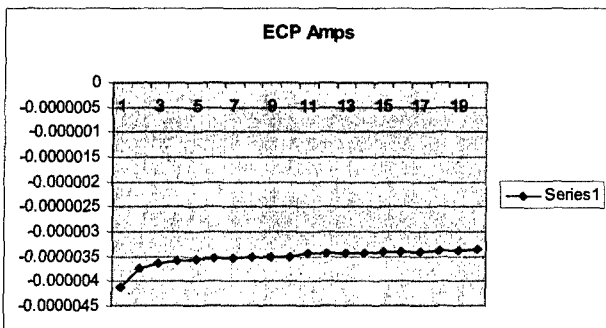
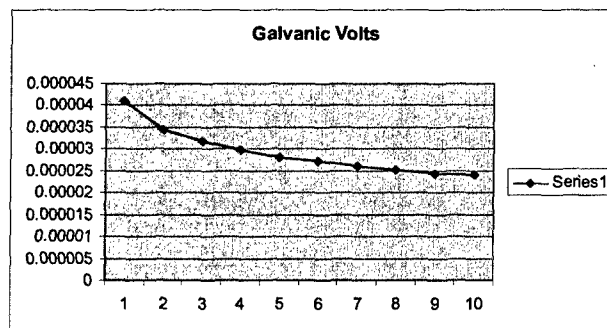
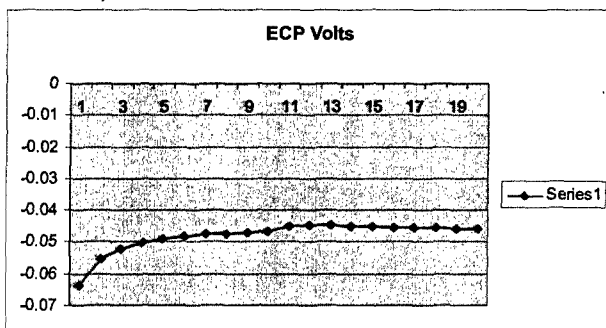
June 15, 2004 – 4 MW run



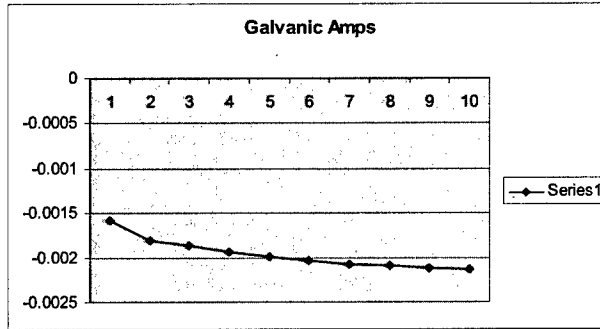
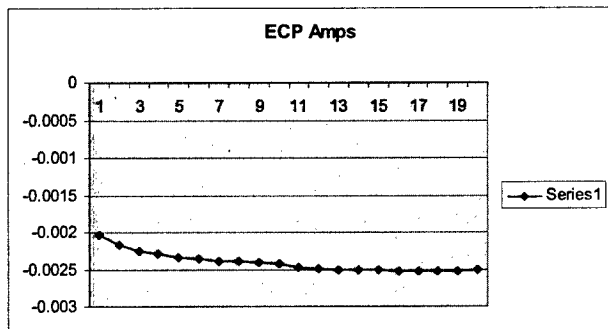
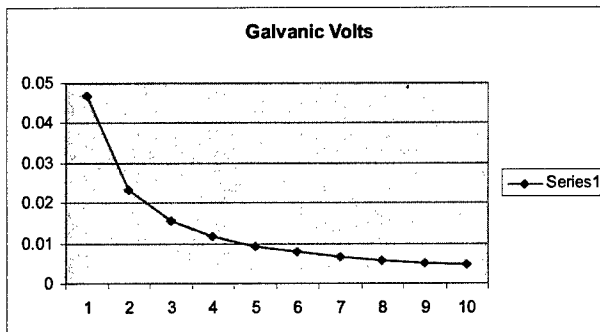
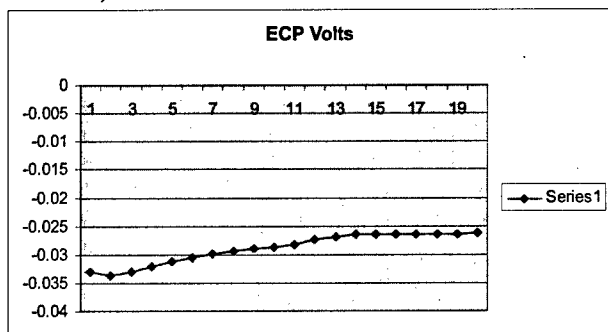
June 16, 2004 – 4 MW run



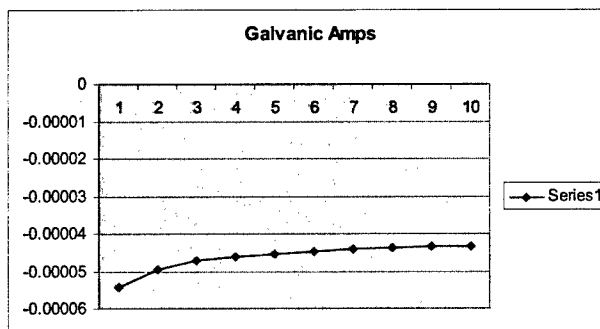
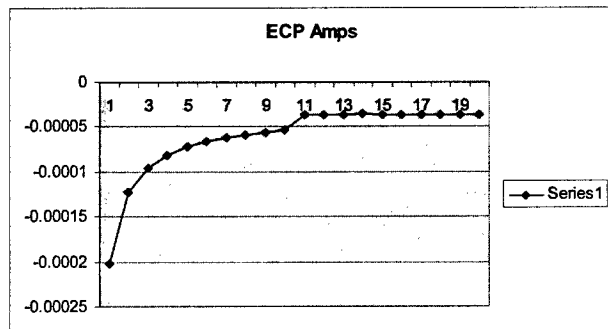
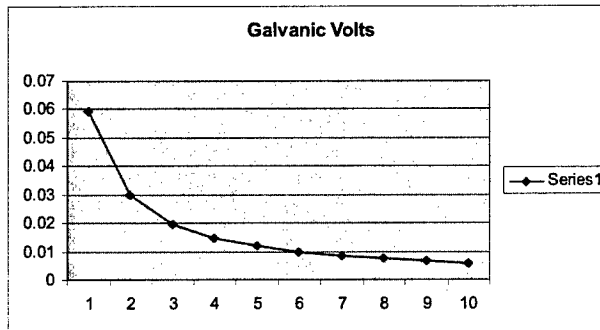
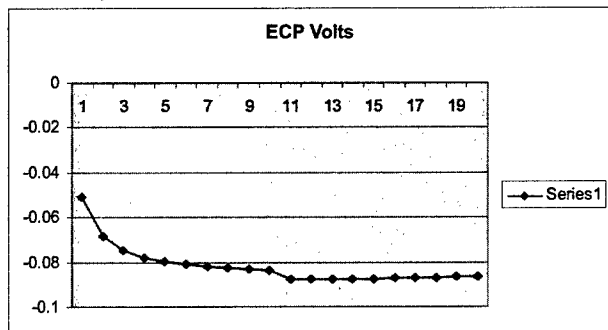
June 18, 2004 – 4 MW run



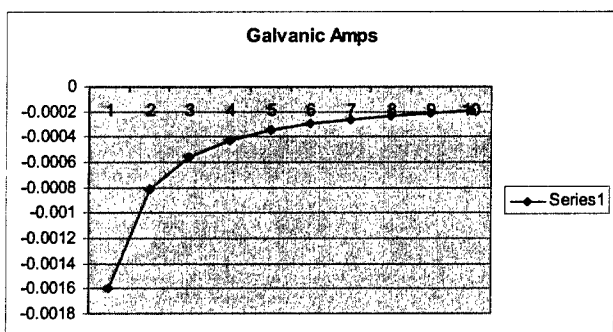
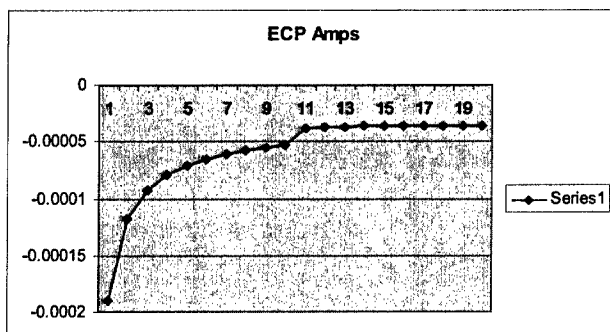
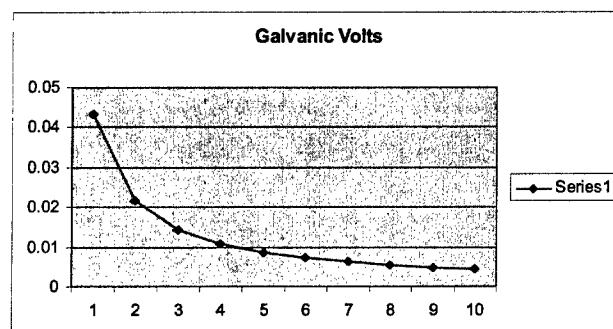
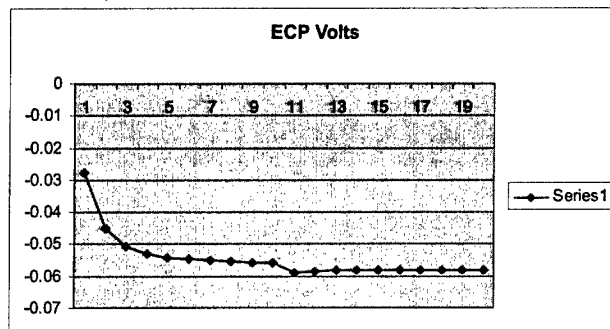
June 22, 2004 – 4 MW run



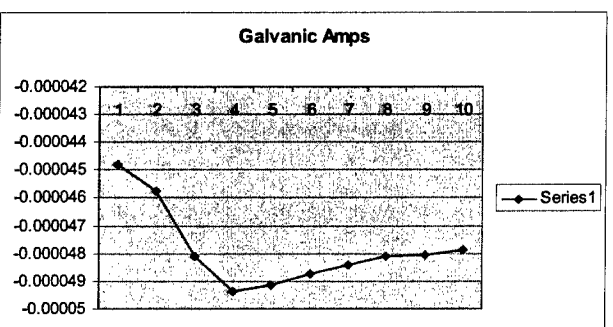
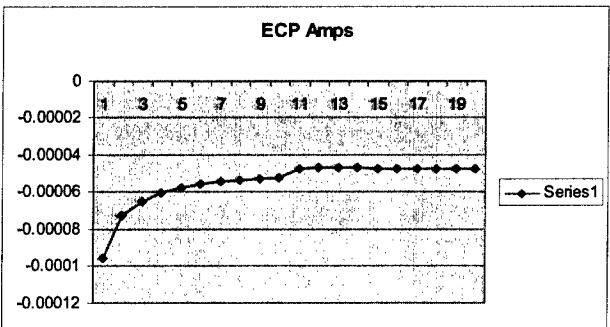
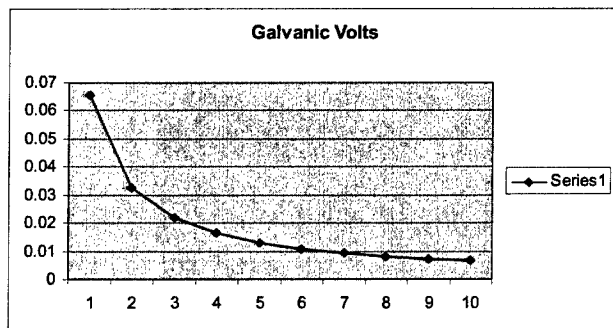
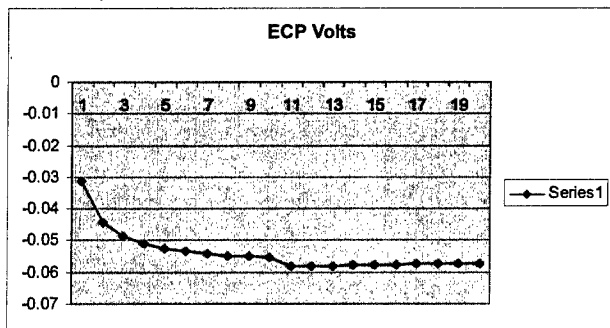
June 23, 2004 – 4 MW run



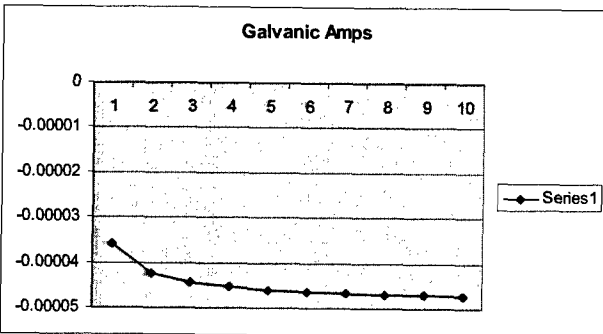
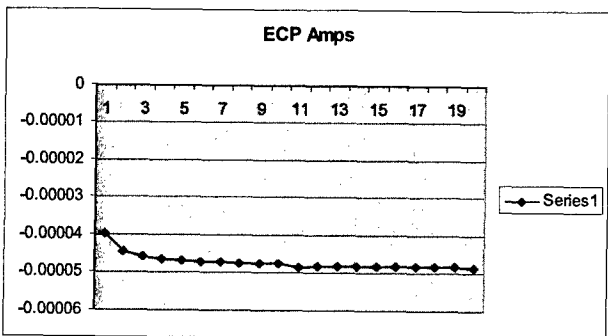
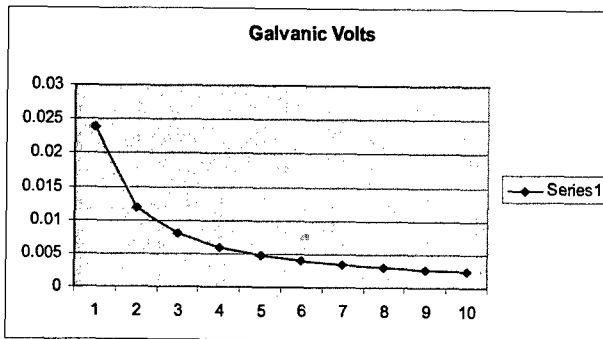
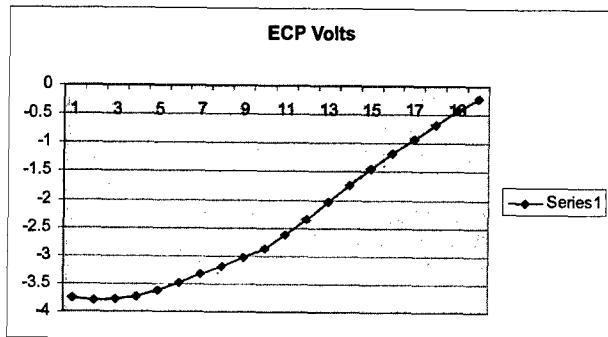
June 24, 2004 – 4 MW run



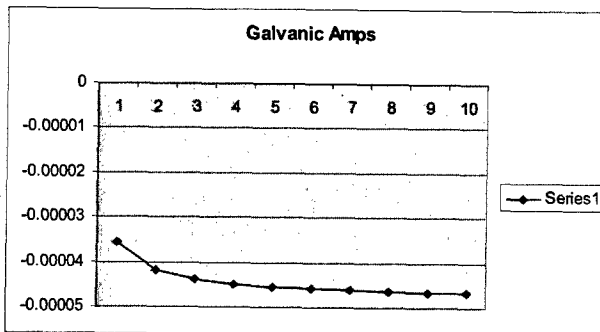
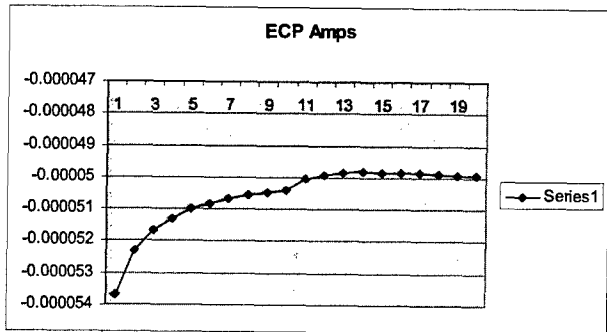
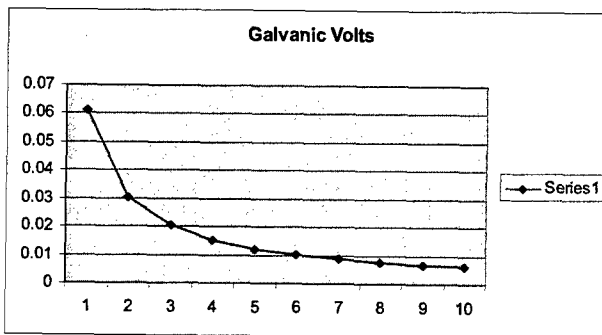
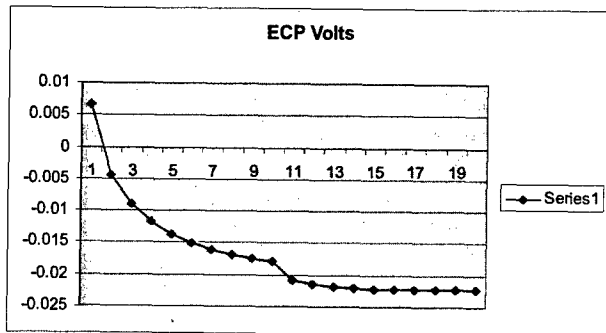
June 28, 2004 – 4 MW run



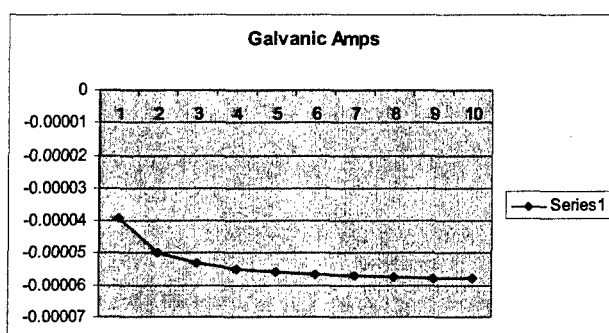
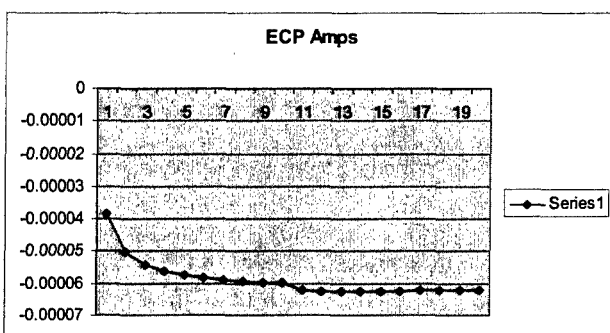
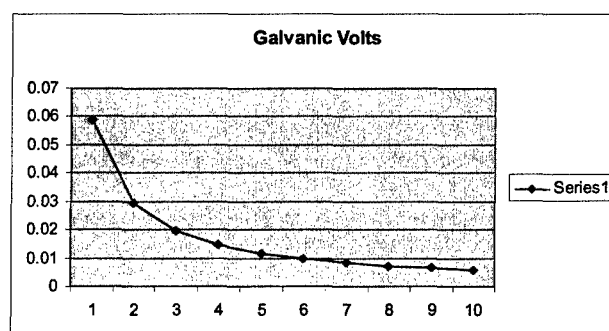
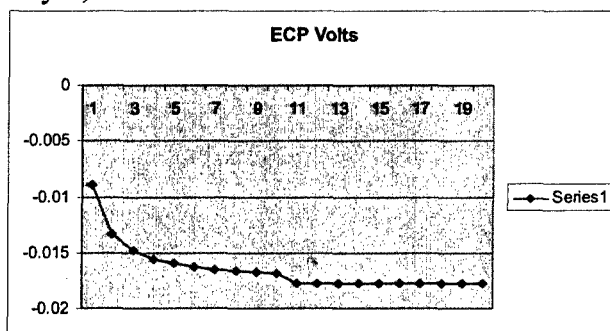
June 29, 2004 – 4 MW run



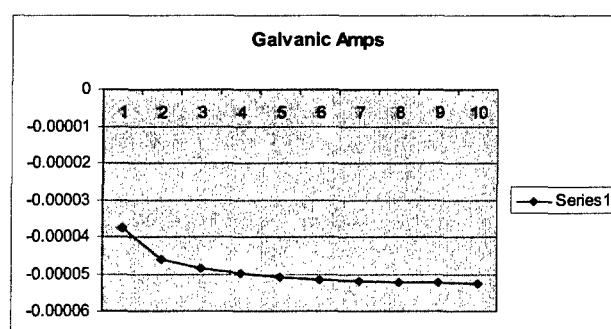
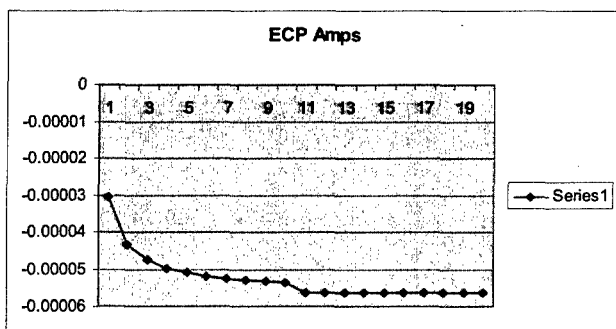
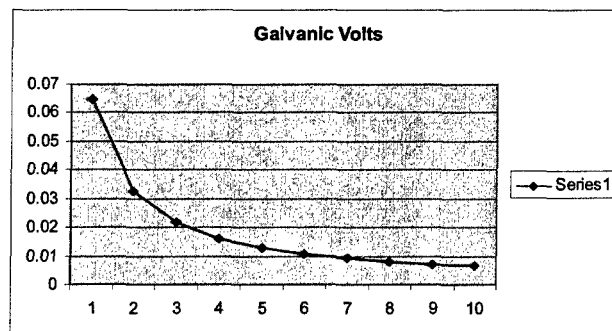
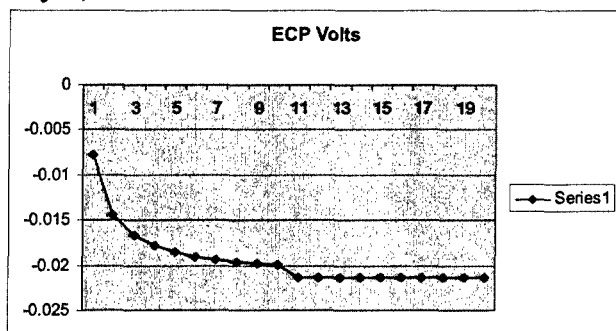
June 30, 2004 – 4 MW run



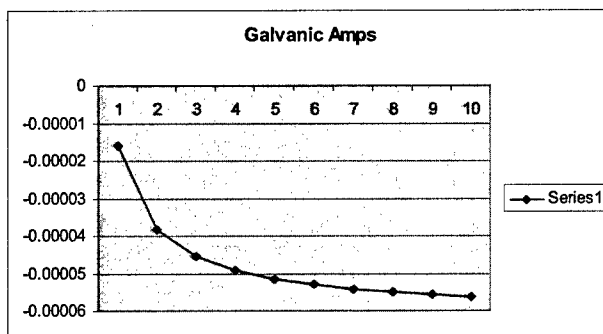
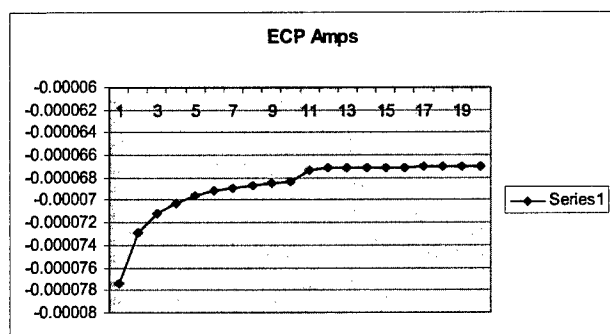
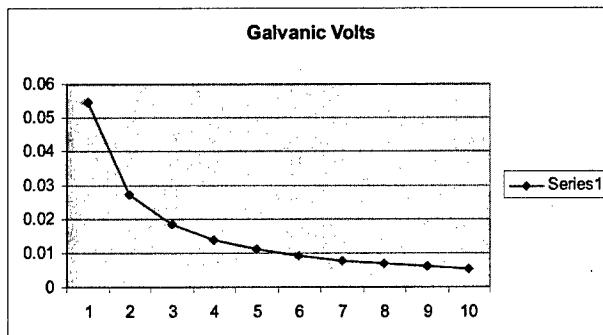
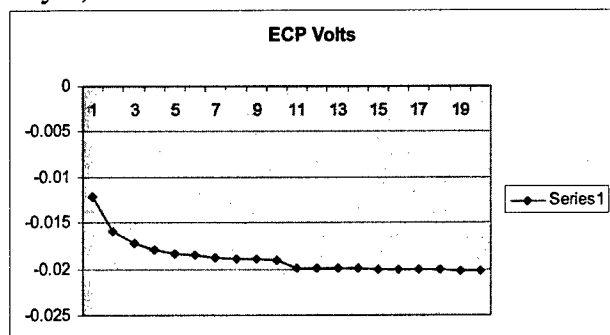
July 2, 2004 – 4 MW run



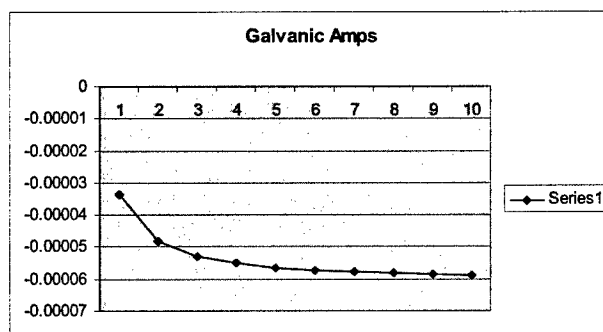
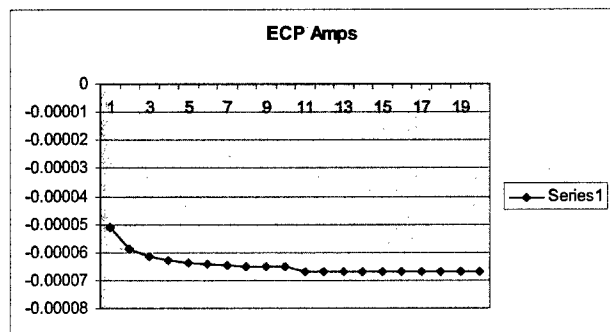
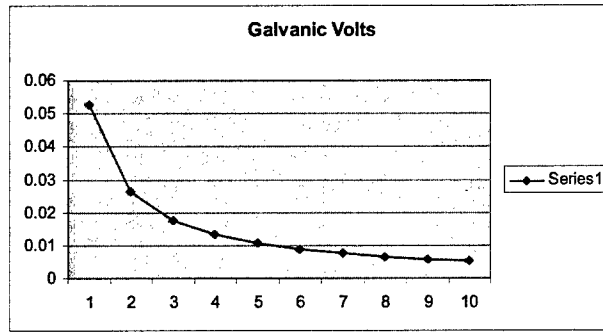
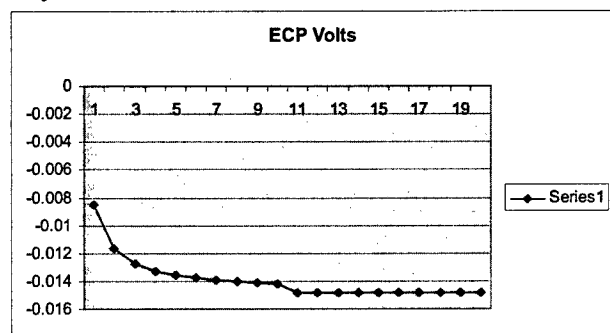
July 6, 2004 – 4 MW run



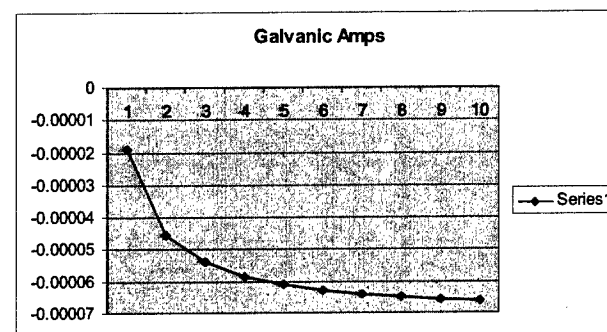
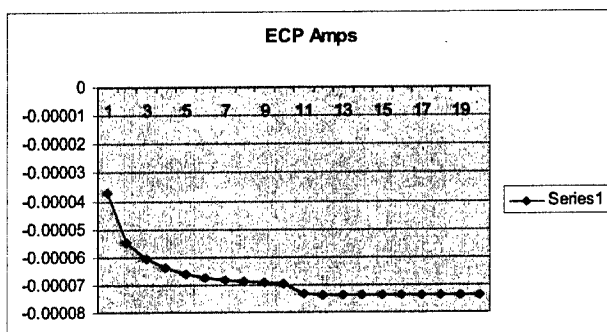
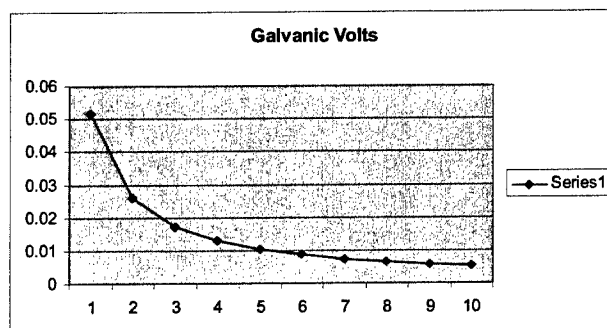
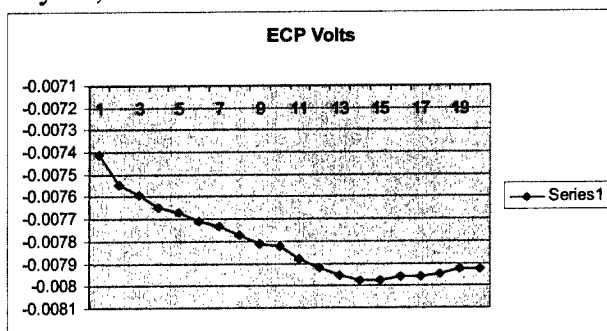
July 7, 2004 – 4 MW run



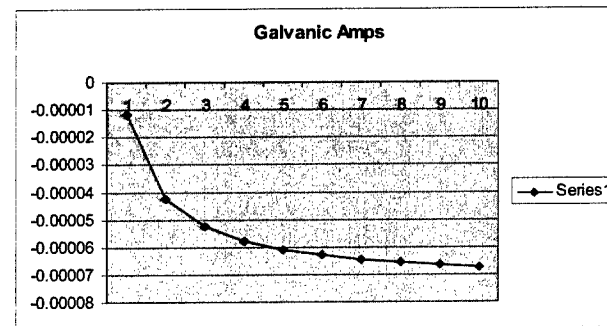
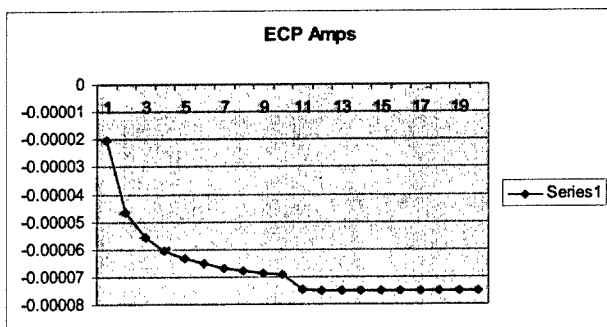
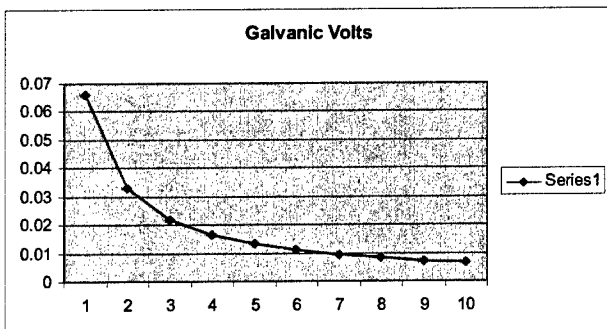
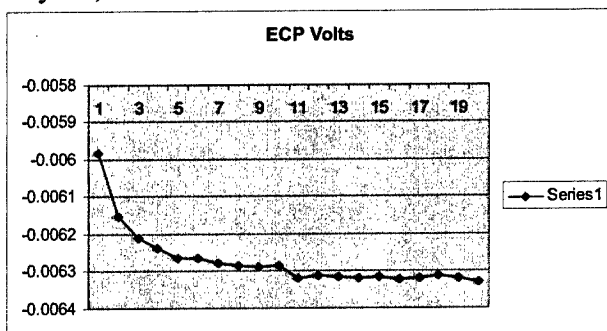
July 9, 2004 – 4 MW run



July 12, 2004 – 4 MW run

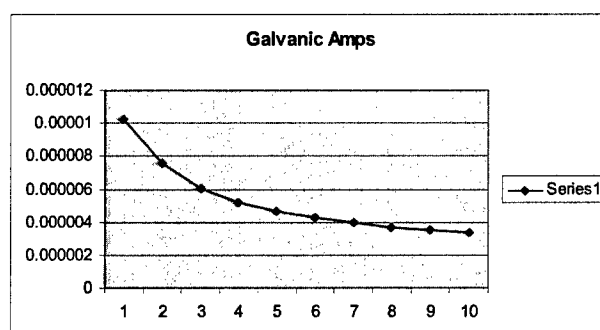
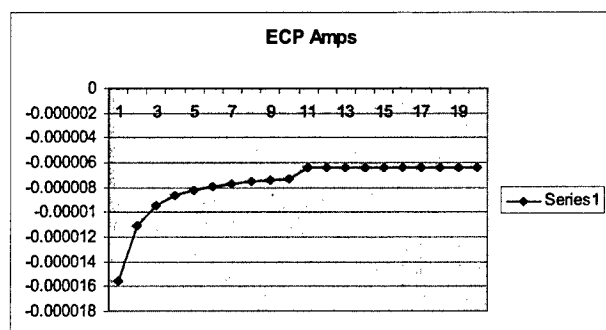
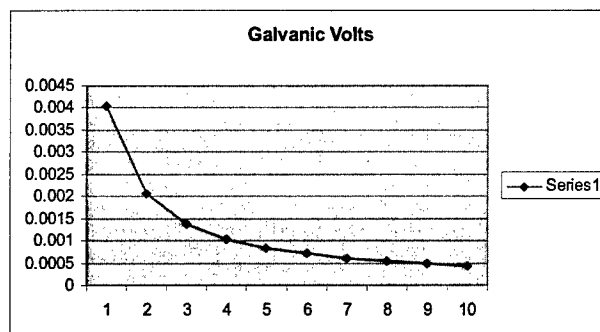
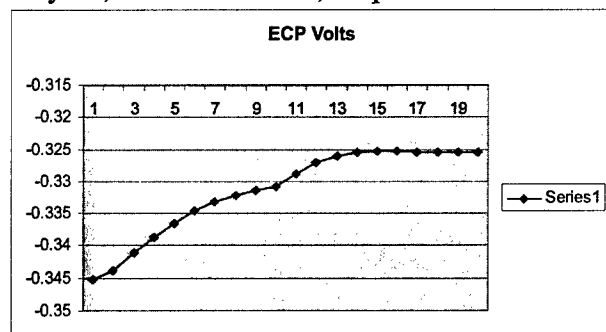


July 15, 2004 – 4 MW run

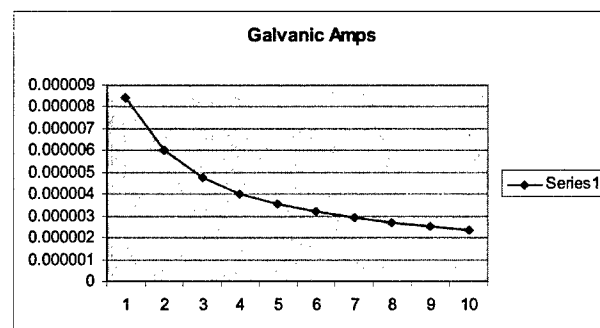
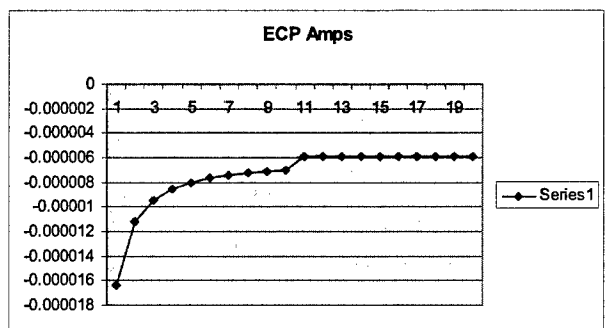
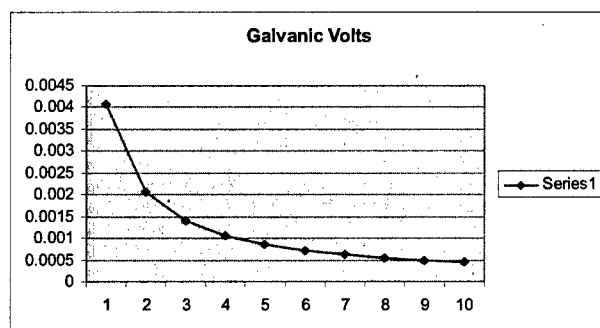
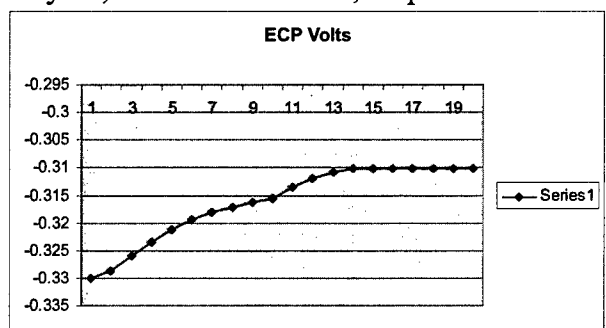


Appendix C – X750-Zr Couple Graphs

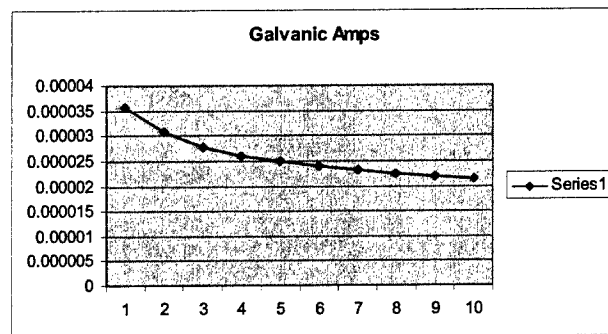
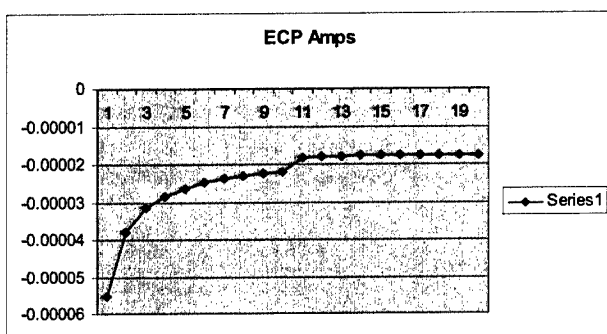
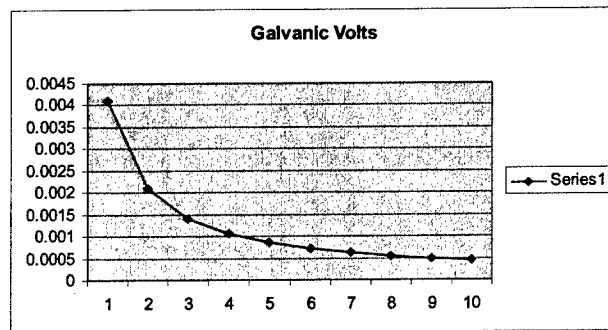
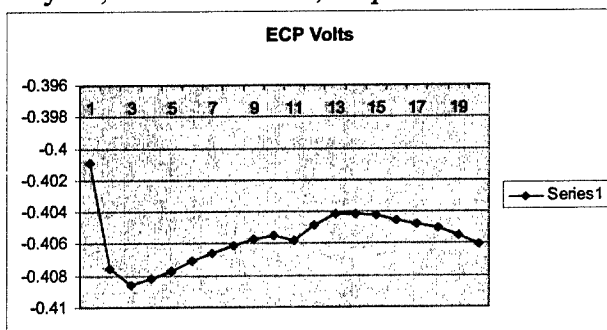
May 27, 2004 – first run, no power



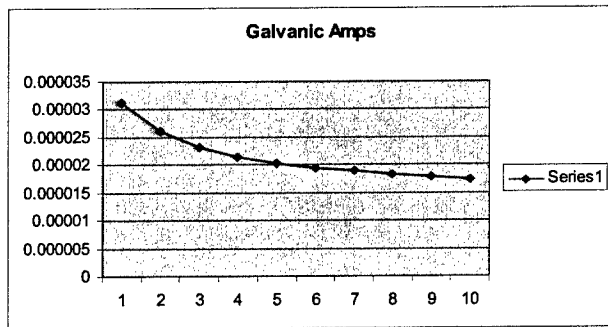
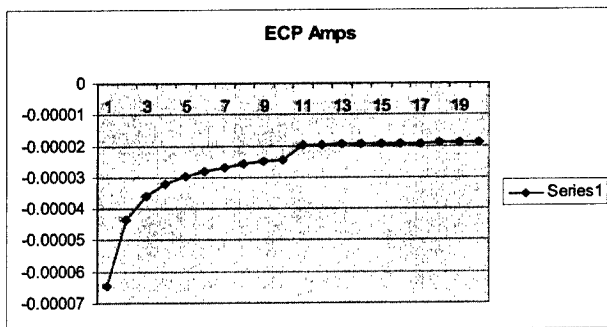
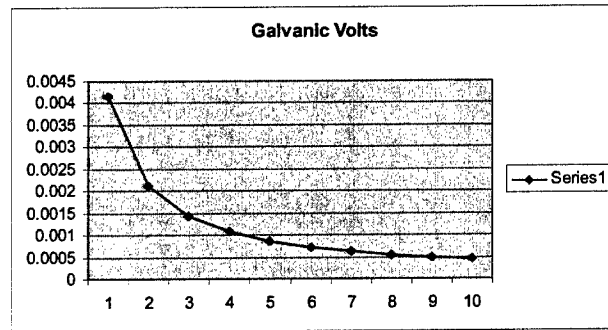
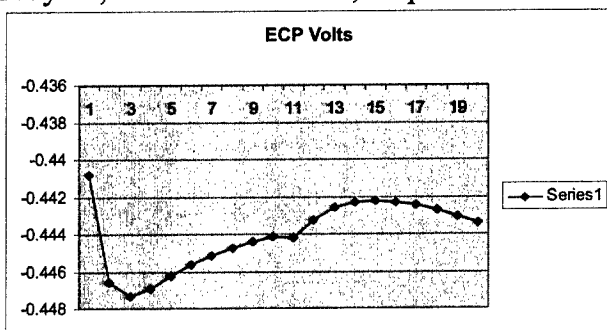
May 27, 2004 – second run, no power



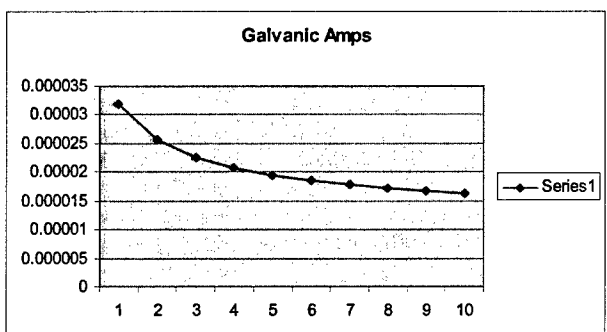
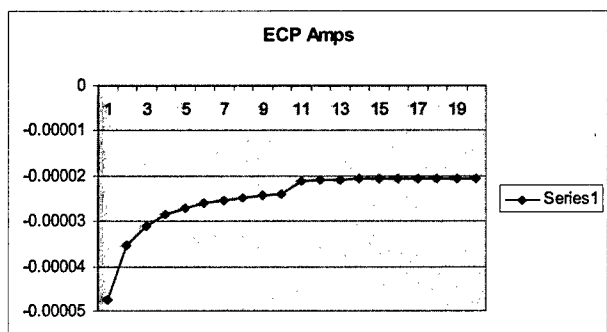
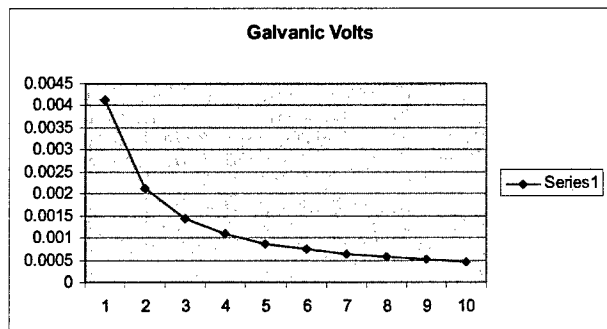
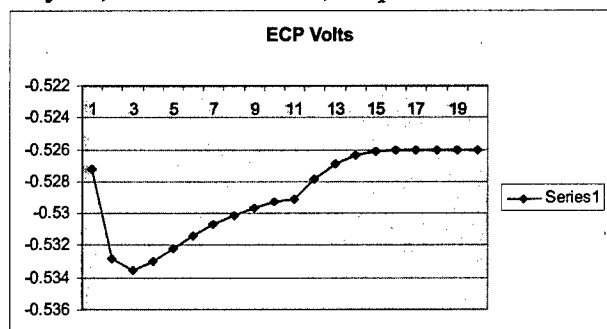
May 28, 2004 – first run, no power



May 28, 2004 – second run, no power

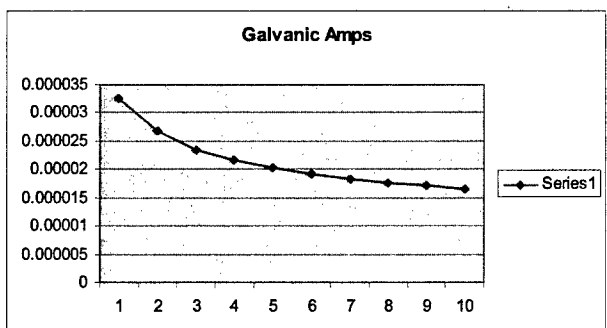
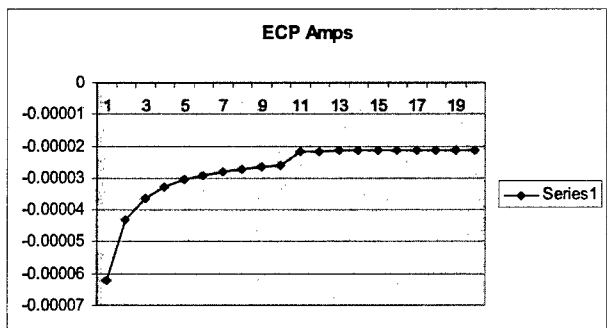
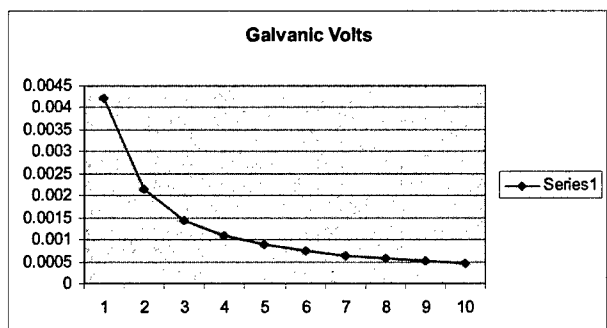
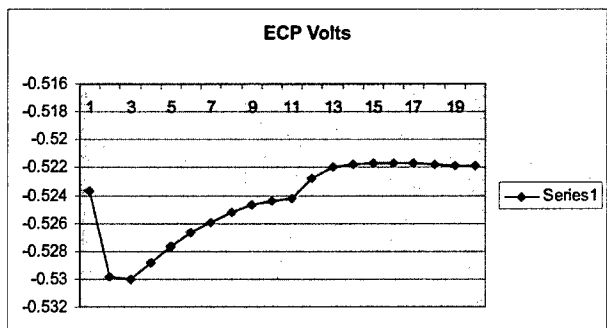


May 28, 2004 – third run, no power

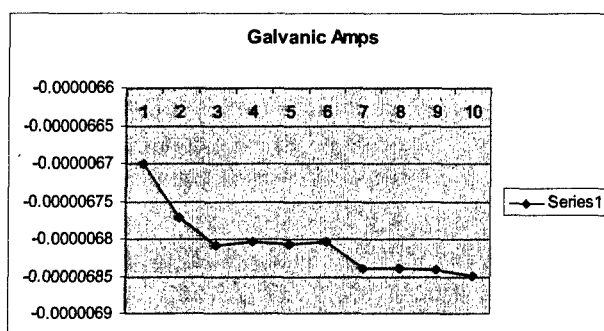
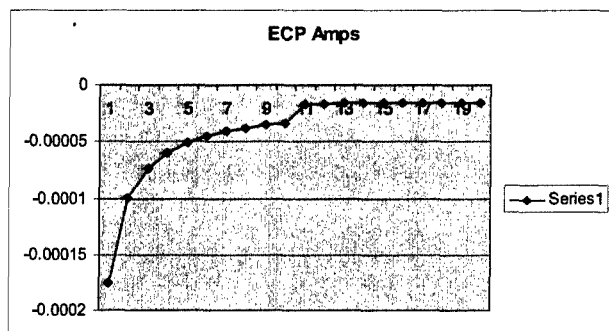
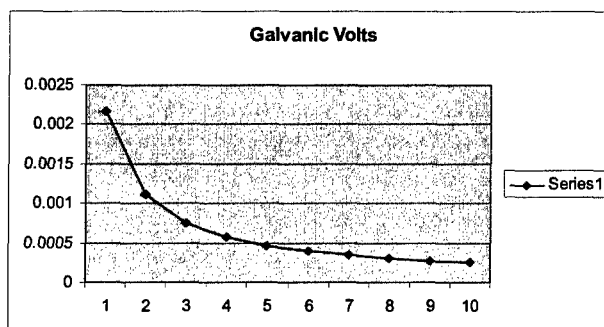
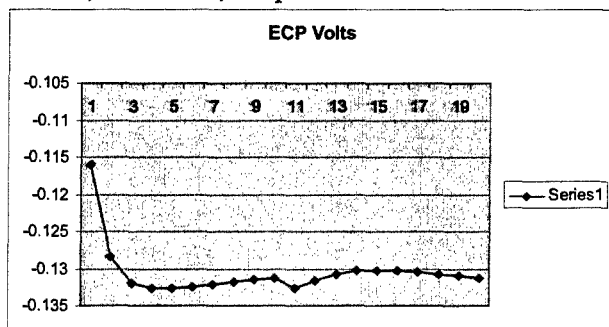


May 28, 2004 – fourth run, no power

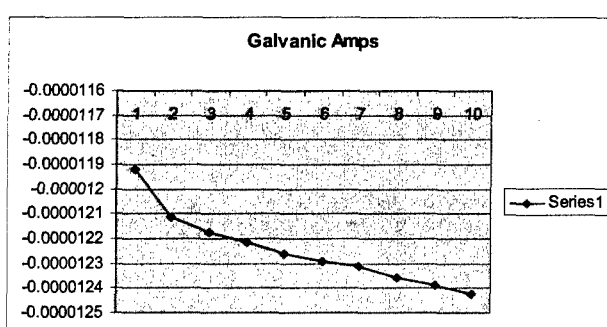
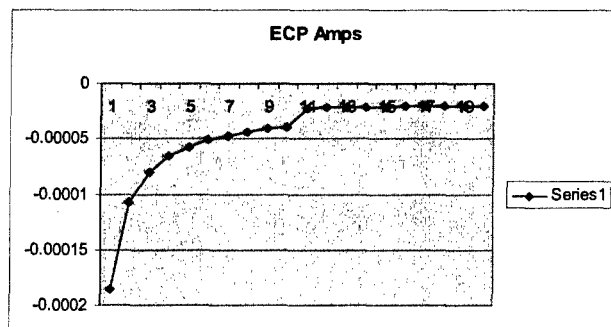
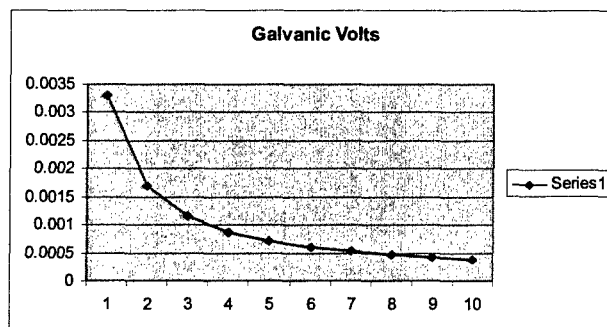
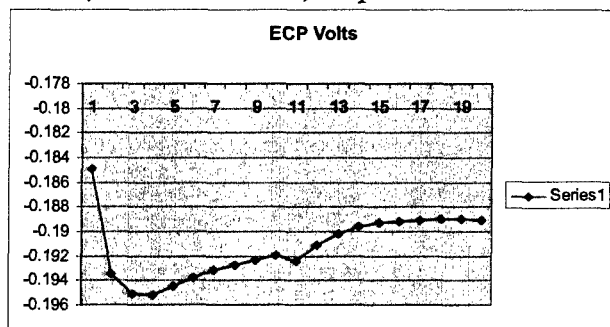
c



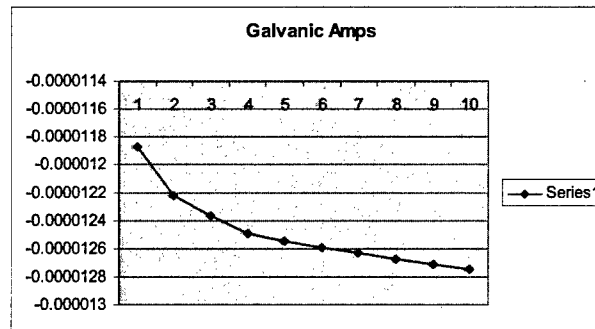
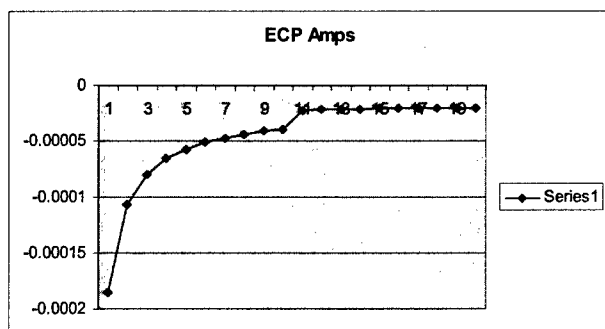
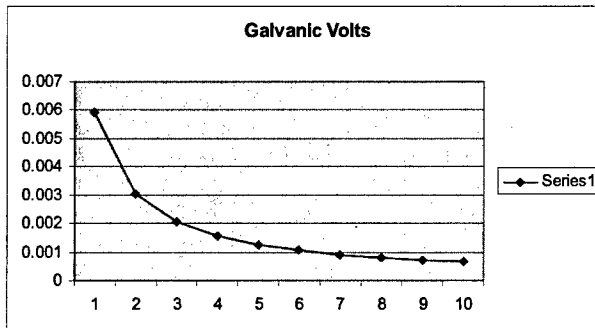
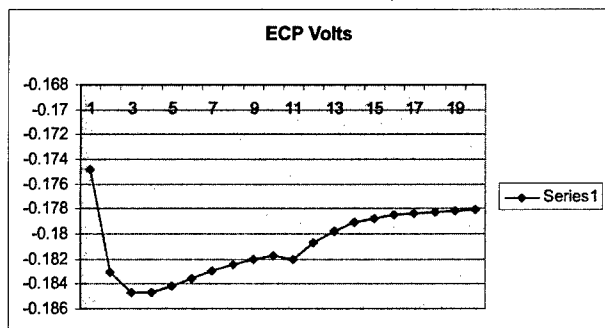
June 3, 2004 run, no power



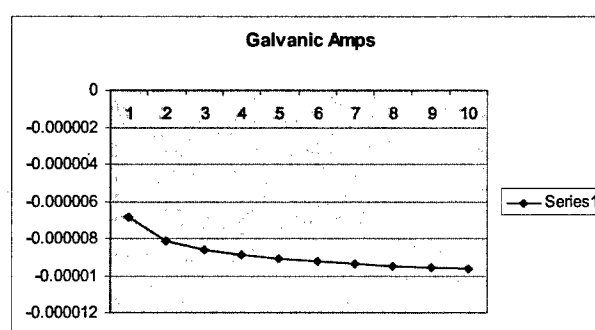
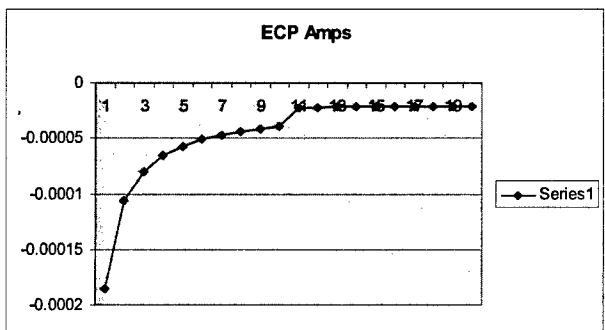
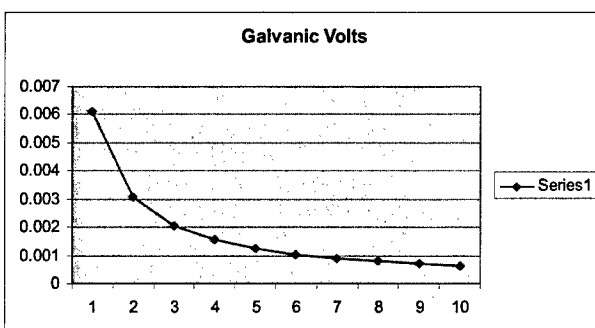
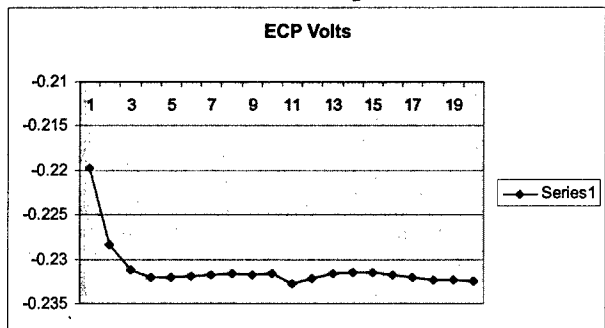
June 4, 2004 – first run, no power



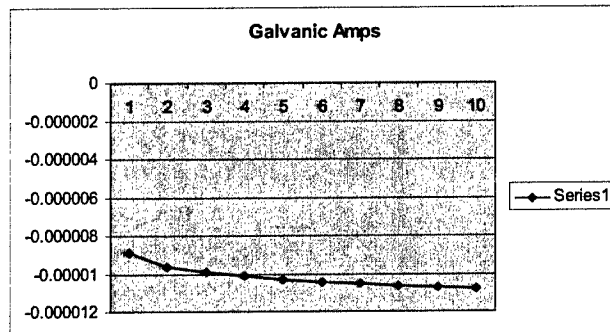
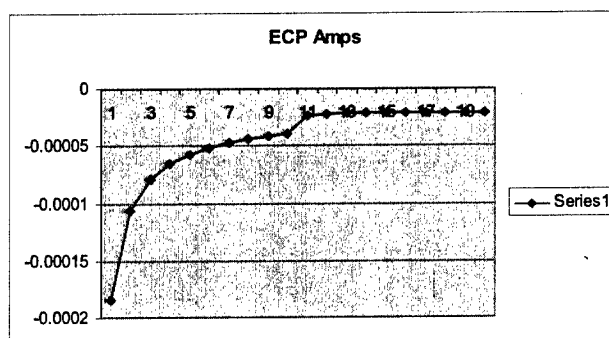
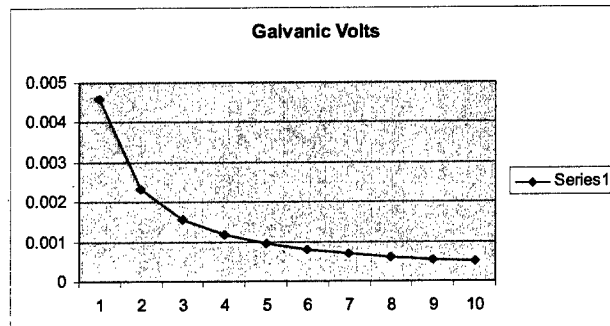
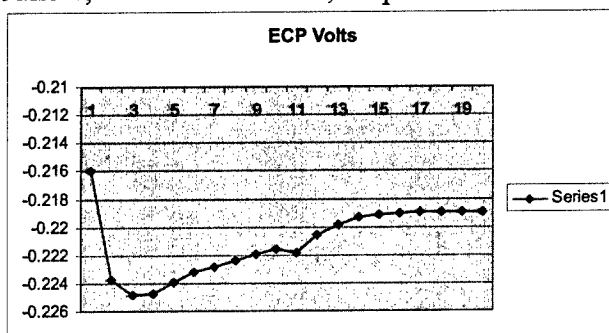
June 4, 2004 – second run, no power



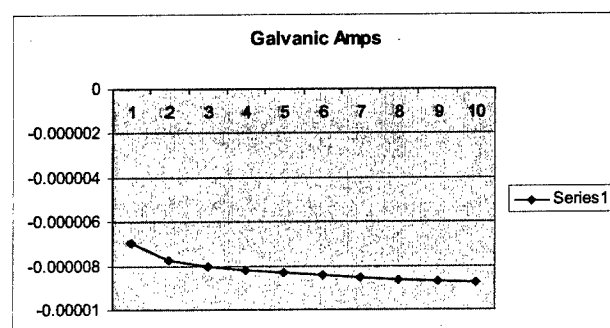
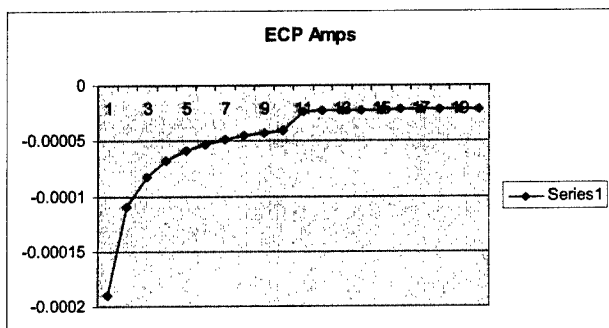
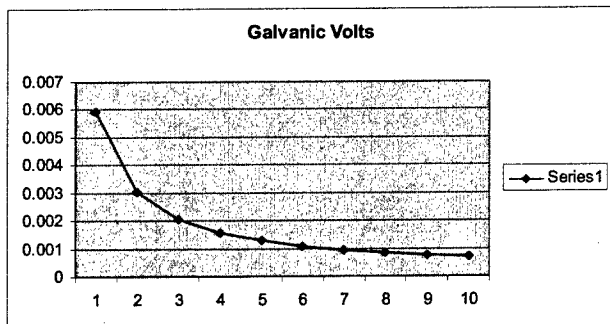
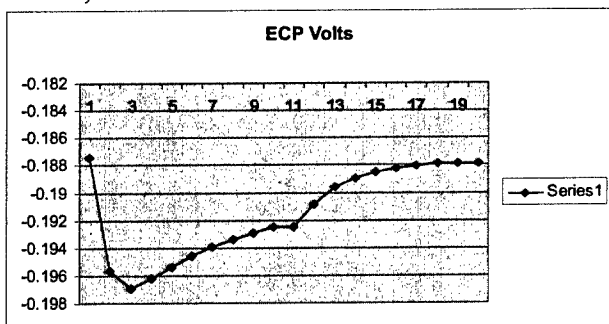
June 4, 2004 –third run, no power



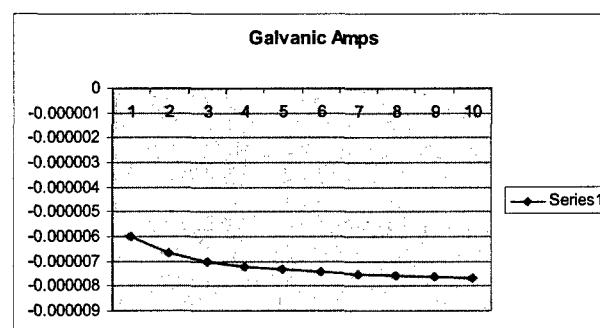
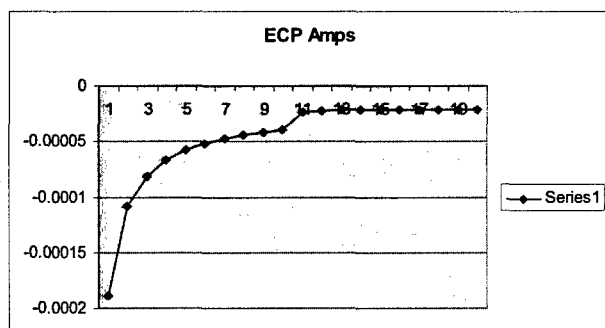
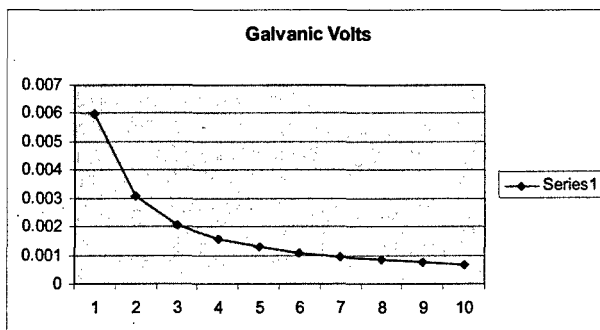
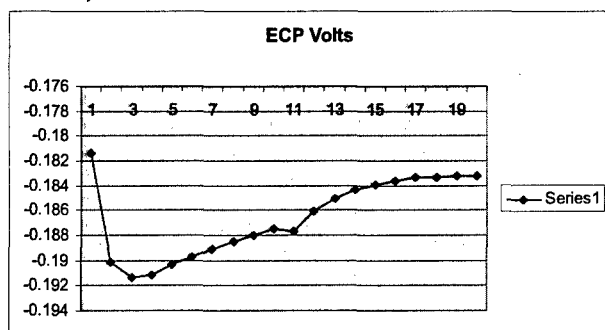
June 4, 2004 – fourth run, no power



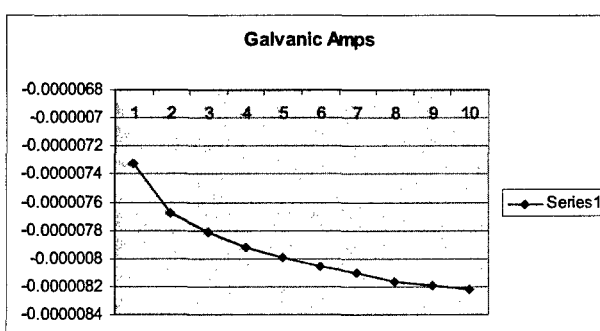
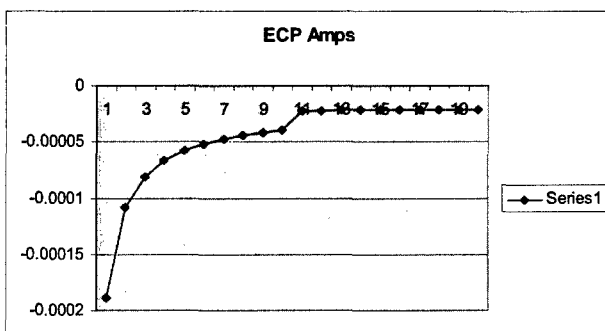
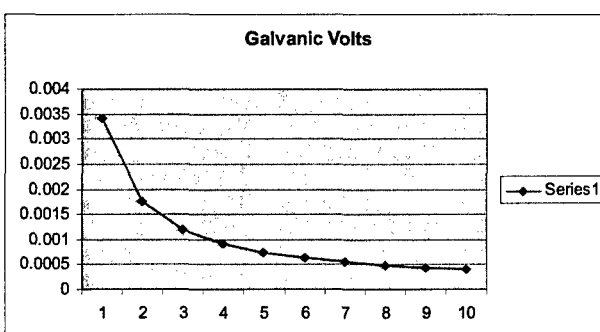
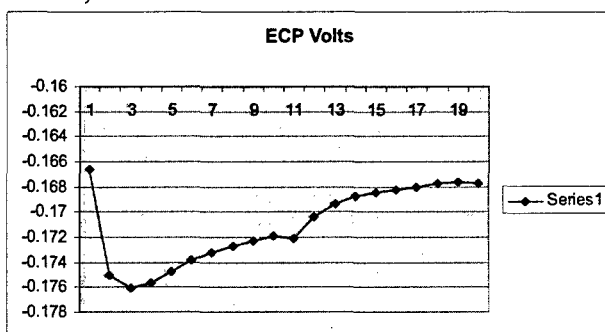
June 4, 2004 – 1 MW run



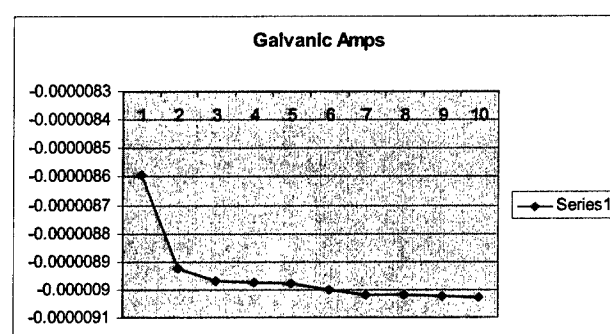
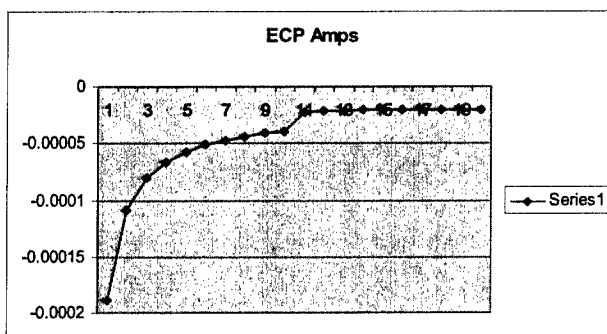
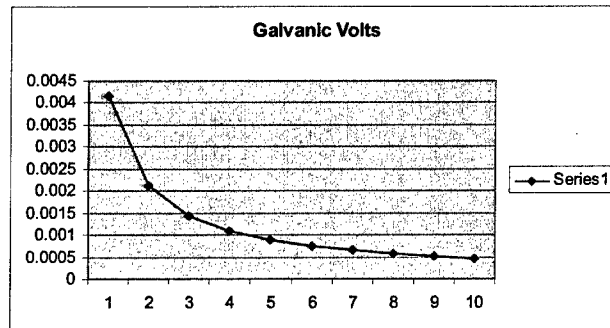
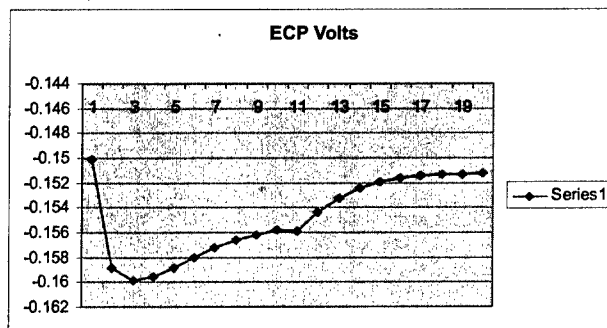
June 4, 2004 – 2 MW run



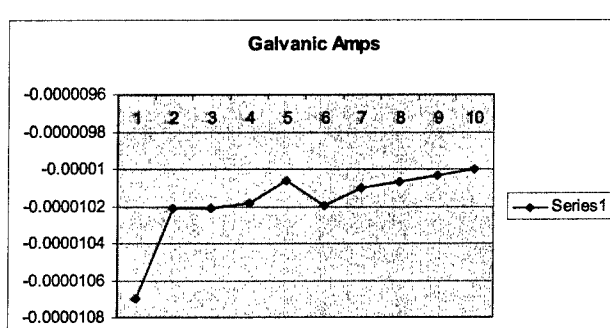
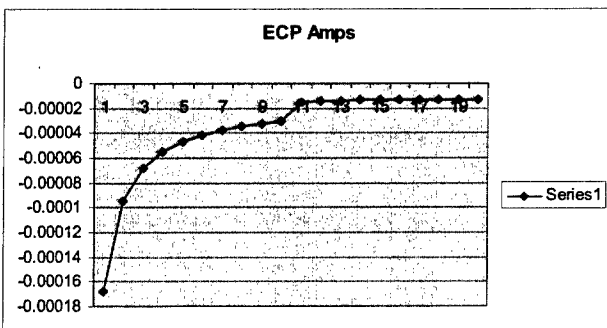
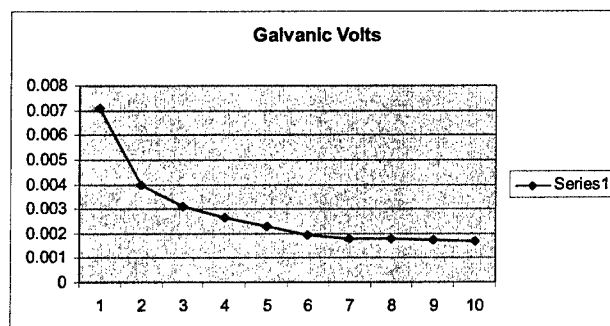
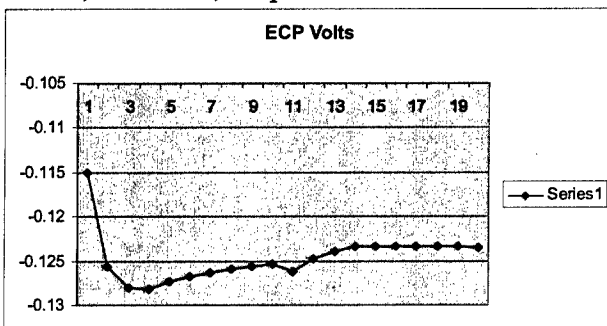
June 4, 2004 – 3 MW run



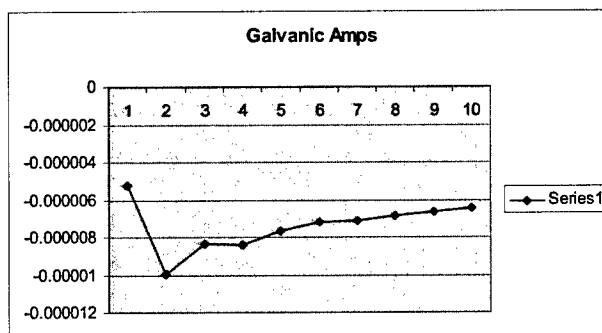
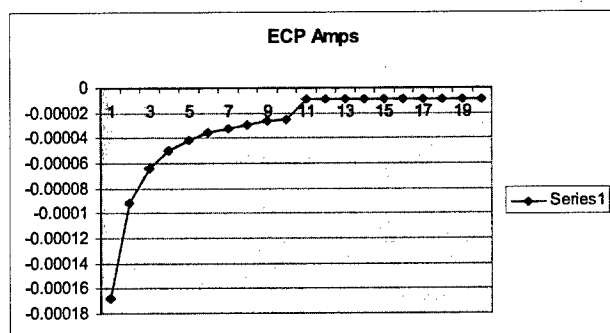
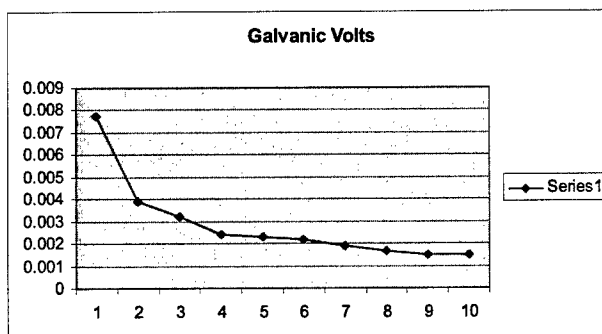
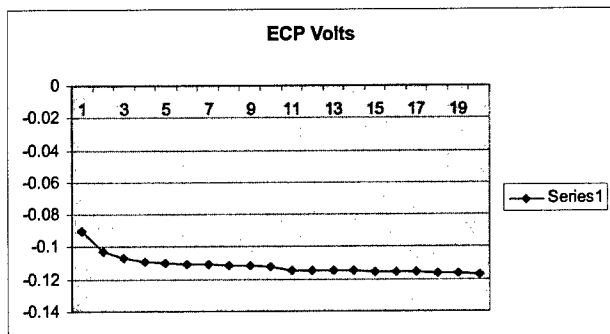
June 4, 2004 – 4 MW run



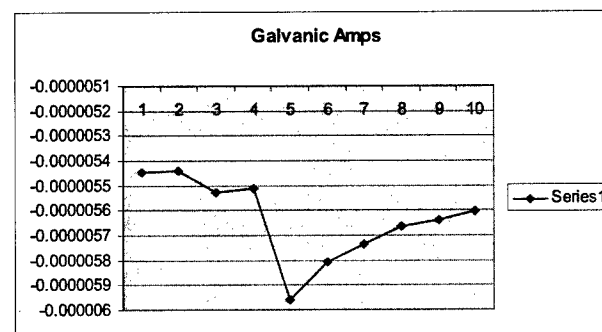
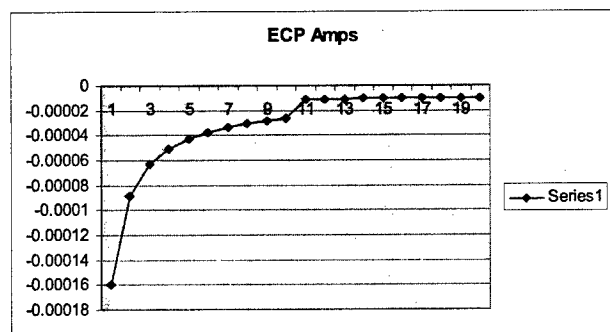
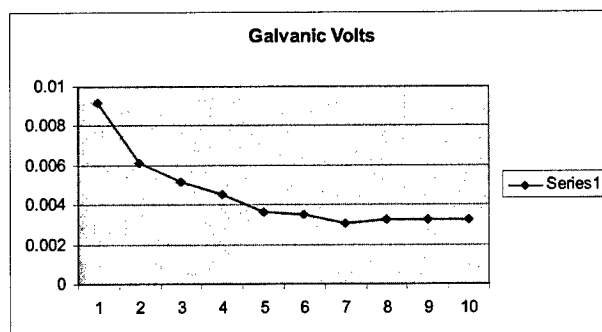
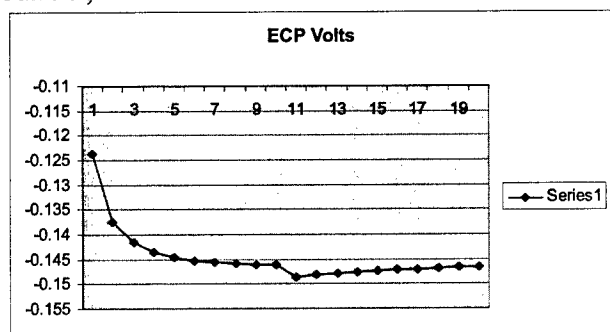
June 7, 2004 run, no power



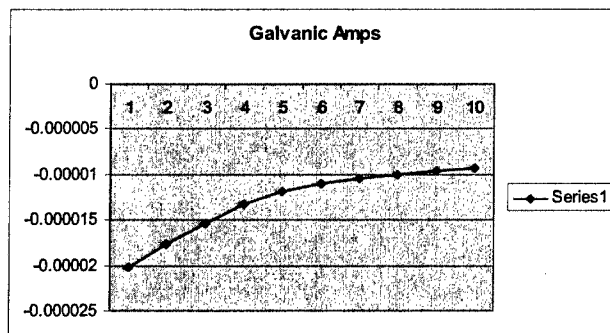
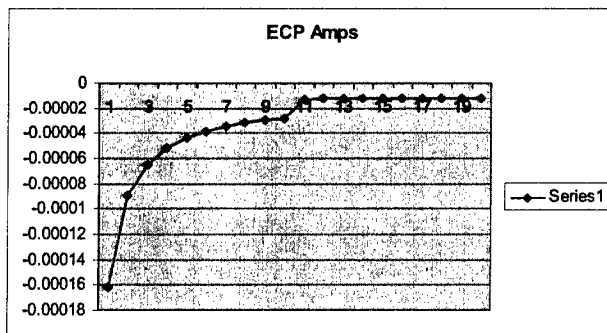
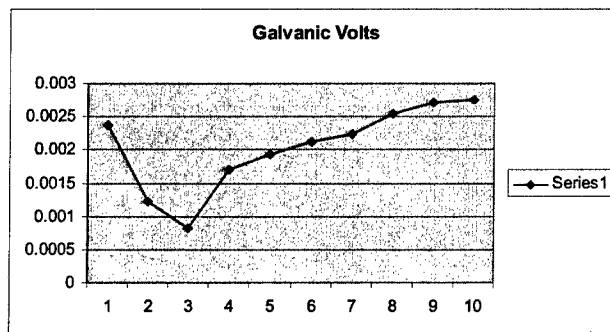
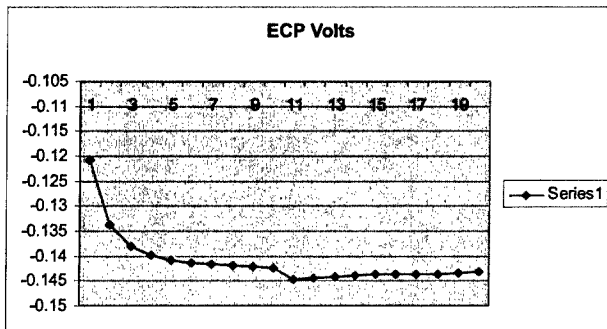
June 8, 2004 – 4 MW run



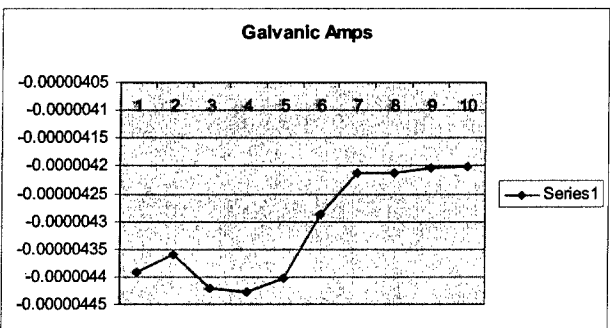
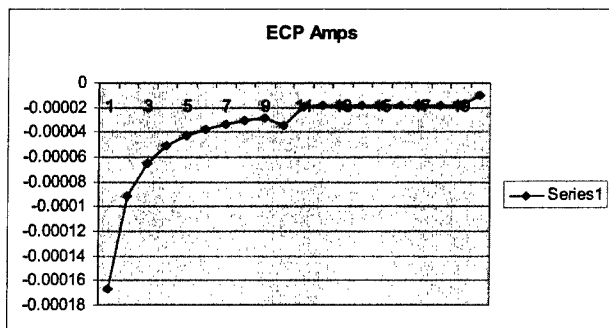
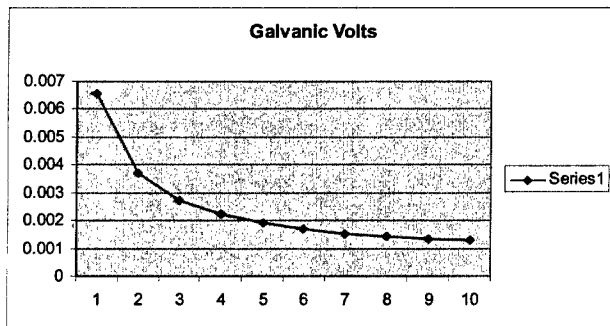
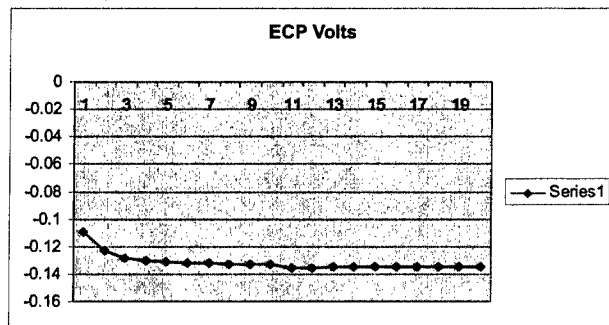
June 9, 2004 – 4 MW run



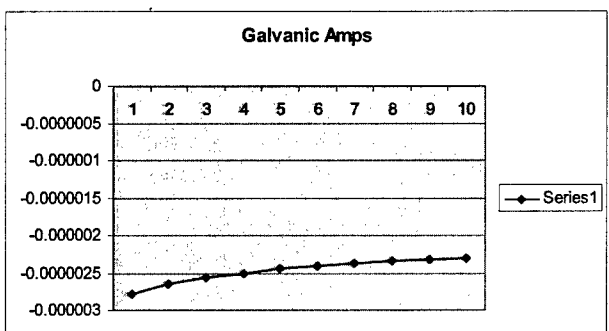
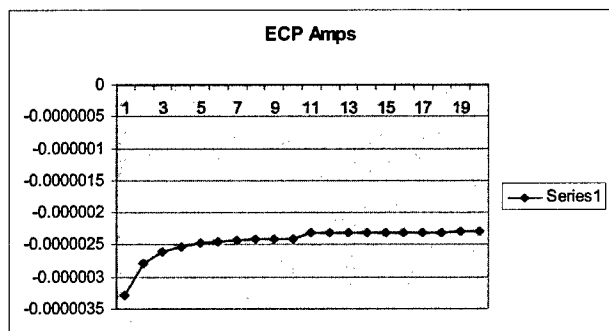
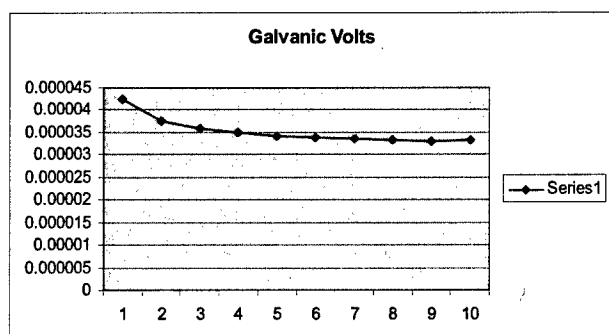
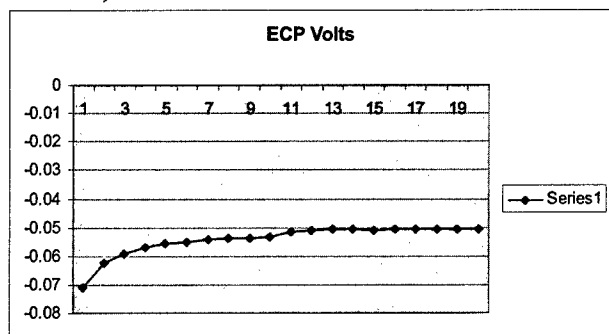
June 10, 2004 – 4.35 MW run



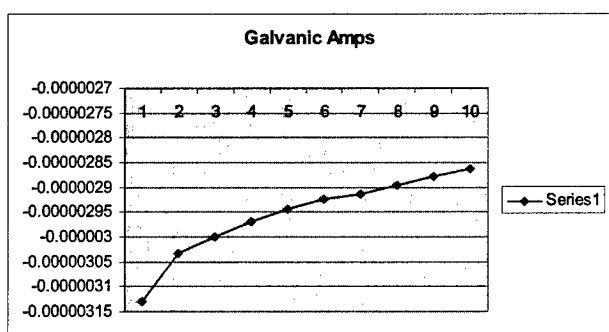
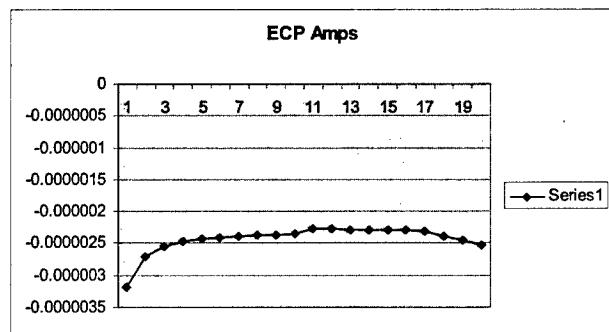
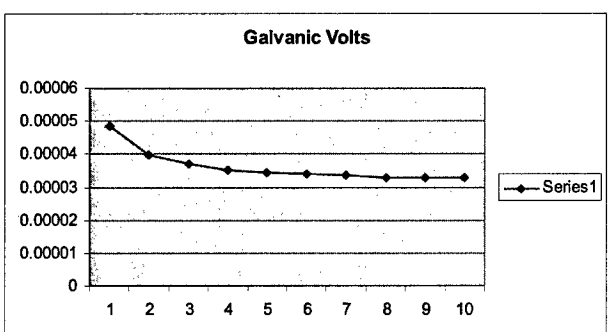
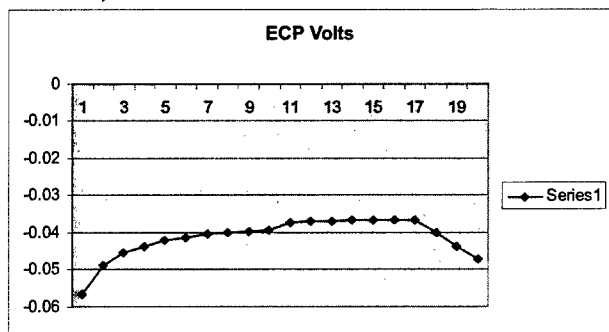
June 11, 2004 – 4 MW run



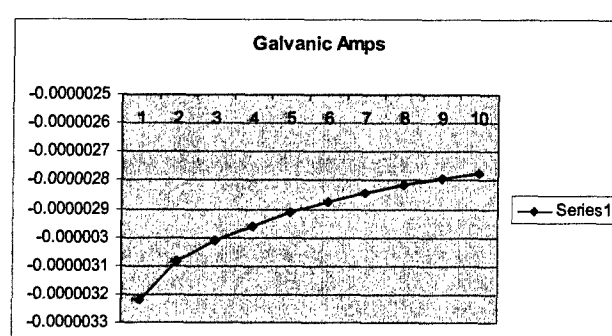
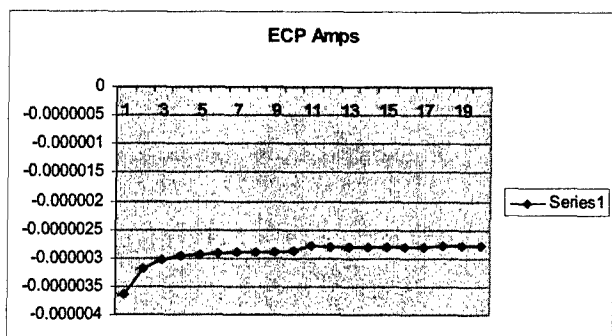
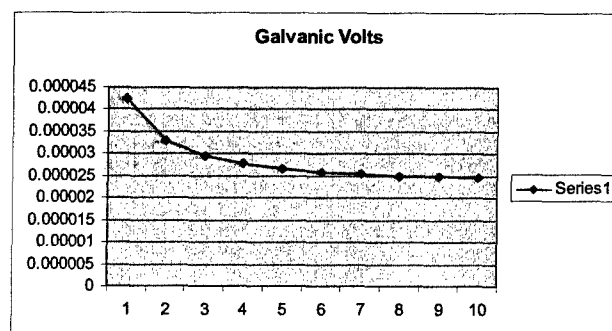
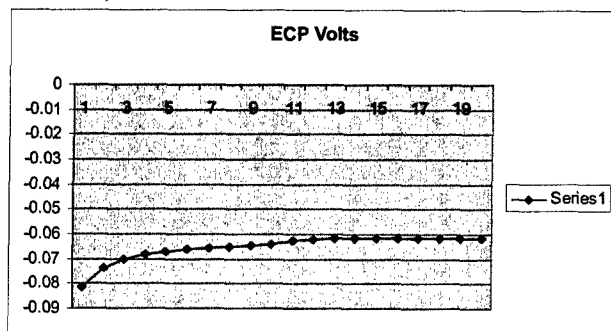
June 14, 2004 – 4 MW run



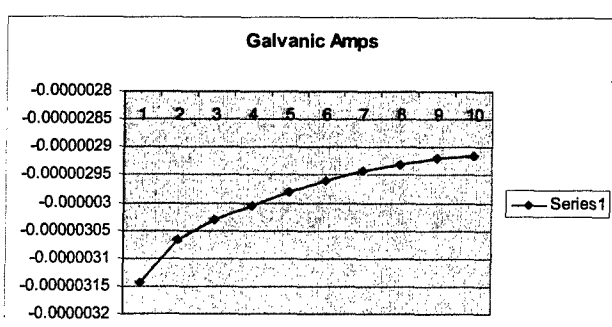
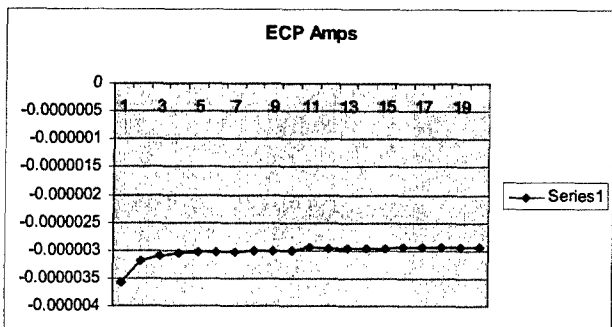
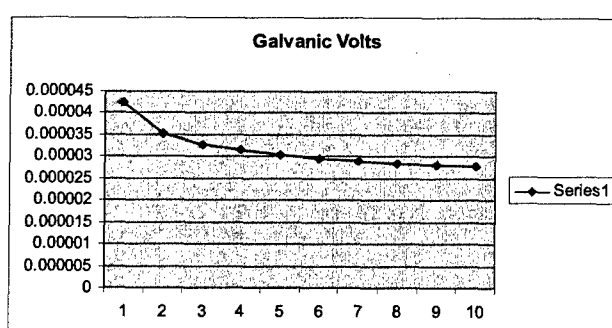
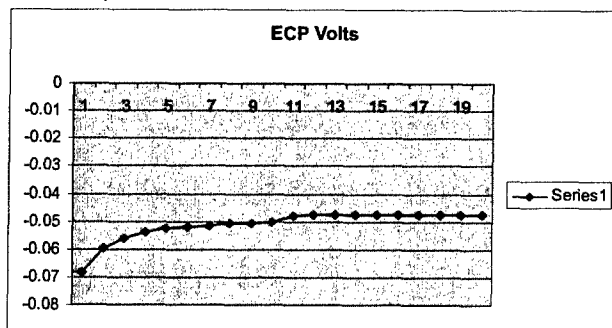
June 15, 2004 – 4 MW run



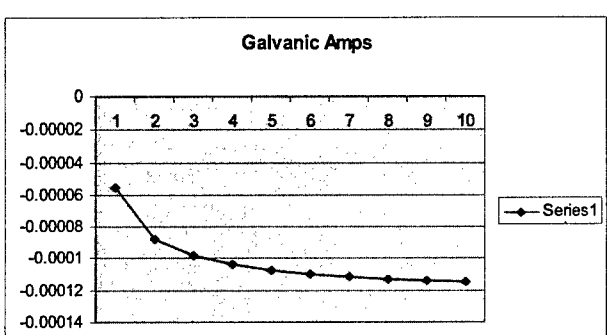
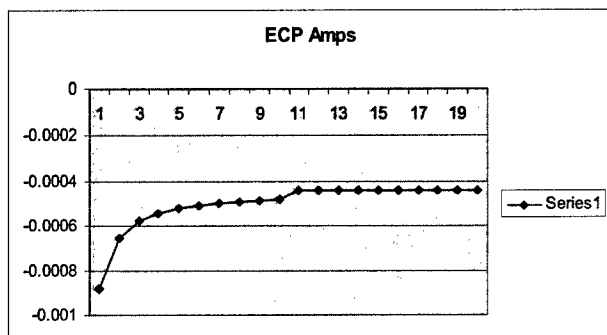
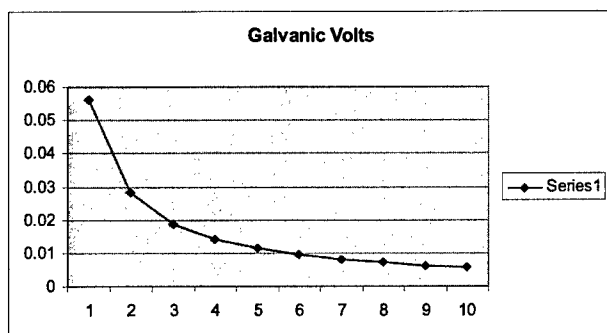
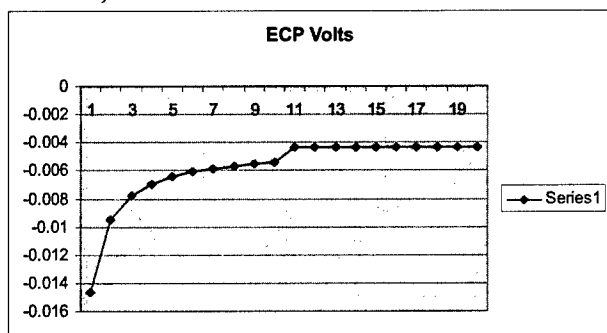
June 16, 2004 – 4 MW run



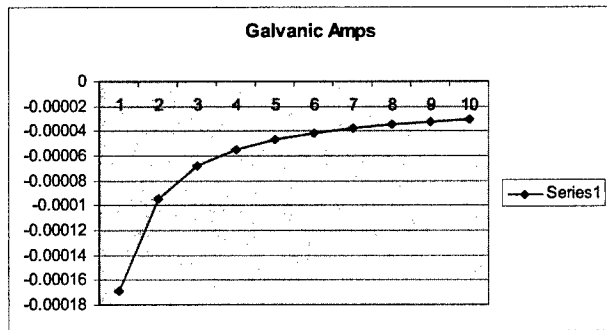
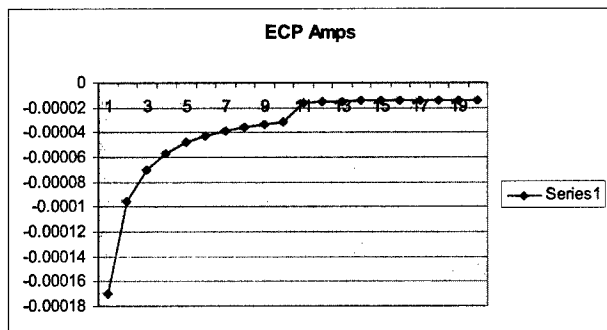
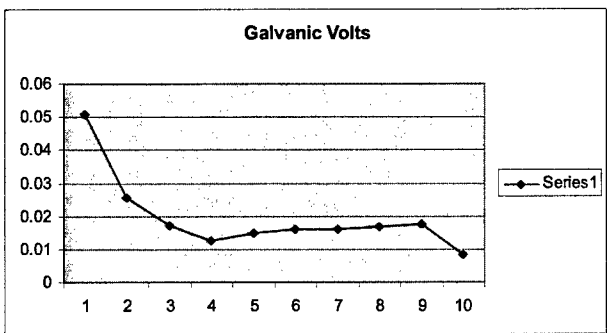
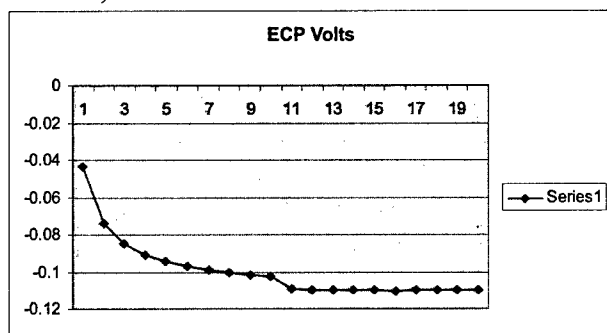
June 18, 2004 – 4 MW run



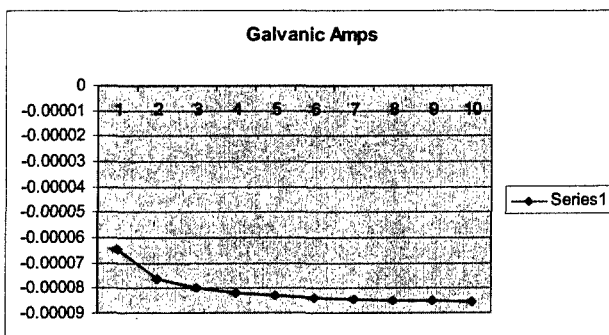
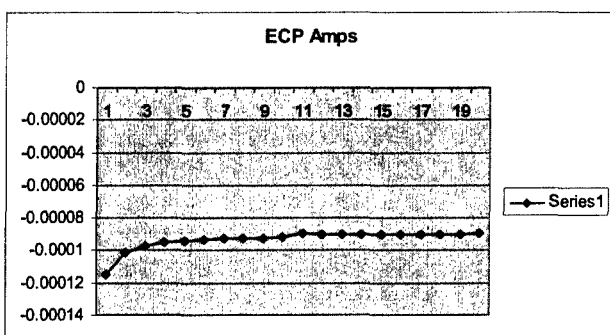
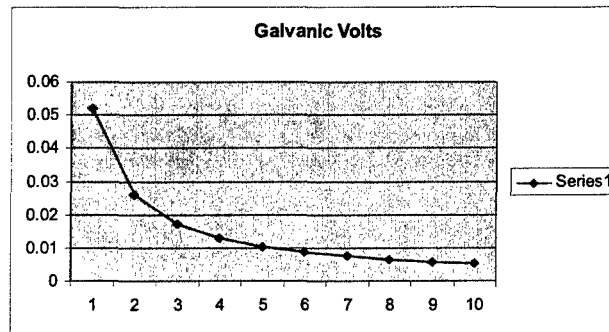
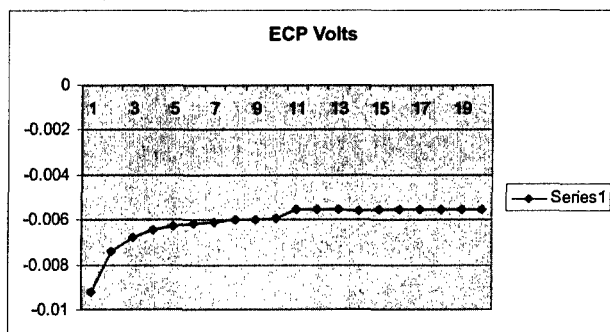
June 22, 2004 – 4 MW run



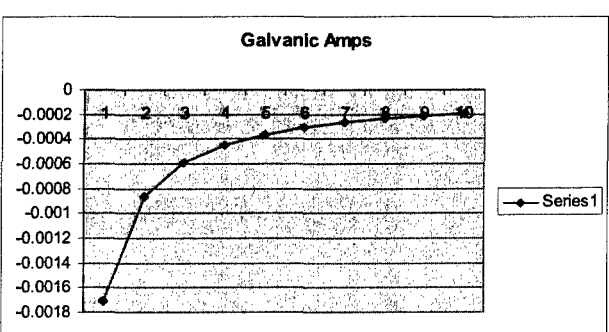
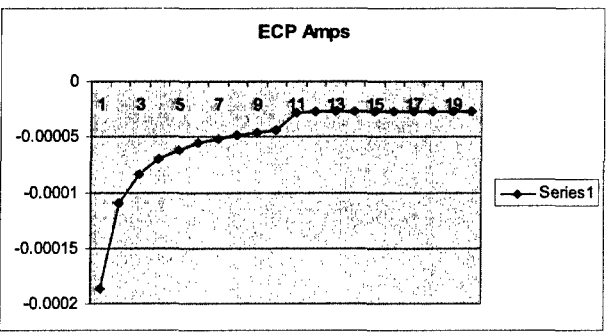
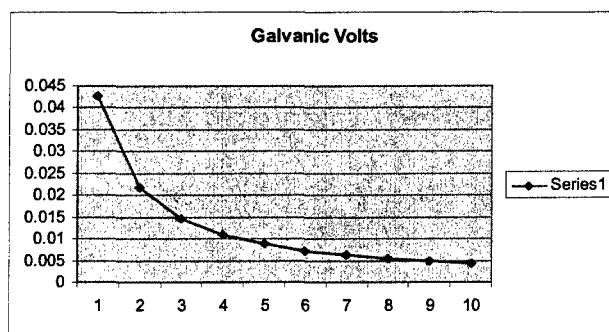
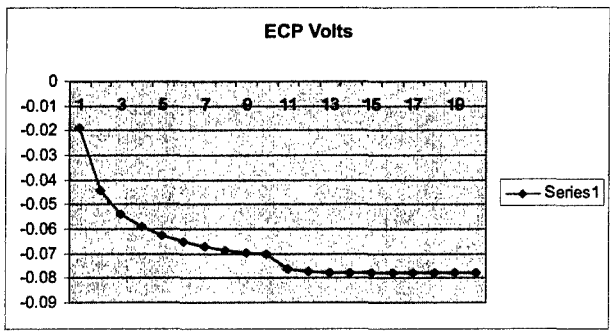
June 23, 2004 – 4 MW run



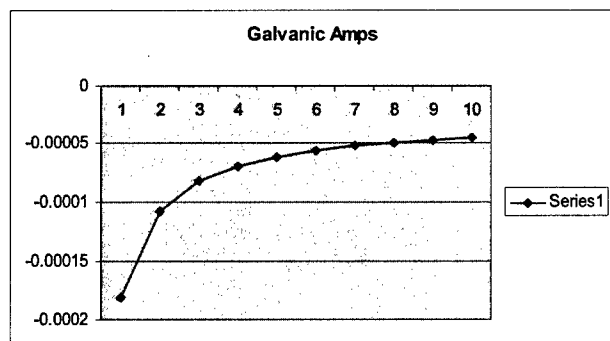
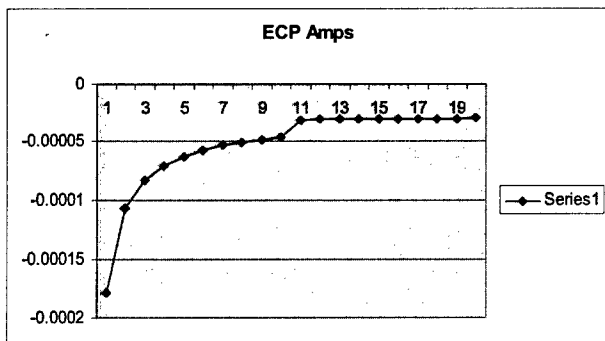
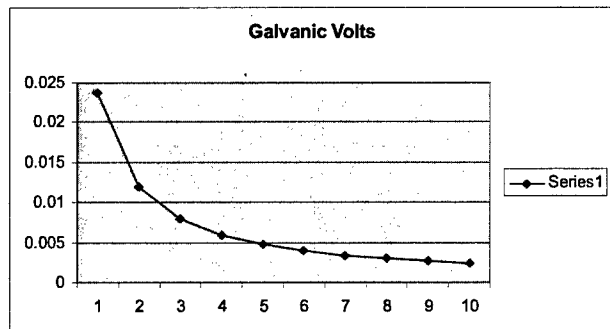
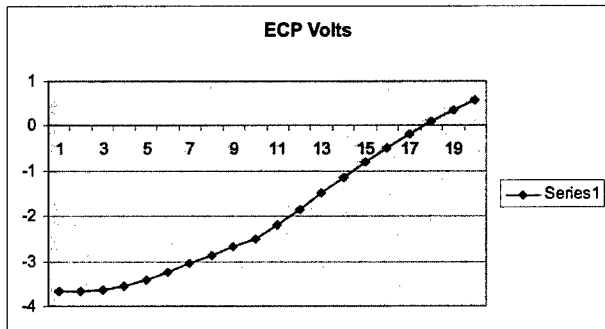
June 24, 2004 – 4 MW run



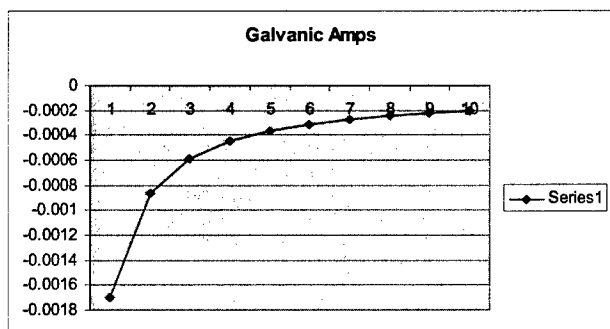
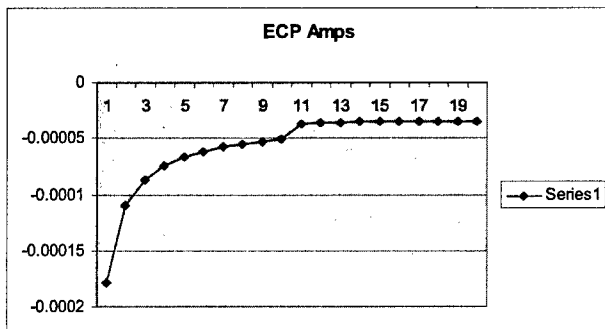
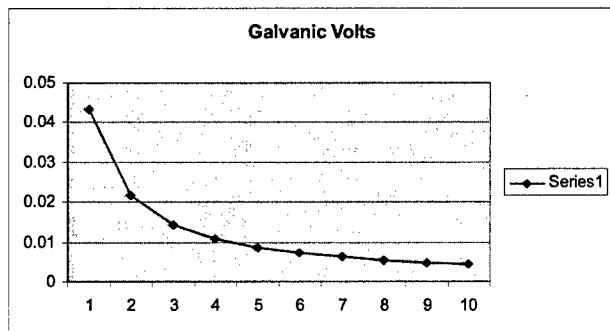
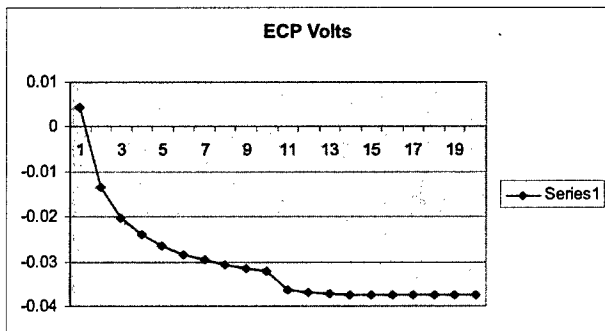
June 28, 2004 – 4 MW run



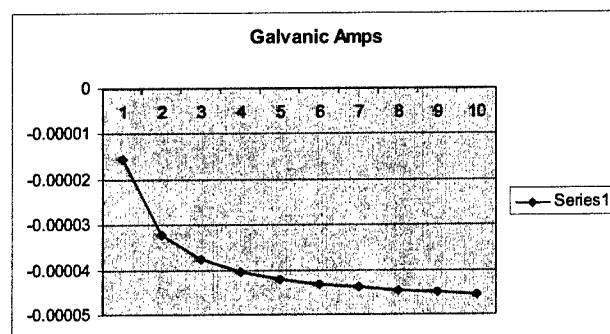
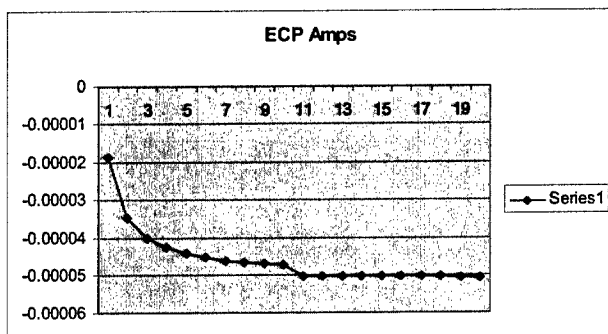
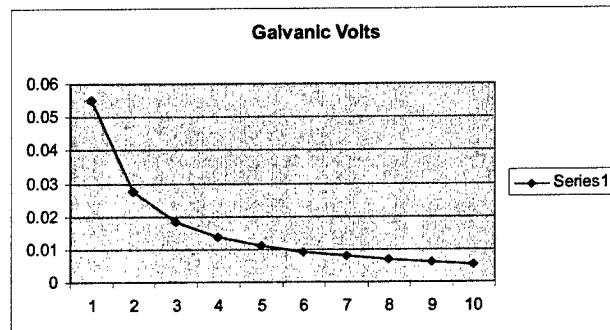
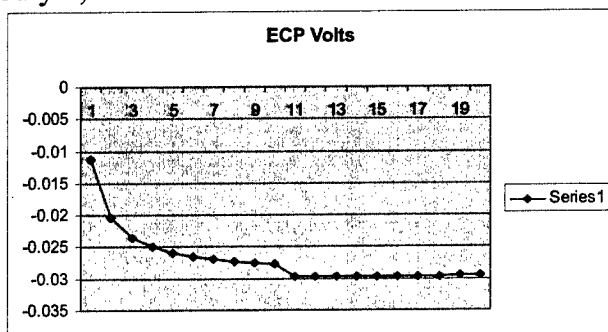
June 29, 2004 – 4 MW run



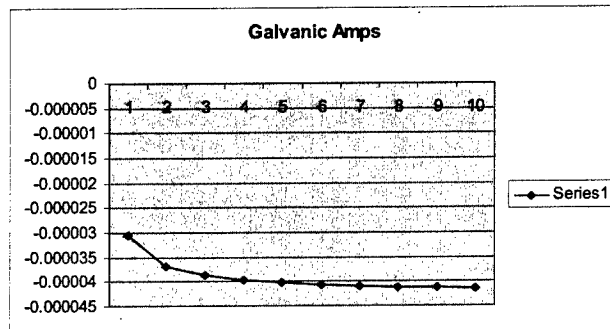
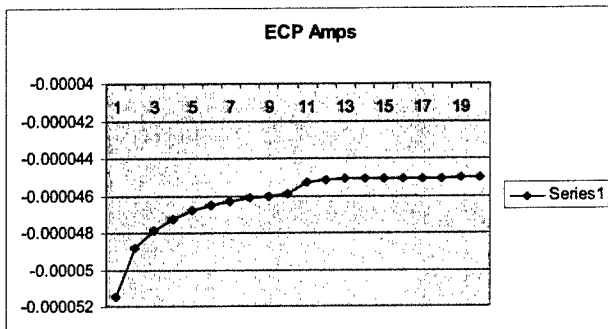
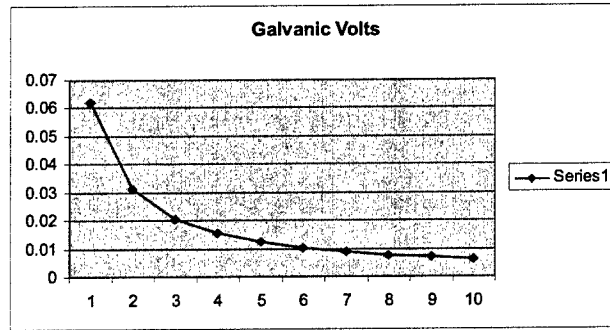
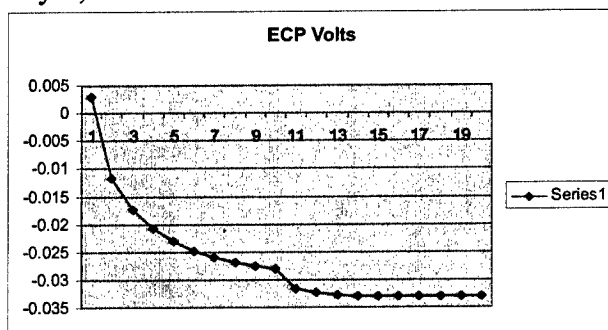
June 30, 2004 – 4 MW run



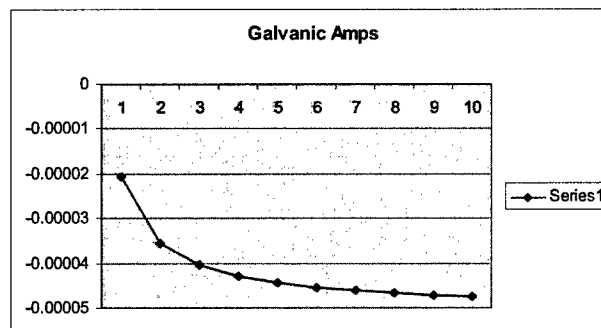
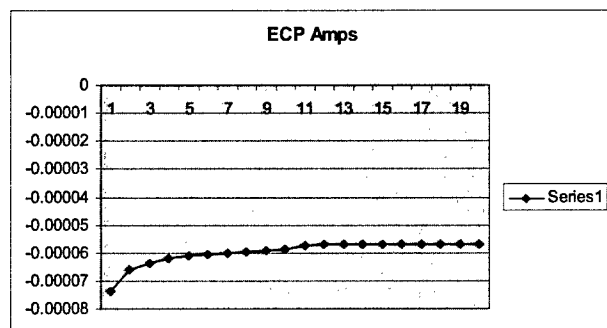
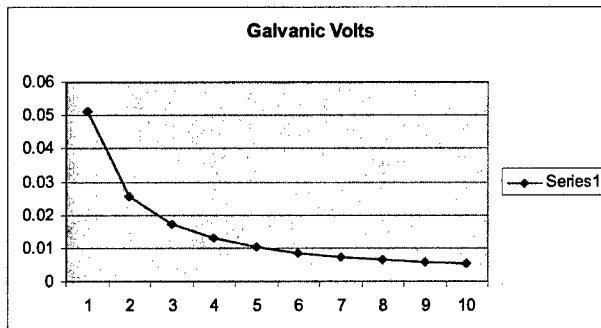
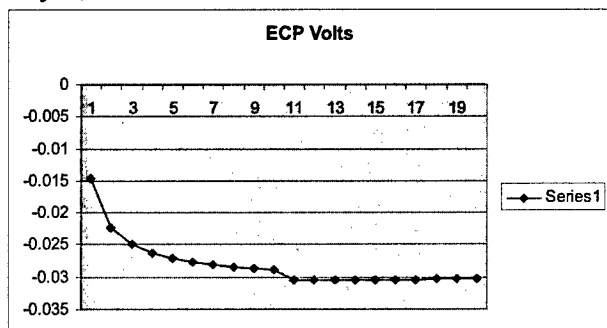
July 2, 2004 – 4 MW run



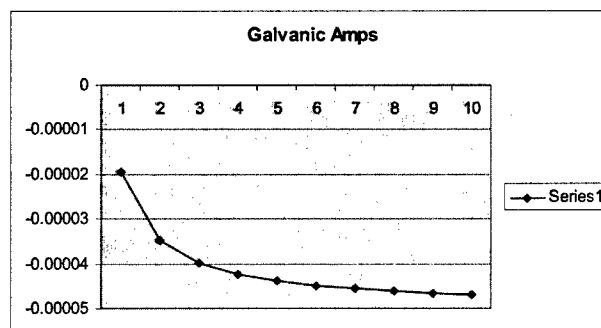
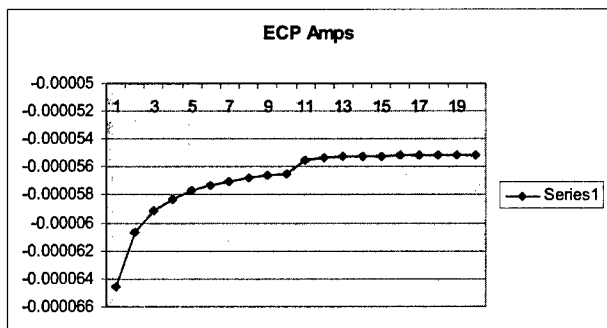
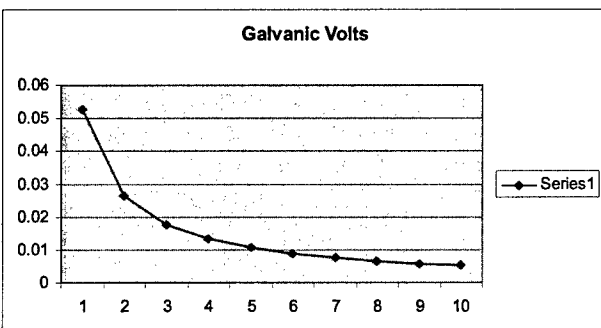
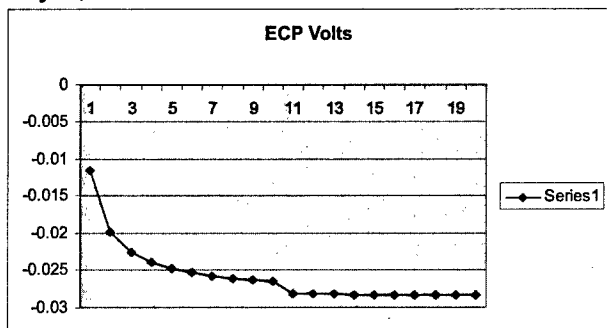
July 6, 2004 – 4 MW run



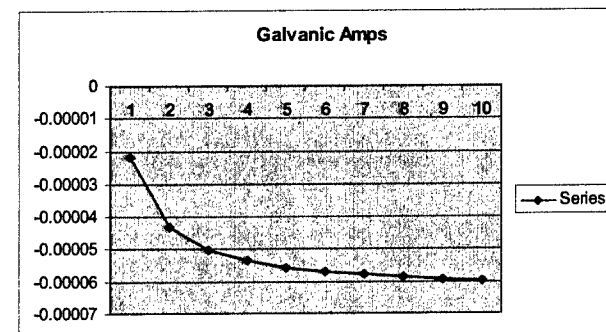
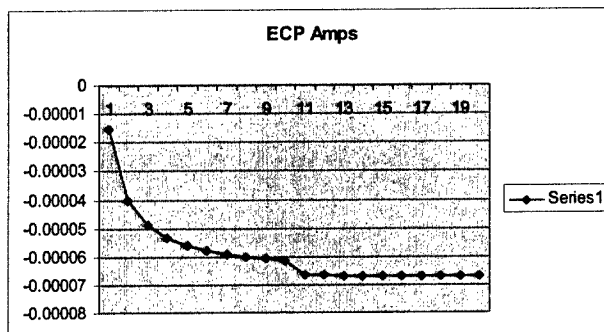
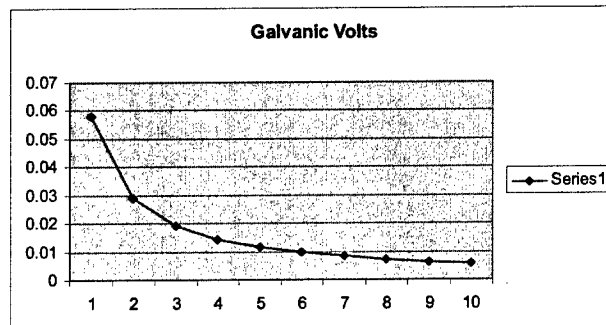
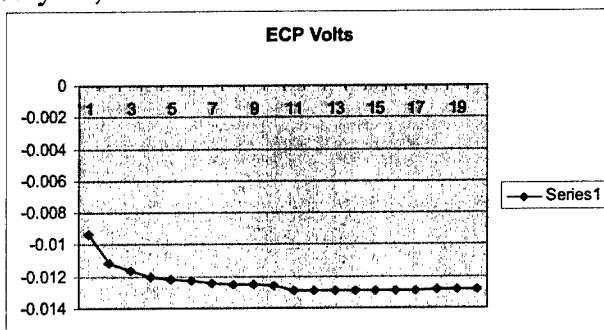
July 7, 2004 – 4 MW run



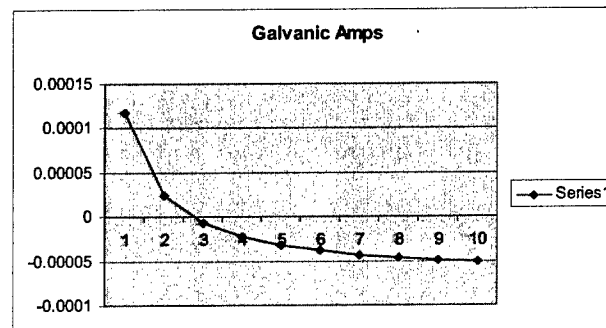
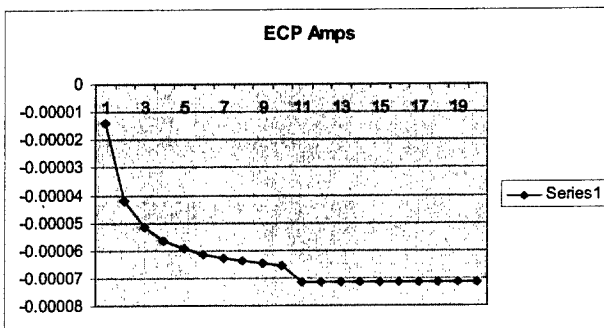
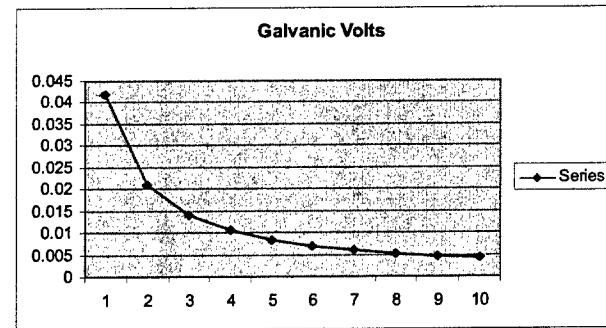
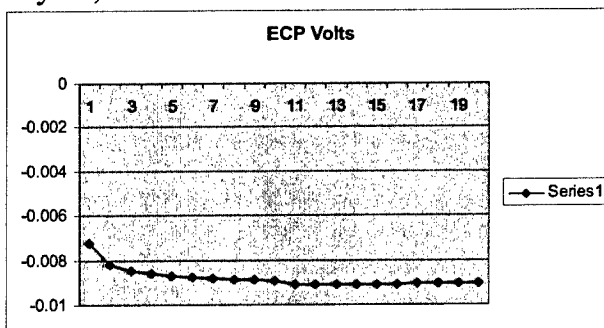
July 9, 2004 – 4 MW run



July 12, 2004 – 4 MW run

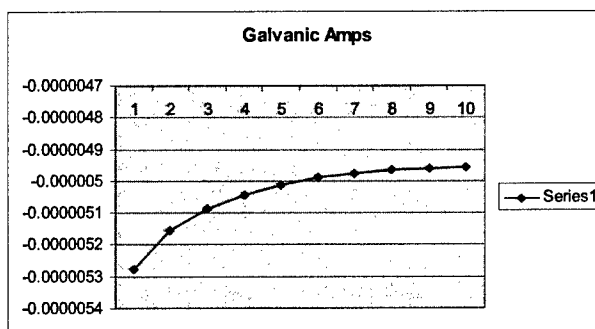
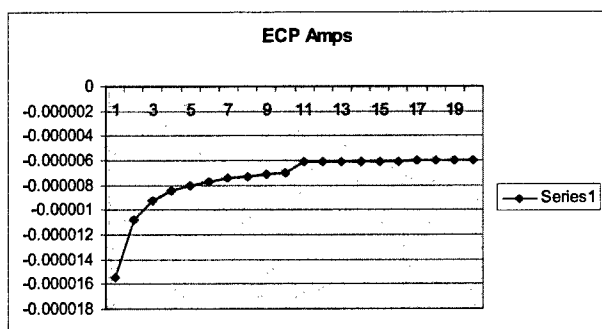
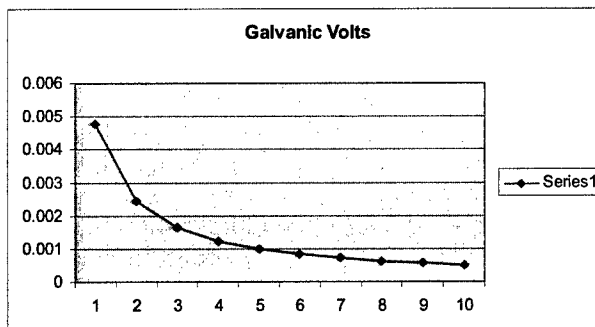
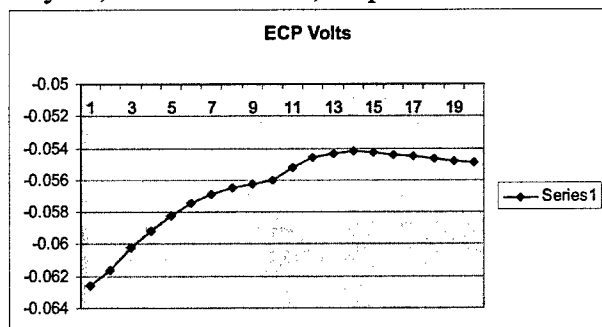


July 15, 2004 – 4 MW run

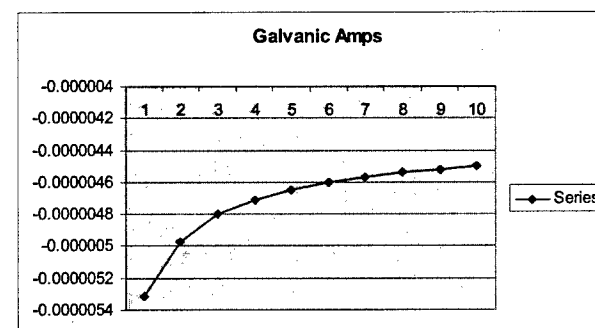
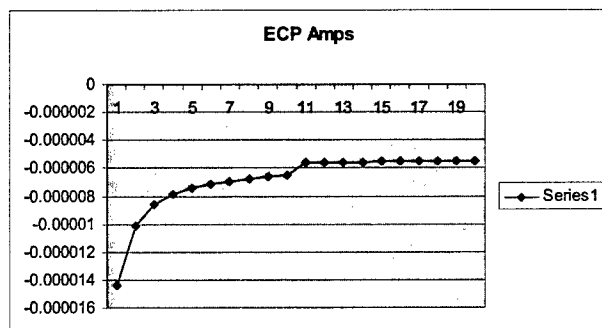
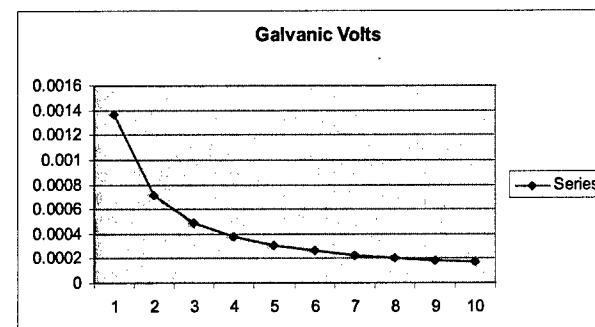
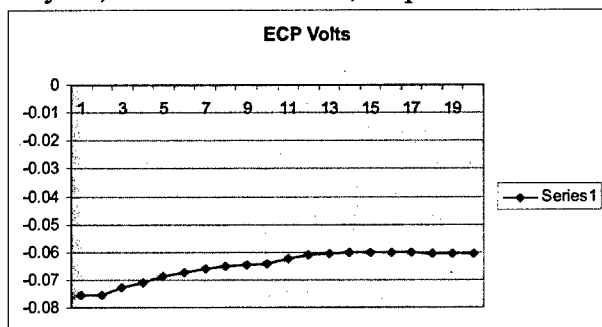


Appendix D – X750-Pt Couple Graphs

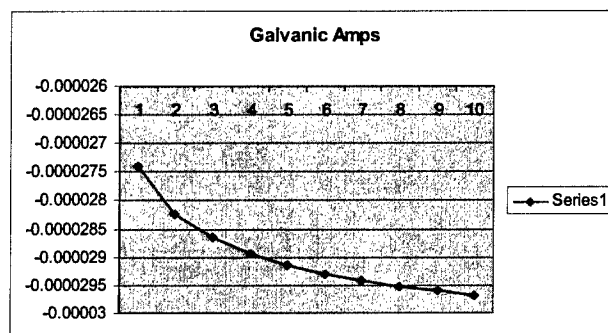
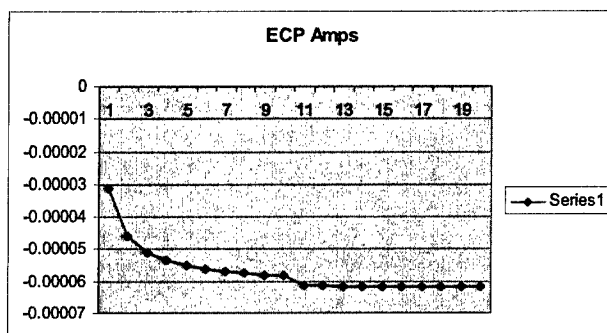
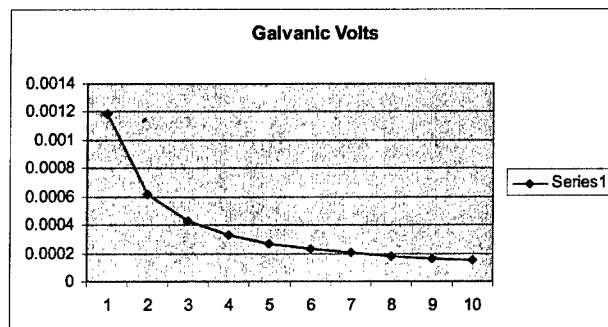
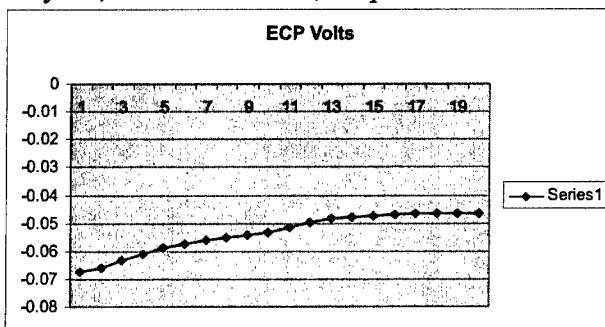
May 27, 2004 – first run, no power



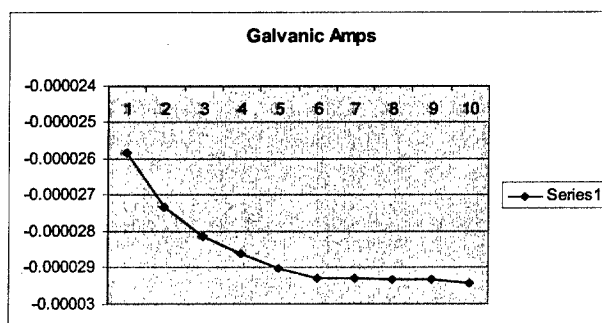
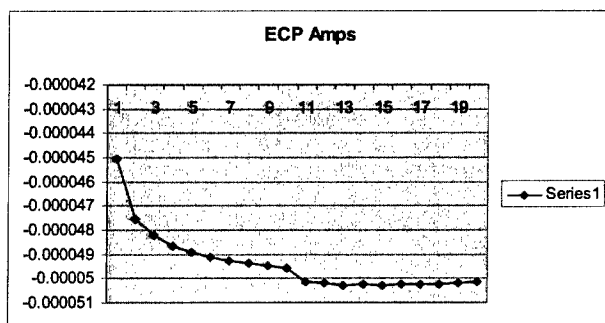
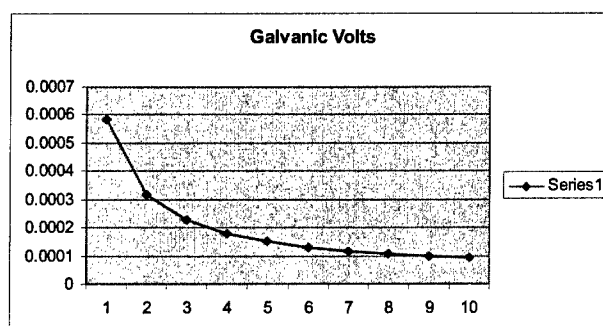
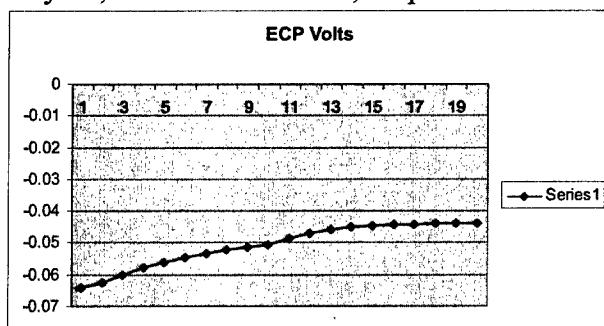
May 27, 2004 – second run, no power



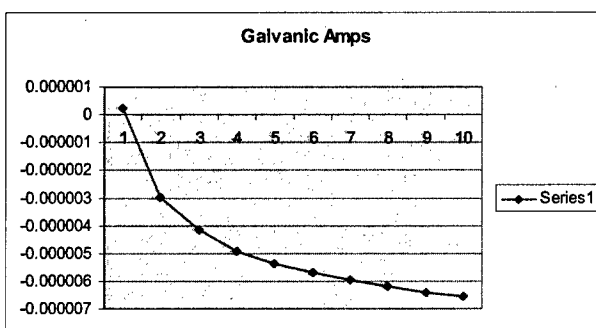
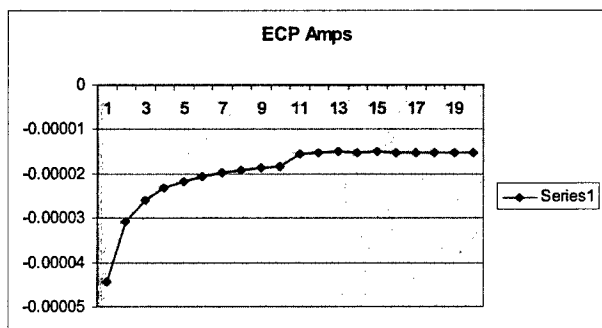
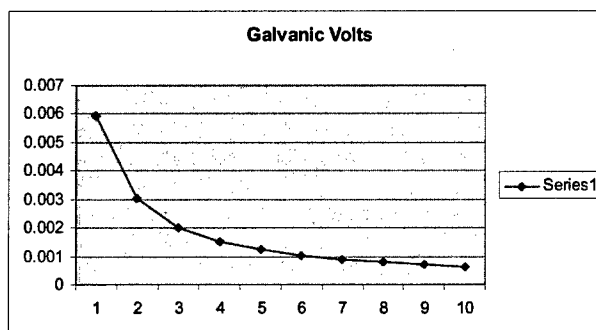
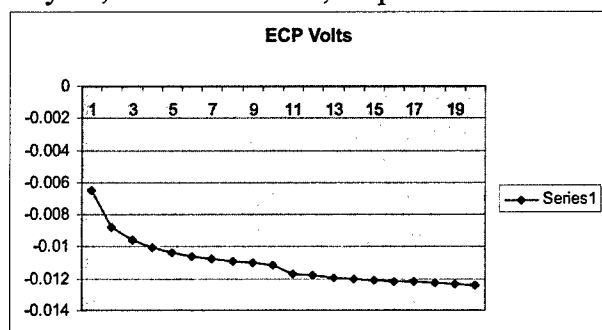
May 28, 2004 – first run, no power



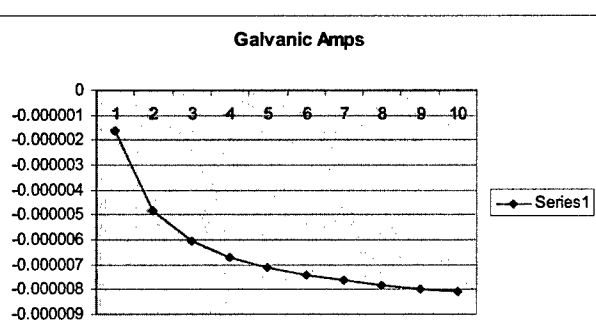
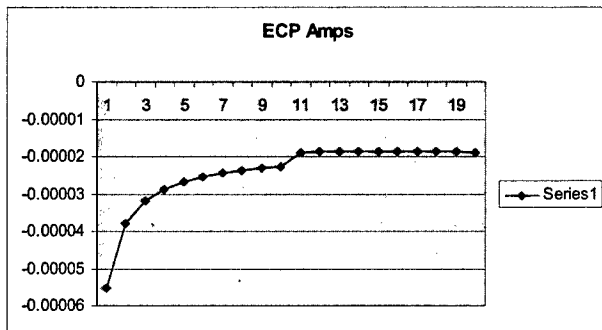
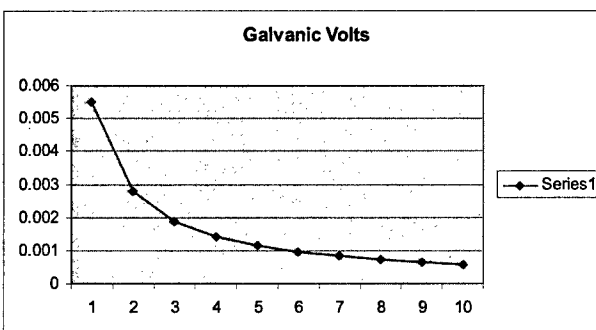
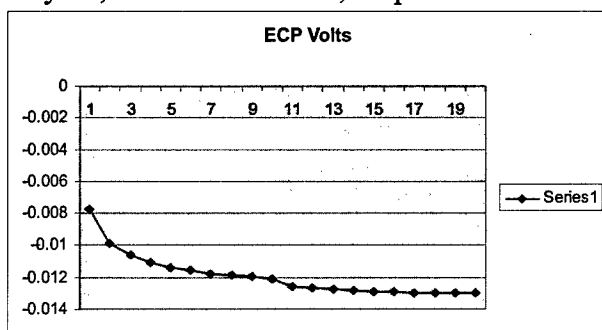
May 28, 2004 – second run, no power



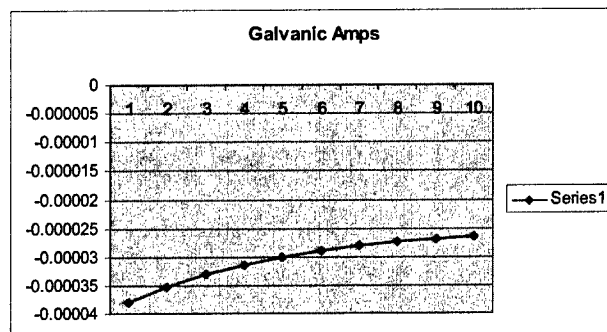
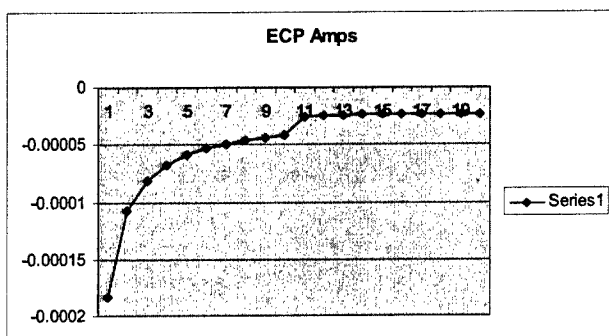
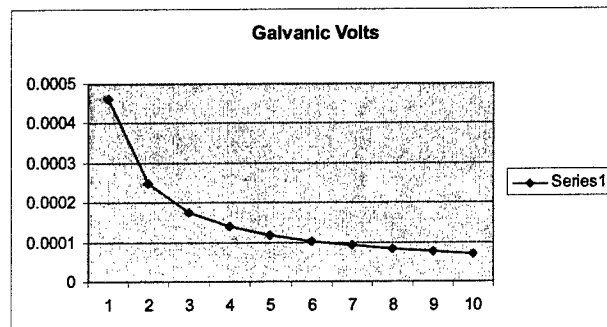
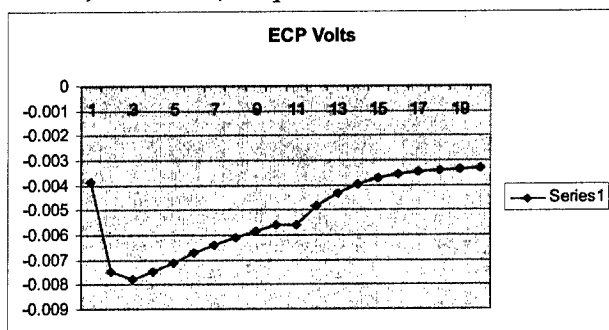
May 28, 2004 – third run, no power



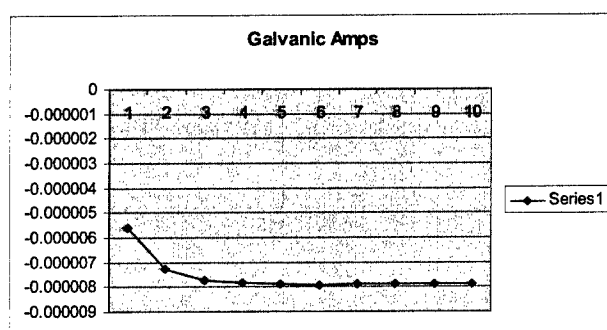
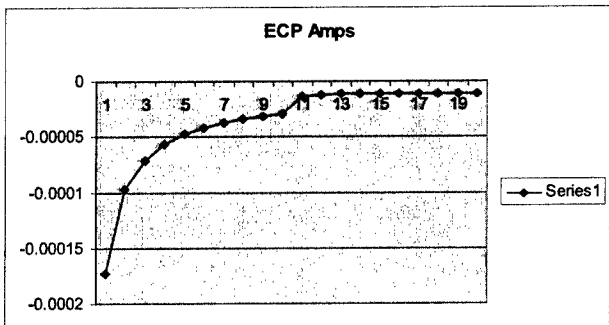
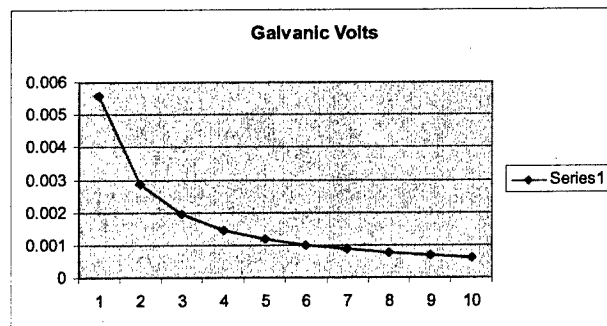
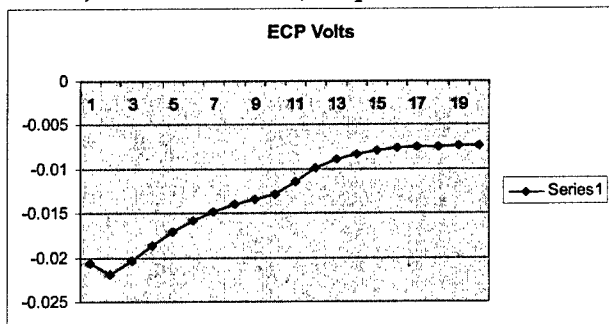
May 28, 2004 – fourth run, no power



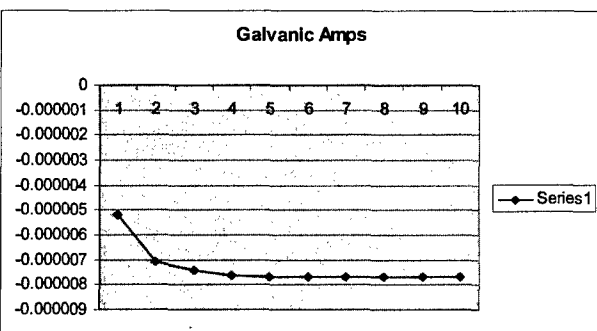
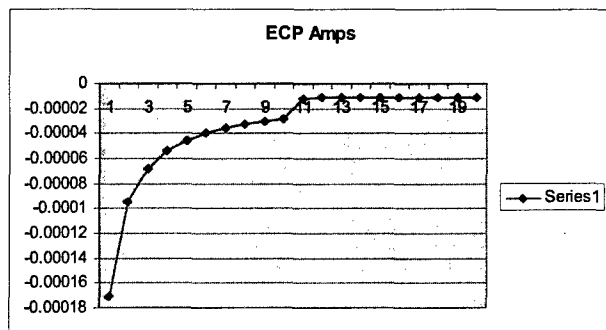
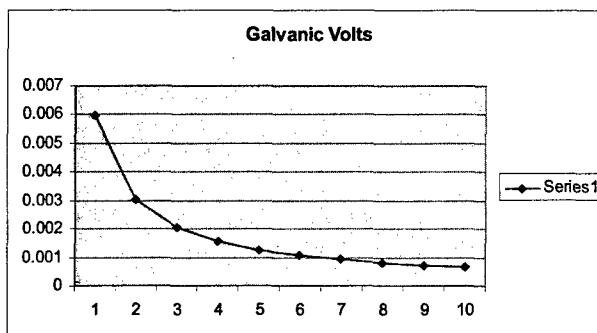
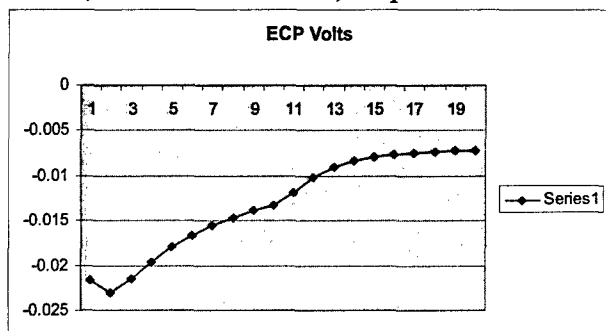
June 3, 2004 run, no power



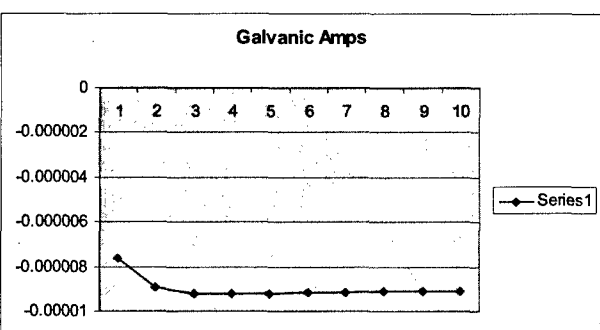
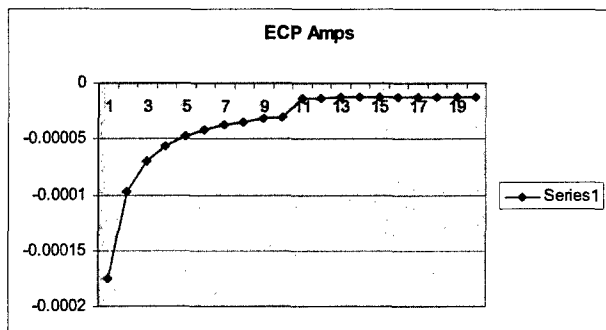
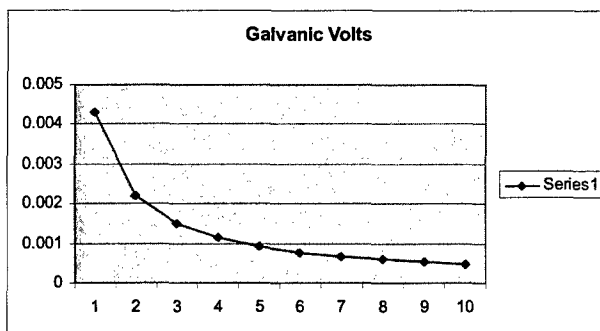
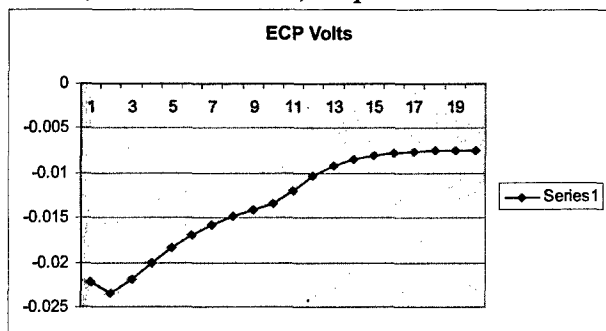
June 4, 2004 – first run, no power



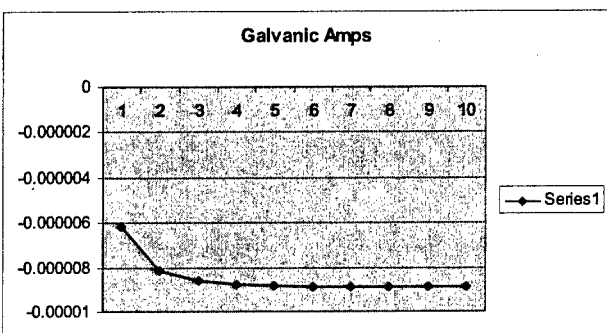
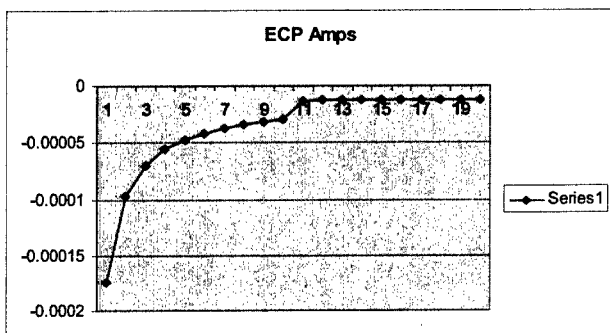
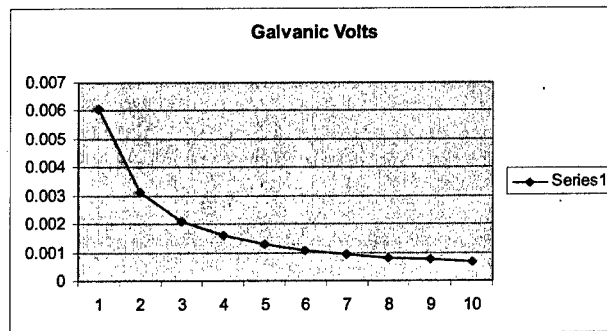
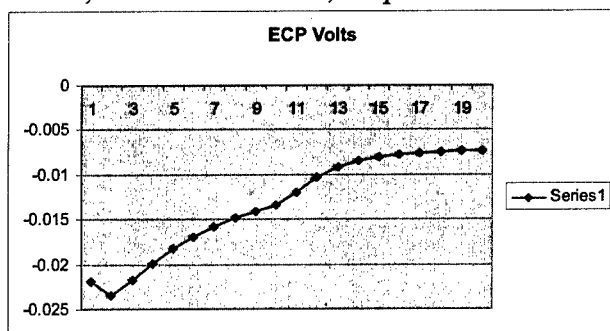
June 4, 2004 – second run, no power



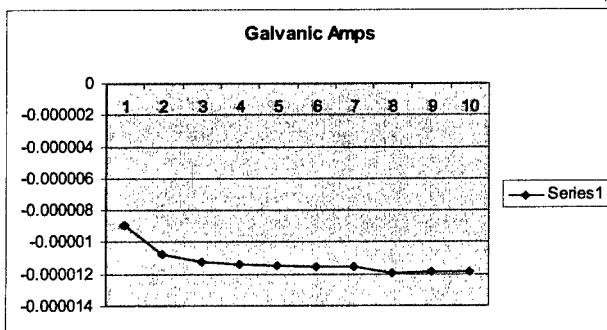
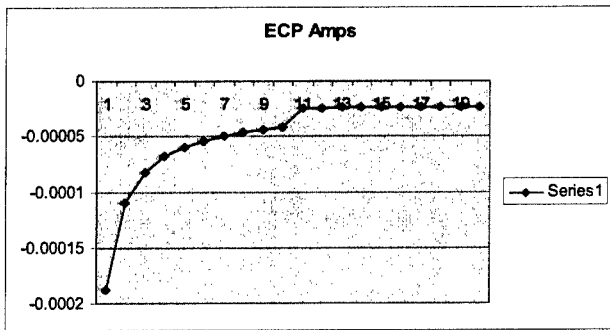
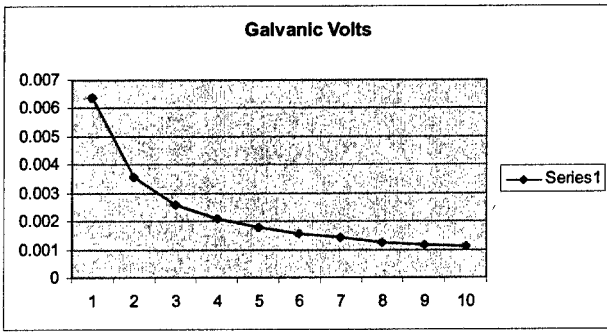
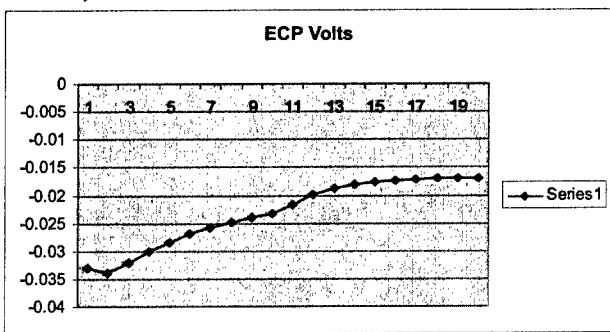
June 4, 2004 –third run, no power



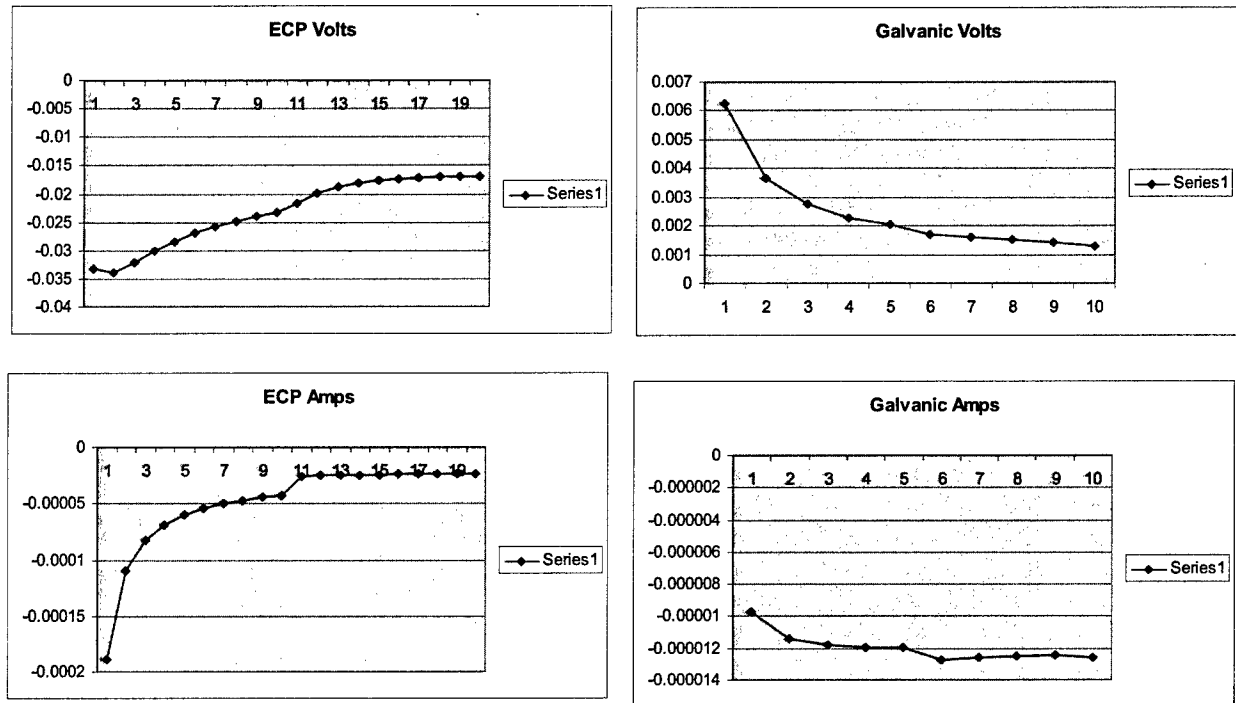
June 4, 2004 – fourth run, no power



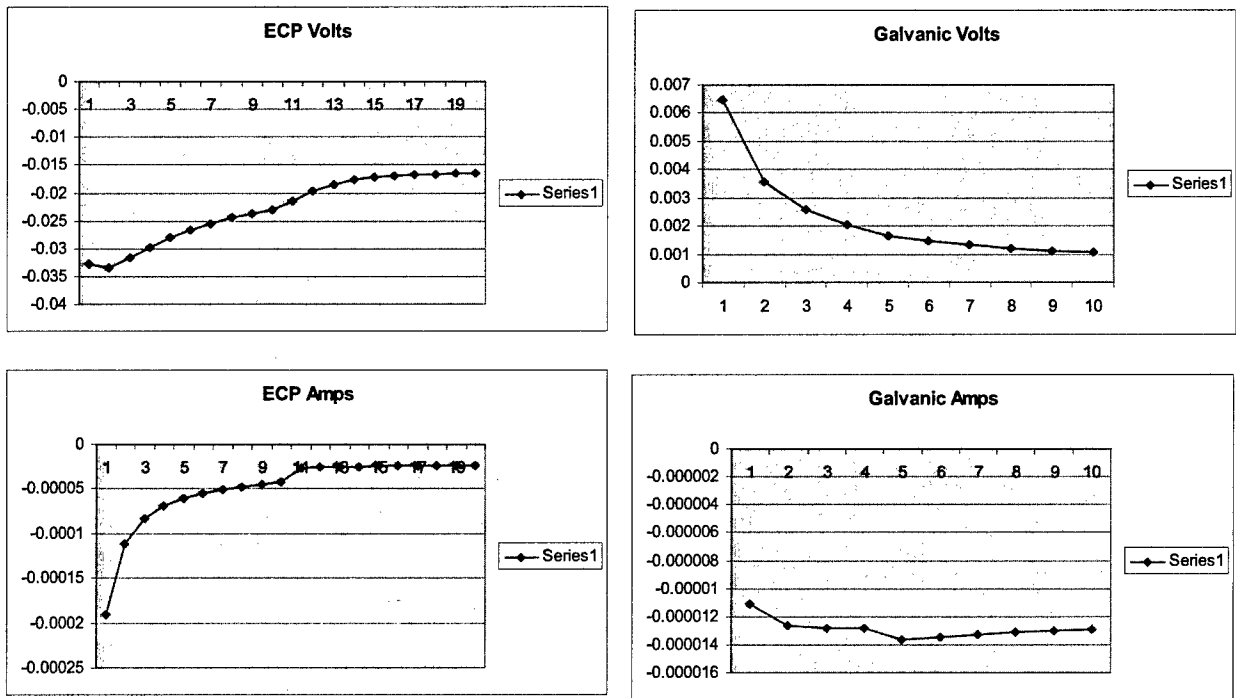
June 4, 2004 – 1 MW run



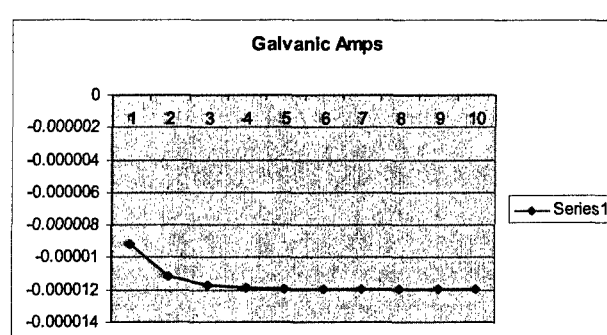
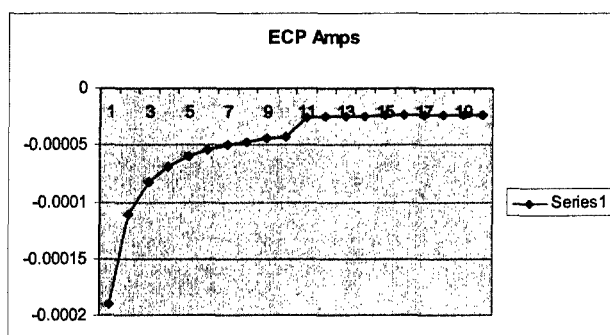
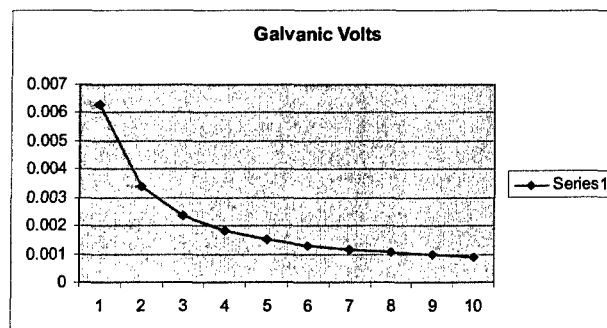
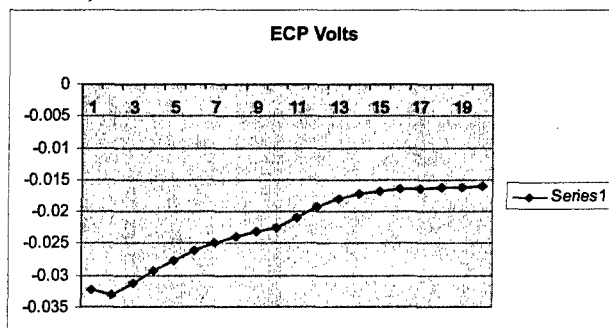
June 4, 2004 – 2 MW run



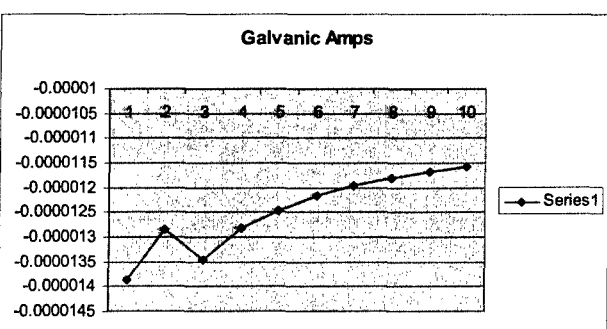
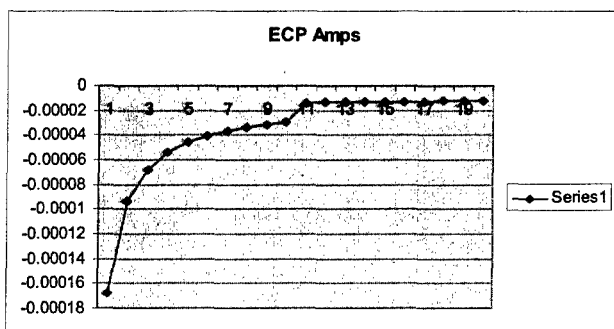
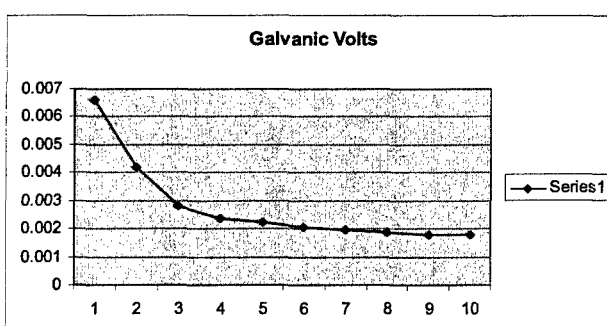
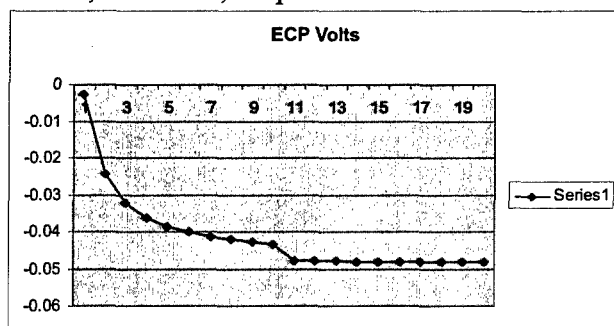
June 4, 2004 – 3 MW run



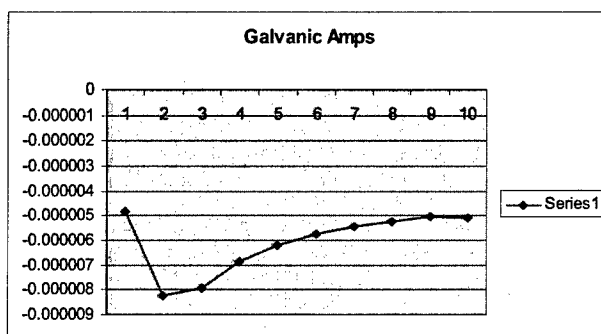
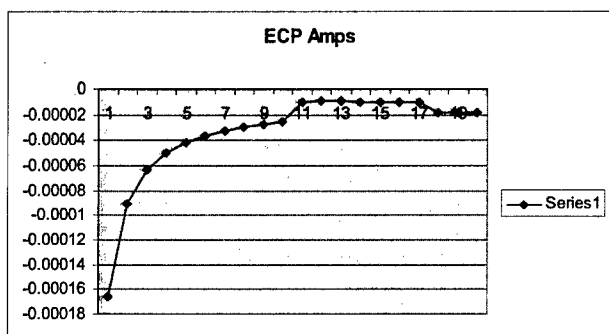
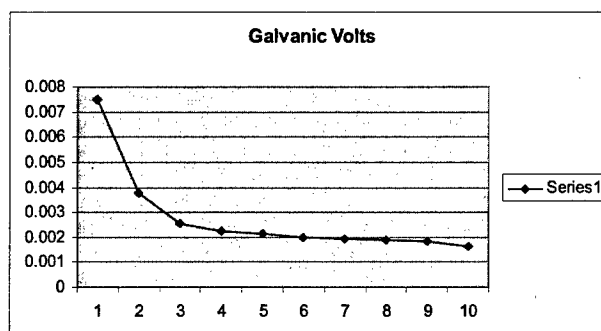
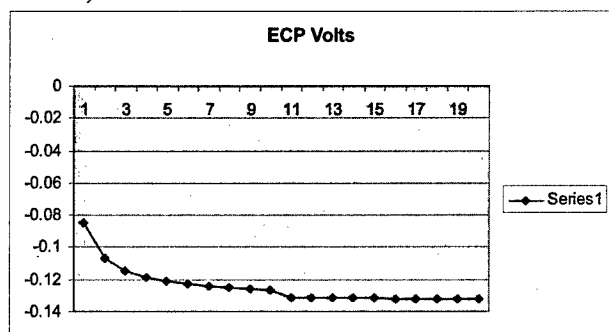
June 4, 2004 – 4 MW run



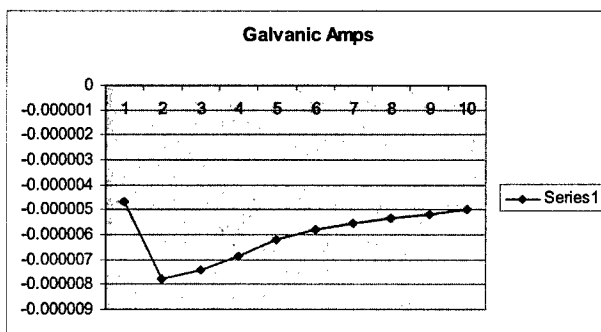
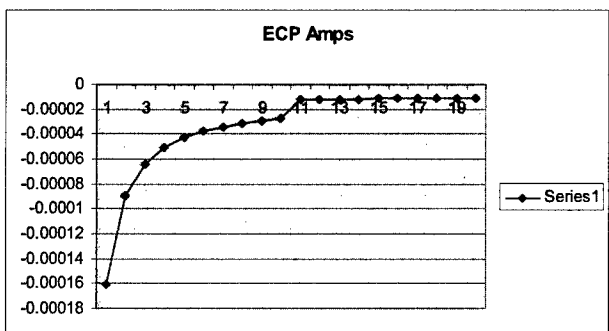
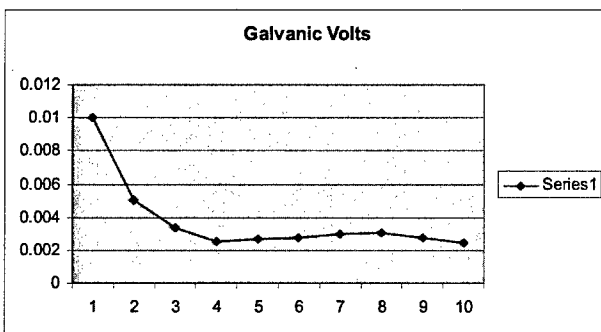
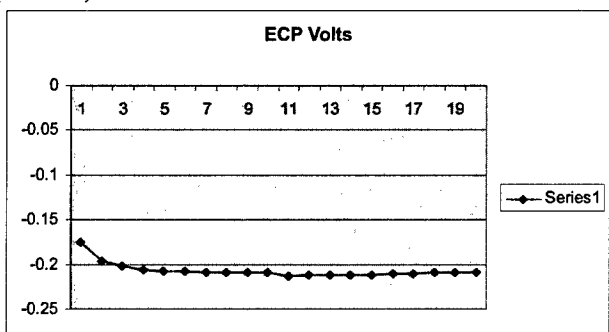
June 7, 2004 run, no power



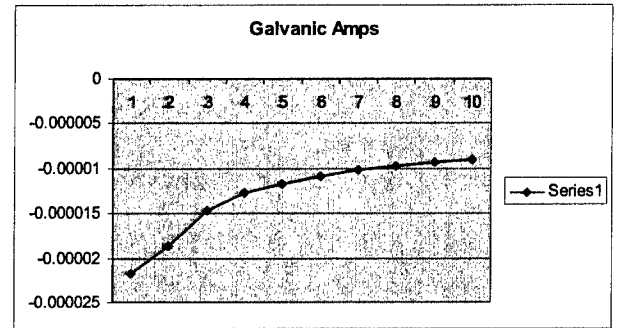
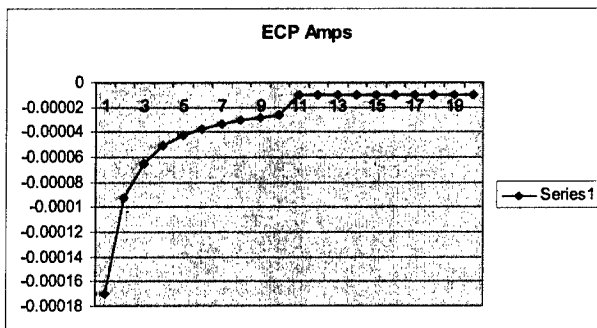
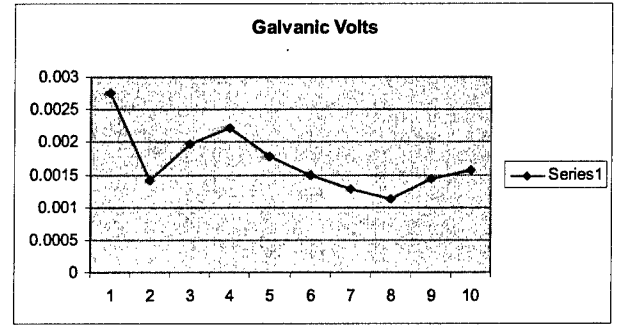
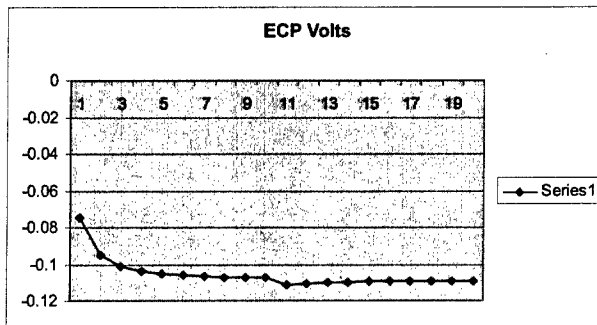
June 8, 2004 – 4 MW run



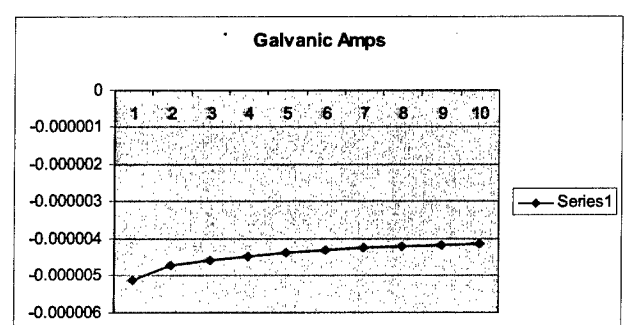
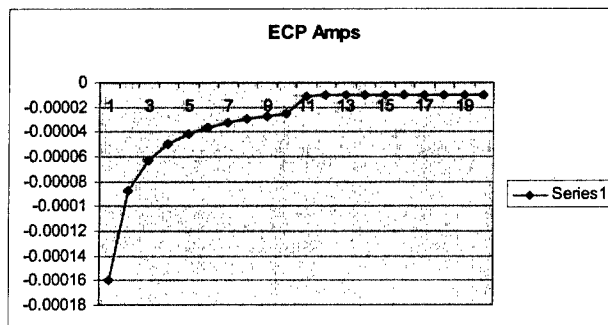
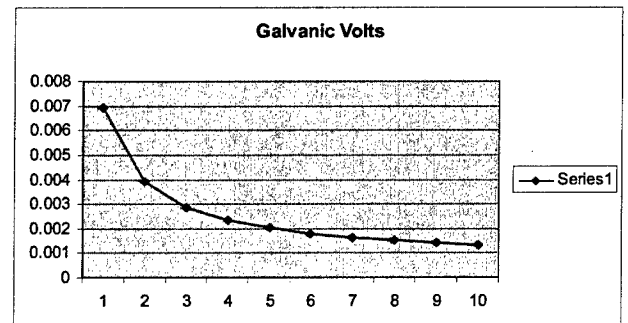
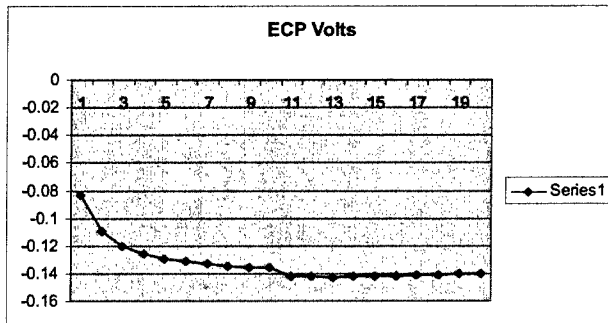
June 9, 2004 – 4 MW run



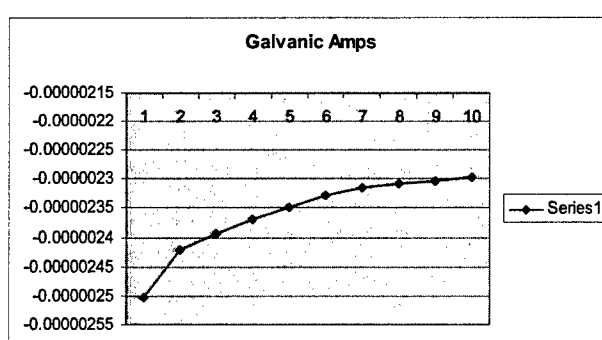
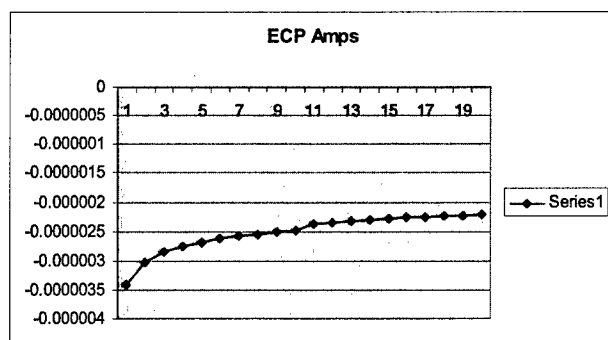
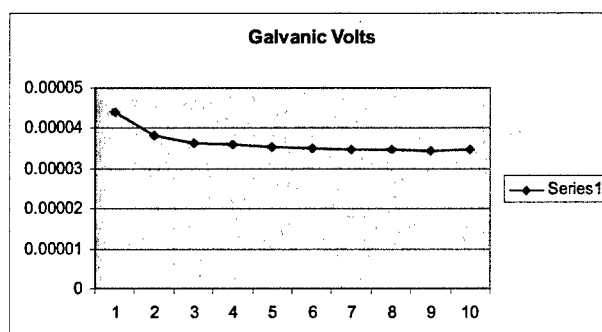
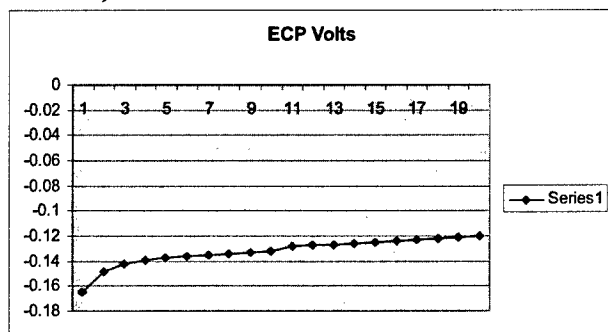
June 10, 2004 – 4.35 MW run



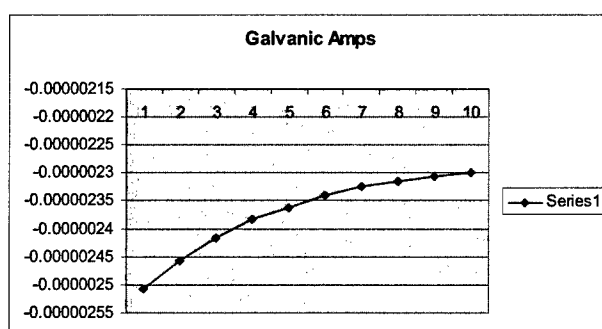
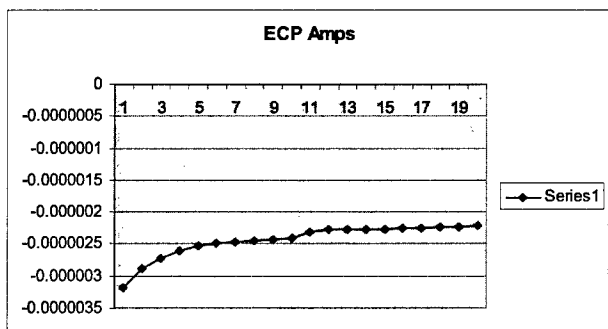
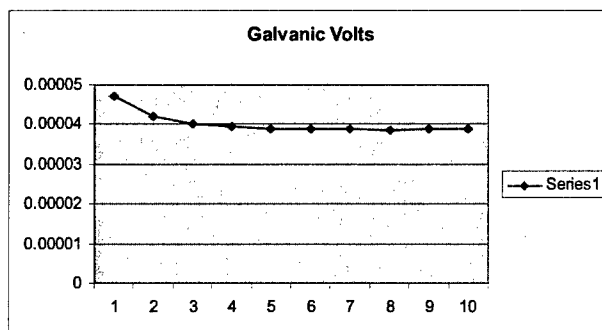
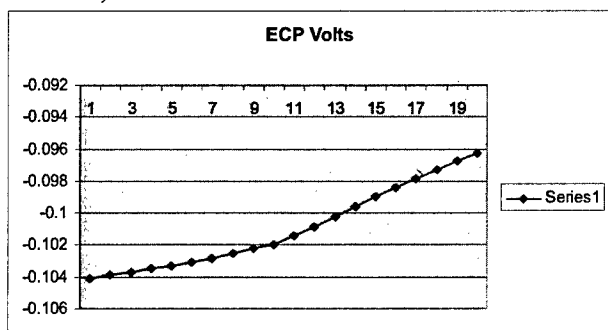
June 11, 2004 – 4 MW run



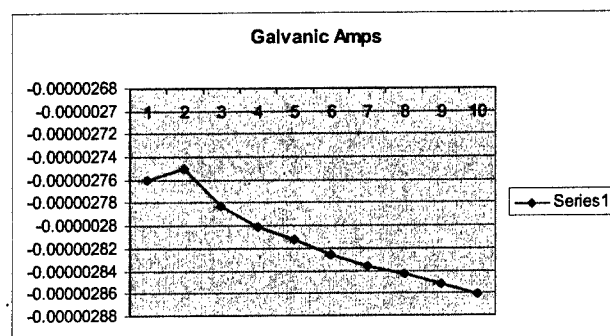
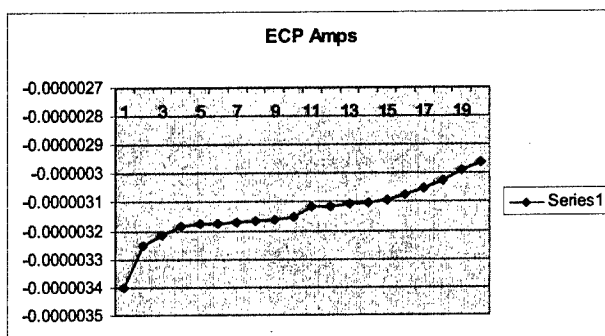
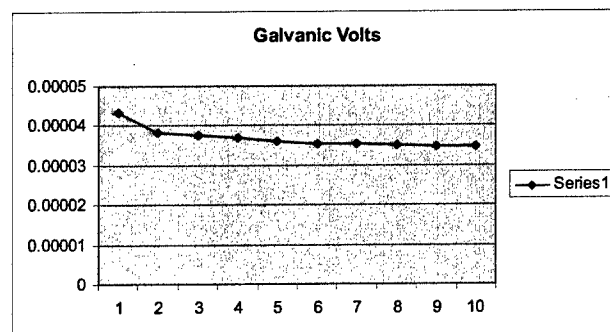
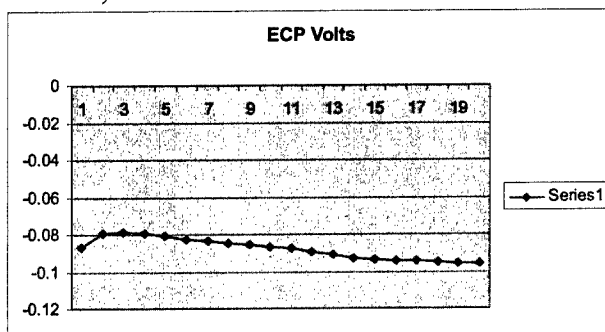
June 14, 2004 – 4 MW run



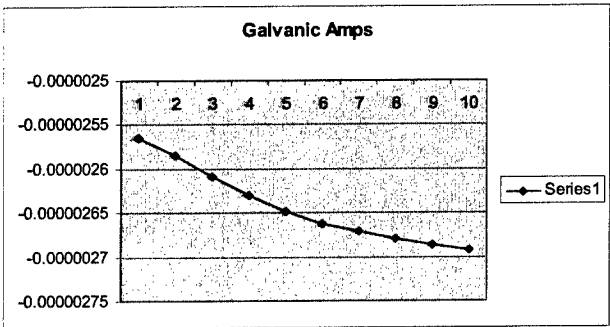
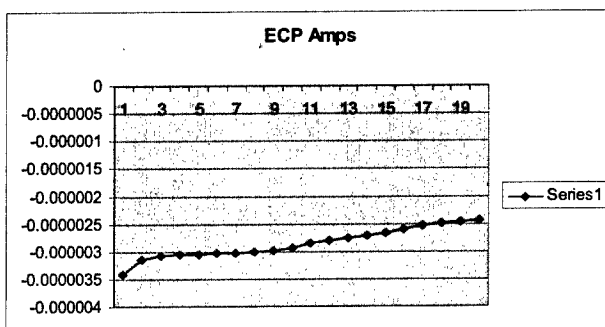
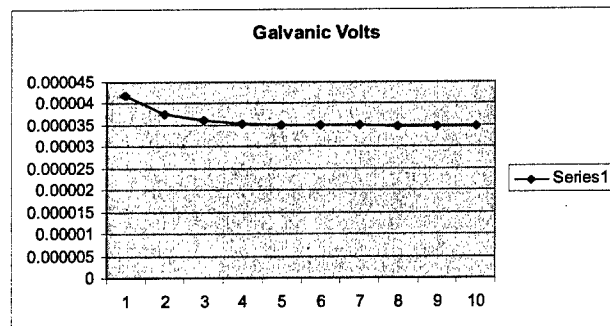
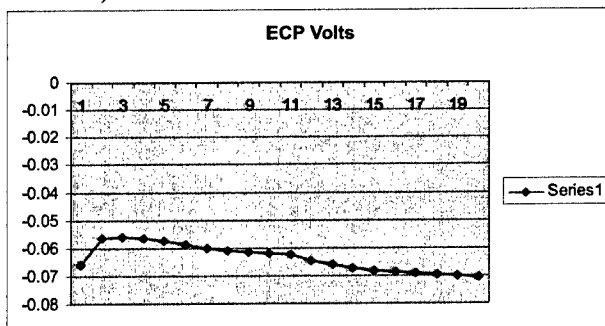
June 15, 2004 – 4 MW run



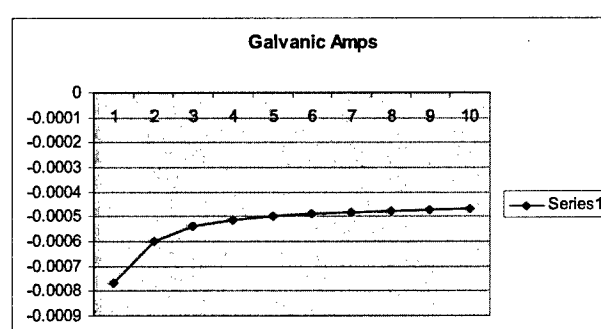
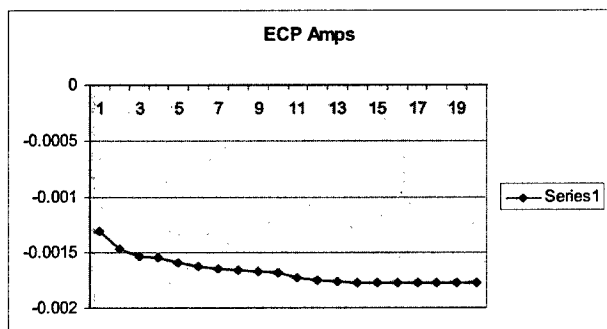
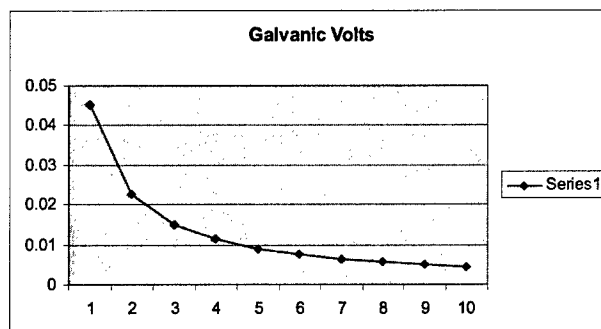
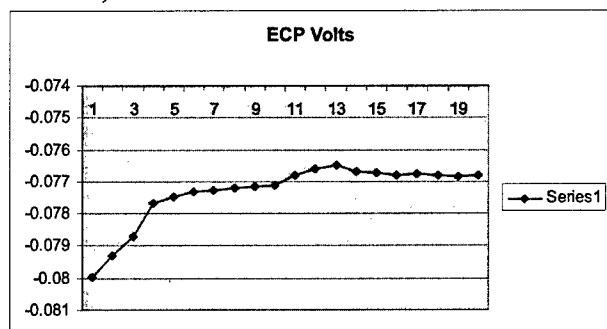
June 16, 2004 – 4 MW run



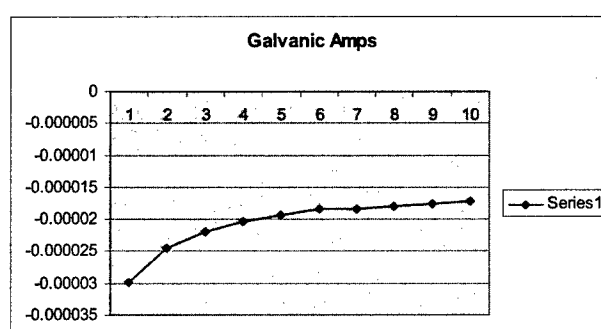
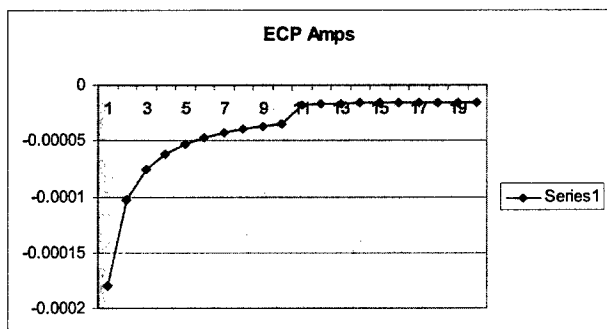
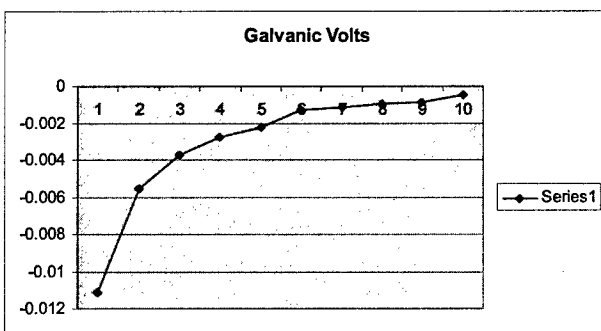
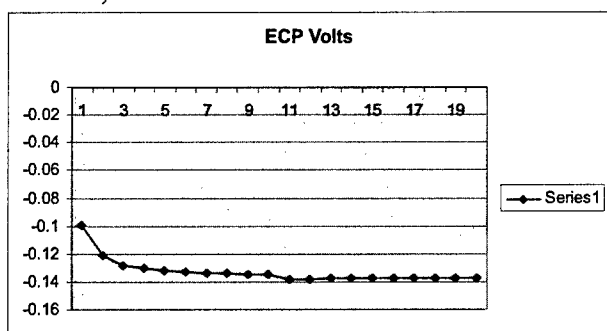
June 18, 2004 – 4 MW run



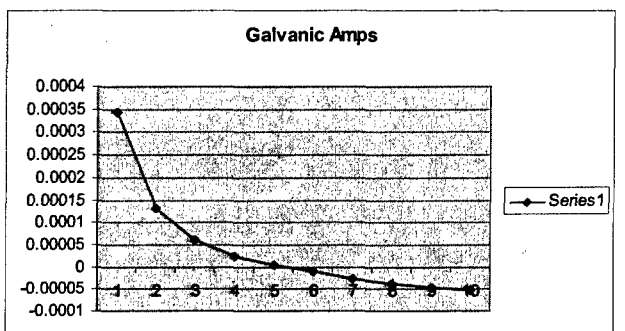
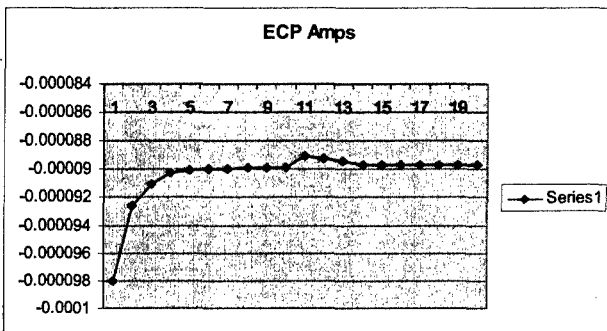
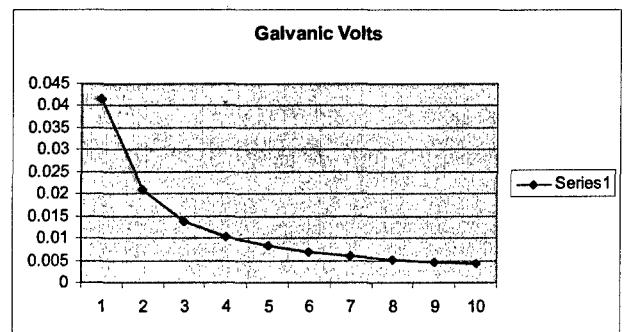
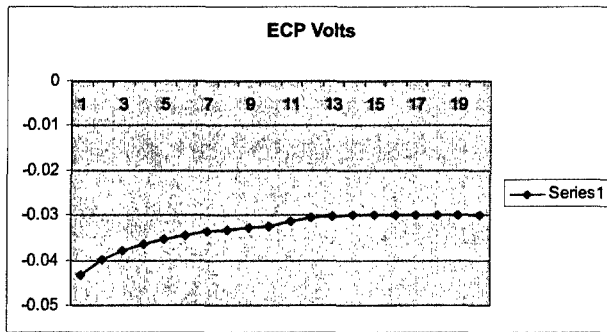
June 22, 2004 – 4 MW run



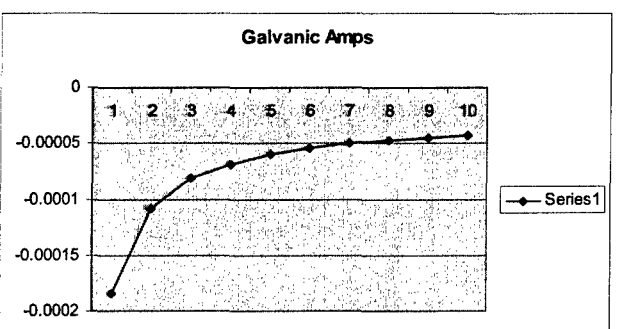
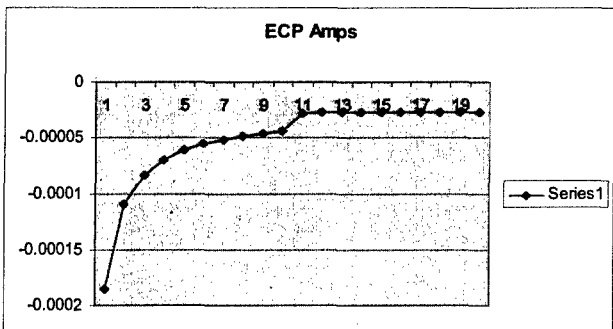
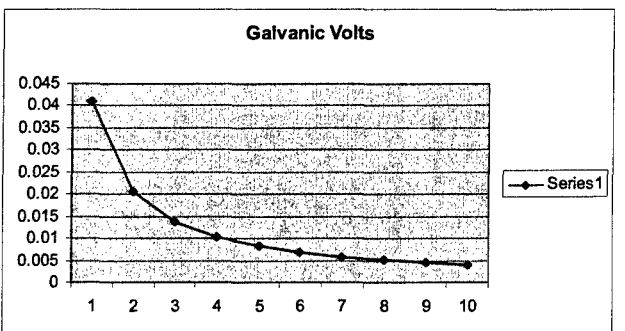
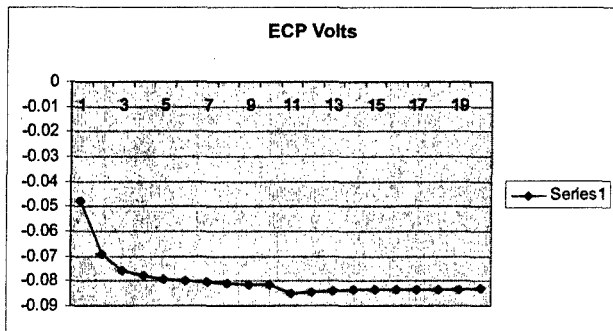
June 23, 2004 – 4 MW run



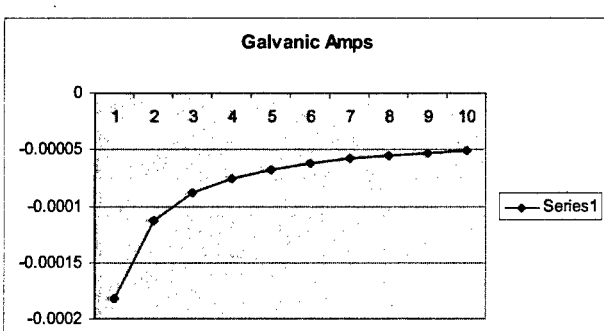
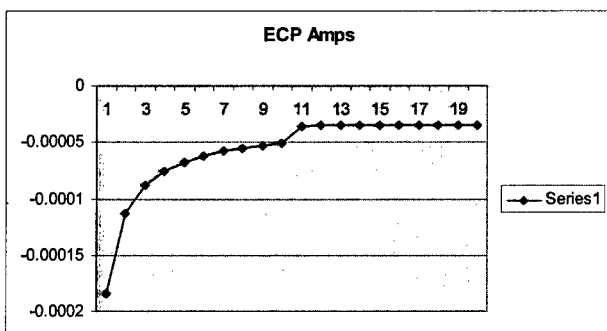
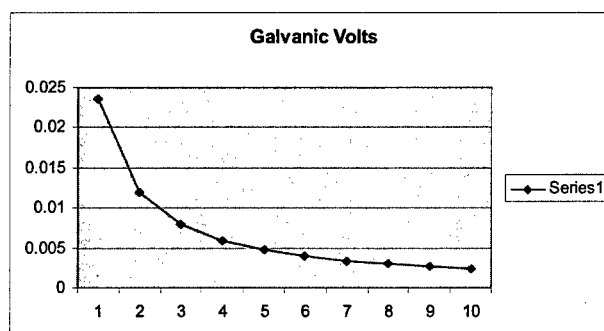
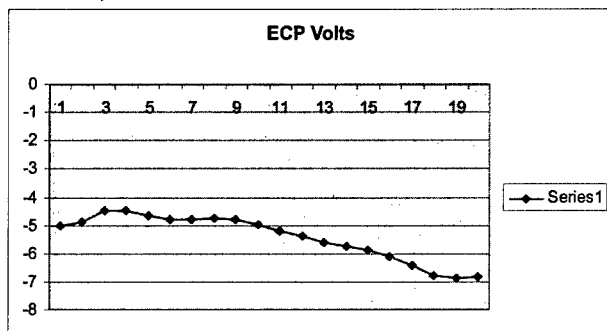
June 24, 2004 – 4 MW run



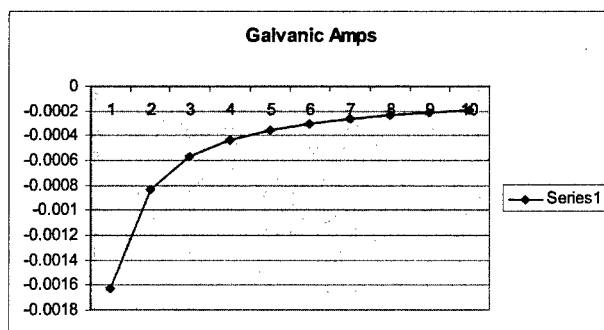
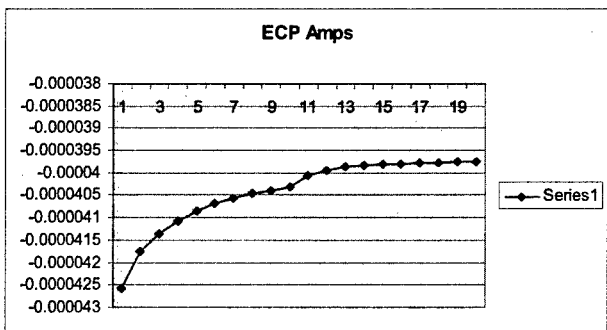
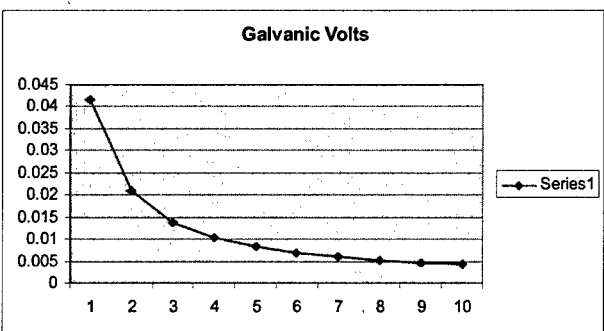
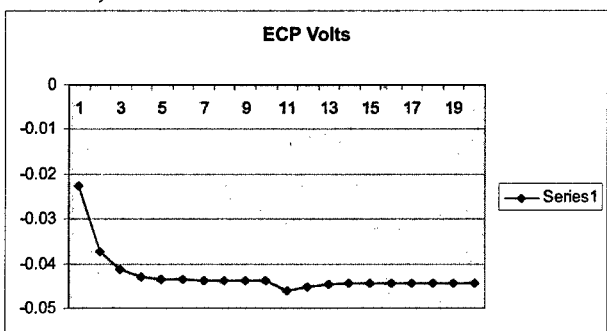
June 28, 2004 – 4 MW run



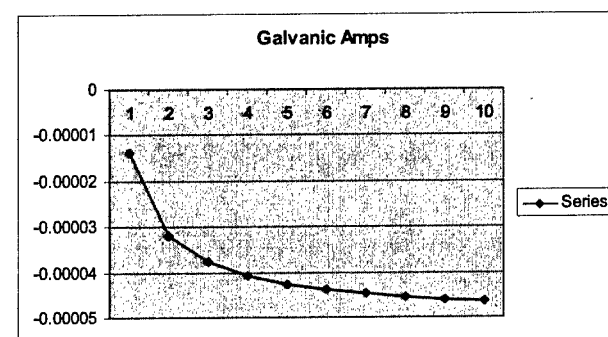
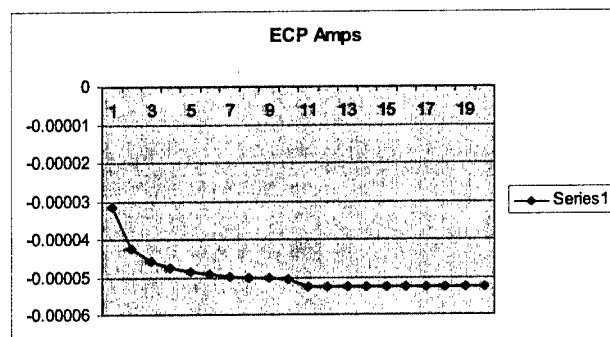
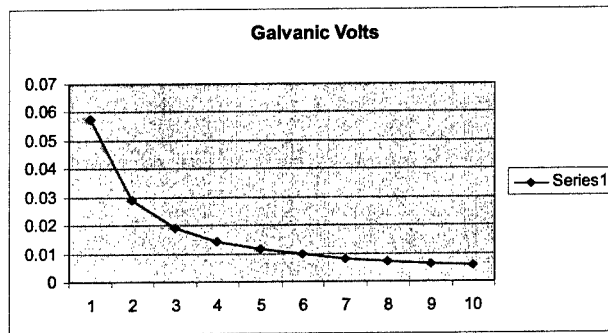
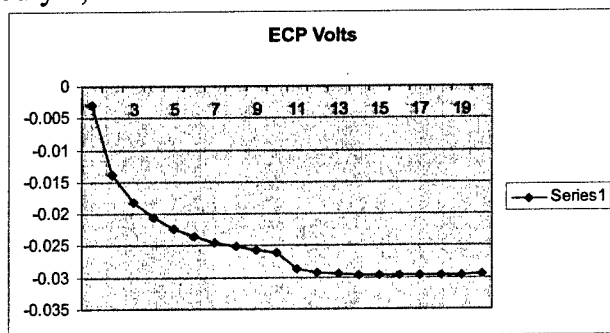
June 29, 2004 – 4 MW run



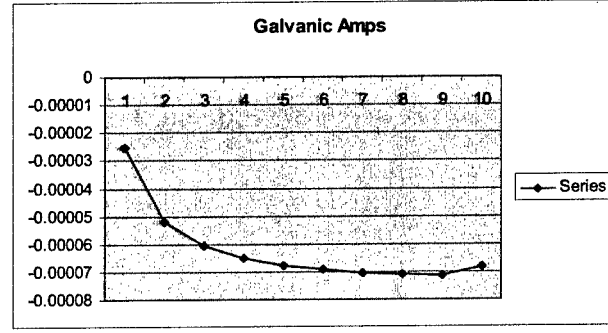
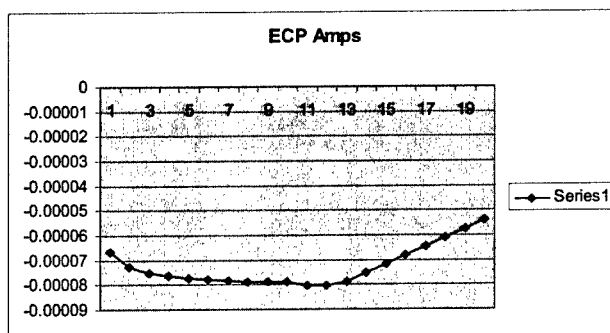
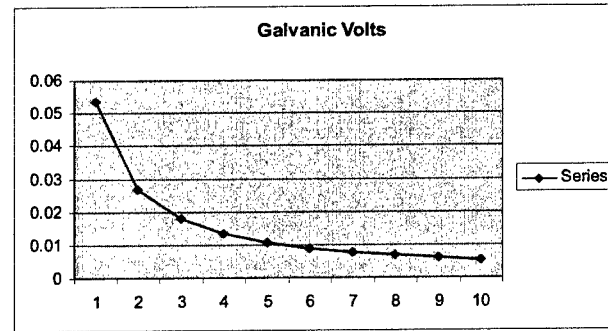
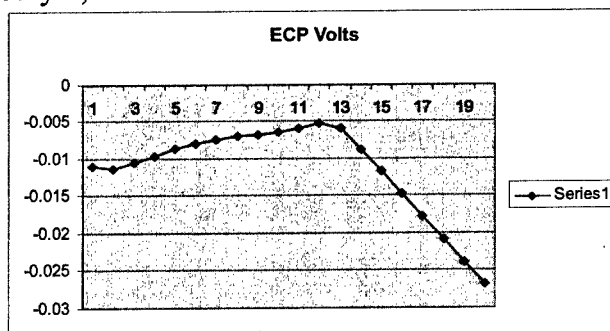
June 30, 2004 – 4 MW run



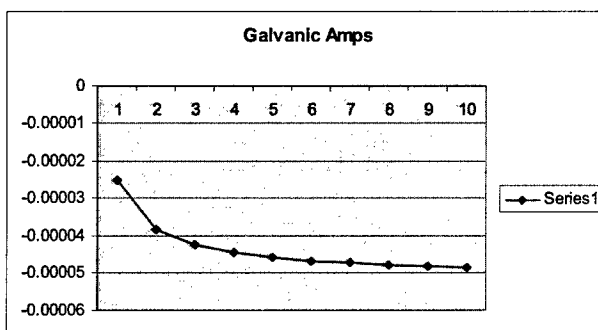
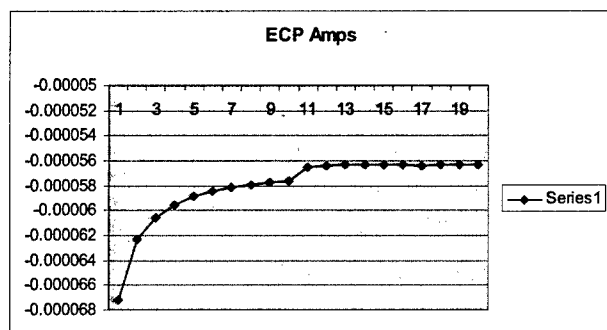
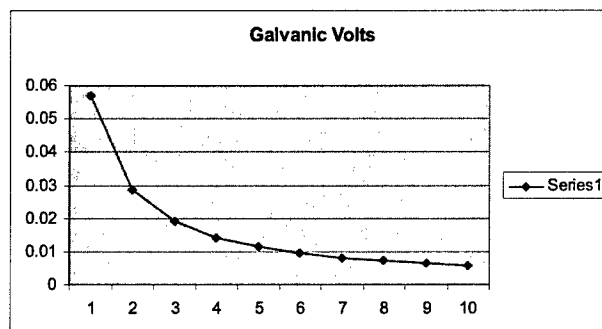
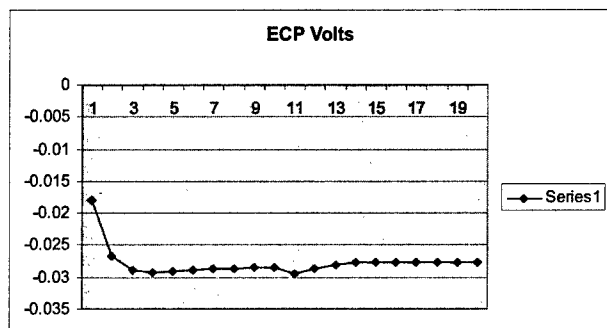
July 2, 2004 – 4 MW run



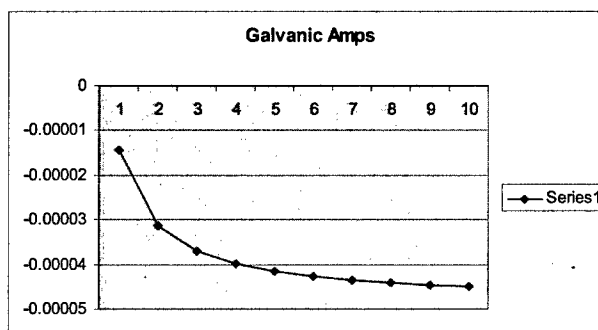
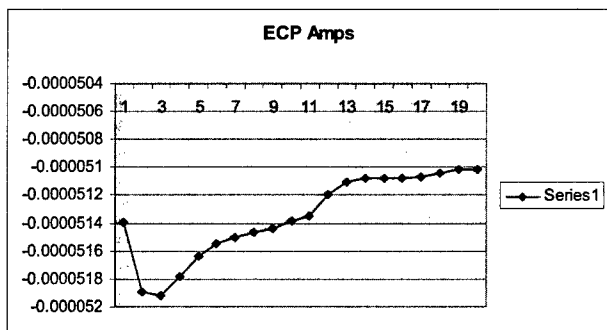
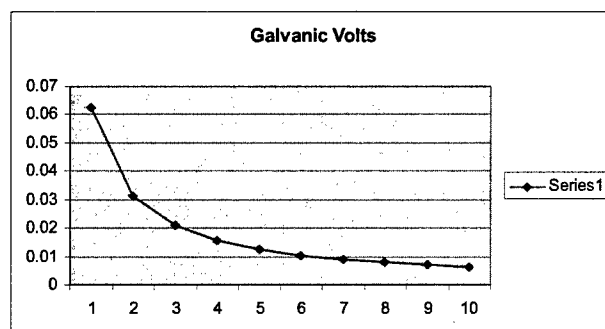
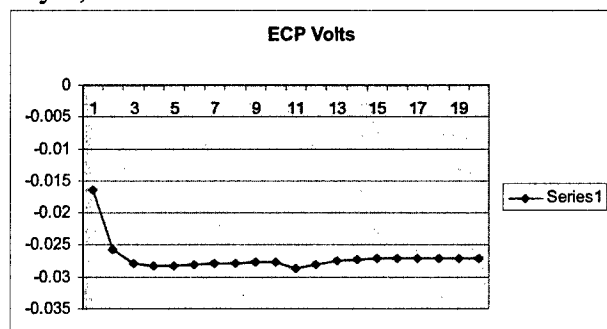
July 6, 2004 – 4 MW run



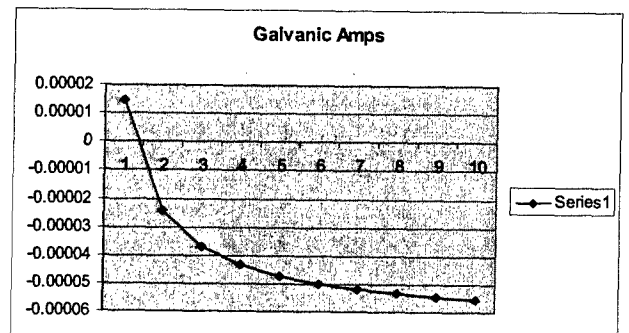
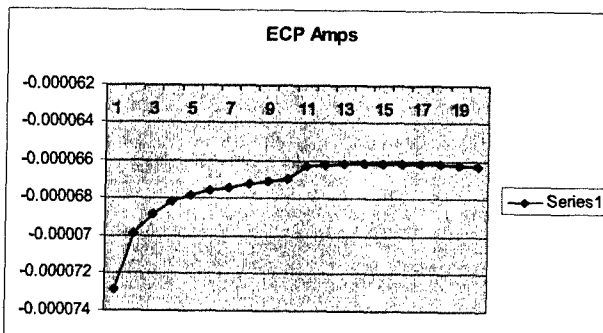
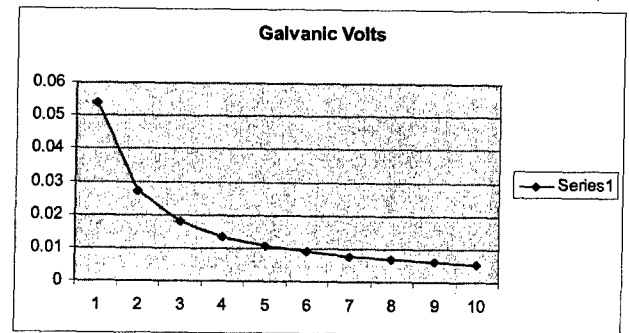
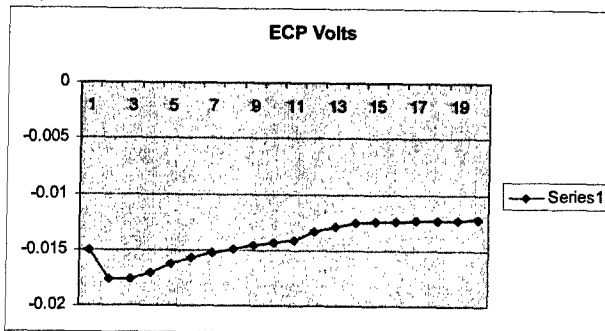
July 7, 2004 – 4 MW run



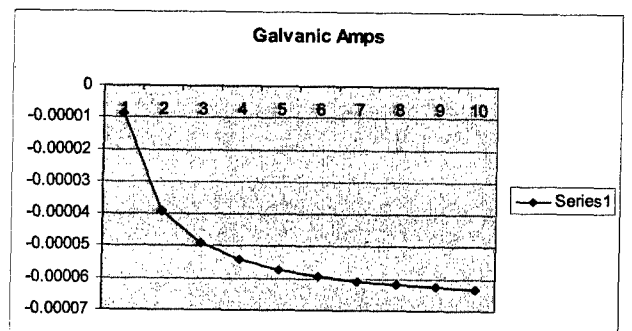
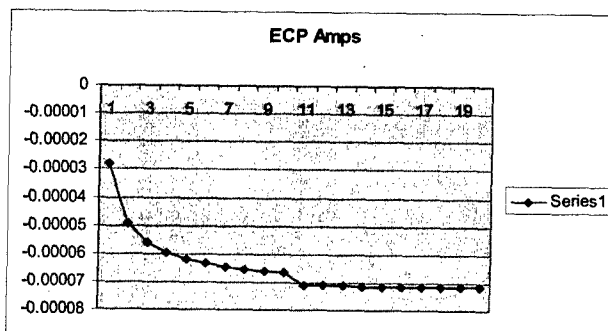
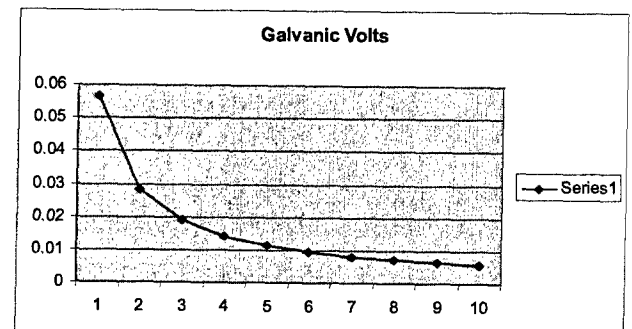
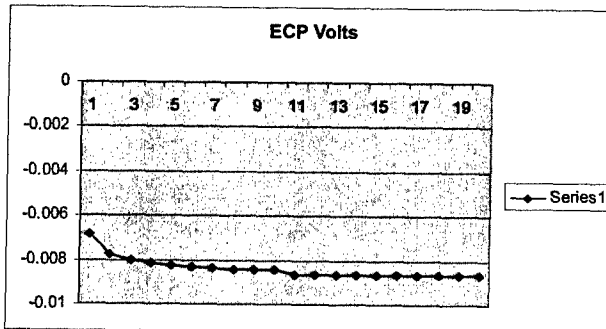
July 9, 2004 – 4 MW run



July 12, 2004 – 4 MW run



July 15, 2004 – 4 MW run



Appendix E – ECP Data

Pt-Pt Couple

Power (W)	Temperature (°C)	ECP Volts (V)	ECP Amps (A)	Resistivity (Ω/cm)	Conductivity (S-cm)
0	300	-0.01498	-5.48E-06	2.73E+03	2.01E-09
0	300	-0.01426	-5.67E-06	2.52E+03	2.25E-09
0	300	-0.04651	-6.16E-05	7.55E+02	8.17E-08
0	300	-0.04386	-0.000050161	8.74E+02	5.74E-08
0	300	-0.0124	-1.53E-05	8.11E+02	1.89E-08
0	300	-0.01301	-1.88E-05	6.91E+02	2.73E-08
0	300	-0.0033	-2.38E-05	1.39E+02	1.71E-07
60	265.556	-0.00733	-1.16E-05	6.29E+02	1.85E-08
60	262.778	-0.0072	-1.16E-05	6.19E+02	1.88E-08
60	271.111	-0.00745	-1.28E-05	5.84E+02	2.18E-08
60	271.111	-0.00736	-1.27E-05	5.78E+02	2.20E-08
1000000	270	-0.01687	-2.33943E-05	7.21E+02	3.24E-08
2000000	271.111	-0.0169	-2.41E-05	7.01E+02	3.44E-08
3000000	268.333	-0.0165	-2.43E-05	6.80E+02	3.57E-08
4000000	265.556	-0.01608	-2.39267E-05	6.72E+02	3.56E-08
30000	223.889	-0.0076	-1.04964E-05	7.24E+02	1.45E-08
4000000	221.111	-0.0311	-2.28E-05	1.36E+03	1.67E-08
4000000	221.111	-0.021	-1.62669E-05	1.29E+03	1.26E-08
4350000	221.111	-0.0273	-2.24E-05	1.22E+03	1.84E-08
4000000	220.556	-0.00765	-1.95641E-05	3.91E+02	5.00E-08
4000000	78.889	-0.07961	-2.55034E-06	3.12E+04	8.17E-11
4200000	78.889	-0.1011	-3.20E-06	3.16E+04	1.01E-10
4200000	77.222	-0.094	-2.86E-06	3.28E+04	8.72E-11
4200000	76.111	-0.0847	-3.08004E-06	2.75E+04	1.12E-10
4100000	248.889	-0.06409	-0.00282352	2.27E+01	1.24E-04
4000000	243.889	-0.0948	-4.53E-05	2.09E+03	2.16E-08
4000000	248.889	-0.0816	-4.02E-05	2.03E+03	1.98E-08
4000000	248.889	-0.06232	-4.72276E-05	1.32E+03	3.58E-08
4000000	248.889	4.29238	-4.90121E-05	8.76E+04	5.60E-10
4200000	248.889	-0.02601	-5.30289E-05	4.90E+02	1.08E-07
4000000	248.889	-0.0191	-0.000062117	3.07E+02	2.02E-07
4000000	248.889	-0.0229	-5.64E-05	4.06E+02	1.39E-07
4000000	248.889	-0.0172	-0.000066141	2.60E+02	2.54E-07
4300000	248.333	-0.0151	-6.71E-05	2.25E+02	2.98E-07
4300000	248.889	-0.00788	-7.24488E-05	1.09E+02	6.66E-07
4300000	248.889	-0.00586	-7.55122E-05	7.76E+01	9.73E-07

Zircaloy-Pt Couple

Power (W)	Temperature (°C)	ECP Volts (V)	ECP Amps (A)	Resistivity (Ω/cm)	Conductivity (S-cm)	Water Resistivity (Ω/cm)	Zr-2 Resistivity (Ω/cm)
0	300	-0.299655	-5.98554E-06	5.01E+04	2.00E-05	2731.956413	4.73E+04
0	300	-0.278868	-6.22213E-06	4.48E+04	2.23E-05	2516.002908	4.23E+04
0	300	-0.0764618	-5.98121E-05	1.28E+03	7.82E-04	754.5290399	5.24E+02
0	300	-0.207006	-4.59451E-05	4.51E+03	2.22E-04	874.384482	3.63E+03
0	300	-0.517888	-1.62577E-05	3.19E+04	3.14E-05	810.8709015	3.10E+04
0	300	-0.494585	-1.88151E-05	2.63E+04	3.80E-05	690.7353332	2.56E+04
0	300	-0.000335344	-2.34669E-05	1.43E+01	7.00E-02	138.9064276	1.25E+02
60	265.556	-0.180272	-1.31499E-05	1.37E+04	7.29E-05	629.2385612	1.31E+04
60	262.778	-0.169355	-1.29969E-05	1.30E+04	7.67E-05	618.5407593	1.24E+04
60	271.111	-0.213451	-1.45668E-05	1.47E+04	6.82E-05	584.0343052	1.41E+04
60	271.111	-0.203464	-1.43306E-05	1.42E+04	7.04E-05	578.2344992	1.36E+04
1000000	270	-0.150256	-2.51411E-05	5.98E+03	1.67E-04	721.1158274	5.26E+03
2000000	271.111	-0.137629	-2.62189E-05	5.25E+03	1.91E-04	701.3175641	4.55E+03
3000000	268.333	-0.122581	-2.65479E-05	4.62E+03	2.17E-04	679.6752388	3.94E+03
4000000	265.556	-0.111465	-2.60624E-05	4.28E+03	2.34E-04	672.0525605	3.60E+03
30000	223.889	-0.110251	-1.16626E-05	9.45E+03	1.06E-04	724.0577722	8.73E+03
4000000	221.111	-0.0549524	-2.38017E-05	2.31E+03	4.33E-04	1364.651575	9.44E+02
4000000	221.111	-0.0802635	-1.94661E-05	4.12E+03	2.43E-04	1290.965089	2.83E+03
4350000	221.111	-0.0913475	-2.06964E-05	4.41E+03	2.27E-04	1217.842055	3.20E+03
4000000	220.556	-0.0996254	-1.88003E-05	5.30E+03	1.89E-04	391.0223317	4.91E+03
4000000	78.889	-0.0496222	-2.62984E-06	1.89E+04	5.30E-05	31215.44578	1.23E+04
4200000	78.889	-0.0667444	-3.28554E-06	2.01E+04	4.98E-05	31611.92686	1.15E+04
4200000	77.222	-0.0619686	-3.08412E-06	1.37E+04	7.30E-05	32825.01126	1.91E+04
4200000	76.111	-0.0459537	-3.35691E-06	1.37E+04	7.30E-05	27499.64286	1.38E+04
4100000	248.889	-0.0262854	-0.00251044	1.05E+01	9.55E-02	22.69861733	1.22E+01
4000000	243.889	-0.0582953	-3.65238E-05	1.60E+03	6.27E-04	2094.948919	4.99E+02
4000000	248.889	-0.0572194	-0.000047771	1.20E+03	8.35E-04	2032.236855	8.34E+02
4000000	248.889	-0.22051	-4.83276E-05	4.56E+03	2.19E-04	1319.567372	3.24E+03
4000000	248.889	-0.0221873	-4.99286E-05	4.44E+02	2.25E-03	-87577.96544	8.80E+04
4200000	248.889	-0.017738	-6.22858E-05	2.85E+02	3.51E-03	490.4872626	2.06E+02
4000000	248.889	-0.017738	-6.22858E-05	2.85E+02	3.51E-03	307.4842636	2.27E+01
4000000	248.889	-0.0212619	-5.63743E-05	3.77E+02	2.65E-03	406.139265	2.90E+01
4000000	248.889	-0.0201533	-6.70171E-05	3.01E+02	3.33E-03	260.0504982	4.07E+01
4300000	248.333	-0.0148352	-6.69196E-05	2.22E+02	4.51E-03	225.1399297	3.45E+00
4300000	248.889	-0.00792714	-7.35919E-05	1.08E+02	9.28E-03	108.7664668	1.05E+00
4300000	248.889	-0.00632854	-7.51463E-05	8.42E+01	1.19E-02	77.60335416	6.61E+00

Zircaloy-X750 Couple

Power (W)	Temp. (°C)	ECP Volts (V)	ECP Amps (A)	Resistivity (Ω/cm)	Conductivity (S-cm)	Water Resistivity (Ω/cm)	Zr-2 Resistivity (Ω/cm)	X-750 Resistivity (Ω/cm)
0	300	-0.32544	-6.3907E-06	5.09E+04	1.96E-05	2731.956413	4.73E+04	8.61E+02
0	300	-0.310167	-5.8804E-06	5.27E+04	1.90E-05	2516.002908	4.23E+04	7.93E+03
0	300	-0.406071	-1.7581E-05	2.31E+04	4.33E-05	754.5290399	5.24E+02	2.18E+04
0	300	-0.443373	-1.9162E-05	2.31E+04	4.32E-05	874.384482	3.63E+03	1.86E+04
0	300	-0.526066	-2.0635E-05	2.55E+04	3.92E-05	810.8709015	3.10E+04	6.36E+03
0	300	-0.521837	-2.1159E-05	2.47E+04	4.05E-05	690.7353332	2.56E+04	1.62E+03
0	300	-0.13123	-1.5573E-05	8.43E+03	1.19E-04	138.9064276	1.25E+02	8.16E+03
60	265.556	-0.18912	-2.0649E-05	9.16E+03	1.09E-04	629.2385612	1.31E+04	4.55E+03
60	262.778	-0.178039	-2.0502E-05	8.68E+03	1.15E-04	618.5407593	1.24E+04	4.35E+03
60	271.111	-0.232452	-2.0979E-05	1.11E+04	9.02E-05	584.0343052	1.41E+04	3.57E+03
60	271.111	-0.218974	-2.1201E-05	1.03E+04	9.68E-05	578.2344992	1.36E+04	3.87E+03
1000000	270	-0.187857	-2.1851E-05	8.60E+03	1.16E-04	721.1158274	5.26E+03	2.62E+03
2000000	271.111	-0.183208	-2.129E-05	8.61E+03	1.16E-04	701.3175641	4.55E+03	3.36E+03
3000000	268.333	-0.16769	-2.1E-05	7.99E+03	1.25E-04	679.6752388	3.94E+03	3.37E+03
4000000	265.556	-0.15127	-2.0412E-05	7.41E+03	1.35E-04	672.0525605	3.60E+03	3.13E+03
30000	223.889	-0.123451	-1.3681E-05	9.02E+03	1.11E-04	724.0577722	8.73E+03	4.30E+02
4000000	221.111	-0.116688	-8.8681E-06	1.32E+04	7.60E-05	1364.651575	9.44E+02	1.08E+04
4000000	221.111	-0.146594	-1.0286E-05	1.43E+04	7.02E-05	1290.965089	2.83E+03	1.01E+04
4350000	221.111	-0.143138	-1.2243E-05	1.17E+04	8.55E-05	1217.842055	3.20E+03	7.28E+03
4000000	220.556	-0.13432	-9.7601E-06	1.38E+04	7.27E-05	391.0223317	4.91E+03	8.46E+03
4000000	78.889	-0.0505826	-2.2916E-06	2.21E+04	4.53E-05	31215.44578	1.23E+04	2.15E+04
4200000	78.889	-0.0472375	-2.5353E-06	1.86E+04	5.37E-05	31611.92686	1.15E+04	2.45E+04
4200000	77.222	-0.0614511	-2.7856E-06	2.21E+04	4.53E-05	32825.01126	1.91E+04	2.99E+04
4200000	76.111	-0.0473553	-2.9369E-06	1.61E+04	6.20E-05	27499.64286	1.38E+04	2.52E+04
4100000	248.889	-0.0043727	-0.00044198	9.89E+00	1.01E-01	22.69861733	1.22E+01	2.50E+01
4000000	243.889	-0.0055496	-8.9744E-05	6.18E+01	1.62E-02	2094.948919	4.99E+02	2.53E+03
4000000	248.889	-0.0780184	-2.67E-05	2.92E+03	3.42E-04	2032.236855	8.34E+02	5.53E+01
4000000	248.889	0.581803	-2.9896E-05	-1.95E+04	-5.14E-05	1319.567372	3.24E+03	2.40E+04
4000000	248.889	-0.0374805	-3.5276E-05	1.06E+03	9.41E-04	-87577.9654	8.80E+04	6.18E+02
4200000	248.889	-0.0294753	-5.0426E-05	5.85E+02	1.71E-03	490.4872626	2.06E+02	1.12E+02
4000000	248.889	-0.0294753	-5.0426E-05	5.85E+02	1.71E-03	307.4842636	2.27E+01	2.54E+02
4000000	248.889	-0.032964	-4.5026E-05	7.32E+02	1.37E-03	406.139265	2.90E+01	2.97E+02
4000000	248.889	-0.030301	-5.6851E-05	5.33E+02	1.88E-03	260.0504982	4.07E+01	2.32E+02
4300000	248.333	-0.0282423	-5.5173E-05	5.12E+02	1.95E-03	225.1399297	3.45E+00	2.83E+02
4300000	248.889	-0.0128056	-6.6737E-05	1.92E+02	5.21E-03	108.7664668	1.05E+00	8.21E+01
4300000	248.889	-0.0090447	-7.1479E-05	1.27E+02	7.90E-03	77.60335416	6.61E+00	4.23E+01

Appendix F – Galvanic Data

Zircaloy-Pt Couple

Power (W)	Temperature (°C)	Volts (V)	Amps (A)
0	300	0.000432307	8.45972E-06
0	300	0.000453008	5.89889E-06
0	300	0.000306517	-2.9958E-05
0	300	0.000571941	-1.2436E-05
0	300	0.000455308	4.17026E-05
0	300	0.000455078	3.69525E-05
0	300	0.000321928	-2.0945E-05
60	265.556	0.000626835	3.20347E-06
60	262.778	0.000653976	2.21947E-06
60	271.111	0.000550628	4.61193E-06
60	271.111	0.000456173	4.22103E-06
1000000	270	0.000845032	-1.3343E-05
2000000	271.111	0.00129392	-1.4019E-05
3000000	268.333	0.00122568	-1.4504E-05
4000000	265.556	0.00101661	-1.5328E-05
30000	223.889	0.00120437	-8.7315E-06
4000000	221.111	0.000413545	-2.5748E-05
4000000	221.111	0.000345235	-1.9471E-05
4350000	221.111	0.000194122	-2.1699E-05
4000000	220.556	0.000385255	-1.9137E-05
4000000	78.889	0.000029057	-2.6274E-06
4200000	78.889	2.93637E-05	-3.1825E-06
4200000	77.222	2.71403E-05	-3.1931E-06
4200000	76.111	0.000023997	-3.1524E-06
4100000	248.889	0.00470505	-0.00212674
4000000	243.889	0.00435627	-0.00019362
4000000	248.889	0.00654239	-4.7894E-05
4000000	248.889	0.00240877	-4.7134E-05
4000000	248.889	0.00610354	-4.6709E-05
4200000	248.889	0.00588922	-5.7866E-05
4000000	248.889	0.00588922	-5.7866E-05
4000000	248.889	0.0064987	-5.2489E-05
4000000	248.889	0.00548663	-5.6247E-05
4300000	248.333	0.00530971	-5.8961E-05
4300000	248.889	0.00519534	-6.6223E-05
4300000	248.889	0.00661039	-6.7212E-05

Zircaloy-X750 Couple

Power (W)	Temperature (°C)	Volts (V)	Amps (A)
0	300	0.000436447	3.33718E-06
0	300	0.000447181	2.35226E-06
0	300	0.000452318	2.13312E-05
0	300	0.000451551	1.74476E-05
0	300	0.000457224	1.61925E-05
0	300	0.000460215	1.65482E-05
0	300	0.00025101	-6.84903E-06
60	265.556	0.000386712	-1.24261E-05
60	262.778	0.000655586	-1.27474E-05
60	271.111	0.000639256	-9.64865E-06
60	271.111	0.0004942	-1.07538E-05
1000000	270	0.000693536	-8.76502E-06
2000000	271.111	0.000677359	-7.69927E-06
3000000	268.333	0.000407106	-8.2148E-06
4000000	265.556	0.000467673	-9.02906E-06
30000	223.889	0.00166905	-1.00024E-05
4000000	221.111	-0.110251	-1.16626E-05
4000000	221.111	0.00146351	-6.42842E-06
4350000	221.111	0.00324626	-5.60431E-06
4000000	220.556	0.00274225	-9.31305E-06
4000000	78.889	0.00127099	-4.20061E-06
4200000	78.889	3.28905E-05	-2.86337E-06
4200000	77.222	0.000024687	-2.77583E-06
4200000	76.111	0.000027907	-2.91526E-06
4100000	248.889	0.00566463	-0.000114533
4000000	243.889	0.0052296	-0.000085416
4000000	248.889	0.00438808	-0.000194056
4000000	248.889	0.00239865	-4.53562E-05
4000000	248.889	0.00436593	-0.000200685
4200000	248.889	0.00552334	-4.53559E-05
4000000	248.889	0.00552334	-4.53559E-05
4000000	248.889	0.00623294	-4.13855E-05
4000000	248.889	0.00516812	-4.73973E-05
4300000	248.333	0.00529675	-4.69493E-05
4300000	248.889	0.00580743	-5.95676E-05
4300000	248.889	0.00421093	-5.07742E-05